Islamic Azad University
Majlesi Branch

International Journal of

ADVANCED DESIGN AND MANUFACTURING TECHNOLOGY

Vol. 15, No. 4, December 2022

SUBSCRIPTION FORM

Please enter my annual subscription to the International Quarterly, Journal of Advanced Design and Manufacturing Technology (ADMT), including 4 quarterly issues for the year……Volume……Numbers……

	Internal	***International***
⌗ Institutional	R 600000	€ 400
⌗ Personal	R 400000	€ 300
⌗ Student	R 300000	€ 200
⌗ Single copy	R 100000	€ 80

Name: ***Tel:*** ***Email:***

Mailing Address:

Payment method: Check or money order must be made to order of:
Iran: Account# 0103249224008 CIBA, Melli Bank of Iran
In the Name of: Islamic Azad University, Majlesi Branch

* Please allow 3-5 weeks for delivery Bank order enclosed

stamp

To:
An International Quarterly, Journal of Advanced Design and Manufacturing Technology
Islamic Azad University Majlesi Branch , Esfahan ,IRAN
Mailbox : 84815/119
Tel: (+98) 31 52472907
Tel: (+98) 31 52472290, Ext : 312
Fax: (+98) 31 52472294

CONTENTS

Volume15, No.4, December 2022

This journal has the permission number 87/5265 from Research Deputy of Islamic Azad University.

COPYRIGHT RELEASE

Title of Manuscript:

AUTHOR(S):

I (we) hereby assign and transfer all copyrights in and to the manuscript named above, in all forms and media of expression now known or later developed, to the effective if and when it is accepted for publication in the International Quarterly, ***Journal of Advanced Design and Manufacturing Technology (ADMT)*** by the Islamic Azad University Majlesi Branch.

I (we) also confirm that the manuscript is not in the public domain and is original on my (our) part except for such excerpts copyrighted works as may be included with the written permission of the copyright owners. I (we) further warrant that the manuscript contains no libelous, obscene, or unlawful statements and does not infringe upon or violate any copyright, trademark, or other right or the privacy of others. I (we) warrant that, in the case of sole authorship, that I am (we are) the sole owner of the manuscript and all copyrights therein and have full power and authority to register all copyrights therein and to make this agreement, and that, in the case of multiple authorship, these powers of ownership are shared with all other contributing authors. I (we) acknowledge that the International Journal of Design and Manufacturing Technology (ADMT) is relying on this release in publishing this manuscript in the Journal.

Regarding with the conflicts of interest, submitted manuscript must be accompanied with a statement form the authors disclosing all financial and personnel relationship that might bias their work, if any. Besides, the authors are requested to evident whether impending conflicts do or do not exist. This should cover the proclamation and if there are further details, could be mentioned in the copyright. If an organization encompasses any financial interest in the outcome of the study, the authors are appealed to provide a declaration that have full access to all the data in the study and take complete responsibility for the integrity of the data and the accuracy of the data analysis.

All authors are requested to sign this form upon acceptance of manuscript and fax in to the Editorial Office. It is preferable to be scanned and then submitted through the Journal email.

(1)Author Signature	Print name	Data
(2)Author Signature	Print name	Data
(3)Author Signature	Print name	Data
(4)Author Signature	Print name	Data
(5)Author Signature	Print name	Data
The corresponding Author signature	Print name	Data

The sole responsibility for the whole content(s) of article (views and statements) remains only with the author (s).

PLEASE NOTE: Manuscripts cannot be processed for publication until the publisher has received this signed form. If the manuscript is not published in the Journal, this release will not take effect.

RETURN TO: Editorial Office,
International Journal of Design and Manufacturing Technology (ADMT),
Department of Mechanical Engineering, IAU, Majlesi Branch, Isfahan, Iran
Mail Box: 86315/111

http://Admt.isfahan.iau.ir
Email: Journalmechanic@gmail.com

Int. J. Advanced Design and Manufacturing Technology, 2022, Vol. 15, No. 4, pp. 1-12

DOI: 10.30486/admt.2023.1959626.1353 *ISSN: 2252-0406* *https://admt.isfahan.iau.ir*

Trajectory Tracking Control of a Novel Planner Continuum Robot

Seyed Shoja Amini
Department of Mechanical Engineering,
Iran University of Science and Technology, Tehran, Iran
E-mail: shjamini@gmail.com

Ali Keymasi Khalaji *
Department of Mechanical Engineering, Faculty of Engineering,
University of Kharazmi, Tehran, Iran
E-mail: keymasi@khu.ac.ir,
*Corresponding author

Received: 30 May 2022, Revised: 18 September 2022, Accepted: 23 October 2022

Abstract: Researchers have a special fondness for continuum robots (CRs) due to their various applications. CRs have been modeled in different ways. One of these methods is called lumped model. Although the lumped modeling of CRs needs multiple degrees of freedom, researchers have considered only a few degrees of freedom. But considering such structures led to some issues in the accuracy of the controller. Therefore, in this paper, the dynamic modeling of a CR which is based on the lumped model is developed in a general form. Additionally, a control strategy based on sliding mode back-stepping control is proposed after introducing the first and second Lyapunov functions for stability proof. Moreover, a new function in the control law is used to avoid chattering phenomena. The proposed controller can reduce the settling time, which is one of the most important factors in controlling such robots. To demonstrate the efficiency of the proposed method, three different case studies are conducted for a planar 8-DOF continuum manipulator and the simulations are compared with the feedback linearization method (FL). The simulations show the effectiveness of the proposed method for controlling the continuum robot.

Keywords: Feedback Linearization, Lagrange Formulation, Model-Based Control, Multi-DOF Continuum Robot, Redundancy, Sliding Mode Control

Biographical notes: Seyed Shoja Amini received his B.Sc. in Mechanical Engineering from the Islamic Azad University, North Tehran Branch in 2015 and his M.Sc. in Mechanical Engineering from Iran University of Science and Technology (IUST), Tehran, Iran in 2018. **Ali Keymasi Khalaji** received his B.Sc. from IUST, Tehran, Iran, in 2007, and his M.Sc. and Ph.D. in Mechanical Engineering from K. N. Toosi University of Technology (KNTU), Tehran, in 2009 and 2014, respectively. His research interests include modeling and control of mechanical systems, nonlinear control, adaptive and robust control with applications to mobile robotic systems, and mechatronics.

Research paper

1 INTRODUCTION

Recently, a new class of robots called continuum robots (CRs) has been introduced. These robots resemble flexible robots with many joints and degrees of freedom that allow them to adapt to and move easily in convoluted places. CRs are considered a special group inspired by some parts of animals such as octopuses, elephants or the tail of reptiles [1-4]. CRs are mainly used in medical surgery [5], e.g., in the cardiorespiratory, digestive and urogenital systems [6-9]. Although CRs have many advantages and applications, nevertheless they do not have sufficiently rigid structures, so this situation makes it hard to find a relationship between actuators and end-effector. There are some different methods for modeling CRs: classical methods [10], emerging techniques [11] and combined methods [12-13]. Although the classical methods provide an exact solution for the statics of the continuum robot, there are pitfalls in extending them to the dynamics, as this would involve the solution of a system of partial differential Equations (PDE) [14]. The PDE can represent the Equations of motion of CRs with Cosserat rod dynamics [15]. Since such Equations are so complicated, emerging techniques have been introduced. Reference [11] attempts to overcome the limitations of constant curvature modeling by replacing circular curves with Euler curves, which were found to be more suitable for a pneumatic continuum robot. Furthermore, some other methods were used in the modeling of the CRs. For instance, the backbone model is like ropes and strings with infinite degrees of freedom. Mochiyama and Suzuki, using the Frenet-Serret formulas, could approximate the kinematics and dynamics of such a model [16]. Yoon and Yi designed a flexible 4-DOF robot, cable-driven CRs, consisting of two modules with a backbone spring [17]. This model was imitated from the biological backbone and its main goal was considering collision avoidance. In another research, the Equations of motion of planar continuum manipulators were extracted by Tatlicioglu et all. considering the effects of potential energy. However, this model has not been experimentally validated [18]. The control of CRs can be divided into three different types. The first would be kinematic control [19]. This method uses a forward and inverse kinematic modeling of the system. The second type is the feedforward position control strategy which is based on a Piecewise Constant Curvature hypothesis. This method improved the robustness against disturbances of the system [20-21]. The third one is differential kinematics, which is partially effective for redundant manipulators because it allows multi-task control [22]. However, this method requires some assumptions that reduce the accuracy of the system. To address this problem, adaptive and learning approaches have been introduced by some researchers. These approaches are based on data gathering [23]. In another study, the authors proposed an observer control based on Youla parameterization for a flexible link with the lumped tip mass [24-25]. The idea of this method was based on the using Youla parameter instead of finding the transfer function. But, the limitation of this method is that the dynamics Equations should be linearized.

There are many challenges in modeling CRs because the structure has an unlimited number of degrees of freedom, which makes the formulation very complex. For this reason, researchers have considered limited degrees of freedom in modeling based on a lumped model [26]. However, modeling and control of CRs require accurate dynamic models. To improve the efficiency of dynamic modeling and the difficulties mentioned in the previous paragraph, this paper extracts the kinematic and dynamic Equations in general form through the Lagrangian formulation. In addition, the accurate position control of the end-effector by the sliding mode back-stepping control (SMBSC) method is investigated. The accuracy and speed in controlling this type of robot are crucial in surgical and medical applications. By introducing such a controller, not only is the error negligible but also the settling time decreases sharply. This paper is organized as follows. In the first section, the dynamic modeling of this robot is presented and the Equations of motion of this system are developed using the Lagrangian formulation. Section 2 explains the formulation of SMBSC. Section 3 shows how to linearize a nonlinear system using the input-output with the feedback linearization method. Simulation using MATLAB software is presented in section 4. Section 5 contains the conclusion of the paper.

2 MODELING

One model of CRs comprises a 2n degrees of freedom arm which is demonstrated in “Fig. 1”. The idea of this model was obtained from [26]. System dynamic is obtained with Lagrange method:

$$\frac{d}{dt}\left(\frac{\partial L}{\partial \dot{q}}\right)-\left(\frac{\partial L}{\partial q}\right)+\left(\frac{\partial D}{\partial \dot{q}}\right)=Q \tag{1}$$

Where, L represents the kinetic energy minus potential energy of the system. In addition, Q is the vector of generalized forces. The Equations of motion are demonstrated as:

$$\begin{aligned}&[I]_{2n\times 2n}[\ddot{q}]_{2n\times 1}+[C]_{2n\times 1}+[G]_{2n\times 1}=[u]_{2n\times 1}+[d]_{2n\times 1}\\ &,\\ &q=[s_1,s_2,...,s_n,\theta_1,\theta_2,...,\theta_n]^T\\ &u=\left[F_1,F_2,F_3,F_4,...,F_{(2n-1)},F_{2n}\right]^T\end{aligned} \tag{2}$$

Where I demonstrates mass matrix which is symmetric positive definite, C (q, q □) represents the forces of centrifugal and Coriolis force, G(q) is the gravity vector and u(t) is the vector of inputs which include the forces acting on the springs and dampers. In the given Equation, q shows the generalized coordinates, d(t) is the torque that expresses finite disturbance, modelling uncertainties, and unmodulated dynamics.

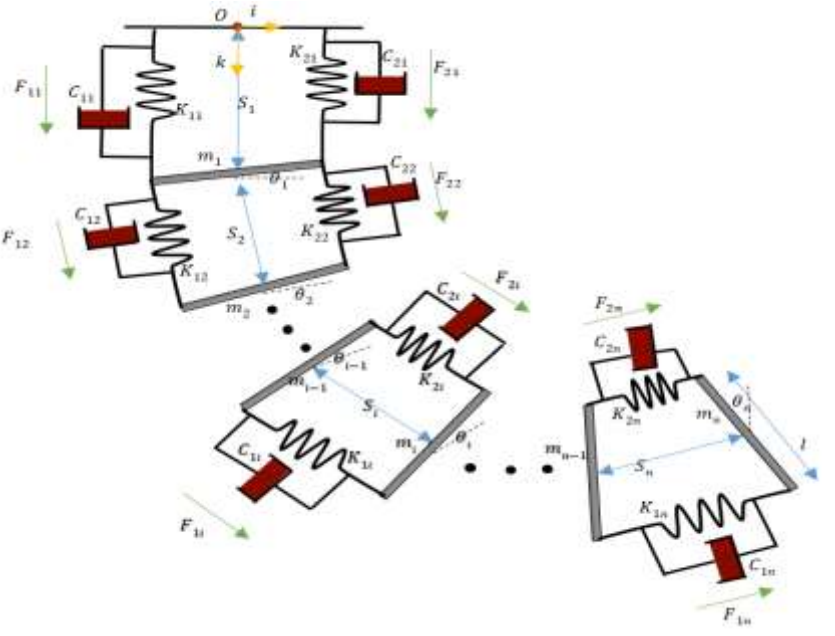

Fig. 1 Continuum robot manipulator via springs and dampers structure.

3 SLIDING MODE BACK-STEPPING CONTROL

In this section, an SMC law for the convergence of robot variables to optimal values is designed. Robust nonlinear SMC control is an effective technique and its applications have greatly increased in recent decades.
The most important feature of SMC is insensitivity to changes and disturbances in system parameters and external disturbances. In addition, it provides a fast-passing response. In the SMC method proposed in this section, by back stepping design, sliding switching plates are introduced, and then, this rule is designed for asymptotic stability of the closed-loop error system. In general, conventional SMC does not have the desired ability to control the system due to the sign (σ) function;
Because the existence of the sign function due to discontinuity around zero, causes the phenomenon of chattering, which is sharp fluctuations around the equilibrium point of error at zero. It is worth mentioning that this problem is considered in the design of the control law.

System description
The first step in designing an SMC law is to define the appropriate sliding plates. But, before that, and in order to start the design process, first the state space of this CR is considered.

$$\begin{aligned} x_1(t) &= q(t) \\ x_2(t) &= \dot{q}(t) \end{aligned} \tag{3}$$

The robot dynamic Equations can be written as follows:

$$\begin{aligned} \dot{x}_1(t) &= x_2(t) \\ \dot{x}_2(t) &= [I]^{-1}_{2n\times 2n}\left\{[u]_{2n\times 1}+[d]_{2n\times 1}-[C]_{2n\times 1}-[G]_{2n\times 1}\right\} \end{aligned} \tag{4}$$

In fact, in the SMBSC method, according to the control diagram showing in the “Fig. 2”, the switching plates are designed in such a way that after applying the controller, the time Equation of this plate and its derivative becomes zero, and when they become zero, the system modes also converge to zero. For this purpose, sliding plates are defined as follows [27].

$$\sigma_i = x_i - \alpha_{i-1} \quad i = 1,2 \tag{5}$$

Where, $\alpha_0 = x_{1d}$ shows the optimal value for x_1, σ_i represents the sliding plate vector, and α_i represents the ideal state vector for x_i and is an intermediate value.

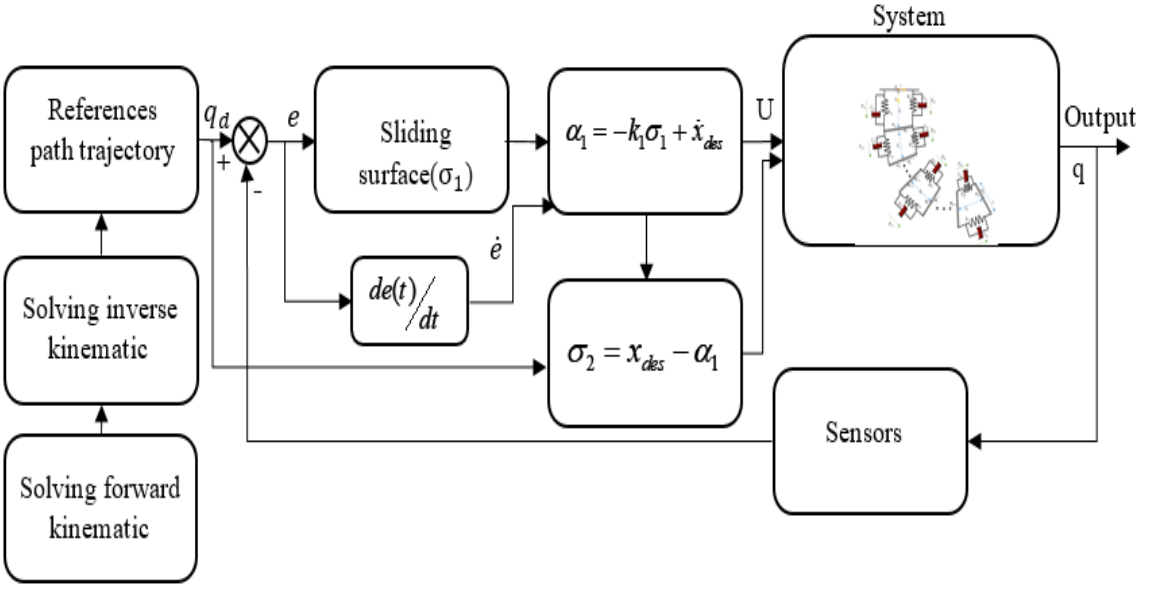

Fig. 2 SM control structure diagram.

Designing sliding mode back-stepping control

The design of the control law in this section will be done in two steps. In the first step, virtual control input is designed and then, the control law will be performed to stabilize the whole design system and prove its stability through Lyapunov. In the first stage, the first subsystem in modeling is the Equation $\dot{x}_1 = x_2$ in which x_2 is a virtual input for this system and the derivative of the first sliding plate ($\sigma_1 = x_1 - x_{1d}$) with respect to time is:

$$\dot{\sigma}_1 = \dot{x}_1 - \dot{x}_{1d} = x_2 - \dot{x}_{1d} \tag{6}$$

On the other hand, according to "Eq. (5)", $\sigma_2 = x_2 - \alpha_1$ and by placing x_2 in "Eq. (6)":

$$\dot{\sigma}_1 = \dot{x}_1 - \dot{x}_{1d} = x_2 - \dot{x}_{1d} = \sigma_2 + \alpha_1 - \dot{x}_{1d} \tag{7}$$

In order to converge the first subsystem to the sliding plate and move on it, the virtual control rule is defined as follows:

$$\alpha_1 = -k_1\sigma_1 + \dot{x}_{1d} \tag{8}$$

Where: $k_1 > 0$.

Now, the first Lyapunov function is considered as follows:

$$V_1 = \frac{1}{2}\sigma_1^T\sigma_1 \tag{9}$$

By calculating the derivative of the Lyapunov function ("Eq. (9)") and placing "Eq. (7)" and "Eq. (8)" in it, "Eq. (10)" is obtained:

$$\dot{V}_1 = \sigma_1^T\dot{\sigma}_1 = -k_1\|\sigma_1\|^2 + \sigma_1^T\sigma_2 \tag{10}$$

In the second stage, the second sliding plate is $\sigma_2 = x_2 - \alpha_1$. The derivative of the second sliding surface with respect to time would be as "Eq. (11)". The "Eq. (4)" and "Eq. (7)" are used as follow:

$$\begin{aligned}&\dot{\sigma}_2 = \dot{x}_2 - \dot{\alpha}_1\\&= I^{-1}(x)[-C(x_1,x_2) - G(x) + u(t) + d(t)]\\&+k_1\dot{\sigma}_1 - \ddot{x}_{1d} = I^{-1}(x)[-C(x_1,x_2) - G(x) + u(t) + d(t)]\\&+k_1(\sigma_2 + \alpha_1 - \dot{x}_{1d}) - \ddot{x}_{1d}\end{aligned} \tag{11}$$

With the following definitions:

$$\begin{aligned}&f(x_1,x_2) \triangleq I^{-1}(x)[-C(x_1,x_2) - G(x)]\\&+k_1(\sigma_2 + \alpha_1 - \dot{x}_{1d}) - \ddot{x}_{1d}\\&g \triangleq I^{-1}(x)\end{aligned} \tag{12}$$

According to the "Eq. (12)", "Eq. (11)" is obtained as follows:

$$\dot{\sigma}_2 = f(x_1,x_2) + gu(t) + gd(t) \tag{13}$$

Now the control law is proposed as follows:

$$u(t) = g^{-1}\left\{-f(x_1, x_2) - k_2\sigma_2 - \sigma_1 - \bar{d}\,\|g\|\,\mathrm{si}\,gn(\sigma_2)\right\} \quad (14)$$

By placing "Eq. (14)" in "Eq. (13)":

$$\dot{\sigma}_2 = -k_2\sigma_2 - \sigma_1 - \bar{d}\,\|g\|\,\mathrm{si}\,gn(\sigma_2) + gd(t) \quad (15)$$

By considering the Lyapunov function:

$$V_2 = V_1 + \frac{1}{2}\sigma_2^T\sigma_2 \quad (16)$$

The derivative of the Lyapunov function with respect to time becomes as "Eq. (17)". In this Equation, "Eq. (10)" has been utilized.

$$\dot{V}_2 = \dot{V}_1 + \sigma_2^T\dot{\sigma}_2 = -k_1\|\sigma_1\|^2 + \sigma_1^T\sigma_2 + \sigma_2^T\dot{\sigma}_2 \quad (17)$$

By placing the derivative of second sliding plate ("Eq. (15)") in "Eq. (17)":

$$\begin{aligned}\dot{V}_2 &= \dot{V}_1 + \sigma_2^T\dot{\sigma}_2\\ &= -k_1\|\sigma_1\|^2 + \sigma_1^T\sigma_2\\ &+\sigma_2^T(-k_2\sigma_2 - \sigma_1 - \bar{d}\,\|g\|\,\mathrm{si}\,gn(\sigma_2) + gd(t))\\ &= -k_1\|\sigma_1\|^2 + \sigma_1^T\sigma_2 - k_2 gd(t)\end{aligned} \quad (18)$$

The expressions ${\sigma_1}^T\sigma_2$ is transpose of ${\sigma_2}^T\sigma_1$ and are therefore equaled and deleted with each other.

$$\begin{aligned}\dot{V}_2 &= -k_1\|\sigma_1\|^2 - k_2\|\sigma_2\|^2 - \bar{d}\,\|g\|\sigma_2^T\,\mathrm{si}\,gn(\sigma_2)\\ &+\sigma_2^T gd(t) = -k_1\|\sigma_1\|^2 - k_2\|\sigma_2\|^2 - \bar{d}\,\|g\|\|\sigma_2\|\\ &+\sigma_2^T gd(t) \le -k_1\|\sigma_1\|^2 - k_2\|\sigma_2\|^2 - \bar{d}\,\|g\|\|\sigma_2\|\\ &+\|\sigma_2\|\|g\|\|d(t)\|\\ &= -k_1\|\sigma_1\|^2 - k_2\|\sigma_2\|^2 + (\|d(t)\| - \bar{d})\|\sigma_2\|\|g\| < 0\end{aligned} \quad (19)$$

On the other hand, according to the assumption $\|d(t)\| \le \bar{d}$ where $\bar{d} \in R^+$, the Equation $\|d(t)\| - \bar{d} \le 0$ is gained and consequently $\dot{V}_2 < 0$. Therefore, the $\dot{V}$ is negative for all values of σ, and as a result, according to the definition of sliding plates and Lyapunov's theorem, it can be concluded that when the sliding plate becomes zero, the error value converges to zero and finally $x_1 \to x_{1d}$.

Improving the discontinuity in the controller

In the controller expressed in "Eq. (14)", the sign function with a coefficient in the Equation is used. The sign function $u = \bar{d}sign(\sigma)$, which can also be expressed as: $u = \bar{d}\,\sigma/\|\sigma\|$, is a discontinuous function around σ = 0. This discontinuity in the law of control can provide difficulty and cause a phenomenon called chattering. This phenomenon causes fluctuations in the input value of the robot system, especially when the system is exposed to noise. To counteract the chattering phenomenon, the value of u in the control law must be changed. To address this issue, proposals such as using $\tanh(\sigma)$ or saturation function (sat (σ)) instead of $\sigma/\|\sigma\|$ have been suggested. However, another idea is used in this paper. Due to the fact that this discontinuity occurs when σ convergences to zero, the best choice to prevent discontinuities and unevenness in u is to add a term and consider it as follows:

$$u = \frac{\bar{d}^2\sigma}{\bar{d}\,\|\sigma\| + \Gamma(t)} \quad (20)$$

Where, Γ(t) is a positive function such that $\int_0^\infty \Gamma(t)dt < \infty$ (tends to zero over time). By selecting the sign function in the control law as "Eq. (20)", the obstacle of discontinuity in the control law will be solved. The choice of this function is arbitrary and for example one of the options can be as follows:

$$\Gamma(t) = \frac{1}{1+t^n}\ , n \ge 2 \quad (21)$$

It should be noted that when Γ(t) becomes zero, the value of u in "Eq. (20)" will be similar to the $\rho\,\sigma/\|\sigma\|$.

4 FEEDBACK LINEARIZATION CONTROL BY INPUT-OUTPUT METHOD

In this method, nonlinear system dynamics transform into a (fully or partly) linear one, so that linear control techniques can be applied. First of all, we have to generate a direct relationship between the output y(t) and the input u(t). By taking two differentiations, the control input will appear to the output of this system and accordingly the relative degree of each of the outputs is equal to 2. It is obvious that if the control input never appears after more than n differentiations, the system would not be controllable. Also, in some cases, internal dynamics must be studied. Since the number of inputs and outputs are the same in this system, there is no internal dynamics. Also, it is indispensable to define a suitable output vector describing the system's attitude properly. The output of the system is all generalized coordinates and is defined as "Eq. (22)":

$$y = [s_1, s_2, ..., s_n, \theta_1, \theta_2, ..., \theta_n] \quad (22)$$

Then, according to the Equations of motion governing the system, the new input of the system is equaled to:

$$[\upsilon]_{2n\times1} = [\ddot{q}]_{2n\times1} = [I]^{-1}_{2n\times2n}\left\{-[C]_{2n\times1} - [G]_{2n\times1} + [u]_{2n\times1} + [d]_{2n\times1}\right\} \quad (23)$$

The state-space representation of the system is:

$$\dot{x} = \frac{d}{dt}\begin{bmatrix}[q]\\ [\dot{q}]\end{bmatrix} = \begin{bmatrix} \dot{s}_1 \\ \dot{s}_2 \\ \vdots \\ \dot{s}_n \\ \dot{\theta}_1 \\ \dot{\theta}_2 \\ \vdots \\ \dot{\theta}_n \\ ------ \\ [I]^{-1}_{2n\times2n}\left\{-[C]_{2n\times1} - [G]_{2n\times1} + [u]_{2n\times1} + [d]_{2n\times1}\right\} \end{bmatrix}_{4n\times1} \quad (24)$$

In this part, u must be selected in such a way as to eliminate the nonlinear terms of the system. Therefore, according to "Eq. (23)", "Eq. (25)" is obtained:

$$[u]_{2n\times1} = [I]_{2n\times2n}[\upsilon]_{2n\times1} + [C]_{2n\times1} + [G]_{2n\times1} - [d]_{2n\times1} \quad (25)$$

The following form of "Eq. (24)" is converted to "Eq. (26)":

$$\dot{x} = \begin{bmatrix}[0]_{(2n\times2n)} & [I]_{(2n\times2n)}\\ [0]_{(2n\times2n)} & [0]_{(2n\times2n)}\end{bmatrix}[x] + \begin{bmatrix}[0]_{(2n\times2n)}\\ [I]_{(2n\times2n)}\end{bmatrix}[\upsilon] \in 4n\times1$$
$$y = [[I]_{(2n\times2n)} \quad [0]_{(2n\times2n)}][x] \in 2n\times1 \quad (26)$$

5 NUMERICAL SIMULATION IN MATLAB

In this section, the model proposed in the first section is considered. This continuum robot contains four masses of rigid rod and eight springs and dampers. The generalized coordinates are chosen as:

$$q = [s_1, s_2, s_3, s_4, \theta_1, \theta_2, \theta_3, \theta_4]^T \quad (27)$$

The dynamic characteristics of the robot are presented in the following "Table 1". In the following, three different cases are considered.

Table 1 The dynamic characteristics of continuum robot

parameters	value	unit
M_i	$M_1 = 0.2$; $M_2 = 0.15$; $M_3 = 0.15$; $M_4 = 0.1$	Kg
I_i	$I_1 = I_2 = I_3 = I_4 = 0.001$	$Kg.m^2$
k_i	$k_{11} = 30$; $k_{12} = 25$; $k_{13} = 15$; $k_{14} = 15$ $k_{21} = 30$; $k_{22} = 25$; $k_{23} = 15$; $k_{24} = 15$	$N.m^{-1}$
c_i	$c_{11} = c_{12} = c_{13} = c_{14} = 10$ $c_{21} = c_{22} = c_{23} = c_{24} = 10$	$N.s.m^{-1}$
S_{0i}	$S_{01} = S_{01} = 0.2$; $S_{03} = S_{04} = 0.15$	m
l	$l = 0.2$	m
g	$g = 9.81$	$N.kg^{-1}$

Case study 1: point-to-point control design

In this subsection, point-to-point controller with SMC and FL is considered. The start and end points of the point-to-point motion are considered as $p_i(0.3, 0.25, 0.2, 0.15)$ and $p_f(0.4, 0.35, 0.3, 0.25)(m)$, respectively. The initial and desired angles are $(0.15, 0.1, 0.05, 0.05)$ and $(0.25, 0.2, 0.1, 0.1)(rad)$, respectively. The results of simulation are shown in "Fig. 3" to "Fig. 9". Figure 3 and "Fig. 4" display the time varying changes of the extension of each module with FL and SMS methods. It is observed that state variables start from their initial conditions and finally reach to their final positions. All the states with SMC method reach their desired values way sooner. Figure 5 and "Fig. 6" represent the change in orientation of the rigid rod angles starting from their initial conditions to their final positions.

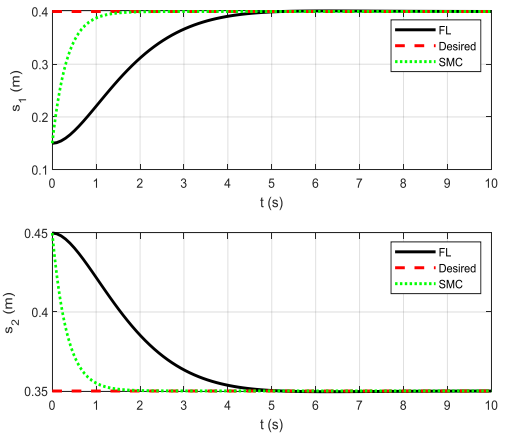

Fig. 3 The time varying changes of parameter s_1 and s_2.

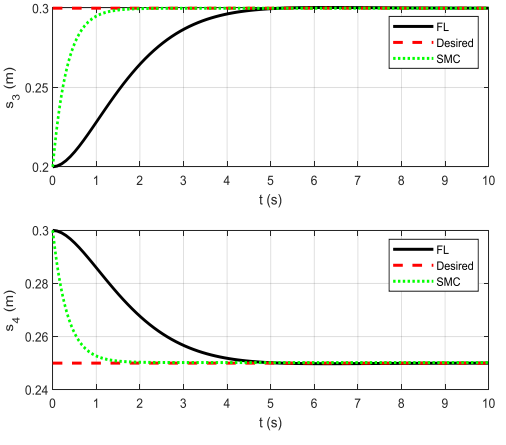

Fig. 4 The time varying changes of parameter s_1 and s_4.

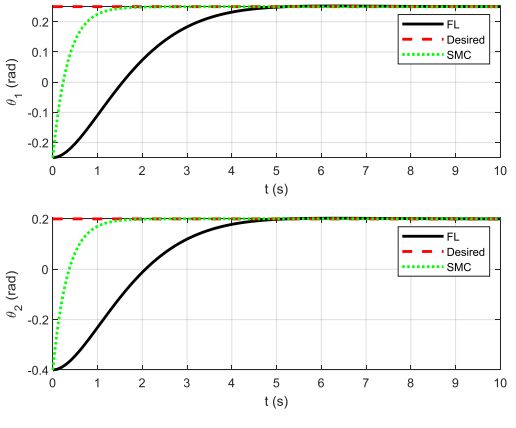

Fig. 5 The change in orientation of the rigid rod (θ_1, θ_2).

In "Fig. 7", the trajectory of the end-effector of robot is shown. The structures of the robot in initial and desired points are demonstrated too. In "Fig. 8" and "Fig. 9", the amount of inputs is indicated.

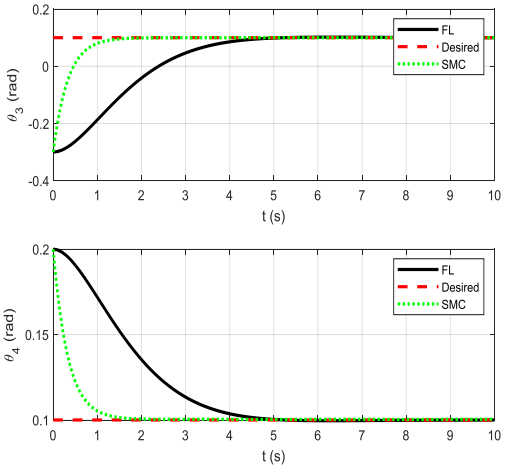

Fig. 6 The change in orientation of the rigid rod (θ_3, θ_4).

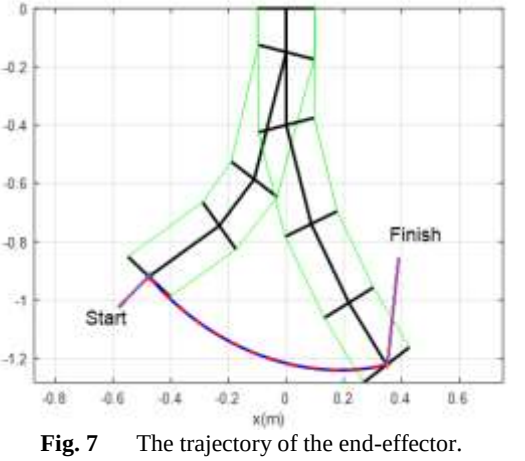

Fig. 7 The trajectory of the end-effector.

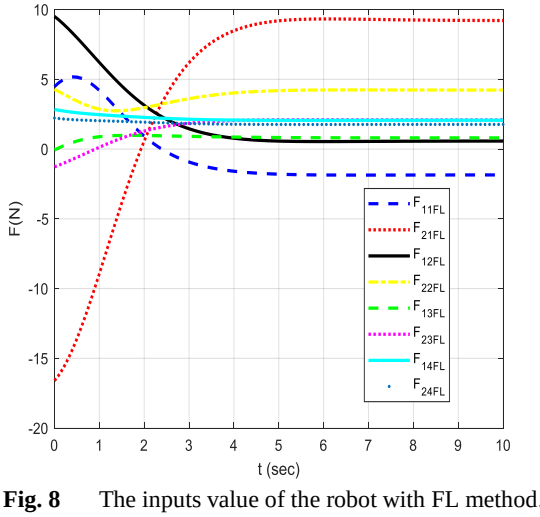

Fig. 8 The inputs value of the robot with FL method.

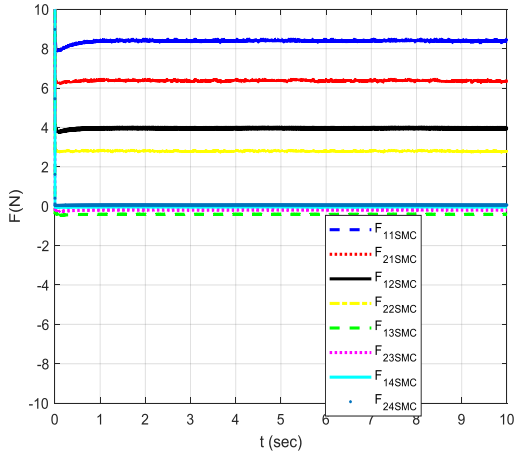

Fig. 9 The inputs value of the robot with SMC method.

According to the input diagram, it is clear that in the FL method, initially, the amount of inputs changes until states reach their references. But, over time these inputs reach fixed values at the end of the path. Due to the fact that the dynamic model of the system has gravitational acceleration, the values of the inputs cannot reach zero. Also, according to the diagrams of the SMC method, it can be seen that in this method states reach their desired value sooner so inputs show the stable trend.

Case study 2: point-to-point control design with disturbances

In this part, some disturbances between 1.5 and 2.5 seconds are introduced to this system. As well as this, all parameters and dimensions of the robot remain unchanged. The target of this case study is to examine the performance of the controllers despite the disturbance. Figure 10 and Fig. 11" illustrate the time-varying changes of the extension of each module with FL and SMS methods.

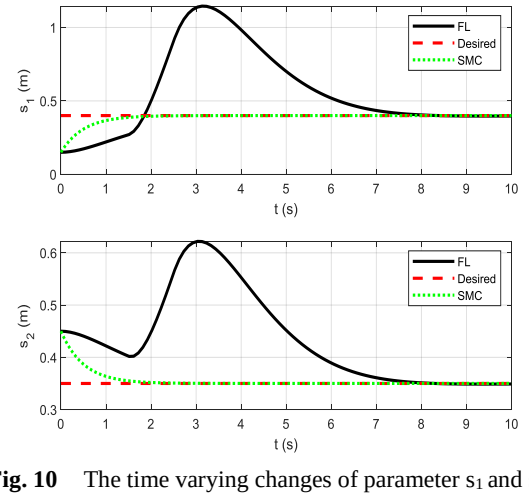

Fig. 10 The time varying changes of parameter s_1 and s_2.

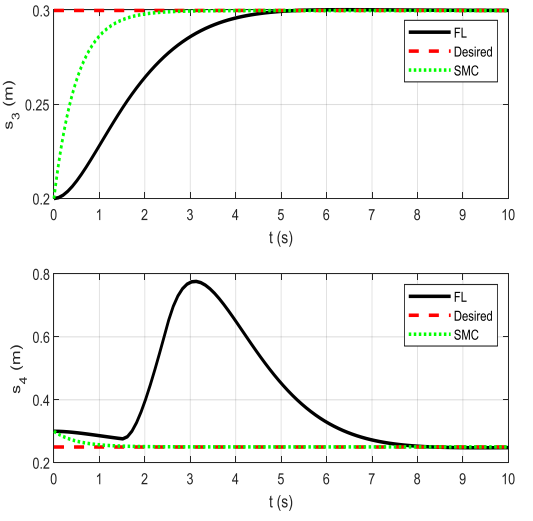

Fig. 11 The time varying changes of parameter s_1 and s_4.

It can be seen that before the time when the disturbances are applied, FL controller tries to reach desired points. But, when figures with FL method reach the time when there are disturbances, their states move away from the desired values. After this period, the controller tries to revise this situation and reach references. On the other hand, these disturbances have little effect on the system with SMC method. Figure 12 and "Fig. 13" represents the change in orientation of the rigid rod angles starting from their initial conditions to their final positions. The trajectory of the end-effector of the robot is indicated in "Fig. 14".

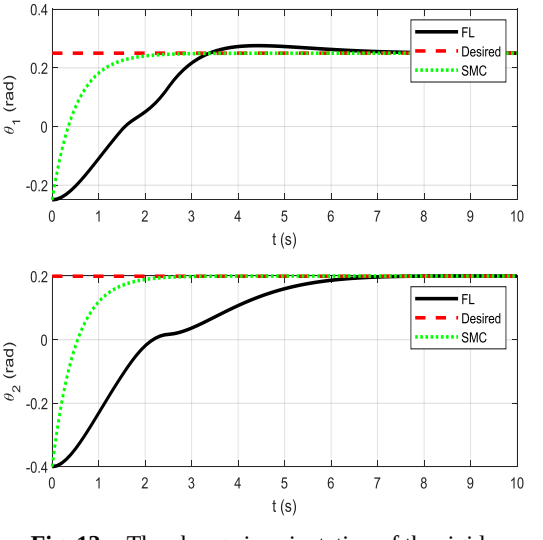

Fig. 12 The change in orientation of the rigid rod(θ_1, θ_2).

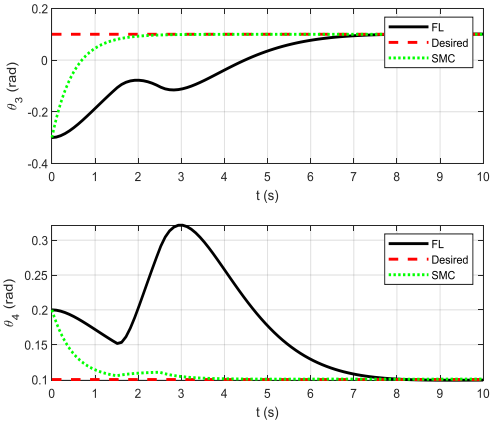

Fig. 13 The change in orientation of the rigid rod(θ_3, θ_4).

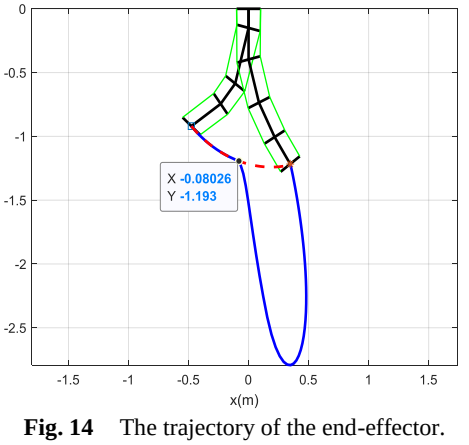

Fig. 14 The trajectory of the end-effector.

The end-effector of the robot until 1.5 seconds (before disturbance time) reaches (-0.08, -1.19) location. When disturbance starts, the trajectory of the end-effector changes. In the simulation, it is shown that the robot's path remains unchanged after 4.93 seconds. To be more exact the end-effector reaches the endpoint. In "Fig. 15" and "Fig. 16", the amount of inputs with disturbances are presented.

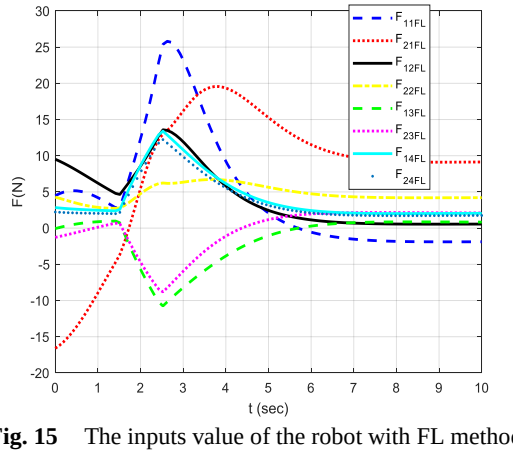

Fig. 15 The inputs value of the robot with FL method.

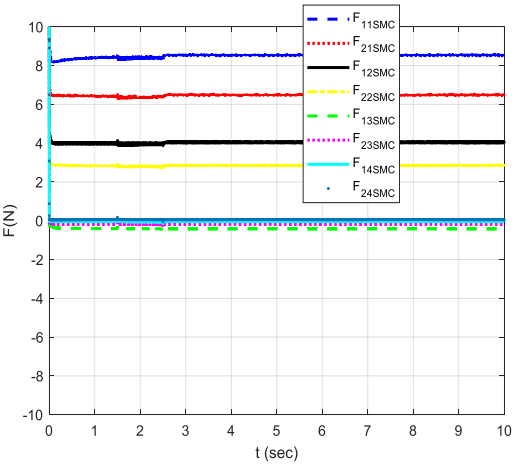

Fig. 16 The inputs value of the robot with SMC method.

According to the input diagram, it is clear that after 1.5 seconds many changes are made in the input charts in the FL method. Compared to the input diagrams in "Fig. 8", the power input changes of force F_{11} are significant. But as it turns out, after 6 seconds it reaches the same input values of the form without disturbance. Moreover, the least change is related to force F_{22}. The main justification for this trend is the small effects of disturbance on the S_3, θ_1 *and* θ_2 variables according to the pattern of "Fig. 11" and "Fig. 12". Likewise, "Fig. 9", the disturbances had little effect on the input diagrams in "Fig.16". Therefore, the SMC controller has better performance.

Case study 3: Circular trajectory design

The desired trajectory selected is a circular path on the plane that needs to be followed by the end-effector. Therefore, this path is assumed to be as follow:

$$\begin{pmatrix} x_{des} & z_{des} \end{pmatrix} = \begin{pmatrix} \cos(2t) & \sin(2t) \end{pmatrix} \quad (28)$$

For this purpose, it is necessary to solve the inverse kinematics to find the desired values of the variables q. The forward kinematic Equations of the robot, which expresses the location of the end-effector is:

$$\begin{aligned} x &= s_2 \sin(\theta_1) + s_3 \sin(\theta_1 + \theta_2) + s_4 \sin(\theta_1 + \theta_2 + \theta_3) \\ z &= s_1 + s_2 \cos(\theta_1) + s_3 \cos(\theta_1 + \theta_2) \\ &+ s_4 \cos(\theta_1 + \theta_2 + \theta_3) \\ \theta &= \theta_1 + \theta_2 + \theta_3 + \theta_4 \end{aligned} \quad (29)$$

Due to the fact that there are 8 variables and the number of variables required to follow a circular path is 2 variables; Therefore, inverse kinematics will definitely have countless answers. To solve it, we give the value of 6 variables:

$$\theta_1 = \frac{\pi}{10}, \theta_2 = \frac{\pi}{8}, \theta_3 = \frac{\pi}{5}, \theta_4 = \frac{\pi}{6}, s_1 = 0.3, s_2 = 0.4 \qquad (30)$$

By placing the values of "Eq. (30)" in the robot kinematic Equation in "Eq. (29)", the other two variables, s_3 and s_4, are obtained as follows:

$$\begin{aligned} s_3 &= 1.65\sin 2t - 0.39\cos 2t - 1.07 \\ s_4 &= 1.29\cos 2t - 1.11\sin 2t + 0.59 \end{aligned} \qquad (31)$$

Therefore, the desired values for q_{des} are selected according to the definition of q ("Eq. (27)"). Besides, the initial condition of the system is demonstrated as:

$$p_{initial} = [-1; 0.8; 1.2; 0.3; 0.5; 0.1; 0.2; 0.7] \qquad (32)$$

In the following, "Fig. 17" to "Fig. 20" show the diagrams of the output systems of the system consisting of 8 variables along with the desired references with FL and SMS methods. The error of all 8 state variables with SMC becomes zero in less than 0.5 seconds, and this is a sign of the high speed of the designed controller.

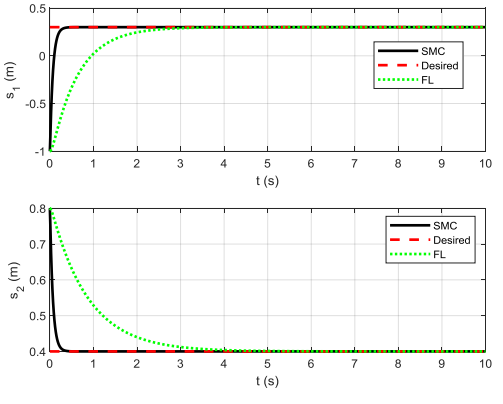

Fig. 17 The time varying changes of parameter s_1 and s_2.

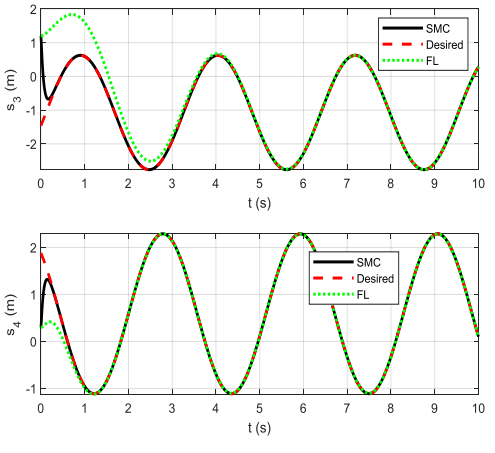

Fig. 18 The time varying changes of parameter s_3 and s_4.

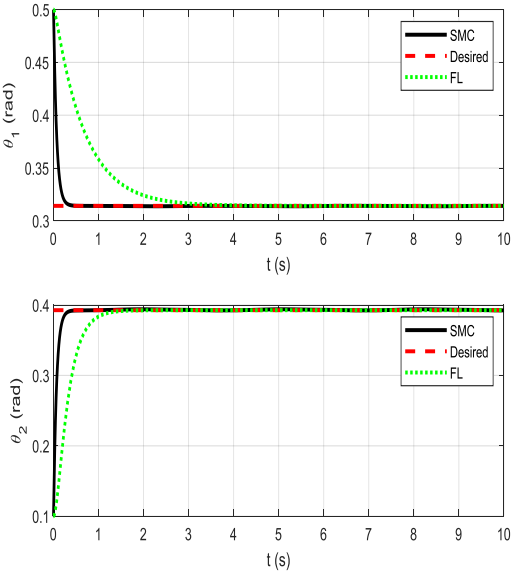

Fig. 19 The change in orientation of the rigid rod (θ_1, θ_2).

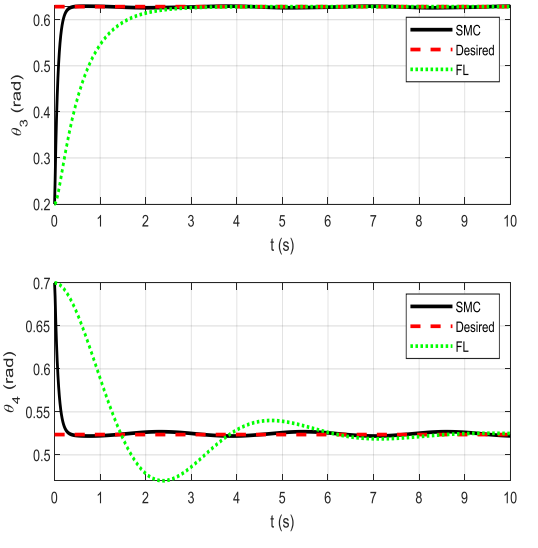

Fig. 20 The change in orientation of the rigid rod (θ_3, θ_4)

According to the results of inverse kinematics in "Eq. (31)", the desired path for the variables s_3 and s_4 is in the form of trigonometric functions shown in "Fig. 18". Besides, by placing the expression t=0 in "Eq. (31)", the initial values of the mentioned variables are calculated. In "Fig. 21", the trajectory of the end-effector of the robot in the 2-D plane is illustrated.

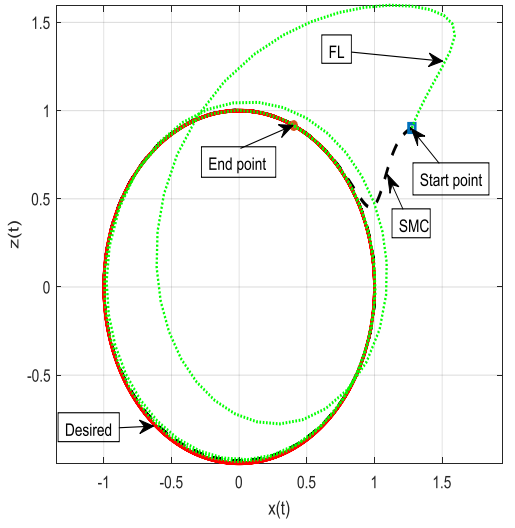

Fig. 21 The trajectory of the end-effector.

In "Fig. 21", the end-effector starts from the initial point which has been shown. This point is calculated with forward kinematic which was represented in "Eq. (29)". For calculation of the initial point of the path, all 8 variables are needed. Such parameters were calculated in "Eq. (30)" and "Eq. (31)". This point would be (1.276, 0.915). Similar to this approach, the final point would be (0.3447, 0.9429).

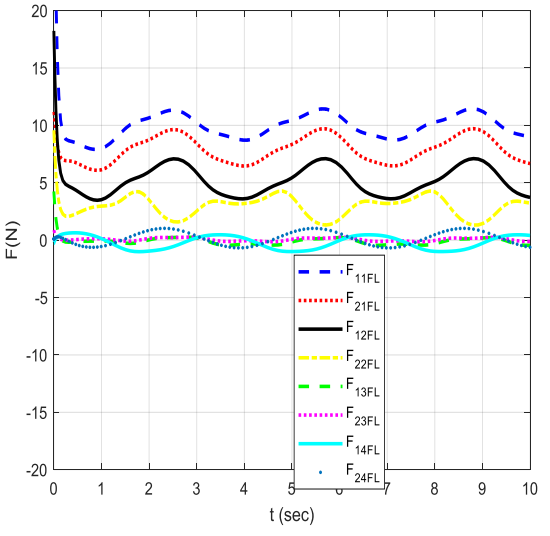

Fig. 22 The inputs value of the robot with FL method.

In addition, the path traveled by SMC method has less mean squared error than FL method. It is seen that, even though both FL and SMC methods have the same dynamic modeling, controllers trace the different paths during the beginning and circular path. The factor of these two paths is the FL approach. In "Fig. 22" and "Fig. 23", the amount of inputs is shown. Now See "Table 2".

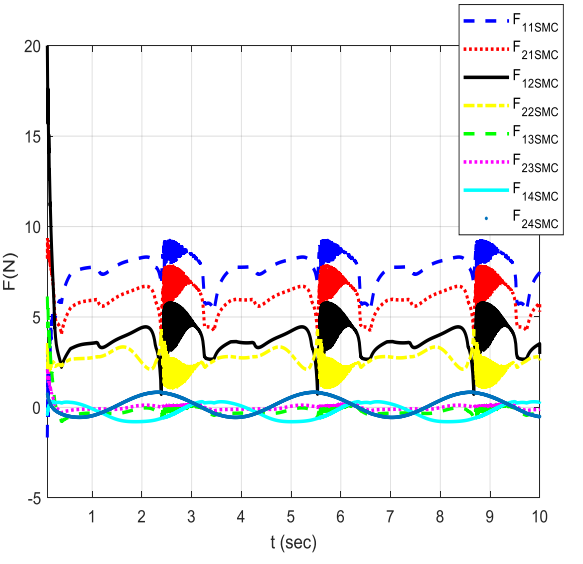

Fig. 23 The inputs value of the robot with SMC method.

Table 2 The comparison between tacking error with SMC and FL methods

Control Method	Mean Squared Error(m^2)
SMC	0.004
FL	0.245

It should be noted that even though the inputs by FL method is higher than SMC method, the trajectory of the end-effector in "Fig. 21" reaches the desired path with SMC method much sooner.

6 CONCLUSIONS

This paper presents a novel nonlinear control law for multi-DOF discrete CR. The dynamic model is based on a new structure established recently. However, in this work, the model of the system is developed into general form. Moreover, the strategy of SMC for a CR was presented in this paper with the stability proof of the system with Lyapunov theory. Besides, control simulation for three different cases was presented with SMC and the results were compared with the input-output feedback linearization method in MATLAB software. The results exhibited that the settling time of the former method is much lesser than the latter approach. It should be noted that the proposed control model can be presented in various applications, including the medicine, where the rapid control of the CRs is so important.

REFERENCES

[1] Hyatt, P., Johnson, C. C., and Killpack, M. D., Model Reference Predictive Adaptive Control for Large-Scale Soft Robots, Frontiers in Robotics and AI, 2020, pp. 558027.

[2] Hsiao, J. H., Chang, J. Y., and Cheng, C. M., Soft Medical Robotics: Clinical and Biomedical Applications, Challenges, and Future Directions, Advanced Robotics, Vol. 33, No. 21, 2019, pp. 1099-1111.

[3] Yeshmukhametov, A., et al. Modeling and Validation of New Continuum Robot Backbone Design with Variable Stiffness Inspired from Elephant Trunk, IOP Conference Series: Materials Science and Engineering, Vol. 417, No. 1, 2018, pp. 012010.

[4] Zheng, Z., et al., Dynamic Analysis of Elastic Projecting Robot Inspired by Chameleon Tongue, IEEE International Conference on Robotics and Biomimetics (ROBIO), 2018, Dec 12, pp. 2088-2094.

[5] Simaan, N., et al., Design and Integration of a Telerobotic System for Minimally Invasive Surgery of The Throat, The International Journal of Robotics Research, Vol. 28, No. 9, 2009, pp. 1134-1153.

[6] Da Veiga, T., et al., Challenges of Continuum Robots in Clinical Context: A Review, Progress in Biomedical Engineering, Vol. 2, No. 3, 2020, pp. 032003.

[7] Ahmad, M. A., et al., Deep Learning-Based Monocular Placental Pose Estimation: Towards Collaborative Robotics in Fetoscopy, International Journal of Computer Assisted Radiology and Surgery, Vol. 15, No. 9, 2020, pp. 1561-1571.

[8] Shi, C., et al., Shape Sensing Techniques for Continuum Robots in Minimally Invasive Surgery: A Survey. IEEE Transactions on Biomedical Engineering, Vol. 64, No. 8, 2016, pp. 1665-1678.

[9] Sarli, N., et al., Preliminary Porcine In Vivo Evaluation of A Telerobotic System for Transurethral Bladder Tumor Resection and Surveillance, Journal of Endourology, Vol. 32, No. 6, 2018, pp. 516-522.

[10] Webster, R., B. A. Jones, Design and Kinematic Modeling of Constant Curvature Continuum Robots: A review, The International Journal of Robotics Research, Vol. 29, No. 13, 2010, pp. 1661-1683.

[11] Gonthina, P. S., et al., Modeling Variable Curvature Parallel Continuum Robots Using Euler Curves, International Conference on Robotics and Automation (ICRA), 2019, May 20, pp. 1679-1685.

[12] Rone, W. S., Ben-Tzvi, P., Mechanics Modeling of Multisegment Rod-Driven Continuum Robots, Journal of Mechanisms and Robotics, Vol. 6, No. 4, 2014, pp. 041006.

[13] Kratchman, L. B., et al., Guiding Elastic Rods with A Robot-Manipulated Magnet for Medical Applications, IEEE Transactions on Robotics, Vol. 33, No. 1, 2016, pp. 227-233.

[14] Till, J., Aloi, V., and Rucker, C., Real-Time Dynamics of Soft and Continuum Robots Based on Cosserat Rod Models, The International Journal of Robotics Research, Vol. 38, No. 6, 2019, pp. 723-746.

[15] Sadati, S. H., et al., TMTDyn: A Matlab Package for Modeling and Control of Hybrid Rigid–Continuum Robots Based on Discretized Lumped Systems and Reduced-Order Models, The International Journal of Robotics Research, Vol. 40, No. 1, 2021, pp. 296-347.

[16] Mochiyama, H., Suzuki. T., Kinematics and Dynamics of a Cable-Like Hyper-Flexible Manipulator, IEEE International Conference on Robotics and Automation, Vol. 3, No. 03CH37422, 2003, pp. 3672-3677.

[17] Yoon, H. S., Yi. B. J., A 4-DOF Flexible Continuum Robot Using a Spring Backbone, International Conference on Mechatronics and Automation, 2009, Aug 9, pp. 1249-1254.

[18] Tatlicioglu, E., Walker, I. D., and Dawson, D. M., New Dynamic Models for Planar Extensible Continuum Robot Manipulators, IEEE/RSJ International Conference on Intelligent Robots and Systems, 2007, Oct 29, pp. 1485-1490.

[19] George Thuruthel, T., et al., Control Strategies for Soft Robotic Manipulators: A Survey, Soft Robotics, Vol. 5, No. 2, 2018, pp. 149-163.

[20] Falkenhahn, V., et al, Model-Based Feedforward Position Control of Constant Curvature Continuum Robots Using Feedback Linearization, IEEE International Conference on Robotics and Automation (ICRA), 2015, May 26, pp. 762-767.

[21] Marchese, A.D., Tedrake, R., and Rus, D., Dynamics and Trajectory Optimization for A Soft Spatial Fluidic Elastomer Manipulator, The International Journal of Robotics Research, Vol. 35, No.8, 2016, pp. 1000-1019.

[22] Chikhaoui, M.T., et al., Toward Motion Coordination Control and Design Optimization for Dual-Arm Concentric Tube Continuum Robots, IEEE Robotics and Automation Letters, Vol. 3, No. 3, 2018, pp. 1793-1800.

[23] Li, M., et al., Model-Free Control for Continuum Robots Based on An Adaptive Kalman Filter, IEEE/ASME Transactions on Mechatronics, Vol. 23, No. 1, 2017, pp. 286-297.

[24] Esfandiar, H., Daneshmand, S., Closed Loop Control of The Planar Flexible Manipulator via Youla-Kucera parameterization, Journal of Mechanical Science and Technology, Vol. 27, No. 11, 2013, pp. 3243-3252.

[25] . Esfandiar, H., Daneshmand, S., and Kermani, R. D., On the Control of a Single Flexible Arm Robot via Youla-Kucera Parameterization, Robotica, Vol. 34, No. 1, 2016, pp. 150-172.

[26] Giri, N., Walker, I. D., Three Module Lumped Element Model of a Continuum Arm Section, IEEE/RSJ International Conference on Intelligent Robots and Systems, 2011, Sep 25, pp. 4060-4065.

[27] Bai, K., et al., Sliding Mode Nonlinear Disturbance Observer-Based Adaptive Back-Stepping Control of a Humanoid Robotic Dual Manipulator, Robotica, Vol. 36, No. 11, 2018, pp. 1728-1742.

Int. J. Advanced Design and Manufacturing Technology, 2022, Vol. 15, No. 4, pp. 13-27

DOI: 10.30486/ADMT.2023.1955746.1345 ISSN: 2252-0406 https://admt.isfahan.iau.ir

Nonlinear Dynamic Behaviour of The Mechanisms Having Clearance and Compliant Joints

Amir Hossein Javanfar*
Department of Mechanical Engineering,
Shahrood University of Technology, Iran
E-mail: Amirhosein.javanfar@yahoo.com
*Corresponding author

Received: 30 March 2022, Revised: 22 July 2022, Accepted: 20 August 2022

Abstract: In this paper, the rigid four-bar linkage with clearance joint has been examined. The effects of design parameters have been analyzed separately. Considering chaotic behaviour and undesirable vibrations of the system induced by joint clearance, it has been suggested to use compliant joints for improving these undesirable behaviours. Therefore, rigid four-bar linkage with clearance joint and compliant joint is investigated by pseudo-rigid-body model. Subsequently, the nonlinear behaviour of the compliant mechanism is examined, using fast Fourier transform analysis, Poincare sections, and bifurcation diagram. Comparative analysis of results clearly shows that using appropriate compliant joints causes notable improvements in the behaviour of the system, reduction of sudden impacts, and lower accelerations. 6 cycles simulations of mechanisms demonstrate the decreasing 207 impacts to 33 impacts using compliant joint. Moreover, the results report 87% decrease in follower top acceleration and 64% in clearance joint top contact force. Although using the compliant joint makes limitations in the workspace, but the appropriate and optimized design of the compliant joint results in good improvement in the performance of the system.

Keywords: Clearance, Compliant, Nonlinear Dynamics of Rigid Four-Bar Mechanism, Vibration

Biographical notes: Amir Hossein Javanfar received his MSc in Mechanical Engineering from Babol Noshirvani University of Technology in 2015. He is currently a student at the Mechanical Engineering, Shahrood University of Technology, Shahrood, Iran. His current research interest includes contact mechanics and nonlinear dynamics.

Research paper

1 INTRODUCTION

The existence of joint clearance results in additional degrees of freedom in the system and the mechanism undergoes sudden impacts, causing undesirable vibrations, lower accuracy, and chaotic dynamical behaviour [1]. Therefore, by considering joint clearance in mechanisms analysis, more accurate information can be obtained and a better design of mechanism can be achieved. Clearance phenomenon in joint causes three modes of relative motion for journal and bearing: (i) free flight mode, (ii) impact mode, and (iii) continuous contact mode [2]. The massless link model [2] is unable to predict these three modes, so to achieve more accurate responses; a more perfect model is required for dynamical analysis.

While ignoring the energy dissipation [3] results in a great error in the response and reduces the accuracy, the model developed by Lankarani and Nikravesh [4] presented a hysteresis damping function in order to account for the dissipated energy during contact, and all motional modes are assumed. The computational and experimental study [5-6] on revolute clearance joints is developed for improving the accuracy of modeling and using the model in applicable cases [7-9]. Respecting the importance of clearance modeling in mechanisms, Lankarani and Nikravesh model is used in [10] to present the nonlinear dynamics of the four-bar linkage mechanism with two clearance joints. Moreover, the perfect contact model should consider other phenomena like friction and lubrication. Javanfar and Bamdad [11] presented a novel friction model for clearance joint modeling to reduce the error of these models. Filipe Marques et al. [12] examined several friction force models for improving the accuracy of clearance joint modeling.

As the researches and studies have been improved in the field of clearance joints, special and practical works have been done in dynamic analysis, control, and design of mechanisms [13-20] to reduce undesirable vibration of mechanisms with clearance joints. Studies [13-14] demonstrate the chaotic behaviour of these mechanisms, then the journal-bearing motion is stabilized by a control method [13-14]. Using the genetic algorithm, the appropriate values for variables design parameters are determined in order to reduce undesirable system vibrations [15]. However, the permanent contact model is assumed in [15]. Sardashti et. al. [16] designed a rigid planar four-bar linkage mechanism with clearance joints via PSO algorithm that uses the massless link method. Although, they [15-16] applied optimization method for reducing vibration of mechanisms with clearance joint, but their modeling is not accurate. Therefore, considering all motional modes in the clearance joint optimal design is used to remove impact in the clearance joint [17]. Some practical examples relate the closed-chain mechanism dynamics to the necessity of the joint clearance model [18-20]. Although mentioned papers [13-20] used optimization and control methods in the field of improving the dynamic behaviour of these mechanisms, some studies using stiffness and flexibility reduce the undesirable vibration of clearance joint in mechanisms [21-22]. They report that the flexibility and stiffness of the linkages [21] and joints [22] can improve these mechanisms' behaviour. Because of limitations and the high cost of optimization and control methods, concentrating on the compliant joint for this goal is efficient. Bending compliant joint is one of the flexible links that has been noted because of their vast utility such as MEMS, robotics, medical usage, and biomechanics application [23].

Studies [22-24], support the idea of adding compliant joints to the mechanisms with clearance for improving accuracy and reducing vibration, while they [22-24] do not consider the nonlinear behaviour by Poincare section, phase diagram, and FFT plot. Studies [21], [25] suggest the link flexibility and passive vibration absorber to improve the chaotic behaviour of the mechanism considering nonlinear behaviour. Although studies [21], [25] apply the link flexibility and passive vibration absorber to improve nonlinear behaviour, they do not use compliant joint, and studies [22], [24] apply compliant joint to improve the dynamic behaviour of the mechanism but do not present the nonlinear behaviour. Therefore, in the present work, it is simply shown how sudden impacts in the system are eliminated, undesirable vibrations are decreased and chaotic behaviour is improved using a compliant joint.

Although joint clearance has been gaining increasing attention in recent years, most works have been devoted to analyzing and controlling undesirable system vibrations, and despite many studies have been carried out in the area of compliant joints, simultaneous effect of both in one mechanism and nonlinear behaviour of them have never been addressed. Therefore, the analysis of the mechanism predicts the influence of compliant joint on the nonlinear dynamic behaviour of mechanisms with clearance joint. The contribution of this paper is:

- Offering and examining a compliant joint to predict the effect of the compliant joint on the behaviour of mechanisms with clearance joint.
- Presenting the nonlinear behaviour of four-bar linkage mechanism with clearance and compliant joint by Poincare section, phase diagram, and FFT plot.

The rest of the paper is structured as follows. The mechanism's model is presented, and the stiffness of the compliant joint is introduced in Section 2. Then, results show the influence of compliant joint on the dynamic behaviour of mechanism with clearance joint in section 3. The results including journal center trajectory and input link required moment and concentrating on the vibrations of mechanisms, nonlinear dynamics plots as

the phase diagram, Poincare section, FFT analysis, and bifurcation diagram are presented.

2 MODELING

In this section Equations of motions for different cases are obtained. "Fig. 1" shows the schematic of the clearance joint that demonstrates the contact point P_B and P_j, the center of journal O_j, the center of bearing O_B, the clearance vector r and α.

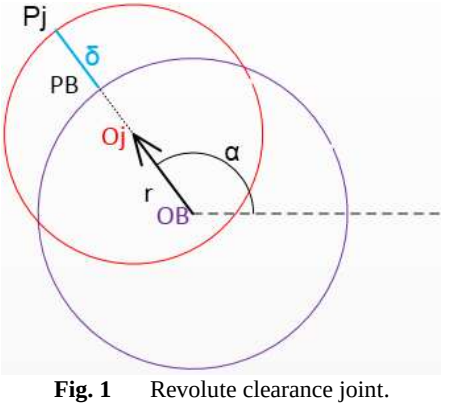

Fig. 1 Revolute clearance joint.

R_j and R_B are the radius of journal and bearing, hence indentation δ is calculated as:

$$\delta = r - (R_B - R_j) \tag{1}$$

The Hertz law as proposed in [3]:

$$F_N = K\delta^n \tag{2}$$

Assuming circular and elliptical contacts n is set to 1.5. The generalized stiffness K is written as:

$$K = \frac{4}{3(\sigma_i + \sigma_j)}\left(\frac{R_i R_j}{R_i + R_j}\right)^{\frac{1}{2}} \tag{3}$$

σ_i and σ_j are material parameters. The values of them are calculated by using Poisson's ratio υ and the Young's modulus E of each sphere as follows:

$$\sigma_k = \frac{1 - \upsilon_k^2}{E_k}, \quad k = i, j \tag{4}$$

The normal contact force is finally expressed as [4]:

$$F_N = K\delta^n\left(1 + \frac{3k(1 - C_e^2)}{4\dot{\delta}^{(-)}}\right)\frac{\dot{\delta}}{\dot{\delta}^{(-)}} \tag{5}$$

For sphere to sphere contact or by similar expressions for the contact of other types of geometry; C_e is the restitution coefficient and $\dot{\delta}^{(-)}$ is the initial normal impact velocity where contact is detected. Note that the direction of normal force is the same with the normal vector (n) in "Fig. 2". The contact force magnitude Q_c and its orientation α are defined contact force vector and Q_c is computed as:

$$Q_c = K\delta^{1.5}\left(1 + \frac{3(1 - c_e^2)}{4}\frac{\dot{r}}{\dot{r}^{(-)}}\right) \tag{6}$$

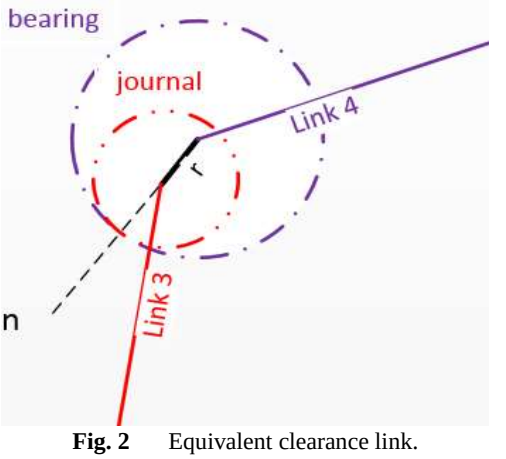

Fig. 2 Equivalent clearance link.

A brief review of compliant joints and their application are presented here. In order to design compliant joint, some criteria should be noted like: (i) range of motion, (ii) stress concentration (iii) axial stiffness. Using these studies of designing [26-28] and investigating [29-30] the revolute joint and the translational compliant joint are applied. The revolute compliant joint which is a bending element, is supposed as a torsional spring, whose stiffness can be calculated by using the Castigliano's theory [30]. According to this theory, the torsional spring coefficient of compliant joint according to "Fig. 3" is calculated as [31]:

$$K = \frac{EI}{L} = \frac{EI}{2R\Delta\theta} \tag{10}$$

Where, L is the length of the flexible segment, E is elasticity modulus, I is moment inertia and R is beam curvature radius.

The EoM (Equation of motion) for the mechanism of "Fig. 4" is derived. It is assumed that joints have clearance. Three cases are considered: (1) one clearance joint, (b) one clearance and compliant joint, and (c) one and two compliant joints. Moreover, the Euler-Lagrange Equation is used to extract the EoM. Figure 4 shows the

mechanism with one clearance joint at joint 3 having the 3 degrees of freedom.

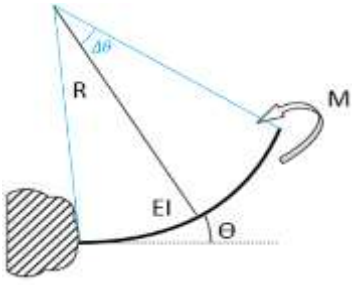

Fig. 3 Compliant joint.

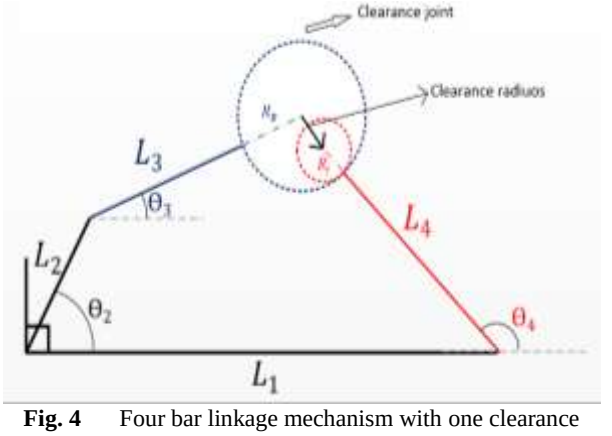

Fig. 4 Four bar linkage mechanism with one clearance joint.

The Equations of motion for this system is as follows:

$$\begin{aligned}(I_3 + m_3a_3^2L_3^2)\ddot{\theta}_3 - m_3a_3L_3L_2\dot{\theta}_2^2\cos(\theta_2 \\ - \theta_3 - \lambda_3) \\ + m_3a_3L_3\mathrm{g}\cos(\theta_3 + \lambda_3) \\ = -L_3Q_c\sin(\theta_3 - \psi)\end{aligned} \tag{11}$$

$$\begin{aligned}(I_4 + m_4a_4^2L_4^2)\ddot{\theta}_4 + m_4a_4L_4g\cos(\theta_4 + \lambda_4) \\ = Q_cL_4\sin(\theta_4 - \psi)\end{aligned} \tag{12}$$

The required moment to drive the crank is obtained as:

$$\begin{aligned}\big(I_2 + m_2a_2^2L_2^2 + m_3L_2^2 \\ + \mathrm{m}_3a_3L_3L_2\dot{\theta}_3\cos(\theta_2 \\ - \theta_3)\big)\ddot{\theta}_2 \\ + \mathrm{m}_3a_3L_3L_2\dot{\theta}_2\big(\ddot{\theta}_3\cos(\theta_2 \\ - \theta_3) - \big(\dot{\theta}_2 \\ - \dot{\theta}_3\big)\sin(\theta_2 - \theta_3)\,\dot{\theta}_3\big) \\ - \mathrm{m}_3a_3L_3L_2\dot{\theta}_2\dot{\theta}_3\sin(\theta_2 \\ - \theta_3) + m_2ga_2L_2\cos\theta_2 \\ + m_3gL_2\cos\theta_2 \\ + Q_cL_2\sin(\theta_2 - \psi) = M\end{aligned} \tag{13}$$

The schematic of the mechanism adding a compliant joint to case (i) is demonstrated in "Fig. 5". Joint 2 is compliant, while joint 3 is clearance joint.

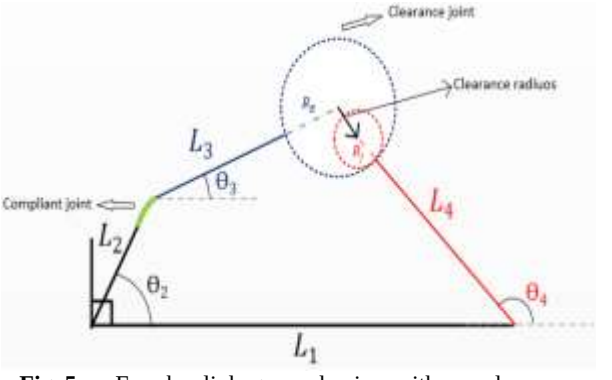

Fig. 5 Four bar linkage mechanism with one clearance joint and one compliant joint.

As mentioned in modeling section, compliant joint modeled as torsional spring, so four-bar linkage mechanism via pseudo-rigid-body model is demonstrated by "Fig. 6".

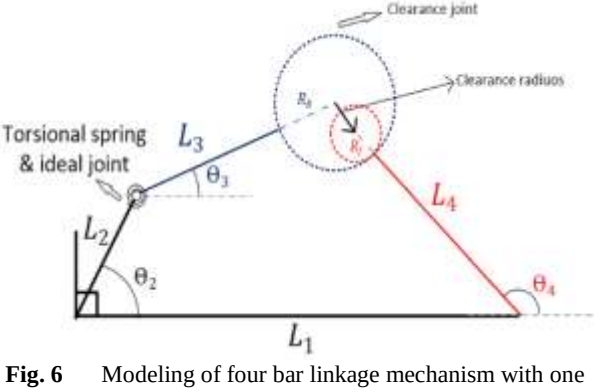

Fig. 6 Modeling of four bar linkage mechanism with one clearance joint and one compliant joint according pseudo-rigid-body model.

According pseudo-rigid-body model of compliant mechanisms, the Equations of motion for this case can be expressed by following Equations.

$$\begin{aligned}(I_3 + m_3{a_3}^2L_3^2)\ddot{\theta}_3 \\ - m_3a_3L_3L_2\dot{\theta}_2^2\cos(\theta_2 \\ - \theta_3 - \lambda_3) \\ + m_3a_3L_3g\cos(\theta_3 + \lambda_3) \\ - k_\theta(\theta_2 - \theta_3) \\ = -L_3Q_c\sin(\theta_3 - \psi)\end{aligned} \tag{15}$$

$$\begin{aligned}(I_4 + m_4a_4^2L_4^2)\ddot{\theta}_4 + m_4a_4L_4\mathrm{g}\cos(\theta_4 + \lambda_4) \\ = Q_cL_4\sin(\theta_4 - \psi)\end{aligned} \tag{16}$$

The required moment driving the crank is written as:

$$
\begin{aligned}
&\big(I_2 + m_2 a_2^2 L_2^2 + m_3 L_2^2 \\
&\quad + \mathrm{m}_3 a_3 L_3 L_2 \dot{\theta}_3 \cos(\theta_2 \\
&\quad - \theta_3)\big)\ddot{\theta}_2 \\
&\quad + m_3 a_3 L_3 L_2 \dot{\theta}_2 \big(\ddot{\theta}_3 \cos(\theta_2 \\
&\quad - \theta_3) - \big(\dot{\theta}_2 \\
&\quad - \dot{\theta}_3\big) \sin(\theta_2 - \theta_3)\, \dot{\theta}_3\big) \\
&\quad - m_3 a_3 L_3 L_2 \dot{\theta}_2 \dot{\theta}_3 \sin(\theta_2 \\
&\quad - \theta_3) + m_2 g a_2 L_2 \cos\theta_2 \\
&\quad + m_3 g L_2 \cos\theta_2 \\
&\quad + Q_c L_2 \sin(\theta_2 - \psi) \\
&\quad + K_\Theta\big(\theta_2 - \theta_3 \\
&\quad - (\theta_{20} - \theta_{30})\big) = M_2
\end{aligned}
\tag{17}
$$

The Eom of mechanism with compliant joints is presented here. In this case, similar to a four-bar mechanism without clearance, the mechanism has a single degree of freedom (DoF). The kinematics solution of the system is the same as the case with ideal joints, however, the required crank moment is different. Figure 7 demonstrates the mechanism with two compliant joints. Compliant joint was modeled as torsional spring, so four-bar linkage mechanism via this modeling demonstrated by "Fig. 8".

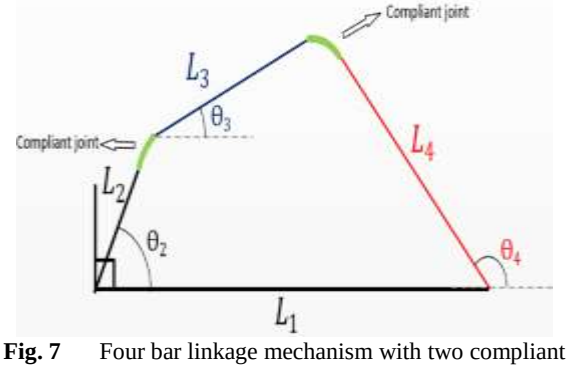

Fig. 7 Four bar linkage mechanism with two compliant joint.

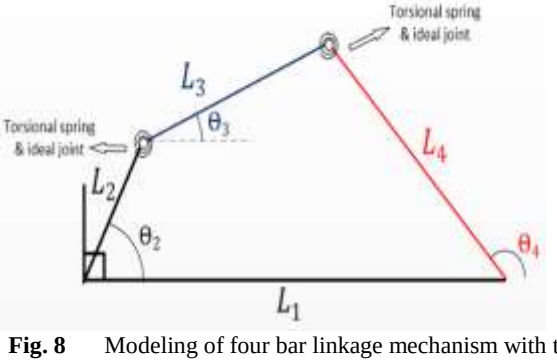

Fig. 8 Modeling of four bar linkage mechanism with two compliant joint

Using kinematic solution of mechanism, the value of kinematic specification of mechanism's links are obtained, so the crank moment of mechanism is calculated by using these values. These values are calculated as:

$$
L_2 e^{i\theta_2} + L_3 e^{i\theta_3} = L_1 e^{i\theta_1} + L_4 e^{i\theta_4} \tag{15}
$$

$$
\begin{aligned}
&\ddot{\theta}_3 \\
&= -\frac{L_2}{L_3}\left[\ddot{\theta}_2 \frac{\sin(\theta_2 - \theta_4)}{\sin(\theta_3 - \theta_4)}\right. \\
&+ \dot{\theta}_2\big(\dot{\theta}_2 - \dot{\theta}_4\big)\frac{\cos(\theta_2 - \theta_4)}{\sin(\theta_3 - \theta_4)} \\
&\left. - \dot{\theta}_2\big(\dot{\theta}_3 - \dot{\theta}_4\big)\frac{\cos(\theta_2 - \theta_4)\cos(\theta_3 - \theta_4)}{\sin^2(\theta_3 - \theta_4)}\right]
\end{aligned}
\tag{16}
$$

$$
\begin{aligned}
&\ddot{\theta}_4 \\
&= \frac{L_2}{L_4}\left[\ddot{\theta}_2 \frac{\sin(\theta_2 - \theta_3)}{\sin(\theta_4 - \theta_3)}\right. \\
&+ \dot{\theta}_2\big(\dot{\theta}_2 - \dot{\theta}_3\big)\frac{\cos(\theta_2 - \theta_3)}{\sin(\theta_4 - \theta_3)} \\
&\left. - \dot{\theta}_2\big(\dot{\theta}_4 - \dot{\theta}_3\big)\frac{\sin(\theta_2 - \theta_3)\cos(\theta_4 - \theta_3)}{\sin^2(\theta_4 - \theta_3)}\right]
\end{aligned}
\tag{17}
$$

Moreover, in this case the input crank moment is determined as:

$$
\begin{aligned}
&\left[I_{G_2} + m_2 \frac{L_2^2}{4} + m_3 L_2^2\right. \\
&+ \left(\frac{L_2}{L_3}\right)^2 \left(I_{G_3} + m_3 \frac{L_3^2}{4}\right)\left(\frac{\sin(\theta_2 - \theta_4)}{\sin(\theta_3 - \theta_4)}\right)^2 \\
&- m_3 L_2^2 \cos(\theta_3 - \theta_2)\frac{\sin(\theta_2 - \theta_4)}{\sin(\theta_3 - \theta_4)} \\
&\left. + \left(I_{G_4} + m_4 \frac{L_4^2}{4}\right)\left(\frac{L_2}{L_4}\right)^2 \left(\frac{\sin(\theta_2 - \theta_3)}{\sin(\theta_4 - \theta_3)}\right)^2\right]\ddot{\theta}_2 \\
&+ \left[2\left(\frac{L_2}{L_3}\right)^2 \left(I_{G_3}\right.\right. \\
&\left. + m_3 \frac{L_3^2}{4}\right)\frac{\sin(\theta_2 - \theta_4)}{\sin^2(\theta_3 - \theta_4)}\left(\cos(\theta_2 - \theta_4)\,(\dot{\theta}_2\right. \\
&\left. - \dot{\theta}_4\big) \right. \\
&\left. - \frac{\sin(\theta_2 - \theta_4)\cos(\theta_3 - \theta_4)}{\sin(\theta_3 - \theta_4)}\big(\dot{\theta}_3 - \dot{\theta}_4\big)\right) \\
&+ m_3 L_2^2\, sin(\theta_3 - \theta_2)\frac{\sin(\theta_2 - \theta_4)}{\sin(\theta_3 - \theta_4)}\big(\dot{\theta}_3 - \dot{\theta}_2\big)
\end{aligned}
\tag{18}
$$

$$
\begin{aligned}
&-m_3 L_2^2 \cos(\theta_3-\theta_2)\left[\frac{\cos(\theta_2-\theta_4)}{\sin(\theta_3-\theta_4)}\left(\dot{\theta}_2-\dot{\theta}_4\right)\right.\\
&\qquad -\sin(\theta_2\\
&\qquad -\theta_4)\frac{\cos(\theta_3-\theta_4)}{\sin^2(\theta_3-\theta_4)}\left(\dot{\theta}_3\right.\\
&\qquad \left.\left.-\dot{\theta}_4\right)\right]\\
&+2\left(I_{G_4}\right.\\
&+m_4\frac{L_4^2}{4}\Big)\Big(\frac{L_2}{L_4}\Big)^2\frac{\sin(\theta_2-\theta_3)}{\sin(\theta_4-\theta_3)}\Big(\frac{\left(\dot{\theta}_2-\dot{\theta}_3\right)\cos(\theta_2}{\sin(\theta_4-\theta_3}\\
&-\frac{\left(\dot{\theta}_4-\dot{\theta}_3\right)\cos(\theta_4-\theta_3)\sin(\theta_2-\theta_3)}{\sin^2(\theta_4-\theta_3)}\Big)\Big]\dot{\theta}_2\\
&-\frac{1}{2}m_3L_2L_3\dot{\theta}_2\dot{\theta}_3\,sin(\theta_3-\theta_2)\\
&+m_2ga_2L_2\cos\theta_2+m_3gL_2cos\theta_2\\
&+\mathrm{m}_3gL_{G_3}\frac{L_2}{L_3}\frac{\sin(\theta_2-\theta_4)}{\sin(\theta_3-\theta_4)}\sin\theta_3\\
&+m_4gL_{G4}\frac{L_2}{L_4}\frac{\sin(\theta_2-\theta_3)}{\sin(\theta_4-\theta_3)}cos\,\theta_4\\
&+\left(1+\frac{L_2}{L_3}\frac{\sin(\theta_2-\theta_4)}{\sin(\theta_3-\theta_4)}\right)K_{\Theta_1}\left(\theta_2-\theta_3\right.\\
&\qquad \left.-(\theta_{20}-\theta_{30})\right)\\
&\qquad -\left(\frac{L_2}{L_3}\frac{\sin(\theta_2-\theta_4)}{\sin(\theta_3-\theta_4)}\right.\\
&\qquad \left.+\frac{L_2}{L_4}\frac{\sin(\theta_2-\theta_3)}{\sin(\theta_4-\theta_3)}\right)K_{\Theta_2}\left(\theta_3\right.\\
&\qquad \left.-\theta_4-(\theta_{30}-\theta_{40})\right)=M
\end{aligned}
$$

Where K_{Θ_1} and K_{Θ_2} are torsional stiffness coefficient of joints 2 and 3. The Equation of mechanism with one compliant joint can be achieved considering $K_{\Theta_2}=0$.

3 RESULTS AND DISCUSSION

The influence of the compliant joints on the dynamic results of mechanism is investigated. The variable angular displacement of crank is:

$$\theta_2=\Theta\cos\omega t+\theta_{0_2} \tag{19}$$

Where, Θ and θ_{0_2} are the amplitude of oscillation and initial configuration. Mass and geometric properties of links are mentioned in "Table 1". Properties of the journal and bearing are mentioned in "Table 2". It is clear that the compliant joint cannot have complete rotation, hence crank must has oscillation. For considered mechanism, Θ and θ_{0_2} are selected as $\frac{441\pi}{180}$ and 2.1, respectively. And "Table 3", shows the specifications of the compliant joint.

Table 1 The specification of different links.

Body number	Length (m)	Mass (kg)	a
1	0.08	-	0.5
2	0.01	1.405	0.5
3	0.075	7.866	0.5
4	0.055	6.407	0.5

Table 2 Geometrical and structural properties of journal and bearing.

Bearing radius	Clearance size	Restitution coefficient	Young's modulus	Poisson's ratio
0.001	0.0005	0.9	207 (Gpa)	0.5

Table 3 The specification of compliant joint.

Modulus of elasticity	$\boldsymbol{E=207\times10^9 pa}$
Radius of curvature	R=0.1981m
widths	W=0.01m
thickness	t=0.001m
joint stiffness	K=4.05

In "Fig. 9", the time histories of the magnitude of the clearance vector are demonstrated. It is obvious that the joint experiences three motional modes. However, in continuous contact mode, the dynamic behaviour of the system is improved, so based on this concept, compliant joint is applied in order to have journal and bearing experience continuous contact mode more than the case that mechanism without compliant joint. Actually, "Fig. 9", shows the clearance trajectory for several stiffnesses of compliant joints, also this figure demonstrates that using proportional stiffness of compliant joint stabilizes the clearance joint in continuous contact mode. Moreover, "Fig. 9b" confirms that using compliant joint impact and free flight mode are decreased. Generally, this figure proves the idea that using proportional compliant joint increases the continuous contact mode. Moreover, the advantage of these figures allowed the investigation of using compliant joints in order to eliminate the undesirable vibration of the mechanism. The influence of clearance size and input link velocity are investigated separately, therefore "Fig. 10" demonstrates the journal center trajectory relative to bearing in several input link velocities, and "Fig. 11" shows the variation of clearance with time in several input link velocities.

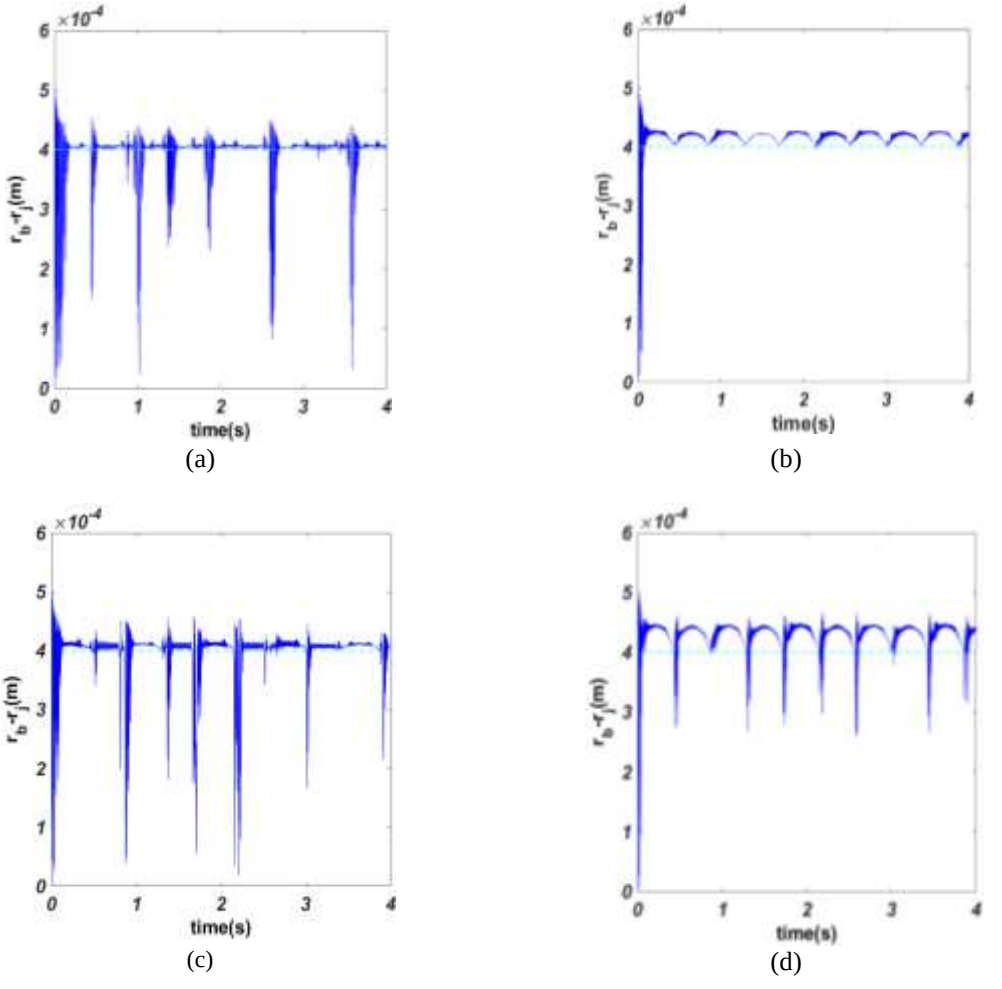

Fig. 9 Variation of clearance with time: (a): four bar linkage mechanism with one clearance joint at joint 3, and four bar linkage mechanism with one clearance joint at joint 3 and compliant joint at joint 2 with stiffness of, (b): 4 N.m, (c): 1 N.m, (d): 10 N.m.

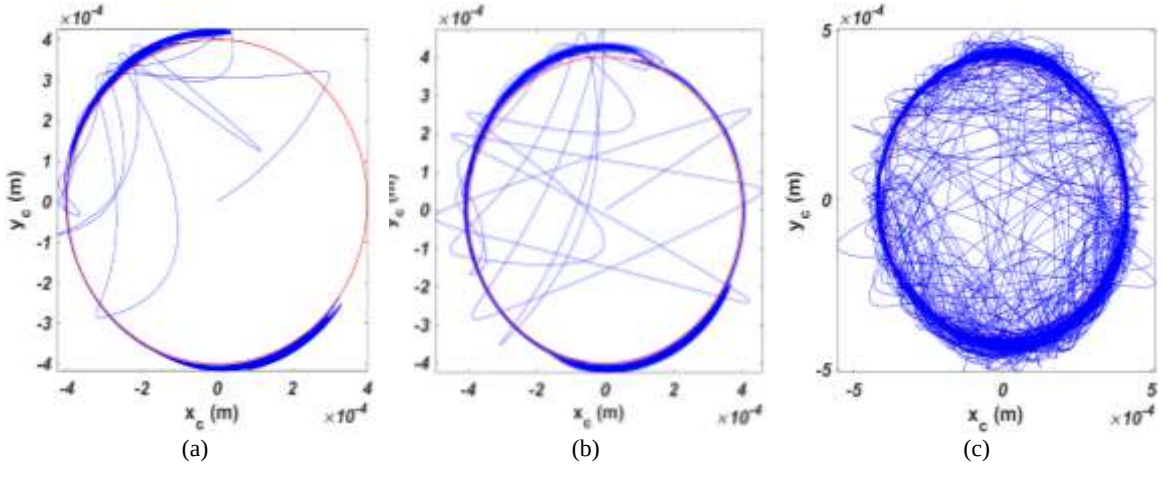

Fig. 10 Journal center trajectory relative to bearing (red circle shows the clearance size) with input link velocity: (a): 20 rpm, (b): 70 rpm, (c): 150 rpm.

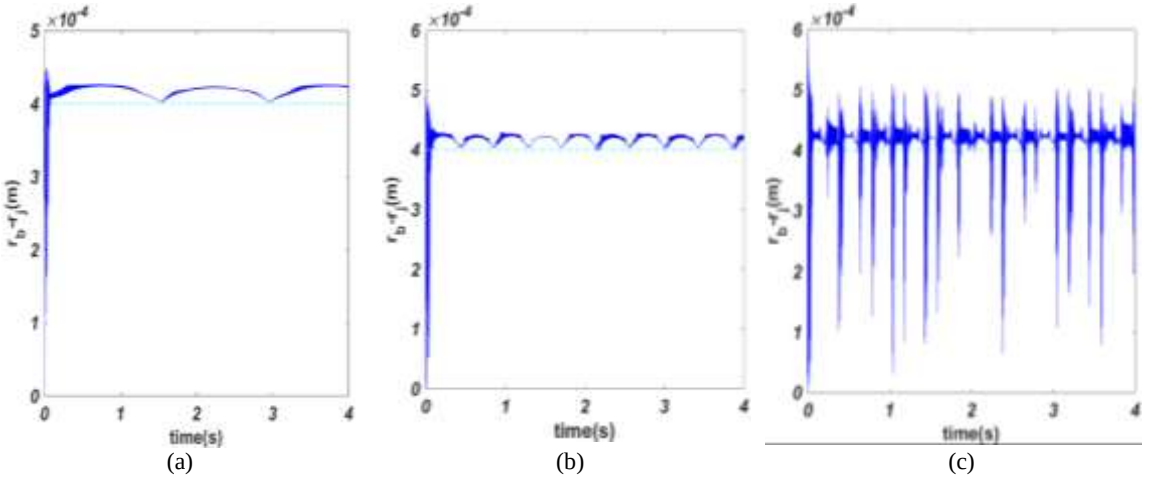

(a) (b) (c)

Fig. 11 Variation of clearance with time with input link velocity: (a): 20 rpm, (b): 70 rpm, (c): 150 rpm.

Figure 12 demonstrates the Journal center trajectory relative to bearing in several clearance sizes and "Fig. 13" shows the variation of clearance with time in several clearance sizes. Actually based on physical concepts increasing these parameters is undesirable. Also, the advantage of these figures verifies that increasing clearance size and input link, velocity is not desirable in fact, increasing these parameters causes more impact and major clearance radius.

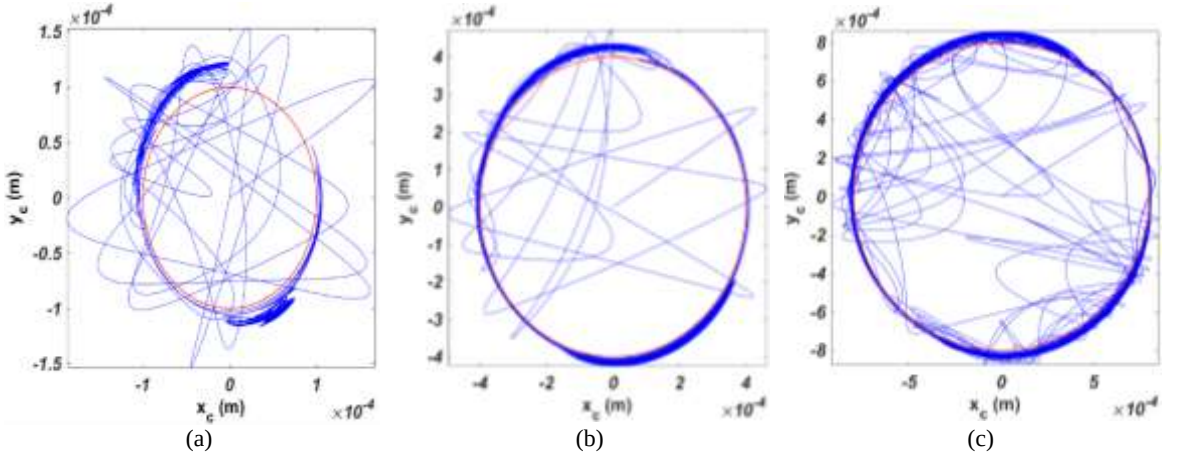

(a) (b) (c)

Fig. 12 Journal center trajectory relative to bearing (red circle shows the clearance size) with clearance size of: (a): 0.0001 m, (b): 0.0004 m (c) 0.0008 m.

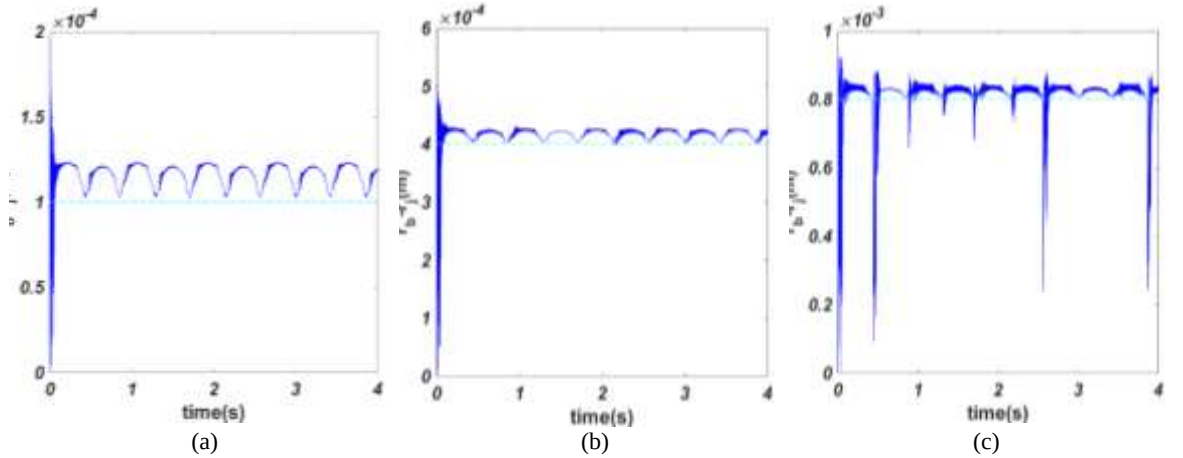

(a) (b) (c)

Fig. 13 Variation of clearance with time with clearance size of: (a): 0.0001 m, (b): 0.0004 m (c) 0.0008 m.

Figures 14 and 15 give the required moment of driving input link for the case of mechanism with clearance joint and with compliant joint. It is obvious when the angular velocity and clearance size are increased, the vibration of the mechanism is increased.

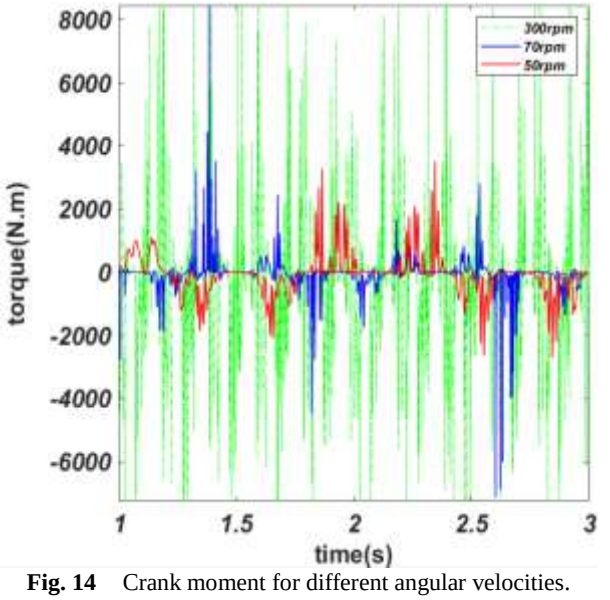

Fig. 14 Crank moment for different angular velocities.

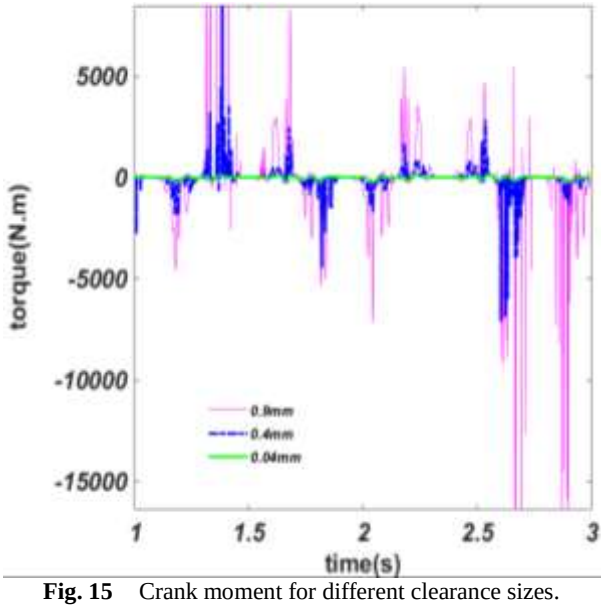

Fig. 15 Crank moment for different clearance sizes.

In this part, two cases are examined. In the first case, a four-bar linkage mechanism with one clearance joint between links 3 and 4 (i) (according to "Fig. 4"), and in the second case (ii) a four-bar linkage mechanism with a clearance joint between links 3 and 4 and a compliant joint between link 2 and 3 (according to "Fig. 5") are considered. Figure 16 shows dynamic behaviour of the second case in several stiffnesses. The yellow curves of "Figs. 16c and 16d" illustrate that the sudden changes of acceleration and moment curves are decreased by applying the compliant joint and this causes the enhancement in the useful life and dynamic behaviour of the system. According to "Fig. 16", the compliant joint with k=4 shows better behaviour than the case of k=10. These figures show that by optimizing the stiffness of compliant joint, the acceleration curve is improved. However, by other stiffness far away from the region of proportional stiffness, the behaviour of mechanism is not improved impressively. Although the sudden change of acceleration and severe collision in clearance joint is not canceled, the behaviour of mechanism via optimized compliant joint stiffness is improved by decreasing impact in clearance joint and maximum acceleration amplitude of linkages.

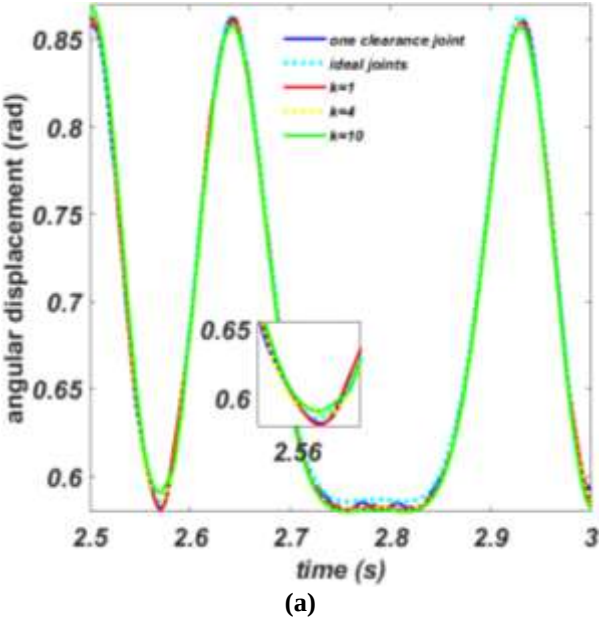

(a)

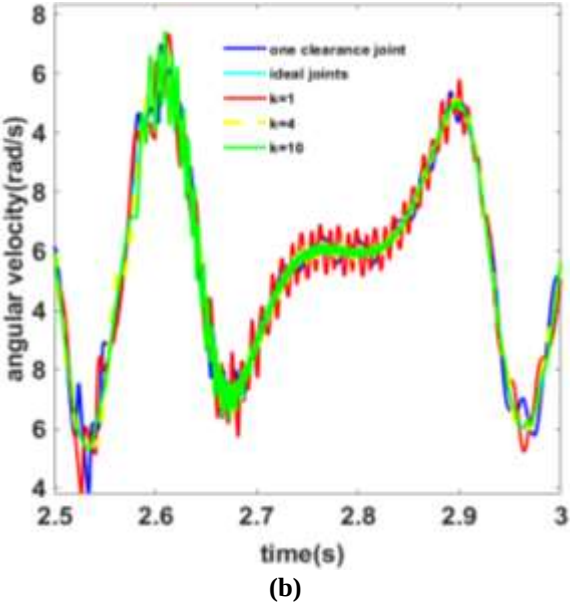

(b)

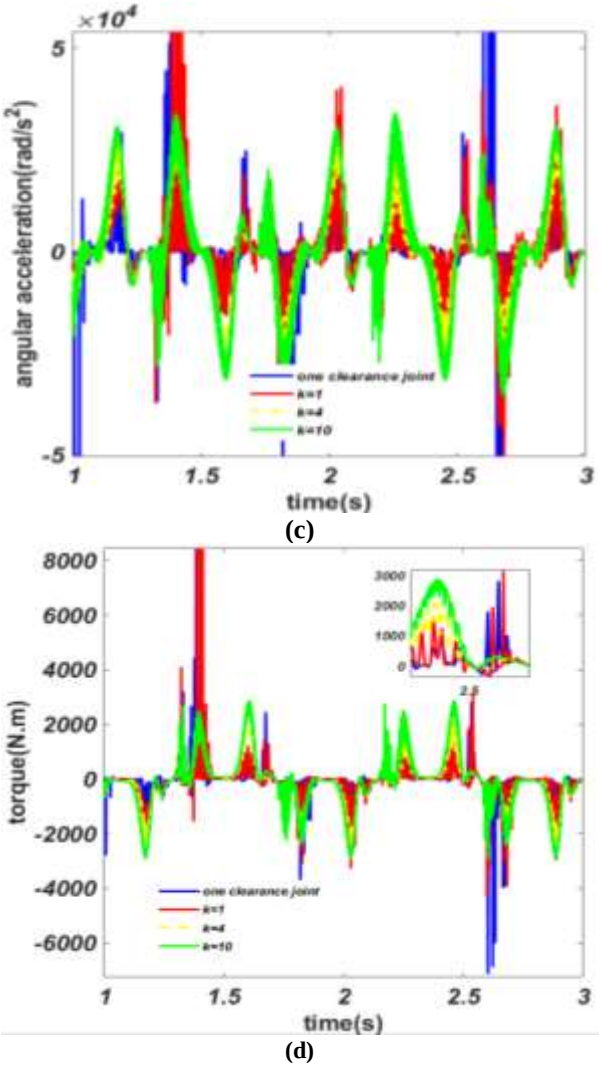

Fig. 16 Angular position, velocity and acceleration of the coupler of case (ii): (a): couple angle displacement, (b): couple velocity, (c): couple acceleration, (d): input torque.

According to previous sections, there are some parameters that affect the clearance in joints like the stiffness of joint, clearance size, and input link velocity. The present study focuses on the effect of compliant joint stiffness. Moreover one of the important ways to improve clearance influence on the vibration of mechanism is selecting the optimized stiffness of compliant joint. Therefore, in this section based on a number of impacts in the clearance joint the stiffness of the compliant joint is optimized. Figure 17 shows the number of impacts in the clearance joint according to the stiffness of the compliant joint. This figure demonstrated the range of stiffness for minimum impact. Therefore, the advantage of this figure is used to optimize the compliant joint in order to eliminate the undesirable vibration of the mechanism with clearance joint. Subsequently, the nonlinear dynamics of the mechanism are investigated in the following section.

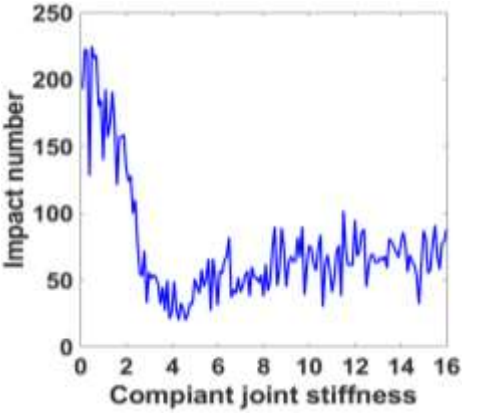

Fig. 17 Impact number versus compliant joint stiffness.

Figyre 18 shows the crank moment in the two mentioned cases. The sudden changes appeared in "Fig. 18" are because of the impact existed in the clearance joint. Figure 16 clearly illustrates that the dynamic behaviour of the system with clearance joint will be improved by using the compliant joint with proper bending coefficient. Figure 18 shows that by using the compliant joint, the clearance joint experiences fewer free flight and impact modes, therefore, the impact of the system and the sudden changes of the moment curve are decreased.

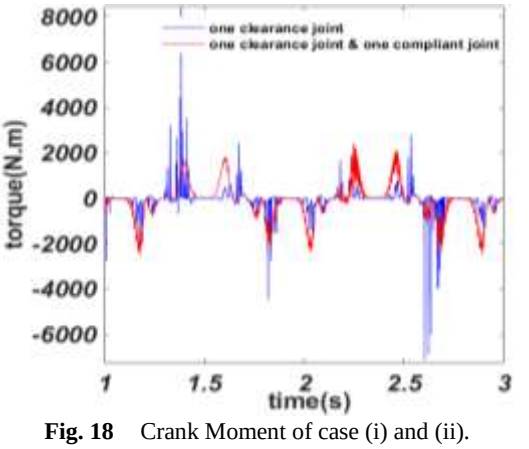

Fig. 18 Crank Moment of case (i) and (ii).

Table 4 The comparative numerical results

Considering case	Number of impact	Follower maximum acceleration	Maximum contact force
4-bar linkage with one clearance	207	2.053×10^5	9988
4-bar linkage with one clearance and one compliant joint	33	2.57×10^4	3587

Consequently, the system performance is improved and the useful life of the system is increased. As a quantitative result, applying optimized compliant joint, 84% of impacts, 87% of follower maximum acceleration, and 64% of Maximum contact force are decreased. "Table. 4" shows the comparative numerical results. The phase diagram is the graph that is commonly used for nonlinear vibration analysis. Figure 19 demonstrates the phase diagram of the ideal mechanism and the two mentioned cases for both 6 cycles (0s-5.16s) and one cycle (1.93s-2.79s). There are undesirable changes in the plots of the two mentioned cases, because of clearance. However, this phenomenon is not seen in ideal mechanism plots.

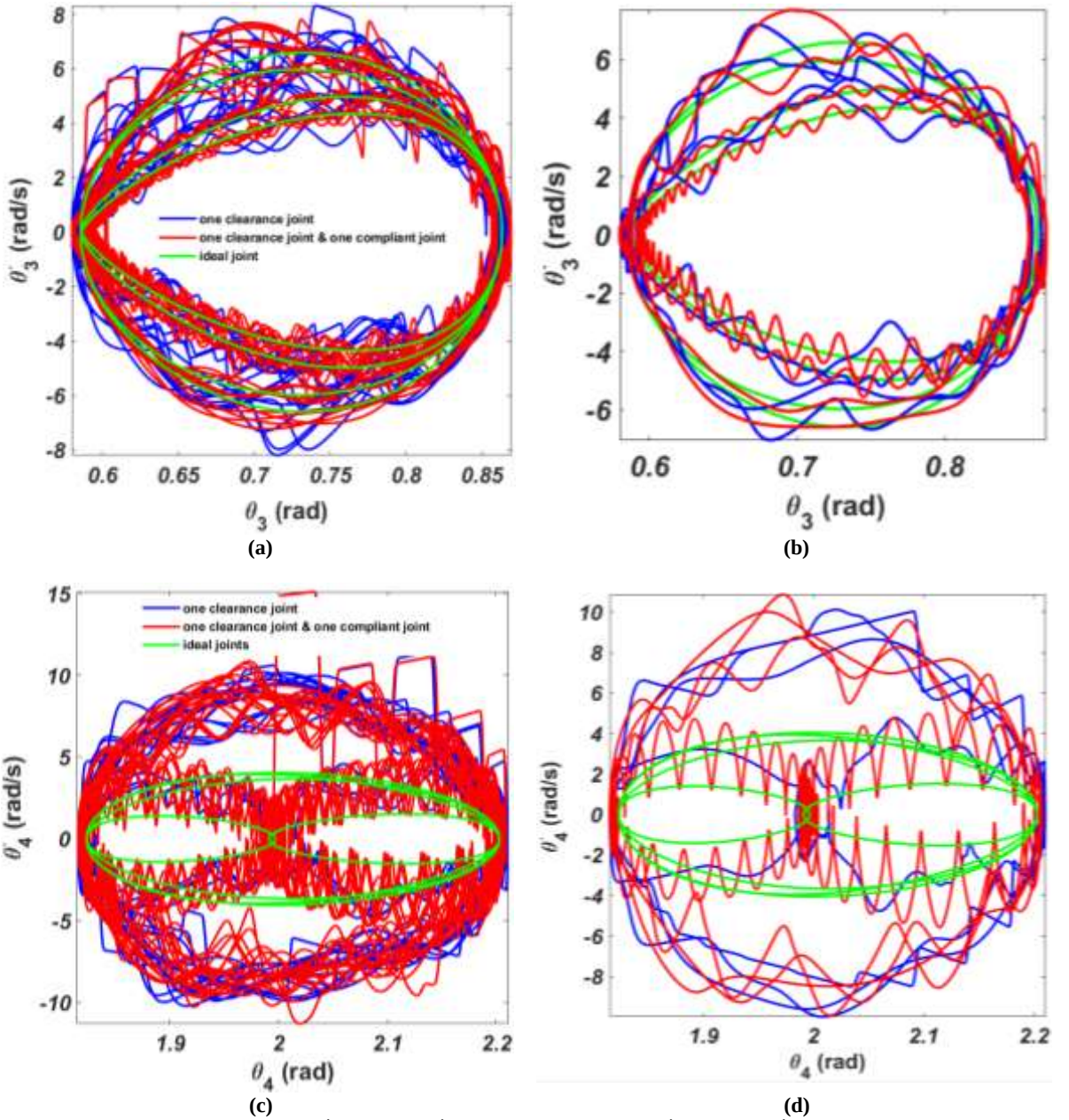

Fig. 19 Phase diagram: (a):$\theta_3 - \dot{\theta}_3$, (b): $\theta_3 - \dot{\theta}_3$ for one cycle, (c): $\theta_4 - \dot{\theta}_4$, (d): $\theta_4 - \dot{\theta}_4$ for one cycle.

Figure 20 shows the Poincare section for cases (i) and (ii). Nonlinear behaviour of these cases because of clearance is proved, since if the Poincare section of the system does not include finite discrete points; nonlinear system behaviour will be likely [10]. By comparing the two cases, it is evident that the system with a complaint joint has less chaotic behaviour given its fewer and finite discrete points.

Figure 21 shows the Poincare section based on the coupler's velocity in terms of clearance size for the two mentioned cases. This figure suggests that the number of discrete points increases with the increase in the clearance size, which in turn leads to a more chaotic system. By conducting a comparison between "Fig. 21a and 21b", the number of Poincare points in "Fig. 21b" is lower than that of "Fig. 21a", hence, the system in the state shown in "Fig. 21b" has less nonlinear behaviour in comparison to "Fig. 21a".

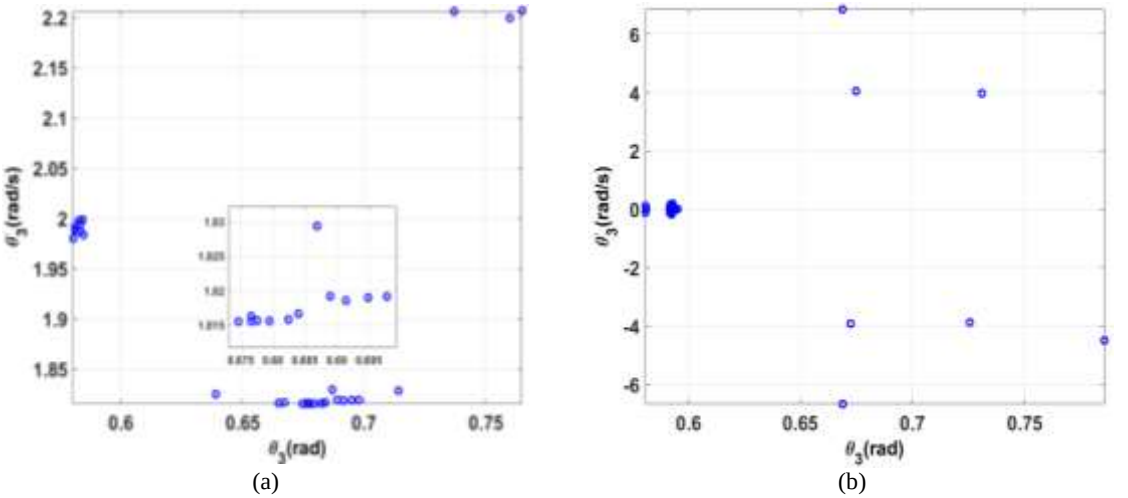

(a) (b)

Fig. 20 Bifurcation diagram of mechanism for clearance size $C = 0.4$, for: (a): clearance joint of 3, and (b): clearance joint 3 with compliant joint 2 for stiffness of k=4.

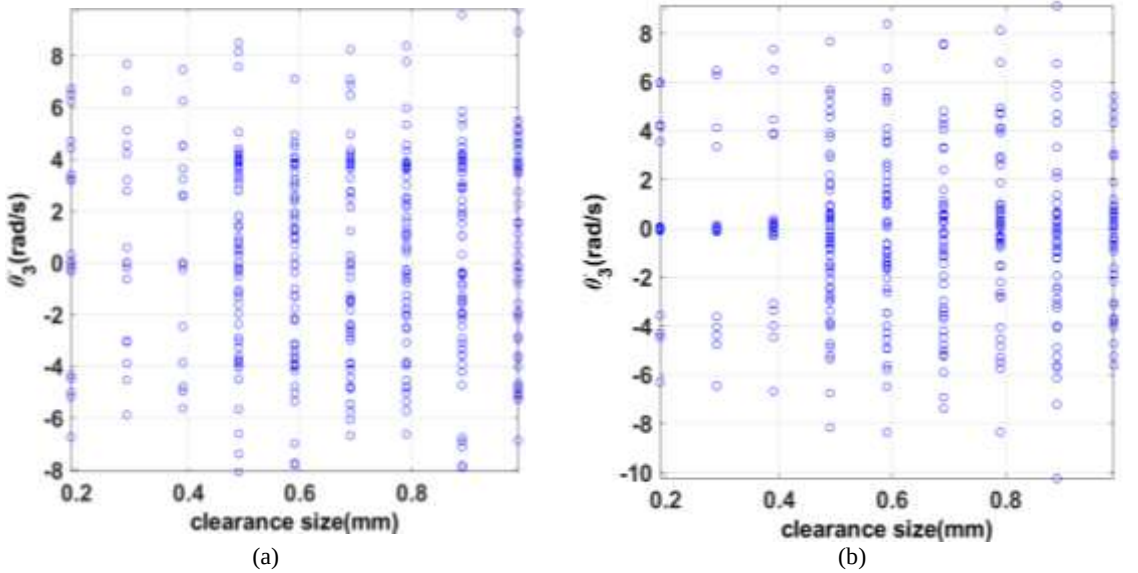

(a) (b)

Fig. 21 Poincare map for angular velocity of coupler for different clearance size: (a): with one clearance joint, (b): with one clearance and one compliant joint.

Figure 22 gives the FFT analysis of the coupler's velocity for cases (i) and (ii) for different compliant joint stiffness. The number of frequencies in the mechanism with a compliant joint is fewer than that of the mechanism with only one clearance joint, leading to fewer vibrations in the mechanism with a compliant joint, while the amplitude of these vibrations is larger. Therefore, the compliant joint improves the system behaviour and reduces undesirable vibrations. As can be seen, the number of frequencies in the mechanism with a compliant joint is fewer when comparing the optimized stiffness case to others. However, the amplitude of vibration is larger for this case. Figure 23 shows the phase diagram, it can be concluded for optimized compliant joint stiffness that the curve of the phase diagram is smoother.

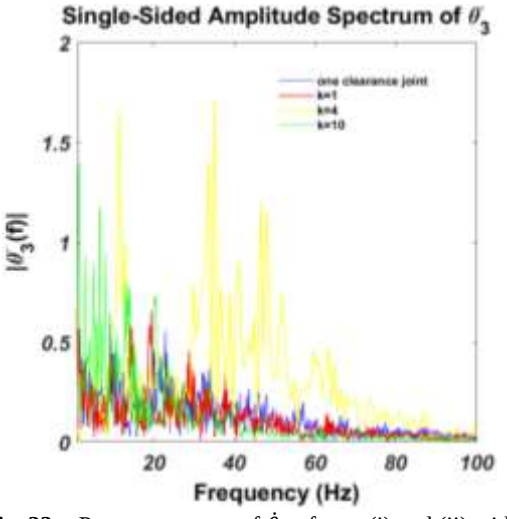

Fig. 22 Power spectrum of $\dot{\theta}_3$ of case (i) and (ii) with different stiffness of compliant joint.

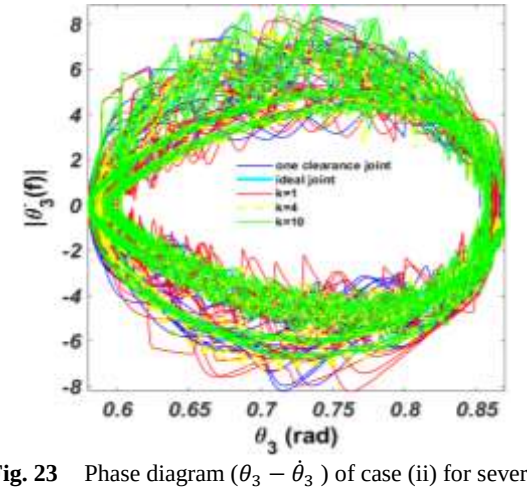

Fig. 23 Phase diagram ($\theta_3 - \dot{\theta}_3$) of case (ii) for several compliant joint stiffness.

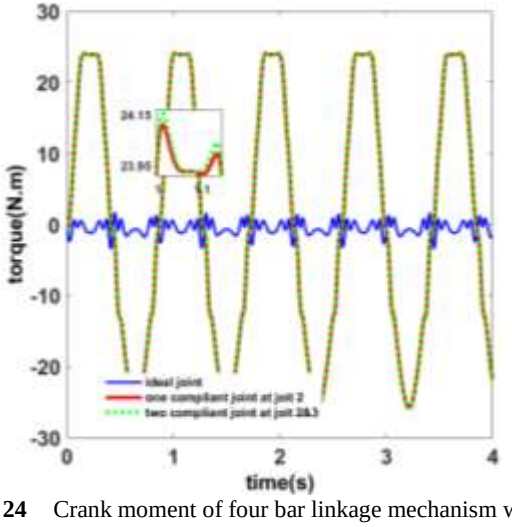

Fig. 24 Crank moment of four bar linkage mechanism with one compliant joint at joint 2 and four bar linkage mechanism with two compliant joint at joint 2 and 3.

A four-bar mechanism with two compliant joints according to "Fig. 24" is considered. The required moment for the movement of the input link in the mechanism with compliant joints is larger than the ideal one; however, this value is significantly lower compared to that of the mechanism with the clearance joint. Therefore, although compliant joints increase the required moment but the advantages of them in mechanism with clearance joint is preferable. Moreover, it is noteworthy that increasing the number of compliant joints in the system increases the value of the required input moment.

4 CONCLUSION

The main goal of this paper is to examine the influence of compliant joints on the nonlinear dynamics of mechanisms with the clearance joint. Lagrange Equations are used to derive EoM, and Lankarani-Nikravesh model is used for contact force calculation. Considering the addition of a clearance joint to a four-bar linkage mechanism with one DoF, three DoFs are obtained, and since the compliant joint is assumed a torsion spring, no change in the number of DoF occurs. Moreover, the Runge-Kutta 4th order method is applied to solve EoM.

The results reveal the significant efficiency of applying a compliant joint for reducing undesirable vibration due to the clearance joint. Furthermore, the outcome of increasing input link velocity and clearance size is the increase of undesirable system vibrations.

Moreover, present research represented that by using a proper bending compliant joint, an improved dynamical behaviour can be achieved. So by concentrating on the bending stiffness of a compliant joint, dimensions of this joint are selected in order to improve dynamical behaviour. The simulation of the mechanism in 6 cycles demonstrates the 207 impacts in clearance joint for mechanism without compliant joint, however compliant joint decreases impacts to 33, the follower maximum acceleration is $2.053 \times 10^5 (\frac{rad}{s^2})$ for the mechanism without compliant joint, however compliant joint decreases follower maximum acceleration to 2.57×10^4, and the maximum contact force in clearance joint is 9988 for the mechanism without compliant joint, however compliant joint decreases maximum contact force to 3587. According to the quantitative results, the compliant joint can increase the life of mechanisms with the clearance joint. Moreover, examining nonlinear behaviour analysis confirmed our conclusion.

Apparently, there are some limitations in our proposed model in terms of considering axial stiffness and translation of compliant joint, and lubrication effect in clearance joint to achieve more accurate models.

However, the suggestion can be extended by considering the 3D vector of clearance radius to simulate 3D mechanisms and robotic systems to eliminate the undesirable effect of clearance joint by using compliant joint.

REFERENCES

[1] Seneviratne, L. D., Earles S. W., and Fenner D. N., Analysis of a Four-Bar Mechanism with a Radially Compliant Clearance Joint, Proceedings of the Institution of Mechanical Engineers, Part C: Journal of Mechanical Engineering Science. Vol. 210, No. 3, 1996, pp. 215-223, DOI: 10.1243%2FPIME_PROC_1996_210_191_02.

[2] Chen, Y., Feng J., Peng, X., Sun, Y., He, Q., and Yu, C., An Approach for Dynamic Analysis of Planar Multibody Systems with Revolute Clearance Joints, Engineering with Computers, Vol. 37, No. 3, 2021, pp. 2159-2172, DOI: 10.1007/s00366-020-00935-x.

[3] Lankarani, H. M., Nikravesh, P. E., A Contact Force Model with Hysteresis Damping for Impact Analysis of Multibody Systems, In International Design Engineering Technical Conferences and Computers and Information in Engineering Conference, Vol. 3691, pp. 45-51. American Society of Mechanical Engineers, DOI: 10.1115/1.2912617.

[4] Pereira C. M., Ramalho A. L., and Ambrósio J. A., A Critical Overview of Internal and External Cylinder Contact Force Models, Nonlinear Dynamics, Vol. 63, No. 4, 2011, pp. 681-697, DOI: 10.1007/s11071-010-9830-3.

[5] Flores, P., Ambrósio, J., Claro, J. C. P., Lankarani, H. M., and Koshy, C. S, A Mechanism and Machine Theory, Vol. 41, No. 3, 2006, pp. 247-261, DOI: 10.1016/j.mechmachtheory.2005.10.002.

[6] Koshy, C. S., Sony, Ch., Flores, P., and Lankarani, H. M., Study of the Effect of Contact Force Model on The Dynamic Response of Mechanical Systems with Dry Clearance Joints: Computational and Experimental Approaches, Nonlinear Dynamics, Vol. 73, No. 1, 2013, pp. 325-338, DOI: 10.1007/s11071-013-0787-x.

[7] Varedi, S. M., Bamdad, M., The Effects of Joint Clearance on the Dynamics of the 3-RPR Planar Parallel Manipulator, Advance Design and manufacturing Technology, Vol. 11, No. 2, 2018, pp. 120-113, DOI: 10.1017/S0263574715001095.

[8] Ebrahimi, S., Salahshoor, E., and Nouri, S., Sensitivity Analysis for Optimal Design of Multibody Systems with Clearance Joint, Advance Design and Manufacturing Technology, Vol. 11, No. 3, 2018, pp. 35-44, ISSN: 2252-0406.

[9] Flores, P., Koshy, C. S., Lankarani, H. M., Ambrósio, J., and Koshy, C. S., Numerical and Experimental Investigation on Multibody Systems with Revolute Clearance Joints, Nonlinear Dynamics, Vol. 65, No. 4, 2011, pp. 383-398, DOI: 10.1007/s11071-010-9899-8.

[10] Javanfar, A., Daniali, H. M., Dardel, M., and Ghasemi, M. H., Dynamic Behaviour Analysis of Four-Bar Linkage Mechanisms with Joints' Clearance, In 2015 3rd RSI International Conference on Robotics and Mechatronics (ICROM), pp. 383-388, IEEE, 2015, DOI: 10.1109/ICRoM.2015.7367815.

[11] Javanfar, A., Bamdad, M., Effect of Novel Continuous Friction Model on Nonlinear Dynamics of The Mechanisms with Clearance Joint, Proceedings of the Institution of Mechanical Engineers, Part C: Journal of Mechanical Engineering Science (2021), Vol. 236, No. 11, 2022, pp. 6040-6052, DOI: 10.1177%2F09544062211063432.

[12] Marques, F., Flores, P., Pimenta, C., and Lankarani, H. M., A Survey and Comparison of Several Friction Force Models for Dynamic Analysis of Multibody Mechanical Systems, Nonlinear Dynamics, Vol. 86, No. 3, 2016, pp. 1407-1443, DOI: 10.1007/s11071-016-2999-3.

[13] Azimi-Olyaei, A., Ghazavi, M. R, Stabilizing Slider-Crank Mechanism with Clearance Joints, Mechanism and Machine Theory, Vol. 53, 2012, pp. 17-29, DOI: 10.1016/j.mechmachtheory.2012.02.006.

[14] Yaqubi, S., Dardel, M., Daniali, H. M., and Ghasemi, M. H., Modeling and Control of Crank–Slider Mechanism with Multiple Clearance Joints, Multibody System Dynamics, Vol. 36, No. 2, 2016, pp. 143-167, DOI: 10.1007/s11044-015-9486-3.

[15] Erkaya, S., Uzmay I., Investigation on Effect of Joint Clearance on Dynamics of Four-Bar Mechanism, Nonlinear Dynamics, Vol. 58, No. 1, 2009, pp. 179-198, DOI: 10.1007/s11071-009-9470-7.

[16] Sardashti, A., Daniali H. M., and Varedi S. M., Optimal Free-Defect Synthesis of Four-Bar Linkage with Joint Clearance Using PSO Algorithm, Meccanica, Vol. 48, No. 7, 2013, pp. 1681-1693, DOI: 10.1007/s11012-013-9699-6.

[17] Varedi, S. M., Daniali, H. M., Dardel, M., and Fathi, A., Optimal Dynamic Design of a Planar Slider-Crank Mechanism with a Joint Clearance, Mechanism and Machine Theory, Vol. 86, 2015, pp. 191-200, DOI: 10.1007/s11012-013-9699-6.

[18] Bai, Z. F., Zhao, Y., A Hybrid Contact Force Model of Revolute Joint with Clearance for Planar Mechanical Systems, International Journal of Non-Linear Mechanics, Vol. 48, 2013, pp. 15-36, DOI: 10.1016/j.ijnonlinmec.2012.07.00.

[19] Liu, X., Ding, J., and Wang, C., Design Framework for Motion Generation of Planar Four-Bar Linkage Considering Clearance Joints and Dynamics Performance, Machines, Vol. 10, No. 2, 2022, pp. 136, DOI: 10.3390/machines10020136.

[20] Hua, G., Jingyu, Z., Hao, Z., Qingkai, H., and Jinguo, L., Dynamic Investigation of a Spatial Multi-Body Mechanism Considering Joint Clearance and Friction Based on Coordinate Partitioning Method, Proceedings of the Institution of Mechanical Engineers, Part C: Journal of Mechanical Engineering Science, Vol. 235, No. 24, 2021, pp. 7569-7587, DOI: 10.1177%2F09544062211025566.

[21] Yaqubi, S, Dardel, M, and Daniali, H. M., Nonlinear Dynamics and Control of Crank–Slider Mechanism with Link Flexibility and Joint Clearance, Proceedings of the Institution of Mechanical Engineers, Part C: Journal of Mechanical Engineering Science, vol. 230, no. 5, 2016, pp. 737-755, DOI: 10.1177%2F0954406215593773.

[22] Erkaya, S., Doğan, S., and Şefkatlıoğlu, E., Analysis of the Joint Clearance Effects on a Compliant Spatial Mechanism, Mechanism and Machine Theory, Vol. 104, 2016, pp. 255-273, DOI: 10.1016/j.mechmachtheory.2016.06.009.

[23] Oh, Y. S., Kota, S., Synthesis of Multistable Equilibrium Compliant Mechanisms Using Combinations of Bistable Mechanisms, Journal of Mechanical Design, Vol. 131, No. 2, 2009, DOI: 10.1115/1.3013316.

[24] Erkaya, S., Effects of Joint Clearance on the Motion Accuracy of Robotic Manipulators, Strojniski Vestnik/Journal of Mechanical Engineering, Vol. 64, No. 2, 2018, DOI: 10.5545/sv-jme.2017.4534.

[25] Amiri, A., Dardel, M., and Daniali, H. M., Effects of Passive Vibration Absorbers on The Mechanisms Having Clearance Joints, Multibody System Dynamics, Vol. 47, No. 4, 2019, pp. 363-395, DOI: 10.1007/s11044-019-09684-2.

[26] Moon, Y. M., Trease, B. P., and Kota, S., Design of Large-Displacement Compliant Joints, InInternational Design Engineering Technical Conferences and Computers and Information in Engineering Conference, Vol. 36533, 2002, pp. 65-76, American Society of Mechanical Engineers, DOI: 10.1115/DETC2002/MECH-34207" \t.

[27] Fowler, R. M., Maselli, A., Pluimers, P, Spencer P. M., and Howell, L. L., Flex-16: A Large-Displacement Monolithic Compliant Rotational Hinge, Mechanism and Machine Theory, Vol. 82, 2014, pp. 203-217, DOI: 10.1016/j.mechmachtheory.2014.08.008.

[28] Wang, N., Xiaohe, L., and Xianmin, Z., Pseudo-Rigid-Body Model for Corrugated Cantilever Beam Used in Compliant Mechanisms, Chinese Journal of Mechanical Engineering, Vol. 27, No. 1, 2014, pp. 122-129, DOI: 10.3901/CJME.2014.01.122.

[29] Li, Z., Tsagarakis, N. G., and Caldwell, D. G., Walking Pattern Generation for a Humanoid Robot with Compliant Joints, Autonomous Robots, Vol. 35, No. 1, 2013, pp. 1-14, DOI: 10.1007/s10514-013-9330-7.

[30] Timoshenko, S., History of Strength of Materials: with a Brief Account of The History of Theory of Elasticity and Theory of Structures, Courier Corporation, 1983, ISBN: 0486611876.

[31] Ugwuoke, I. C., Abolarin, M. S., and Ogwuagwu, O. V., Dynamic Behaviour of Compliant Slider Mechanism using the Pseudo-Rigid-Body Modeling Technique, AU JT, Vol. 12, No. 4, 2009, pp. 227-234.

Int. J. Advanced Design and Manufacturing Technology, 2022, Vol. 15, No. 4, pp. 29-38

DOI: 10.30486/admt.2023.1955556.1344 *ISSN: 2252-0406* *https://admt.isfahan.iau.ir*

Heat Transfer of Wavy Microchannel Heat Sink with Microtube and Ag/Water-Ethylene Glycol Hybrid Nanofluid

Akram Jahanbakhshi
Department of Mechanical Engineering,
University of Shahrekord, Iran
E-mail: a_jahanbakhshi@stu.sku.ac.ir

Afshin Ahmadi Nadooshan*
Department of Mechanical Engineering,
Shahrekord University, Shahrekord, Iran
E-mail: ahmadi@sku.ac.ir
*Corresponding author

Morteza Bayareh
Department of Mechanical Engineering,
Shahrekord University, Shahrekord, Iran
E-mail: m.bayareh@sku.ac.ir

Received: 25 March 2022, Revised: 28 April 2022, Accepted: 30 April 2022

Abstract: In the present study, novel channel geometries in a wavy channel heat sink (HS) are investigated using ANSYS-FLUENT software. The Ag/water-ethylene glycol (50%) nanofluid is selected for cooling the CPU in this HS. The second-order upwind method is employed to discretize the momentum Equation and the SIMPLEC algorithm is employed for coupling velocity and pressure fields. Comparison of the two HSs with and without microtube shows that the presence of the microtube increases the uniformity of the CPU surface temperature distribution and decreases the mean surface temperature of the CPU (TCPU-Mean). However, the pumping power consumption of the system increases about 10 times. The results also demonstrate that the addition of nanoparticles results in intensification in the Performance Evaluation Criterion (PEC) of the system and up to 30%, especially at high Reynolds numbers.

Keywords: Heat Sink, Heat Transfer, Hybrid Nanofluid, Microtube, Numerical Simulation, Wavy Microchannel

Biographical notes: Akram Jahanbakhshi received his PhD in Mechanical Engineering from Shahrekord University in 2022. Her field of research is study of heat transfer in microchannel and micro heatsink, energy efficiency and nanofluid heat transfer. **Afshin Ahmadi Nadooshan** received his PhD in Mechanical Engineering from Isfahan University of Technology in 2007. He is currently Professor at the Department of Mechanical Engineering at Shahrekord University, Iran. His current research interest includes heat transfer, thermodynamics and multi-phase flows. **Morteza Bayareh** is Associated Professor of Mechanical engineering at Shahrekord University, Iran. He received his PhD in Mechanical engineering from Isfahan University of technology in 2013. His current research focuses on Turbulent flows, multi-phase flows and thermodynamics.

Research paper

1 INTRODUCTION

Various methods and techniques have been developed over the past few decades to improve heat transfer rate (HTR) in heat exchangers. Wavy channels have attracted a lot of attention due to that they have extremely high HTR relative to straight channels. The secondary flow formed by the wavy surfaces enhances the mixing between the fluid adjacent to the wall and the fluid in the middle of the channel, improving the thermal performance of these geometries [1]. Dean [2] was the first one who studied the effective parameters of wavy-surface flows to obtain the effects of the centrifugal force and the pressure difference between the outer and inner walls of a wavy channel. Cheng [3] investigated the influence of the aspect ratio of rectangular channels with constant wall heat flux on convective heat transfer numerically and observed that the improvement of heat transfer due to the wavy surface is higher than the intensification in flow pressure drop compared to straight channels. Kalb and Seader [4] analyzed heat transfer of fully developed flow in wavy circular tubes exposed to fixed heat flux considering the relationship between the path curvature radius and the diameter of the tube. Guo [5] performed a second law-based analysis and found that wavy channel parameters have an important influence on thermodynamic performance. Yang et al. [6] investigated the influence of alternating curvature of a channel and understood that the HTR is improved as the frequency is enhanced or the curvature wavelength decreases. Experimental studies on wavy surfaces have also shown that the thermal performance of these surfaces is better than that of straight channels [6-8]

In recent years, microchannel heat sinks (MCHS) established by Tuckerman and Pease [9] are one of the most widely used cooling techniques in microelectronic equipment. The HS microchannel, which is known as one of the cooling methods with a high heat transfer coefficient (HTC) (h), provides good conditions for rejecting high heat flux because of the small geometric dimensions and the high surface-to-volume ratio of the channel. In fact, HSs are passive heat exchangers that transfer the heat generated by mechanical or electrical devices to a fluid. For example, HSs are used for cooling the CPU of computers or used to moderate temperatures. Many studies have been done in this regard, for example, the theoretical study of Knight et al. [10] who investigated MCHS optimization. Various experimental studies have also been performed to show that the wavy walls result in the improvement of their performance [11-15]. Lin et al. [16] designed a wavy channel HS and proposed an appropriate geometry by varying the wavelength and frequency of the channels when the pumping power of the system was constant. These studies showed that MCHS performs much better than conventional energy absorbers but still needs to be studied and improved.

Nanofluid refers to a mixture of nanoparticles dispersed in a common liquid. The improvement of the base fluid (BF) thermal conductivity is because of the nanoparticle Brownian motion and the transport mechanisms inside the mixture, resulting in higher HTRs [17] Various properties of new nanofluids obtained from the composition of nanoparticles added to the BF have been reported in various experimental investigations. Esfe et al. [18] investigated the viscosity of motor oil-Al_2O_3 nanofluid at dissimilar concentrations and temperatures (5-65 °C) and presented new correlations. They showed that this nanofluid is Newtonian at dissimilar shear rates for all volume concentrations. It was also demonstrated that the nanofluid viscosity intensifies with growing the nanoparticles volume fraction (ϕ) and diminishing the temperature, which is more evident at low temperatures. Selvakumar and Suresh [19] considered the effects of water-copper oxide nanofluid on a HS with thin channels under fixed heat flux. They found that h increases with increasing the ϕ, and the pump power consumption increases by 15.11% for nanofluid with a volumetric concentration of 2%. Ermagan and Rafee [20] simulated three types of the rectangular microchannel HS with smooth, hydrophobic, and superhydrophobic wall surfaces. The results showed that microchannel HS with superhydrophobic walls has higher thermal efficiency compared to the other two types. The new HS design with rectangular and triangular two-layer channels is proposed by Ahmed et al. [21]. They used water-alumina and water-silica nanofluids. Their results revealed that the temperature of the walls of triangular channels is decreased by about 27.4% compared to that of rectangular ones. Tafarroj et al. [22] employed an artificial neural network for modeling h and the Nusselt number (Nu) of TiO_2-water in a microchannel. Their results showed that a trained network could be used as an appropriate method for costly and time-consuming nanoscale experiments in the microchannel. Esfahani and Toghraie [23] studied the thermal conductivity of silica/ethylene glycol (EG)-water nanofluid at temperatures ranging from 25 to 50 °C and ϕ = 0.1, 0.5, 1, 1.5, 2, 3 and 5%. Their results demonstrated that the thermal conductivity intensifies with growing temperature and ϕ. Their results indicated that the maximum thermal conductivity (45.5%) occurs at ϕ = 5% at 50 °C. Ghasemi and Karimipour [24] studied the effect of mass fraction of copper oxide nanoparticles and temperature on the viscosity of liquid paraffin. They prepared CuO nanoparticles by sedimentation method in which $Cu(NO_3)_23H_2O$ was employed as the leading material. They revealed that an increase of the nanoparticles in the BF greatly increases the viscosity. It was shown that the nanofluid viscosity falls significantly with the temperature. Karimipour et al. [25] studied the

effect of CuO mass fraction and temperature on viscosity and thermal conductivity of nanofluid. In this experiment, viscous paraffin was considered as the BF. TEM and DLS tests, as well as the Zeta potential test, were implemented to obtain the morphology and stability of the nanoparticles within the BF. Afrand et al. [26] examined the effect of temperature and concentration of nanoparticles on the dynamic viscosity of silicon dioxide- carbon nanotubes/motor oil (SAE40) hybrid nanofluid at temperatures 25 and 60 °C. They found that larger nanoclusters are formed due to the van der Waals forces between the particles by increasing the concentration of nanoparticles. Adio et al. [27] inspected the viscosity of magnesium oxide-EG nanofluid with ϕ = 0-5%. They concluded that the effective viscosity of all samples is decreased exponentially with the temperature. Also, at a constant ϕ, nanofluid containing magnesium oxide with a diameter of 21 nm has a greater effective viscosity than the one containing magnesium oxide with dimensions of 105 and 125 nm. Asadi et al. [28] evaluated the viscosity of magnesium oxide (80%)/carbon nanotubes (20%)/SAE 50 oil with the ϕ = 0.25-2% at the temperatures between 25 and 50 °C. They reported that nanofluid exhibits Newtonian behavior at all temperatures and ϕ. He also reported the lowest increase (20%) in the viscosity for ϕ = 0.26%. Esfe et al. [29] provided a high-precision model for predicting the thermal conductivity of zirconium-EG nanofluid using a neural network, where ϕ = 0.0625-5%.

Zhou et al [30] used a novel response surface methodology (RSM) and revealed that the boundary layer thickness is reduced due to the creation of vortex, resulting in an increment in HTR. Hatami et al [31] also demonstrated that enhancing the Reynolds number intensifies HTR. Al-Rashed et al. [32] investigated the use of Ag/water nanofluid prepared by tea leaves synthesis method. They evaluated the effect of the addition of nanofluid on the system performance at different values of Reynolds number in a wavy channel HS and obtained the maximum efficiency.

In the present work, the optimal geometry introduced by Al-Rashed et al. [32] is used as the reference geometry and the effect of microtube mounted on the microchannel walls and the use of Ag/water-EG (50%) nanofluid are investigated. The nanofluid can be prepared through biosynthesis and thus is recognized as a bioenvironmental method.

2 NANOFLUID PROPERTIES

Sarafraz and Hormozi [33] produced Ag nanoparticles using tea leaves, which is a clean method. In the present work, water-EG (50%) is employed as the base fluid. Ag nanoparticles are suspended in the base fluid to prepare a hybrid nanofluid. The density, specific heat capacity, viscosity, and thermal conductivity of nanofluid are calculated based on volume fraction (ϕ) using the following Equations:

$$\rho_{nf} = (1-\phi)\rho_{bf} + \phi\rho_{p} \quad (1)$$

$$\rho_{nf}C_{p,nf} = (1-\phi)\rho_{bf}C_{p,bf} + \phi\rho_{p}C_{p,p} \quad (2)$$

$$\mu_{nf} = \mu_{bf}(1+2.5\phi) \quad (3)$$

$$k_{nf} = k_{bf}(0.981 + 0.00114T(c^{\circ}) + 30.661\phi) \quad (4)$$

Where, ρ is the density, C_p is the specific heat capacity, μ is the viscosity, k is the thermal conductivity, and T shows the temperature. Subscript *b*f refers to the BF, *p* to the nanoparticles, and *nf* to the nanofluid.

3 MODEL DESCRIPTION

3.1. Geometry and Boundary Conditions

Geometry and boundary conditions: "Fig. 1" shows the schematic of the HS with two geometries: the first one has 50 wavy channels and another one has microtubes placed on the channel walls. Due to the symmetry of the problem, only a domain containing one channel and half tubes is solved. The channel walls have a surface symmetry condition and the middle plane of the two half tubes is coupled to each other. Since the plane of symmetry is located on the solid fin, the temperature gradient perpendicular to the plate is zero. For coupling the middle plane of the two half tubes, the difference of the components of velocity, temperature, and pressure on these two planes are equal to zero. "Table 1" shows the dimensions specified in "Fig. 1".

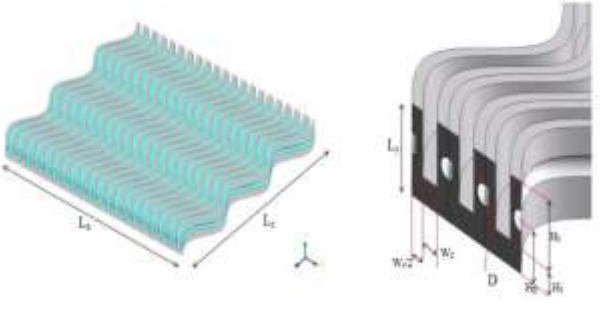

Fig. 1 Schematic of the problem.

The flow inlet temperature is assumed to be 300 K. All HS surfaces that are in contact with the surrounding are insulated.

Table 1 Dimensional parameters of the present problem

Parameter	Value
LX	10mm
LY	350μm
LZ	15mm
Wf	120 μm
WC	80 μm
D	80 μm
Hf	100 μm
HC	250 μm
HD	200 μm

Uniform inlet velocity (u) is calculated using different Reynolds numbers (300, 500, 700, 1000, and 1500) and the other velocity components (v, w) are zero. Also, the inlet pressure gradient is considered as zero.
Reynolds number is defined as follows:

$$\mathrm{Re} = \frac{\rho u D}{\mu} \tag{5}$$

Where, D is the hydraulic diameter. It is assumed that the HS is mounted on a CPU and thus the heat flux of 50 W/cm^2 is applied on its bottom. The waveform of the channel and microtube along the HS is a sinusoidal function:

$$S(z) = a_w \sin(\frac{2\pi z}{L_w}) \tag{6}$$

Where, a_W and L_W are selected according to the work of Al-Rashed et al. [33] who investigated a wavy microchannel HS. According to this study, $a_W = 138\mu m$ and $L_W = 5mm$ resulted in the highest HTR and PEC. In the present study, the same profile is used for the channel and tube along with the HS. In this study, the geometry is constant and the effect *Re* and ϕ is investigated. The microchannel Reynolds number is 10 times of the microtube.

3.2. Governing Equations

The present work investigates the hydraulic and thermal behavior of Ag/water-EG (50%) nanofluid with ϕ = 0.1%, 0.5%, and 1%. To do this, the conservation Equations of mass, momentum, and energy should be solved. The nanofluid is considered Newtonian and incompressible and hence the governing Equations are as follows [32], Continuity Equation:

$$\nabla.(\rho_{nf}) = 0 \tag{7}$$

Momentum Equation:

$$\nabla.(\rho_{nf}\vec{u}\vec{u}) = -\nabla p + \nabla.(\mu_{nf}\nabla\vec{u}) \tag{8}$$

Energy Equation for liquid phase:

$$\nabla.(\rho_{nf}\vec{u}C_{Pnf}T) = -\nabla.(K_{nf}\nabla T) \tag{9}$$

Energy Equation for solid phase:

$$\nabla.(K_S\nabla T) = 0 \tag{10}$$

In the above Equations, $\vec{u}$ is velocity vector and p is the pressure. Subscript *s* refers to the properties of the solid region. The uniformity of the CPU surface temperature cooled by the HS can be controlled by defining the parameter θ ("Eq. (10)"). As the value of θ reduces, the surface temperature of the HS is more uniform.

$$\theta = \frac{T_{cpu-\max} - T_{cpu-\min}}{T_{cpu-mean}} \tag{11}$$

Where, $T_{CPU,Max}$, $T_{CPU,Mean}$ and $T_{CPU,min}$ are maximum, mean, and minimum CPU surface temperature, respectively. Convective HTC is defined as follows:

$$h = \frac{q''}{T_{cpu-mean} - T_{in}} \tag{12}$$

The amount of pumping power required for the HS is calculated as follows:

$$W_{pump} = \dot{V}\nabla p \tag{13}$$

To assess the overall performance of nanofluid in the HS, the PEC is also defined:

$$PEC = \frac{h_{nf}/h_{bf}}{\Delta p_{nf}/\Delta p_{bf}} \tag{14}$$

4 NUMERICAL METHOD

ANSYS FLUENT 18.0 software is used to solve the governing Equations. The second-order upwind method is employed to discretize the momentum Equation and the SIMPLEC algorithm with the staggered grid is employed to couple pressure and velocity fields. The convergence criterion is set at 10^{-8} for the energy Equation and 10^{-6} for the other Equations based on the scaled residuals. The independence of the grid is investigated. "Table 2" shows the results for channel and tube Reynolds numbers of 700 and 70, respectively, when ϕ = 1%.

Table 2 Grid study results

W_{pump} $[W]$	ΔT $[K]$	Number of elements
0.0186	3.386	24000
0.0475	3.387	27000
0.0568	3.388	74000
0.0587	3.388	128000
0.0591	3.388	195000
0.0591	3.388	330000

Based on "Table 2", the grid resolution of 195,000 is selected for further simulations ("Fig. 2").

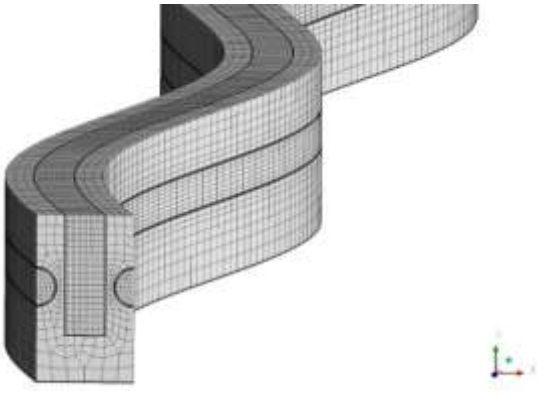

Fig. 2 An image of the grid used for current simulations.

The present work is verified with the experimental findings of Sui et al. [8]. Figure 3 illustrates a comparison between the *Nu* calculated by present numerical simulations and the one reported by Sui et al.

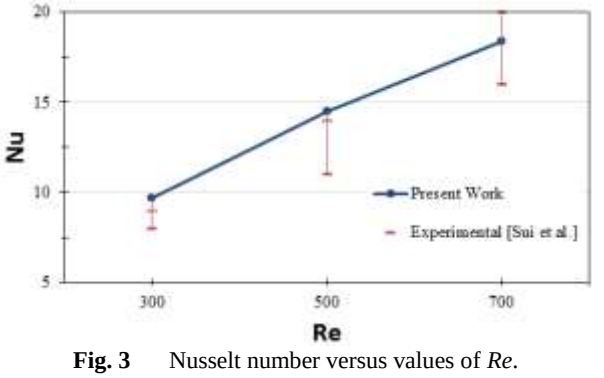

Fig. 3 Nusselt number versus values of *Re*.

According to this paper, a wavy microchannel is modeled based on the parameters presented in "Table 3". A comparison between the amount of *Nu* calculated by numerical solution and the experimental results of Sui et al. is shown in "Fig. 3". This figure displays that the present results are in good agreement with experimental data. The maximum error between the present study and the experimental data is 8%, which is related to the flow with *Re* = 300. For *Re* = 500, the error is 3% and for *Re* = 700, the present results are in agreement with the experimental data.

Table 3 Geometric parameters of the validation problem (Sui et al. 2011)

Value	Parameter
193 μm	W_f
207 μm	W_C
100 μm	H_f
406 μm	H_C
138 μm	a_W
25 mm	L_Z

Sivakumar et al. [34] conducted an experimental study on a serpentine microchannel in the presence of alumina/water nanofluid. Their work is used to validate the present simulations for various values of hydraulic diameter including 810, 830, 860, and 890 μm ("Table 4").

Table 4 Dimensions of the copper microchannel considered (Sivakumar et al. 2016)

Hydraulic diameter (μm)	Height (μm)	Width (μm)	Spacing (μm)
810	830	800	13000
830	870	800	13500
860	920	800	13800
890	990	800	14000

A comparison between the amount of heat transfer coefficient calculated by numerical solution and the experimental results of Sivakumar et al. [34] is shown in "Fig. 4" for the hydraulic diameter of 810 μm. This figure displays that the present results are in good agreement with experimental data for Al_2O_3 nanofluid with ϕ = 0.01%.

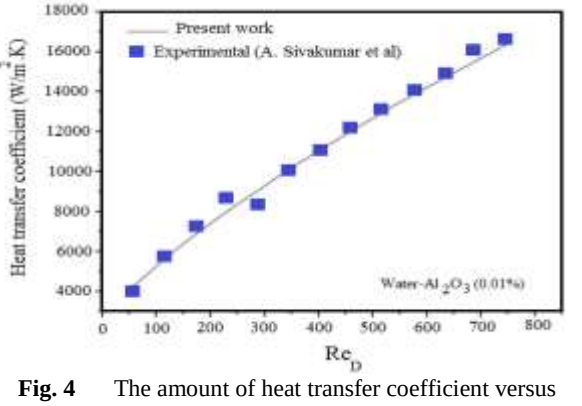

Fig. 4 The amount of heat transfer coefficient versus Reynolds number.

5 RESULTS AND DISCUSSION

The purpose of the current numerical study is to investigate the hydraulic and thermal behavior of a wavy microchannel HS with Ag/water-EG (50%) nanofluid for cooling digital processors. The influence of microtubules on HS performance is also investigated. The simulations are based on ϕ = 0%, 0.1%, 0.5%, and 1%, and *Re* = 300, 500, 700, 1000, and 1500. *h* is shown in "Fig. 5" for the HS with and without microtubes at different values of *Re* and ϕ. The dashed lines correspond to the ones without microtubes and solid lines are for that with the microtubes.

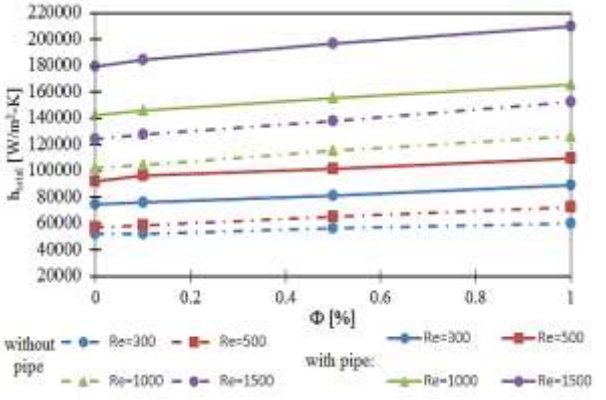

Fig. 5 Total HTC for the heat sink with and without microtubes at various values of *Re* and ϕ.

The figure shows that *h* increases by increasing ϕ for all the cases. On the other hand, as *Re* increases, the effect of ϕ becomes stronger. It is found that the addition of microtubes results in a substantial increase in the overall thermal coefficient of the system such that *h* for the system with microtubes at *Re* = 500 and 700 is 80% and 110% higher than that without microtubes at *Re* = 1000 and 700, respectively. This is due to that the presence of microtubes along the channel rises the heat exchange between the HS body and the fluid. On the other hand, the separation of the microchannel and tube paths and the creation of higher temperature mixing in the fluid stream cause the fluid temperature to increase along the channel wall decreases. In other words, the temperature difference between the fluid and solid does not decrease significantly, leading to an increase in the HTR. The enhancement effect of nanoparticles and microtubes can also be investigated based on $T_{CPU,Max}$ and $T_{CPU\text{-}Mean}$. As ϕ increases, the performance of the CPU is improved, leading to a reduction in the surface temperature. This is due to that a low-temperature gradient is required to transfer the heat generated by the processor ("Fig. 6"). Figure 6 displays the decreasing trend of $T_{CPU\text{-}Mean}$ due to the addition of nanoparticles. The performance of nanoparticles at lower values of *Re* is better: the addition of nanoparticles at lower values of *Re* causes the processor surface temperature to change more. On the other hand, the addition of microtubules leads to a much stronger performance. For example, in a HS without microtubes, $T_{CPU\text{-}Mean}$ = 315 K at *Re* = 300. The addition of microtubes causes the temperature to decrease by 309 K, while the addition of 1% nanoparticles decreases the surface temperature by 313 K.

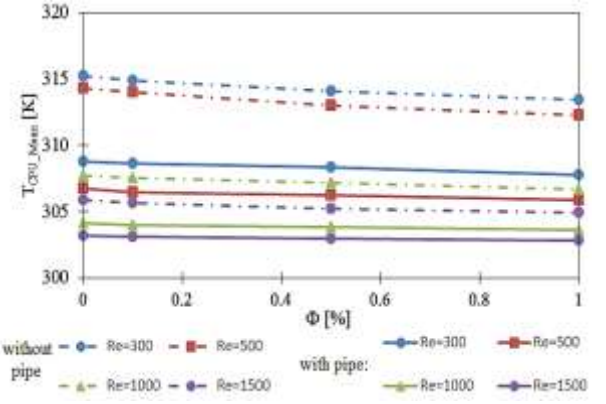

Fig. 6 $T_{CPU\text{-}Mean}$ for different values of ϕ.

Apart from the T_m of the CPU surface, another important parameter is $T_{CPU,Max}$ and the uniformity of the CPU temperature because very high CPU temperature and its high-temperature difference result in negative effects on the CPU performance. To evaluate this point, $T_{CPU,Max}$ is plotted in "Fig. 7" for different amounts of ϕ.

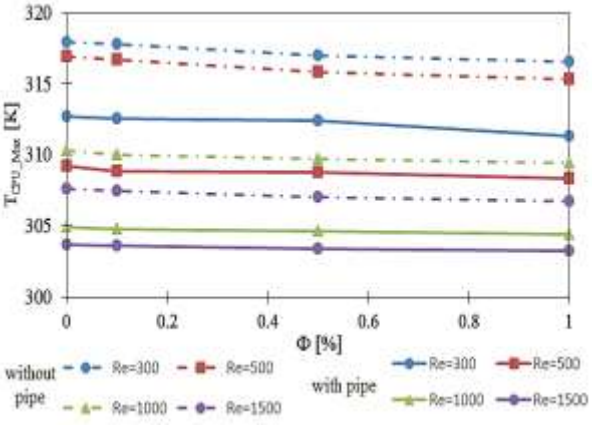

Fig. 7 $T_{CPU,Max}$ for different values of ϕ.

Figures 6 and 7 demonstrate that CPU surface temperature is 308 K for the case without microtubes at *Re* = 1000, while $T_{CPU,Max}$ is 310 K. This difference is due to the nonuniformity of heat transfer at the CPU surface due to different heat-transfer conditions and various thermal resistances of the points on the CPU surface, leading to the temperature difference at the surface. The nanoparticles improve cooling performance and reduce $T_{CPU,Max}$. In the same case, the presence of microtubes improves the HTR of various parts of the

processor and reduces the thermal resistance of its points, resulting in a reduction in the difference between $T_{CPU\text{-}Mean}$ and $T_{CPU,Max}$. As the temperature inside the ducts becomes more uniform, the mixing of the fluid flow is improved and the thermal performance of the duct enhances. In "Fig. 8", the nanofluid temperature contour is shown at the outlet.

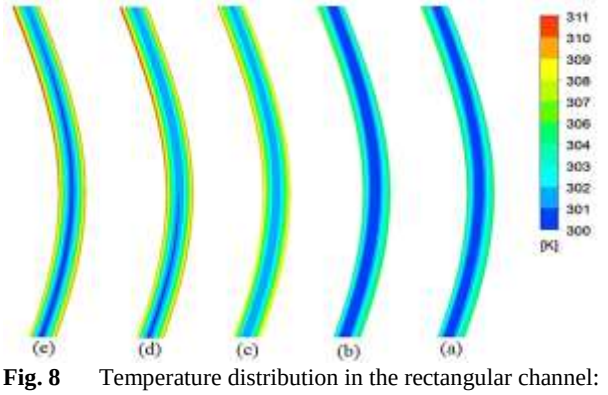

Fig. 8 Temperature distribution in the rectangular channel: (a): Re = 700, φ = 1%, (b): Re = 700, φ = 0.1%, (c): Re = 300, φ = 1%, (d): Re = 300, φ = 0.5%, and (e): Re = 300, φ = 0.1%.

In order to display the desired information properly, the image of the microtube is enlarged and is shown only in the lateral direction so that a complete arc of the microtube can be seen and also its color image and contour can be recognized. In all cases, the outer region of the fluid flow is hotter than its central part, but the central part temperature remains unchanged for cases *a* and *b*, and the influence of the addition of nanoparticles on heat diffusion from the walls to the center of the flow is not detectable.

This result is due to the high flow velocity and stronger convective HTR in the direction perpendicular to the conductive HTR. Because of the no-slip boundary condition on the walls and the establishment of the mass conservation and momentum laws, the fluid flow rate in the central part is stronger, leading to more concentration of heat capacity in the central part of the flow. As the fluid mixing enhances, the heat near the walls is transferred better and faster to the central fluid flow, which reduces the amount of temperature gradient required to transfer a certain amount of heat from the wall to the flow center. In the present work, two factors lead to the improvement of the fluid mixing: (i) the curvature in the geometry of the channel and the microwave and (ii) adding nanoparticles to the BF and the intensification in the thermal conductivity of the fluid. In the present work, the influence of the geometry of a HS is compared with the influence of adding nanoparticles, and the combined effect of the two is also investigated. In "Figs. 8c, 8d, and 8e", which relate to *Re* = 300, thermal diffusion in the perpendicular direction is better due to the lower strength of convective heat transfer. The addition of nanoparticles accelerates this phenomenon so that the temperature changes reach the center of the flow. To reach the temperature changes to the central part of the flow, a temperature gradient perpendicular to the flow path is required, which means an increase in the outer region fluid temperature, leading to a reduction in *h* between the fluid and the solid body and intensification in the solid surface temperature for transferring heat flux. Similar to the case of the rectangular channel, this is true for the channel with microtubes, as shown in "Fig. 9". Here, the effect of heat transfer is much higher in the vertical direction because of the smaller cross-sectional area, resulting in much higher temperature variations

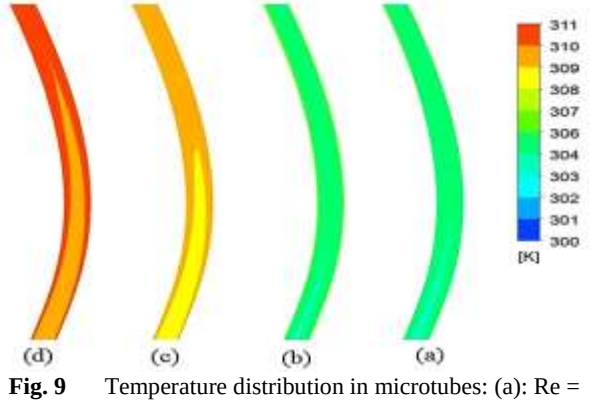

Fig. 9 Temperature distribution in microtubes: (a): Re = 700, φ = 1%, (b): Re = 700, φ = 0.1%, (c): Re = 300, φ = 1%, and (d): Re = 300, φ = 0.1%.

Figures 8 and 9 show that the effect of the addition of nanoparticles on microchannel and microtube performance is positive, but its positive effect decreases with increasing *Re*. According to the contours presented in "Fig. 8", the temperature in the center of the flow is more variable than in the microchannel. In fact, the HTR to the center of the microchannel flow is better. This may be due to the smaller diameter of the microtube than the microchannel, which reduces the distance between the center of the flow and the walls in the microtube Another point is that the flow rate in the microtube is lower because *Re* in the microtube is 10 times less than the microchannel, which reduces its heat capacity. This makes it more effective to determine the temperature of the HS wall based on the heat capacity of the microchannel. Hence, the temperature of the walls increases, and more thermal pressure is applied to the microtube, leading to that more heat reaches the central fluid flow and the temperature enhances.

Figure 10 shows the parameter θ for different values of ϕ and *Re*. Smaller values of θ indicate more uniformity of the temperature distribution. As *h* increases because of adding nanoparticles into the BF, the thermal performance is improved. It is observed that the temperature is more uniform on the surface but there is

an inverse relationship between the effect of nanofluid concentration and *Re*. As *Re* increases, the uniformity in temperature distribution is created due to the stronger convection heat transfer, and therefore the effect of nanofluid is not significant. On the other hand, the creation of microtubes results in a more uniform distribution of CPU surface temperature as a result of the increase in the HTR and reduction in thermal resistance of the furthest points of the processor. For example, the surface temperature distribution for a flow at *Re* = 700 with microtubes is more uniform than that without microtubes at *Re* = 1500.

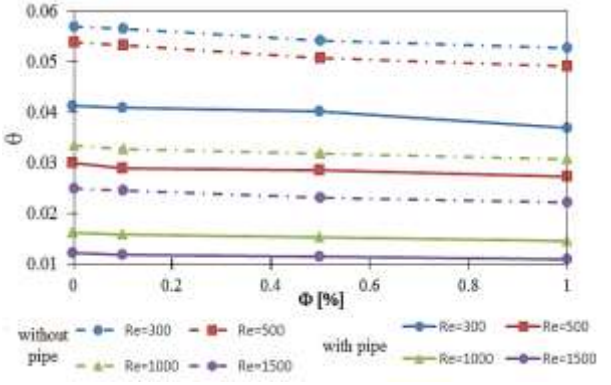

Fig. 10 Flow uniformity based on θ for different values of ϕ and *Re*.

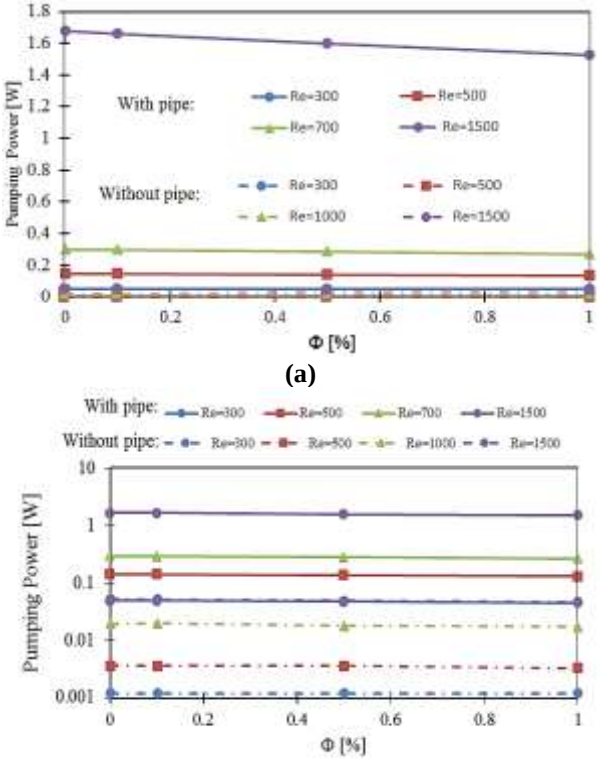

Fig. 11 The amount of pumping power required for different cases.

Thermal performance improvement requires generating a flow by the pump. In "Fig. 11a", the amount of pumping power required for different cases is presented. In "Fig. 11b", this comparison is presented as semi-logarithmic. It is observed that the addition of microtubes to the system increases the need for pumping power so that the pumping capacity of a HS without microtubes at *Re* = 1500 is equal to that with microtubes at *Re* = 300. At *Re* = 700, the power about 6 times is required compared to the case without microtubes for *Re* = 1500. On the other hand, this figure displays that the addition of nanoparticles reduces the pumping power required. This phenomenon occurs due to the decrease in the flow velocity due to an increase in the fluid density when *Re* is kept constant.

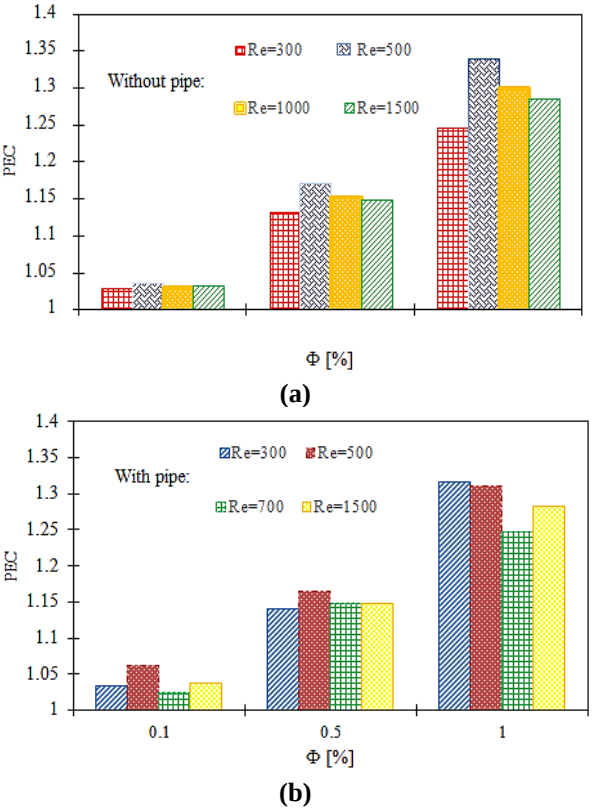

Fig. 12 PEC values for dissimilar values of ϕ and *Re* :(a): without microtubes, and (b): with microtubes.

The PEC of the system is calculated for comparison between the thermal performance improvement and the pumping power costs. This parameter considers thermal and hydraulic effects together by using a reference model. In "Fig. 12", different states are compared by defining the BF state as the reference case.

This figure displays that the addition of nanofluids does not have the same effect in different modes. While at 0.1% concentration, it has a maximum improvement of 5%, this improvement is greater for the case with microtubes. For 0.5% concentration, maximum

improvement is 15% that is almost identical in both cases (with and without microtubes). The concentration of 1% leads to a 35% improvement, whereas the addition of nanoparticles improves the performance of the system without microtubes.

The reason for this is the proper performance of the BF system because adding nanoparticles improves the thermal diffusivity of the fluid. When the effective factor in improving the performance of the system depends on the fluid thermal diffusivity, the addition of nanoparticles enhances the performance of the system. In this section, the previous process is repeated and only the results are presented. The pressure drop is set to a constant value of 500 kPa, which is applied to the microtubule and microchannel when Re = 530. The power consumption of the pump is less than 60 mW.

6 CONCLUSIONS

In this work, the influence of microtubes placed on the walls of a wavy microchannel HS was examined. Furthermore, the influence of using a bio nanofluid was evaluated. This study was performed using experimental data for Ag/water-EG (50%) nanofluid prepared by tea leaves synthesis. To investigate the cooling effects under different flow conditions and concentrations of nanoparticles, the processor was considered and simulated. It was understood that the microtubes improve the thermal performance and intensify the pumping power consumption by about 10 times. The influence of nanofluid concentration on HTR was evaluated and it was demonstrated that the influence of nanofluid is more dominant at low Reynolds numbers. It was also observed that the system performance is improved with increasing *Re*. The presence of microtubes increased the uniformity of the CPU surface temperature distribution and a reduction in its TCPU-Mean. As ϕ increases, the pumping power decreases when Re is kept constant. It was revealed that an increase in ϕ results in intensification in the PEC of the system, which is higher at larger values of Re. It also seems that the idea of the same pressure drop for microtubules and microchannels is more practical and operational

REFERENCES

[1] P. D. Mc Cormack, P. D., Welker, H., and Kelleher, M., Taylor-Goertler Vortices and Their Effect on Heat Transfer, J. Heat Transfer, Vol. 92, No. 1, 1970, pp. 101-112.

[2] Dean, W. R, Fluid Motion in a Curved Channel, Proceedings of The Royal Society of London, Series A, Containing Papers of a Mathematical and Physical Character, Vol. 121, No. 787, 1928, pp. 402-420.

[3] Cheng, K., Akiyam, M., Laminar Forced Convection Heat Transfer in Curved Rectangular Channels, International Journal of Heat and Mass Transfer, Vol. 13, 1970, pp. 471-490.

[4] Kalb, C, J. Seader, Heat and Mass Transfer Phenomena for Viscous Flow in Curved Circular Tubes, International Journal of Heat and Mass Transfer, Vol. 15, 1972, pp. 801-817.

[5] Guo, J., Xu, M., and Cheng, L., Second Law Analysis of Curved Rectangular Channels, International Journal of Thermal Sciences, Vol. 50, 2011, pp. 760-768.

[6] Yang, R., Chang, S., and Wu, W., Flow and Heat Transfer in a Curved Pipe with Periodically Varying Curvature, International Communications in Heat and Mass Transfer, Vol. 27, 2000, pp. 133-143.

[7] Yang, R., Chiang, F. P., An Experimental Heat Transfer Study for Periodically Varying-Curvature Curved-Pipe, International Journal of Heat and Mass Transfer, Vol. 45, 2002, pp. 3199-3204.

[8] Sui, Y., Lee, P., and Teo, C., An Experimental Study of Flow Friction and Heat Transfer in Wavy Microchannels with Rectangular Cross Section, International Journal of Thermal Sciences, Vol. 50**,** 2011, pp. 2473-2482.

[9] Tuckerman, D. B., Pease, R. F. W., High-Performance Heat Sinking for VLSI, IEEE Electron Device Letters, Vol. 2**,** 1981, pp. 126-129.

[10] Knight, R. W., Hall, D. J., Goodling, J. S., and Jaeger, R. C., Heat Sink Optimization with Application to Microchannels, IEEE Transactions on Components, Hybrids, and Manufacturing Technology, Vol. 15**,** 1992**,** pp. 832-842.

[11] Peng, X., Peterson, G., Forced Convection Heat Transfer of Single-Phase Binary Mixtures Through Microchannels, Experimental Thermal and Fluid Science, Vol. 12**,** 1996, pp. 98-104.

[12] Qu, W., Mudawar, I., Experimental and Numerical Study of Pressure Drop and Heat Transfer in A Single-Phase Micro-Channel Heat Sink, International Journal of Heat and Mass Transfer, Vol. 45**,** 2002, pp. 2549-2565.

[13] Tiselj, I., Hetsroni, G., Mavko, B., Mosyak, A., Pogrebnyak, E., and Segal, Z., Effect of Axial Conduction on The Heat Transfer in Micro-Channels, International Journal of Heat and Mass Transfer, Vol. 47, 2004, pp. 2551-2565.

[14] Lee, P. S., Garimella, S. V., and Liu, D., Investigation of Heat Transfer in Rectangular Microchannels, International Journal of Heat and Mass Transfer,Vol. 48**,** 200, pp. 1688-1704.

[15] do Nascimento, F. J., Leão H. L. S. L., and Ribatski, G., An Experimental Study on Flow Boiling Heat Transfer of R134a in a Microchannel-Based Heat Sink, Experimental Thermal and Fluid Science, Vol. 45**,** pp. 117-127.

[16] Lin, L., Zhao, J., Lu, G., Wang, X. D., and Yan, W. M., Heat Transfer Enhancement in Microchannel Heat Sink by Wavy Channel with Changing Wavelength/Amplitude, International Journal of Thermal Sciences, Vol. 118**,** 2017**,** pp. 423-434.

[17] Chon, C. H., Kihm, K. D., Lee, S. P., and Choi, S. U., Empirical Correlation Finding the Role of Temperature and Particle Size For Nanofluid (Al 2 O 3) Thermal Conductivity Enhancement, Applied Physics Letters, Vol. 87**,** 2005, 153107.

[18] Esfe, M. H., Afrand, M., Gharehkhani, S., Rostamian, H., Toghraie, D., and Dahari, M., An Experimental Study on Viscosity of Alumina-Engine Oil: Effects of Temperature and Nanoparticles Concentration, International Communications in Heat and Mass Transfer, Vol. 76, 2016, pp. 202-208.

[19] Selvakumar, P., and Suresh, S., Convective Performance of Cuo/Water Nanofluid in an Electronic Heat Sink, Experimental Thermal and Fluid Science, Vol. 40**,** 2012, pp. 57-63.

[20] Ermagan, H., and Rafee, R., Geometric Optimization of an Enhanced Microchannel Heat Sink with Superhydrophobic Walls, Applied Thermal Engineering, Vol. 130**,** 2018, pp. 384-394.

[21] Ahmed, H. E., Ahmed, M., Seder, I. M., F., and Salman, B. H., Experimental Investigation for Sequential Triangular Double-Layered Microchannel Heat Sink with Nanofluids, International Communications in Heat and Mass Transfer, Vol. 77, 2016, pp. 104-115.

[22] Tafarroj, M. M., Mahian, O., Kasaeian, A., Sakamatapan, K., Dalkilic, A. S., and Wongwises, S., Artificial Neural Network Modeling of Nanofluid Flow in a Microchannel Heat Sink Using Experimental Data, International Communications in Heat and Mass Transfer, Vol. 86**,** 2017, pp. 25-31.

[23] Esfahani, M. A., Toghraie, D., Experimental Investigation for Developing a New Model for The Thermal Conductivity of Silica/Water-Ethylene Glycol (40%–60%) Nanofluid at Different Temperatures and Solid Volume Fractions, Journal of Molecular Liquids, Vol. 232**,** 2017, pp. 105-112.

[24] Ghasemi, S., Karimipour, A., Experimental Investigation of The Effects of Temperature and Mass Fraction on the Dynamic Viscosity of CuO-Paraffin Nanofluid, Applied Thermal Engineering, Vol. 128**,** 2018, pp. 189-197.

[25] Karimipour, A., Ghasemi, S., Darvanjooghi, M. H. K., and Abdollahi, A., A New Correlation for Estimating the Thermal Conductivity and Dynamic Viscosity of CuO/Liquid Paraffin Nanofluid Using Neural Network Method, International Communications in Heat and Mass Transfer, Vol. 92, 2018**,** pp. 90-99

[26] Afrand, M., Najafabadi, K. N., and Akbari, M., Effects of Temperature and Solid Volume Fraction on Viscosity of SiO2-MWCNTs/SAE40 Hybrid Nanofluid as a Coolant and Lubricant in Heat Engines, Applied Thermal Engineering, Vol. 102**,** 2016**,** pp. 45-54.

[27] Sharifpur, M., Adio, S. A., and Meyer, J. P., Experimental Investigation and Model Development for Effective Viscosity of Al2O3–Glycerol Nanofluids by Using Dimensional Analysis and GMDH-NN Methods, International Communications in Heat and Mass Transfer, Vol. 68**,** 2015, pp. 208-219.

[28] Asadi, A., Asadi, M., Rezaei, M., Siahmargoi, M., and Asadi, F., The Effect of Temperature and Solid Concentration on Dynamic Viscosity of MWCNT/MgO (20–80)–SAE50 Hybrid Nano-Lubricant and Proposing a New Correlation: an Experimental Study, International Communications in Heat and Mass Transfer, Vol. 78, 2016, pp. 48-53.

[29] Esfe, M. H., Saedodin, S., Naderi, A., Alirezaie, A., Karimipour, A.,Wongwises, S., Goodarzi, M., and Bin Dahari, M., Modeling of Thermal Conductivity of ZnO-EG Using Experimental Data and ANN Methods, International Communications in Heat and Mass Transfer, Vol. 63, 2015, pp. 35-40.

[30] Zhou, J., Hatami, M., Song, D., and Jing, D., Design of Microchannel Heat Sink with Wavy Channel and Its Time-Efficient Optimization with Combined RSM and FVM Methods, International Journal of Heat and Mass Transfer, Vol. 103**,** 2016, pp. 715-724.

[31] Hatami, M., Sun, L., Jing, D., Günerhan, H., and Kameswaran, P. K., Rotating Cylinder Turbulator Effect on The Heat Transfer of a Nanofluid Flow in a Wavy Divergent Channel. Journal of Applied and Computational Mechanics, 2020, Doi 10.22055/JACM.2020.34587.2440.

[32] Al-Rashed, A. A., Shahsavar, A., Rasooli, O., Moghimi, M., Karimipour, A., and Tran, M. D., Numerical Assessment Into the Hydrothermal and Entropy Generation Characteristics of Biological Water-Silver Nano-Fluid in a Wavy Walled Microchannel Heat Sink, International Communications in Heat and Mass Transfer, Vol. 104, 2019, pp118-126.

[33] Sarafraz, M., Hormozi, F., Intensification of Forced Convection Heat Transfer Using Biological Nanofluid in a Double-Pipe Heat Exchanger, Experimental Thermal and Fluid Science, Vol. 66**,** 2015**,** pp. 279-289.

[34] Sivakumar, A., Alagumurthi, N., and Senthilvelan, T., Investigation of Heat Transfer in Serpentine Shaped Microchannel Using Al2O3/Water Nanofluid, Heat Transfer—Asian Research, Vol. 45**,** 2016**,** pp. 424-433.

Int. J. Advanced Design and Manufacturing Technology, 2022, Vol. 15, No. 4, pp. 39-46

DOI: 10.30486/ADMT.2023.1959121.1350 *ISSN: 2252-0406* *https://admt.isfahan.iau.ir*

Design and Analysis of Two Pass Rolling Dies

Kondapalli Siva Prasad*
Department of Mechanical Engineering,
Anil Neerukonda Institute of Technology & Sciences, India
E-mail: kspanits@gmail.com
*Corresponding author

Vishnu Vardhan Reddy
Department of Mechanical Engineering,
Anil Neerukonda Institute of Technology & Sciences, India
E-mail: ravigurram606@gmail.com

Received: 19 May 2022, Revised: 10 October 2022, Accepted: 12 October 2022

Abstract: Sheet metal forming is widely used in automotive and aerospace industry. In this paper analysis of sheet metal forming process by deep drawing was discussed. Static analysis on the deep drawing operation was carried out to find the stresses, strains and total deformation of deep drawing cup. CAD models are generated using CATIA from the dimensions obtained by theoretical calculations and analysis is carried out using ANSYS software. The force required to develop the cup, deformation and defect like tearing, wrinkles etc. can be obtained through simulation. By using this method it is easy to make stress and strain analysis for different materials. From the analysis, it is observed that Titanium has the maximum stress with standing ability when compared to copper and Aluminum.

Keywords: ANSYS, CATIA, Rolling

Biographical notes: Kondapalli Siva Prasad obtained PhD from Andhra University, India, in 2014. He is currently working as Professor in Department of Mechanical Engineering, Anil Neerukonda Institute of Technology & Sciences, India. His current research interest includes Manufacturing and product design. He received research funds from UGC, DST, AICTE of Government of India. He has published 108 papers in various journals and 8 research scholars are working under his guidance. He served as Editorial Board member and reviewer for various international journals. **Vishnu Vardhan Reddy** is final year Bachelor's student in Department of Mechanical Engineering, Anil Neerukonda Institute of Technology & Sciences, India.

Research paper

1 INTRODUCTION

Rolling is a process to form metals where the metal strip is pressed by two or multiple rollers, thus the uniform thickness is formed. The rolling process is a metal forming process, in which stock of the material is passed between one or more pairs of rollers in order to reduce and to maintain the uniform thickness. This process is mainly focused on the cross-section of the ingot or the metal which is forming. Mainly by this process, we reduce the thickness of the metal workpiece. Now, the rolling processes are mainly focused on the increasing length and the decreasing thickness without changing the width of the workpiece. There are certain types of the rolling process, whereas, in the hot rolling process, the metal is heated at its desirable temperature, when the metal is properly heated then the metal should be passed between the one or more rolling mills to gain the proper desirable shape.

Mesay Alemu Tolcha, et.al [1], used numerical modelling to indicate a set of equations, derived from the contact principle, that transfer the physical event into the mathematical equations. Alexander Schowtjak, et.al [2] analysed the evolution of damage and voids in the sequence of caliber rolling to cold forward rod extrusion. The analysis is performed with the help of a variant of the Lemaitre model, microstructural analysis of the void area fraction and density measurements. Huiping Hong [3] used three dimensional elastoplastic finite element simulation with thermal mechanically coupled analysis which is applied to study the roll pass design of the hot continuous rolling of Φ100mm alloy steel round bar from 200mm×200mm square cast bloom.

Yavtushenko A.V, et.al [4], studied the possibility of application of the program complex called Mathcad Prime 5 for calculation of normal contact stresses in the centre of deformation during cold rolling of the strips. O.M. Ikumapayi, et.al [5] studied rolling techniques in metal forming operation, or as part of the industrial manufacturing process. Comparison in performance of different rolling methods, while analysing their defects, and areas of application of rolled products or components is presented. Yingxiang Xiaa, et.al [6] analysed the existing problems, e.g. cracking, many forming passes, difficult control of dimensional accuracy, in thin-walled pipe fittings hot extrusion forming process.

Mesay Alemu Tolcha, et.al [7] carried out modelling of rolling die contact with the slab primarily needs to describe the Tribology of contact phenomena. Jian-guo CAO, et.al [8] carried out finite element method for the behaviour analysis of mechanical, thermal, deformation and other characters of strip and rolling mills. Kondapalli Siva Prasad, M. Lalitha Kavya [9], made an attempt to summarize the various works reported by earlier researchers on certain specific areas of rolling like Finite Element Analysis (FEA), die and rolling material and summarized the results, so that the gaps can be identified, which in turn helps the researchers to carry their research in rolling. Andre Lim, et.al [10] examined and studied the residual stress distributions caused by the deep cold rolling (DCR) process, with a focus on the distributions at the boundary of the treatment zone.

In the present work, roller and billet assembly of dimensions are as 50mm and 40mm as diameter and width of the roller and 100mm, 15mm, 10mm as length, input width and output width, respectively. The rollers are made to rotate at 4 different speeds i.e. 0.24rad/s, 0.3rad/s, 0.46rad/s, 0.6rad/s and billet is made to move between the rollers. The temperatures are considered to be constant throughout the process. The contact stress between the roller and the billet, maximum equivalent stress and directional deformation can be found out. Simultaneously the material of the billet is changed. We have considered 4 different materials which are commonly used in the industry. Aluminium alloy, copper alloy, magnesium alloy and stainless steel are considered as workpiece materials.

2 MODELING & ANALYSIS

The materials used for blank, blank holder, die and punch are presented in "Table 1"

3D modelling was done using SOLIDWORKS software for roller and billet assembly is designed with the dimensions as mentioned in the "Table 1".

Table 1 Dimensions of the roller and billet

	Volume (mm^3)	Surface area (mm^2)	Dimensions (mm)
Roller	74895.57	11787.26	Dia=50mm Width= 40mm
Billet	24892.41	7014.22	Input=15mm Output=5mm

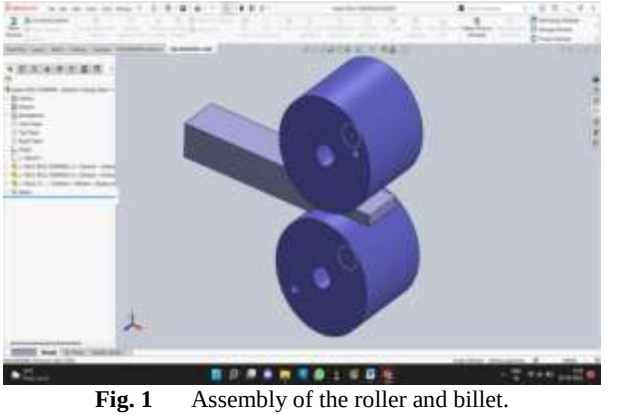

Fig. 1 Assembly of the roller and billet.

The roller and the billet are connected together by the use of mate option, eight mating are given for the complete assembly. The mating can be given in many ways. Here the curved surface area of billet and matching surface area of the billet are selected. The assembled roller and billet is as shown in the "Fig. 1". It is saved in the 'igs' format to be used in the ANSYS WORKBENCH for the analysis work. The properties of the roller material and the four billet materials have been added to the ANSYS workbench for the analysis. The properties of materials are shown in the below tables. The load setup is given to the model as below. Rotation of rollers is given by selecting the joint rotation in the z-axis. Four different speeds are considered for the entire analysis. The chemical and physical properties of D2 material are presented in "Tables 2 and 4".

Table 2 D2 steel metal composition (weight %)

Steel Grade	carbon	Mn	silicon	Cr	Nickel	S	P	Hardness HRC
D2	1	0.25	0.25	1	0.2	0.005	0.003	60-62

Table 3 Properties of D2 steel

Young's modulus	2.09×10^11 pa
Poisson's ratio	0.3
Bulk modulus	1.7417×10^11 pa
Shear modulus	8.038×10^10 pa
Coefficient of thermal expansion	1.04 ×10^-5 /c
Density	7700 kg/m^3
Tensile ultimate strength	2.4×10^9

Table 4 Properties of the Billet material

	Aluminium alloy	Copper alloy	Magnesium allly	Stainless steel
Young's modulus	7.1×10^10 pa	1.1×10^11 pa	4.5×10^10 pa	1.93×10^11 pa
Poisson's ratio	0.33	0.34	0.35	0.31
Bulk modulus	6.960×10^10 pa	1.1458×10^11 pa	5×10^10 pa	1.693×10^11 pa
Shear modulus	2.669×10^10 pa	4.10×10^10 pa	1.667×10^10 pa	7.366×10^10 pa
Tangent modulus	5×10^8 pa	1.15×10^9 pa	9.2×10^8 pa	1.8×10^9 pa
Density	2770 kg/m^3	8300 kg/m^3	1800 kg/m^-3	7750kg/m^3
Yield strength	2.8×10^8 pa	2.8×10^8 pa	1.93×10^8 pa	2.1×10^8 pa

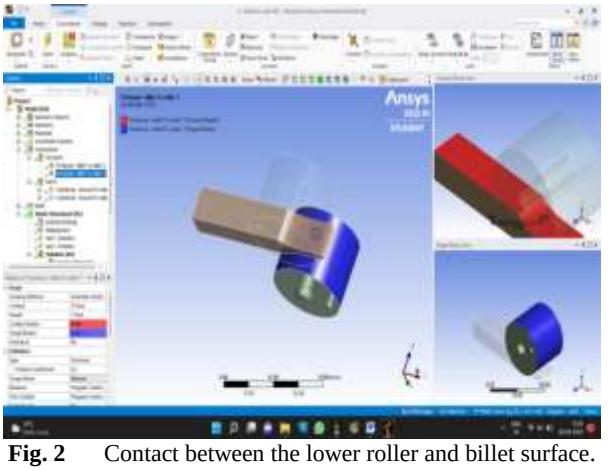

Fig. 2 Contact between the lower roller and billet surface.

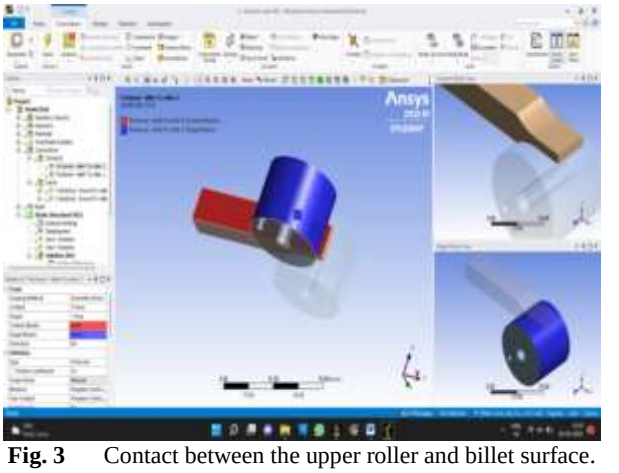

Fig. 3 Contact between the upper roller and billet surface.

The saved 3D model is imported into ANSYS workbench. In the static. structural module is selected from the Analysis system toolbox menu of ANSYS WORKBENCH. Contact regions are given as the 3D solid assembly consists of a roller and billet. A solid-solid bonded contact was given at the region as the bond strength of roller and billet and joints are given to the ground and roller, the contacts are shown in the "Figs. 2 and 3".

The 3D model is meshed in two different methods, the roller is meshed with the sweep method with automatic sizing quad/tri elements nodes and billet is meshed with body sizing method with 3mm, (See "Figs. 4 to 5").

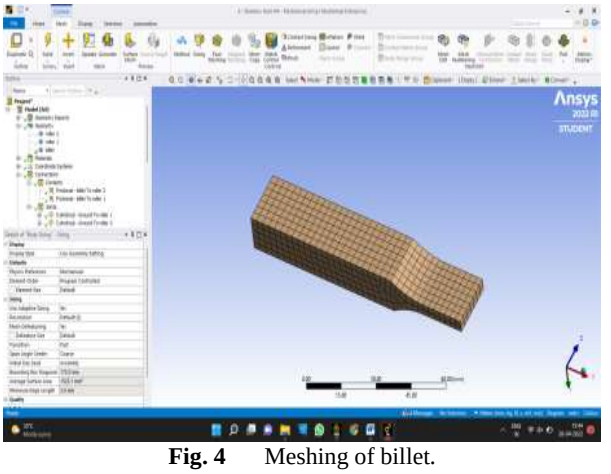

Fig. 4 Meshing of billet.

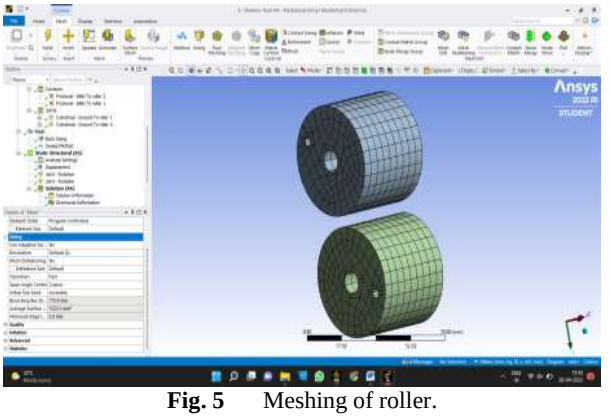

Fig. 5 Meshing of roller.

The rotation of the rollers is given as one roller in clockwise and another as Anti-clockwise direction. The roller speeds are given as 0.24, 0.3, 0.48, 0.6 rad/s. The solver module is used to obtain the solution for the given boundary conditions to the model. The required stress distribution and contact stress are evaluated for given loading conditions. The analysis for aluminium billet at different roller speeds has been presented in "Figs. 6 to 17".

1- At Roller Speed of 0.24 Rad/S for Aluminium Alloy

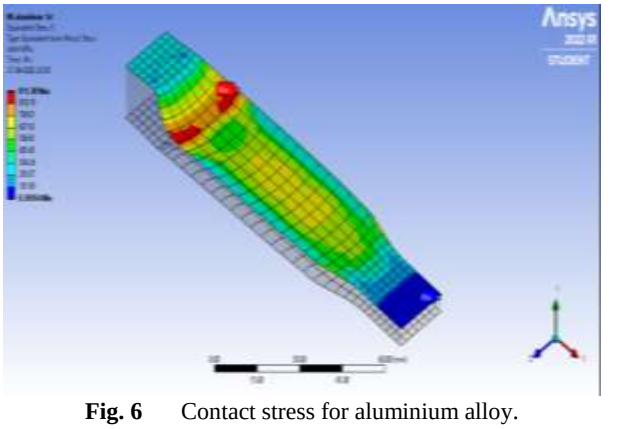

Fig. 6 Contact stress for aluminium alloy.

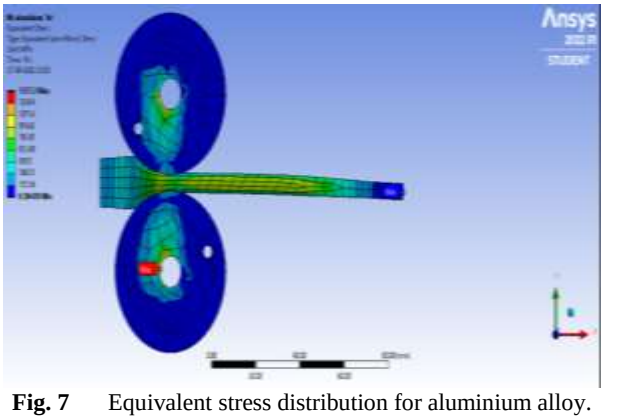

Fig. 7 Equivalent stress distribution for aluminium alloy.

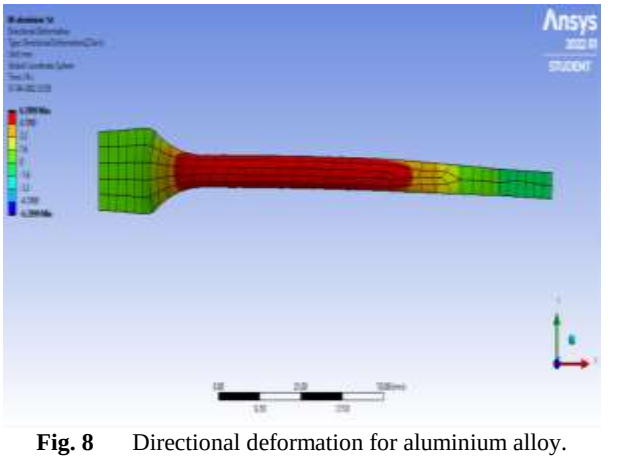

Fig. 8 Directional deformation for aluminium alloy.

2- At Roller Speed of 0.3 Rad/S for Aluminium Alloy

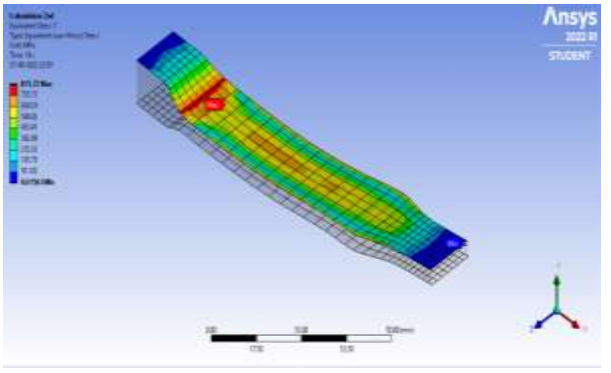

Fig. 9 Contact stress for aluminium alloy.

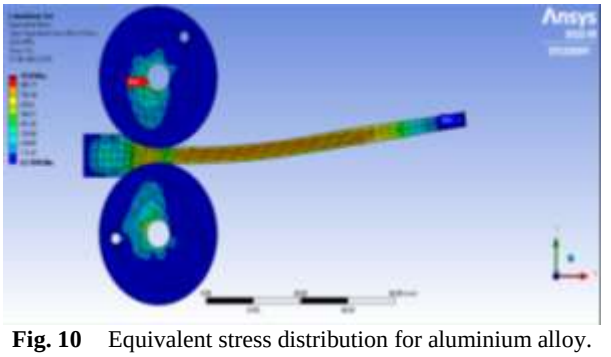

Fig. 10 Equivalent stress distribution for aluminium alloy.

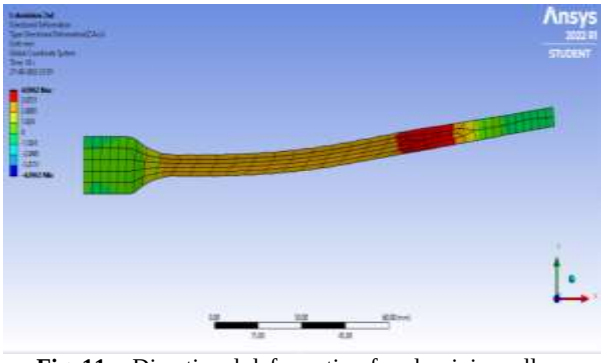

Fig. 11 Directional deformation for aluminium alloy.

3- At Roller Speed of 0.48 Rad/S for Aluminium Alloy

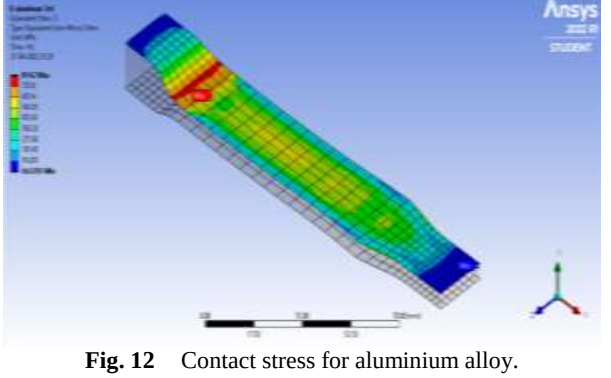

Fig. 12 Contact stress for aluminium alloy.

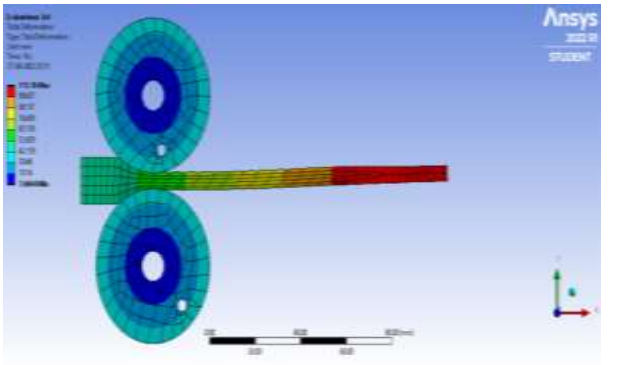

Fig. 13 Equivalent stress distribution for aluminium alloy.

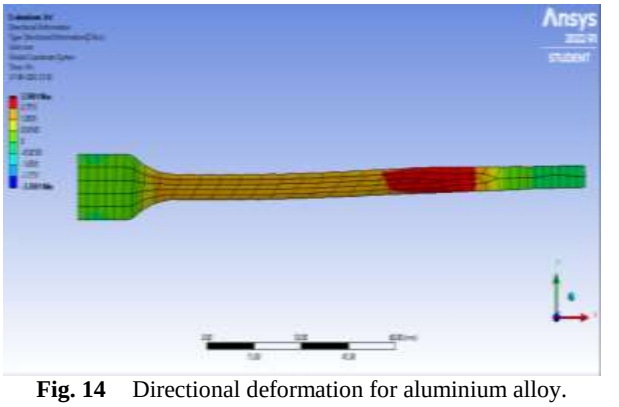

Fig. 14 Directional deformation for aluminium alloy.

4- At Roller Speed of 0.6 Rad/S for Aluminium Alloy

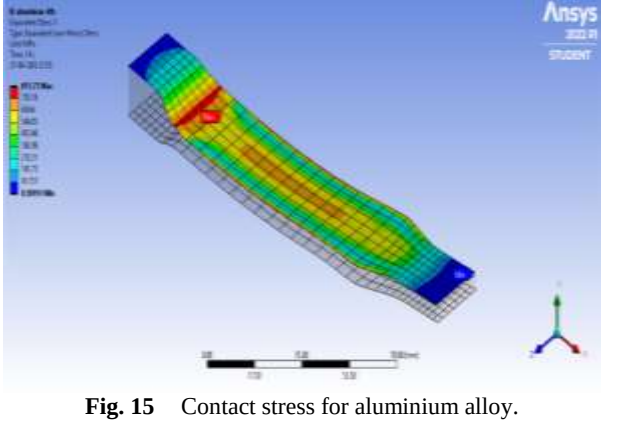

Fig. 15 Contact stress for aluminium alloy.

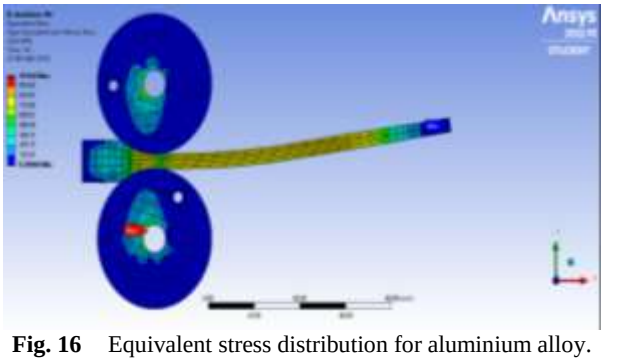

Fig. 16 Equivalent stress distribution for aluminium alloy.

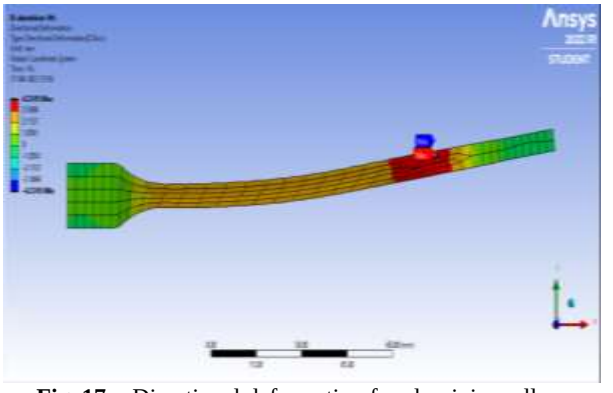

Fig. 17 Directional deformation for aluminium alloy.

Similarly for other billet materials, analysis is carried out at different roller speeds, which are presented in "Tables 5 to 7".

Table 5 Contact stresses

Speed (rad/s)	Aluminium alloy	Copper alloy	Magnesium alloy	Stainless steel
0.24	911.38	1738.4	1303.2	2640.1
0.3	814.2	1544.9	1197.1	2245.1
0.48	815.72	1560.1	1169.2	2296
0.6	815.75	1548.3	1169.3	2406.1

3 RESULTS & DISCUSSION

From the analysis carried out on different billet materials by varying the roller speed, the following observations are made. From the contact stresses Table 5, it is observed that maximum contact stresses were observed at 0.4 rad/s for stainless steel and minimum value was observed for aluminium alloy. Similar trend was observed for 0.3 rad/s 0.48 rad/s and 0.6 rad/s. Higher contact stresses was observed at lower roller speeds of 0.24 rad/s and minimum contact stresses were observed at 0.3 rad/s.

From the directional deformation in Table.6, it is observed that the maximum directional deformation was observed for aluminium alloy at roller speed of 0.24 rad/s and the minimum directional deformation was observed for stainless steel at a roller speed of 0.6 rad/s. Directional deformation decreases with increase in roller velocity.

Table 6 Directional deformation

Speed (rad/s)	Aluminium alloy	Copper alloy	Magnesium alloy	Stainless steel
0.24	6.339	5.8974	5.6377	4.4164
0.3	3.7001	3.9951	3.8693	4.4539
0.48	4.0962	4.3762	4.224	4.6514
0.6	4.2245	4.5054	4.3644	3.587

From the directional deformation in "Table 7", it is observed that the maximum equivalent stress was observed for stainless steel at roller speed of 0.24 rad/s and minimum equivalent stress was observed for aluminium alloy at roller speed of 0.48 rad/s. Equivalent stress decreases with increase in roller speed from 0.24 rad/s to 0.48 rad/s.

Table 7 Equivalent stress

Speed (rad/s)	Aluminium alloy	Copper alloy	Magnesium alloy	Stainless steel
0.24	1377.3	2411.76	1712.6	4019.8
0.3	1136.7	1809.4	1407.3	2564.9
0.48	1019	1704.7	1266.1	2344.5
0.6	1079.8	1793.7	1335.4	3183.2

Graphs are drawn for contact stresses, Equivalent stresses and directional deformation for four different types of billet materials at different roller speeds as shown in "Figs.18 to 20".

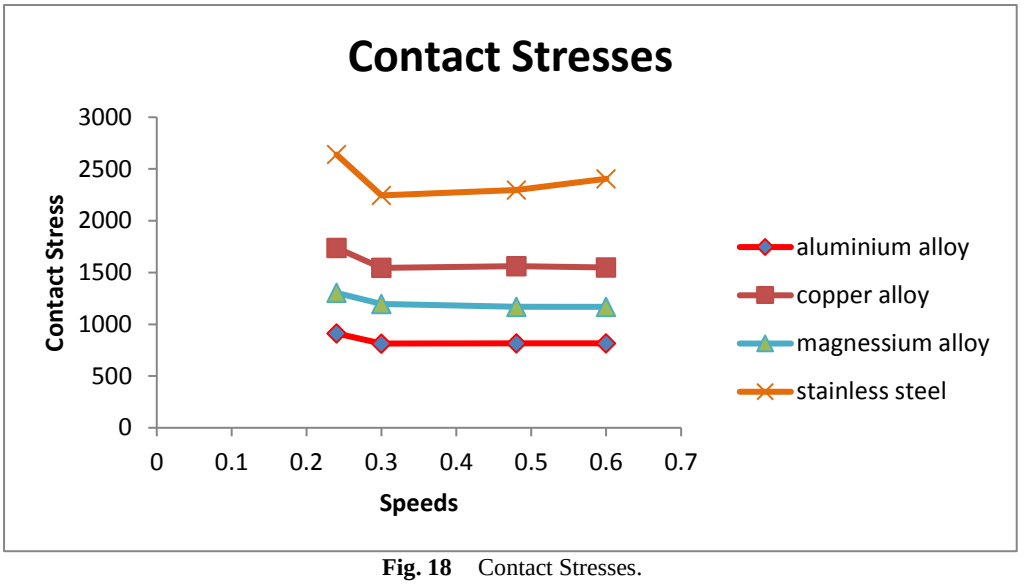

Fig. 18 Contact Stresses.

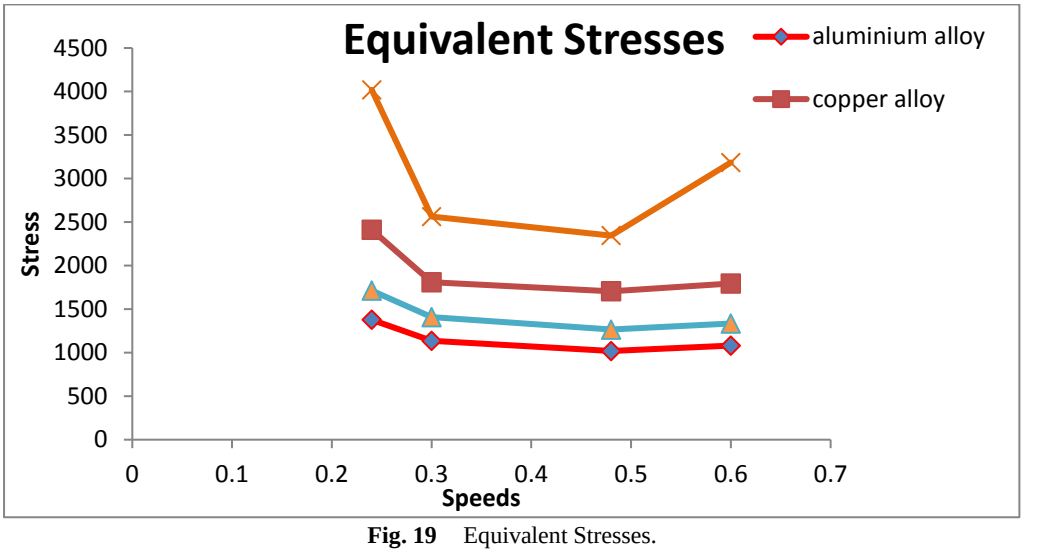

Fig. 19 Equivalent Stresses.

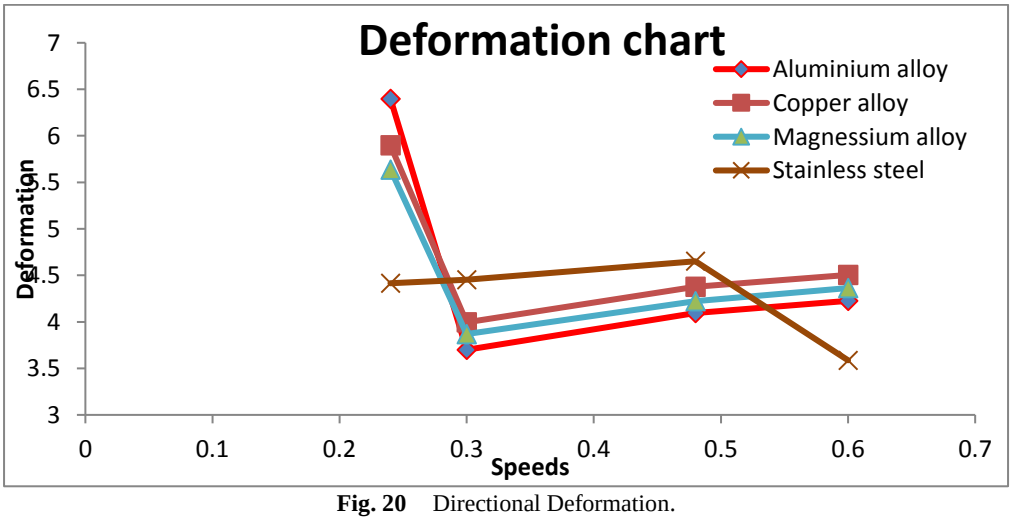

Fig. 20 Directional Deformation.

4 CONCLUSIONS

Based on analysis work carried on different billet materials, the following conclusions are drawn:
The optimal contact stress of 814.2 MPa is obtained for aluminium alloy at roller speed of 0.3 rad/s. The optimal equivalent stress of 1019 MPa is obtained for aluminium alloy at roller speed of 0.48 rad/s. The optimal directional deformation of 3.587 mm was observed for stainless steel at roller speed of 0.6 rad/s.

REFERENCES

[1] Alemu Tolcha, A., Altenbach, H., Numerical Modeling Rolling Contact Problem and Elasticity Deformation of Rolling Die under Hot Milling, Metals, Vol. 9, 2019, pp. 226.

[2] Clausmeyer, T., Schowtjaka, A., Wangb, Sh., Gitschela, R., Heringa, O., P., Lohmarb, J., Ostwaldc, R., Hirtb, G., and Tekkaya, E., Prediction of Ductile Damage in the Process Chain of Caliber Rolling and Forward Rod Extrusion, 23rd International Conference on Metal Forming, Procedia Manufacturing, Vol. 47, 2020, pp. 649–655.

[3] Hong, H., Roll Pass Design and Simulation on Continuous Rolling of Alloy Steel Round Bar, Procedia Manufacturing, Vol. 37, 2019, pp. 127-131.

[4] Yavtushenko A. V., Protsenko, V. M., Bondarenko, Y. V., Kirichenko, A. G., and Ping F. Y., Numerical Experiment for the Calculation of Normal Contact Stress in the Deformation Center when Rolling a Metal Strip, Journal of Engineering Sciences: 10.21272/jes.2019.6(2).e5.

[5] Ikumapayi, O. M., Akinlabi, E. T., Onu, P., and Abolusoro, O. P., Rolling Operation in Metal Forming: Process and Principles – A Brief Study, Materials today, Vol. 26, No. 2, 2020, pp. 1644-1649.

[6] Alemu Tolcha, M., Altenbach, H., Numerical Modeling Rolling Contact Problem and Elasticity Deformation of Rolling Die under Hot Milling, Metals, Vol. 9, 2019, pp. 226, doi:10.3390/met9020226.

[7] Jian-Guo, C. A. O., Zhang, J., Kong, N., and Kai-Fu M. I., Finite Element Analysis of Strip and Rolling Mills, Finite Element Analysis, 2010.

[8] Siva Prasad, K., Lalitha Kavya, M., Critical Review on Design of Rolling Process, Journal of Mechanical Engineering and Technology, Vol. 9 No. 2. 2017.

[9] Lim, A., Castagne, S., and Cher Wong, Ch., Effect of Deep Cold Rolling on Residual Stress Distributions Between the Treated and Untreated Regions on Ti–6Al–4V Alloy, Journal of Manufacturing Science and Engineering, Vol. 13, No. 11, 2016, DOI: 10.1115/1.4033524.

[10] Colgan, M., Monaghan, J., Deep Drawing Process: Analysis and Experiment, Journal of Materials Processing Technology, Vol. 132, 2003, pp. 35 -41.

Int. J. Advanced Design and Manufacturing Technology, 2022, Vol. 15, No. 4, pp. 47-60

DOI: 10.30486/ADMT.2022.1957347.1348 ISSN: 2252-0406 https://admt.isfahan.iau.ir

Numerical Investigation of Forced Convection Heat Transfer for Different Models of PPFHS Heatsinks

Soheil Sadrabadi Haghighi, Hamid Reza Goshayeshi *, Iman Zahmatkesh

Department of Mechanical Engineering,
Mashhad Branch, Islamic Azad University, Mashhad, Iran
E-mail: soheilsadrabadi@gmail.com, goshayshi@yahoo.com, Zahmatkesh55310@mshdiau.ac.ir
*Corresponding author

Received: 24 April 2022, Revised: 13 September 2022, Accepted: 17 September 2022

Abstract: In his research article, several models of heatsink were optimally designed in fin length, width and height along with pin placement which consists of 4 pin fin heatsink models heatsink (including square with different pin angles, circular, truncated cone, and cone pin heatsinks and one model of the plate-fin heatsink (PFHS)) in order to achieve better thermal performance as well as less energy consumption and were numerically investigated under high air velocity and heat fluxes. Different parameters such as peak temperature, Nusselt number, heat resistance, pressure drop, and energy consumption were compared. The results show that the square PPFHS with the pin angle of 45 degrees has the highest thermal performance compared to the rest of the models while also having the highest pressure drop and energy consumption between the models consuming more than 255 and 358 percent more energy in order to have the same air velocity in the pathway, while the truncated and the fully formed cone model despite having 25% and 30% less thermal performance, have the least pressure drop between the pin models of the heatsinks and therefore consume the least energy out of the PPFHS.

Keywords: Energy Consumption, Nusselt Number, Thermal Resistance, Thermal Performance, Truncated Cone

Biographical notes: Soheil Sadrabadi Haghighi received his BSc and MSc in Mechanical Engineering from the Islamic Azad University in Mashhad in 2016. He is currently a PhD student in Islamic Azad University, Mashhad Branch. His current research interests include improving pool boiling heat transfer by nanoparticles and computational fluid dynamics (CFD) and optimization of energy systems. **Hamid Reza Goshayeshi** received his PhD from South Bank University in London, England in 1999, and did his post-doctoral research on the same university in 2003. His current research interest includes solar still, nanofluid, heat sink, boiling heat transfer and other heat transfer enchantments methods. **Iman Zahmatkesh** is Associate Professor of Mechanical Engineering at Islamic Azad University, Mashhad Branch. He received his PhD in the Mechanical Engineering from Shiraz University, Iran in 2011.

Research paper

1 INTRODUCTION

Heat transfer is one of the most important concepts which is used in chemical engineering and mechanical engineering and other fields [1-2]. This includes wide applications such as electronic systems, robotics, MEMS, and housing temperature regulation. There are various methods of cooling available which include heat exchangers, heat pipes, water cooling, and more [3-5]. One of the most important pieces of cooling equipment used today is the heats sink. The most important feature of a heatsink is heat dissipation and cooling. A heatsink is a piece of metal with a high thermal conductivity that is mounted on electrical or electronic components and captures the heat and heat generated by the part, then through heat exchange with the surrounding environment and cooling with air (in some models Water) reduces heat [6-9]. This part is even used in various voltage converters or car inverters and audio and video. There are two methods of cooling solution and heat generation management for heatsinks which are active cooling and passive cooling. In passive type heatsink, the temperature control operation is performed by convection process, which is one of the concepts of heat transfer science [10]. In this way, the passive heatsink absorbs heat from the desired part and distributes the heat in that fluid by maximizing the contact surface with the surrounding fluid through the fins (blades). The absence of moving parts has increased the reliability of this type of heatsink. Of course, it is important to realize the fact that in order to transfer heat in passive heatsinks, a constant flow of air must be constantly passing through the fans [11-14]. One of the most important aspects of the heat sink that must be considered in its design is a simpler structure, high heat transfer rate, and low-pressure drop.

Liquid cooling methods can dissipate more heat at smaller footprints. However, they have the disadvantage of complexity of design, expense, and require maintenance regularly [15]. In active cooling, a fan or blower is usually used as the heat transfer element. This type of heatsink has very high efficiency. Of course, due to the higher price, it is less used than the passive type [16]. Extended surfaces used in cooling systems, which are commonly named fins, are utilized across all electronic application as arrays or heat sinks name. Generated heat transfers to the heat sinks by conduction heat transfer, and the transported heat dissipates through the environment around it via convection heat transfer [17]. Kim et al. [18] compared and evaluated the thermal characteristics of plate-fin and plate pin-fin heat sinks experimentally. Both of these models were subjected to a parallel airflow. They have discovered that there is a correlation between Nusselt number and the friction coefficient factor for both models of heat sinks. They also discovered that pumping power and length of the heat sink are important factors that affects heatsinks thermal performance. Ambreen & Kim [19] numerically experimented on and investigated the thermal characteristics of a square cylinder under a laminar flow. Scholten et al. [20] developed an empirical model in order to study the heat flow and heat transfer rate of a cylinder. This model also allowed them to study the velocity and velocity profile under a transverse flow. A. Bhattacharyya et al. [21] have performed numerical studies in order to predict the thermal behaviour of hexagonal cylinder under a cross-flow. They have discovered that both Nusselt number as well as Reynolds number have a significant effect on the intensity of the turbulence flow as well as the pressure coefficient in the flow regime. Benim et al. [22] investigated fluid passing around a circular cylinder. In this experiments they proposed several turbulence modelling strategy in order to simulate an incompressible turbulent fluid passing around the circular cylinder. Kitti et al [23] discovered that in plate pin heat sinks, pin fin configuration is an important parameter and has significant effects on thermal performance and airflow characteristic. They also discovered that changing fin characteristics such as fin shape, pin fin orientation, and the ratio of the distance between pin and plate-fin centre to pin fin size affects thermal performance, heat transfer coefficient and pressure drop.

Nilpueng & Wongwises [24] investigated the twist ratio and perforation diameter and its influence on a model of PFHS with twisted tape. The results show that lowering the twist ration with the same perforation diameter has a positive effect on the enhancement ratio. Ahmet et al. [25] experimentally discovered that pin geometry such as height and other factors such as pin spacing and orientation is vital for better thermal performance in natural convection heat transfer. This experiment was performed with inline pin fin and plate heat sinks. They also discovered that the upward-facing orientation of 0° orientation angle has the highest heat transfer, while the lowest heat transfer rate was for the heat sink with the downward-facing 180° orientation angle. Emad et al. [26] experimented the thermo-hydraulic performance by changing the twist angle on a heat sink with square and hexagonal pin fin array under forced convection heat transfer. They discovered that by twisting the fins the thermal resistance decreases when compared to the non-twisted pins. They have also concluded that increasing the twisting angle lowers the friction factor and pressure drop while also lowering the efficiency when compared to no twisted fins. Singh et al. [27] investigated the heat transfer and thermal-hydraulic performance of a heat sink with square micro pin fins under forced convection heat transfer. The results show that by increasing the fin height, thermal resistance decreases while pressure drop increases. Thermal performance and heat coefficient increase with the increase of fin height and Reynolds

number but it decreases with increasing fin spacing. The percentage of improvement in efficiency was observed to be about 2 to 9% due to the presence of fins on the impingement surface, flow mixing, disruption of the boundary layers, and augmentation of turbulent transport. Dnyaneshwar & Vithoba [28] investigated pin fin arrangement effectiveness on heat sink heat transfer characteristics. Davoudi et al. [29] numerically investigated the effects of using nanofluid on heat transfer in a conical spiral heat exchanger. The nanofluids used in this numerical simulation were aluminum oxide/water (Al2O3/water) and copper oxide/water (CuO/water). They have discovered from the results that enhancing the concentration of the nanofluid causes the pressure drop to increase and heat transfer rate is slightly increased by adding nanoparticles to the base water fluid in very low concentration. They also discovered that vortices formed at the top and bottom of the tube slightly increases by enhancing the concentration of nanofluids and this flow produces more power.

While there are many different forms of heatsinks with different fin and pin arrangements, most models used are usually plate fin based heatsink or have circular pin fin arrangement. Rarely heatsink uses square shape, truncated cone or cone shaped pin in their designs. In this research, several new models of heatsinks are designed with the focus on different fin geometry and arrangement. These pin-fin based heatsink models consist of a plate fin heatsink and several other models of pin fin based heatsinks which were optimized in length, width, height and fin arrangement in order to produce optimized results and achieve better thermal performance and as well as to reach lover energy consumption. Most studies on heatsinks also tend focus on lower Reynolds numbers. In this research higher Reynolds number and therefore higher air velocity are considered for this study in order to study the effects of such high air velocity on thermal performance, pressure drop, energy consumption and Nusselt numbers. The purpose of this research is to numerically investigate these heatsink models in order to find out with models is suited for higher air velocity as well as compare thermal performance and energy consumption in height and relatively low Reynolds number.

2 MODEL DESIGN

The shape and geometric parameters of this model are based on the model of Yu et al. [30]. The types of heatsinks are shown in "Figs. 1 to 8" and the properties are shown in Table 1. These models were numerically tested. The distance between the pins and the fin is measured to be at least 1D and the distance between the pins is 10D. These models include the PFHS model, and PPFHS models with a circle, truncated, cone, and square pins. The Square PPFHS pins have three arrangements with the angles of 0,22.5, and 45 degrees which are shown in "Figs. 4, 7, and 8". The computer model in this experiment is based on the model of Yu et al. [30], which is shown in "Fig 9".

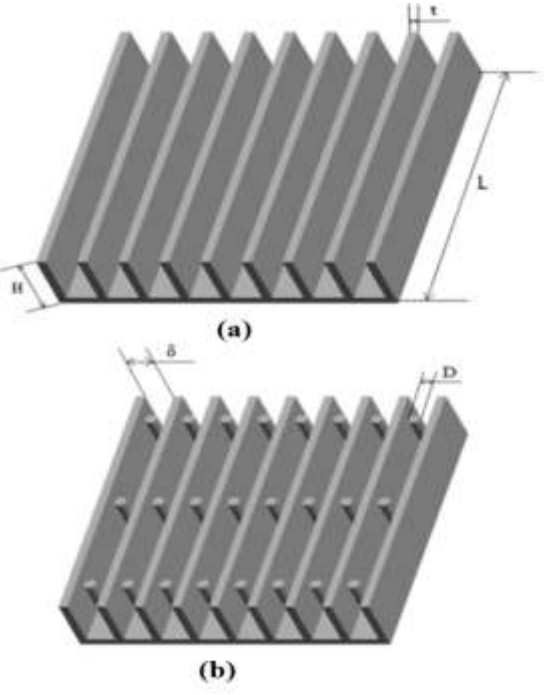

Fig. 1 Heatsink model dimensions: (a): plate pin fin heatsink, and (b): circular pin fin heatsink.

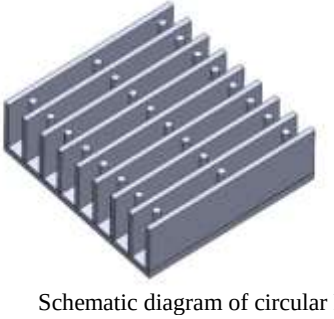

Fig. 2 Schematic diagram of circular PPFHS.

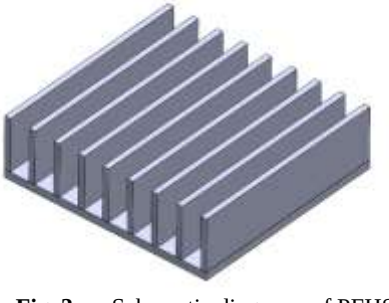

Fig. 3 Schematic diagrams of PFHS.

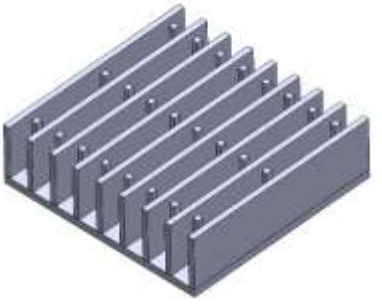

Fig. 4 Schematic diagram of square PPFHS.

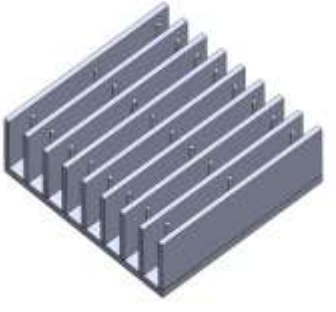

Fig. 5 Schematic diagram of truncated cone PPFHS.

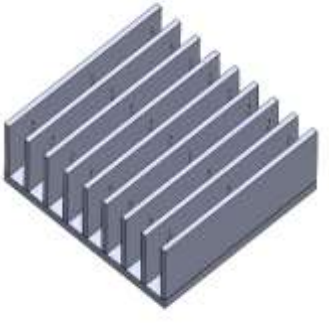

Fig. 6 Schematic diagram of cone PPFHS.

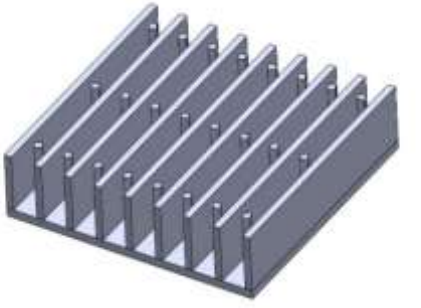

Fig. 7 Schematic diagram of square PPFHS with pin angle of 22.5 degrees.

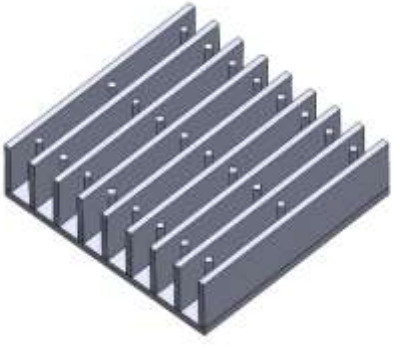

Fig. 8 Schematic diagram of square PPFHS with pin angle of 45 degrees.

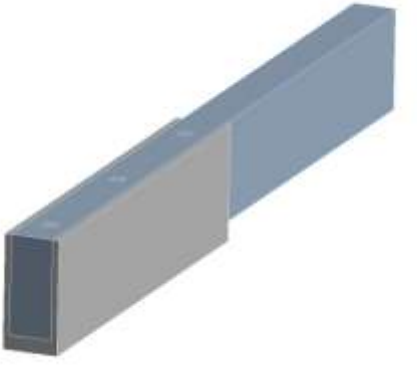

Fig. 9 Computer model of square PPFHS

Table 1 Types of heatsink under numerical experiment

Type of Heat sink	Type of Pin	Base Diameter (D)	End Diameter	Fin spacing	Fin Height (H)	Fin Thickness (δ)	Angle of pin
PFHS	N/A	N/A	N/A	5mm	10mm	1.5mm	N/A
PPFHS	Circular	2mm	2mm	5mm	10mm	1.5mm	N/A
PPFHS	Square	2mm	2mm	5mm	10mm	1.5mm	0
PPFHS	Truncated Cone	2mm	1mm	5mm	10mm	1.5mm	N/A
PPFHS	Cone	2mm	0.1mm	5mm	10mm	1.5mm	N/A
PPFHS	Square	2mm	2mm	5mm	10mm	1.5mm	22.5
PPFHS	Square	2mm	2mm	5mm	10mm	1.5mm	45

3 MATHEMATICAL EQUATION OF HEAT SINK MODEL AND NUMERICAL SIMULATION

As shown in the geometric model, both region of the heat sink model (fluid and solid) participates in the numerical simulation of heat sink models. For this numerical simulation, the k-epsilon turbulent model is used to simulate the turbulent fluid flow in the heat sink passage. The mathematical Equation governing this are as follows:

The dimensionless continuity, momentum, and energy Equation can be written as:

$$\frac{\delta U}{\partial X}+\frac{\delta V}{\partial Y}+\frac{\delta W}{\partial Z}=0 \tag{1}$$

$$U\frac{\partial U}{\partial X}+V\frac{\partial U}{\partial Y}+W\frac{\partial U}{\partial Z}=-\frac{dP}{dX}+\frac{1}{\mathrm{Re}}(\frac{\partial^2 U}{\partial X^2}+\frac{\partial^2 U}{\partial Y^2}+\frac{\partial^2 U}{\partial Z^2}) \tag{2}$$

$$U\frac{\partial V}{\partial X}+V\frac{\partial V}{\partial Y}+W\frac{\partial V}{\partial Z}=-\frac{dP}{dY}+\frac{1}{\mathrm{Re}}(\frac{\partial^2 V}{\partial X^2}+\frac{\partial^2 V}{\partial Y^2}+\frac{\partial^2 V}{\partial Z^2}) \tag{3}$$

$$U\frac{\partial W}{\partial X}+V\frac{\partial W}{\partial Y}+W\frac{\partial W}{\partial Z}=-\frac{dP}{dY}+\frac{1}{\mathrm{Re}}(\frac{\partial^2 W}{\partial X^2}+\frac{\partial^2 W}{\partial Y^2}+\frac{\partial^2 W}{\partial Z^2}) \tag{4}$$

$$U\frac{\partial \theta}{\partial X}+V\frac{\partial \theta}{\partial Y}+W\frac{\partial \theta}{\partial Z}=\frac{1}{\mathrm{Re.Pr}}(\frac{\partial^2 \theta}{\partial X^2}+\frac{\partial^2 \theta}{\partial Y^2}+\frac{\partial^2 \theta}{\partial Z^2}) \tag{5}$$

For the solid part of the thermal heatsink, the energy Equation is as follows:

$$\frac{\partial^2 \theta}{\partial X^2}=0 \tag{6}$$

The dimensionless parameters in the previous Equations can be found as:

$$X=\frac{x}{Dh},\frac{y}{Dh},Z=\frac{z}{Dh},U=\frac{u}{u_{in}},V=\frac{v}{u_{in}},$$
$$P=\frac{p}{\rho u_{in}},W=\frac{w}{u_{in}},\theta=\frac{T_f-T_{in}}{T_w-T_{in}}$$

The pressure difference is obtained from the following relation:

$$\Delta p=p_{in}-p_{out} \tag{7}$$

Heat sink heat resistance can be defined as follows [31]:

$$R_{th}=\frac{\Delta T}{Q} \tag{8}$$

ΔT is the temperature difference between the fin base and ambient air temperature, while Q shows the thermal power pumped to base of the heatsink fin. This Equation is used to measure the thermal performance of the heat sink models. In order to find the power needed to support the heat flux, the heat sink can be found via Sparrow and Ramsey [32] Equation:

$$E=U_{in}A_p\Delta p \tag{9}$$

$$A_p=H\delta(N-1) \tag{10}$$

Reynold's number can be calculated using this Equation:

$$\mathrm{Re}=\frac{\rho V D_H}{\mu} \tag{11}$$

And the Nusselt number can be calculated from:

$$Nu=\frac{hD_h}{k} \tag{12}$$

The downstream boundary is located at a distance L from the edge of the fin in the x direction to prevent backflow. In this simulation, the input and output boundary conditions of the pressure are assumed to be uniform. The two side walls are symmetrically adjusted using the periodic structure assumption. It is assumed that all enclosed walls, except the heating zone, have non-slip condition and are adiabatic. Furthermore, to simulate the heat transfer between the fin and base surfaces, the fluid is characterized as a wall-coupled condition, through which the process is performed automatically without external interference. The output of the model is pressure outlet and can be seen in "Fig. 9". The air current inlet is uniform with the velocity of 6,8,10, and 12 m/s with constant flux conditions of 0.5,1.5, and 2.5 watts per square centimetre. The ambient temperature is 294 kelvins.

General computational fluid dynamics software has been selected for the heat sink model simulation. It is an advanced CFD software which offers many different turbulence models. The software uses a semi-implicit method for the pressure-related Equation algorithm (SIMPLE) based on a volume control program using a pressure-based solver. The Equation used to solve the turbulent flow of the k-epsilon method and the remainder for the continuity, momentum, energy, and k and epsilon Equations are less than 10^{-3}, 10^{-5}, 10^{-6}, 10^{-3}, 10^{-3}.

4 VALIDATION AND REVIEW OF RESULTS

In order to validate the model, the laboratory and numerical model of Yu et al. [33] has been used, which can be seen in "Fig. 10 and Fig. 11". Examination of these two shows that the result obtained is an acceptable value. For the Grid independence test for each of these models, the minimum of 234990 nodes was used in creating a triangular mesh model and the results showed that the properties change was less than 1 percent for the thermal performance when we increased the mesh from that number.

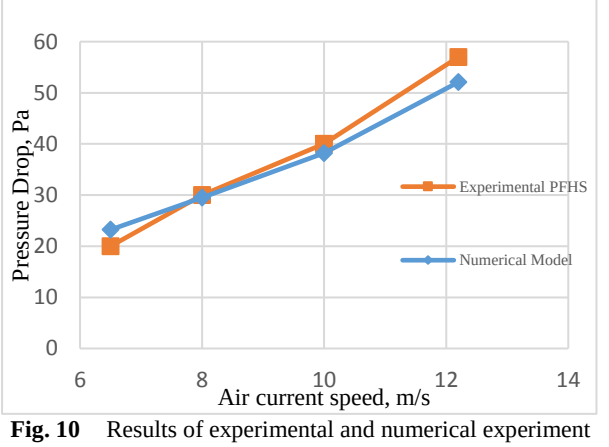

Fig. 10 Results of experimental and numerical experiment of PFHS models.

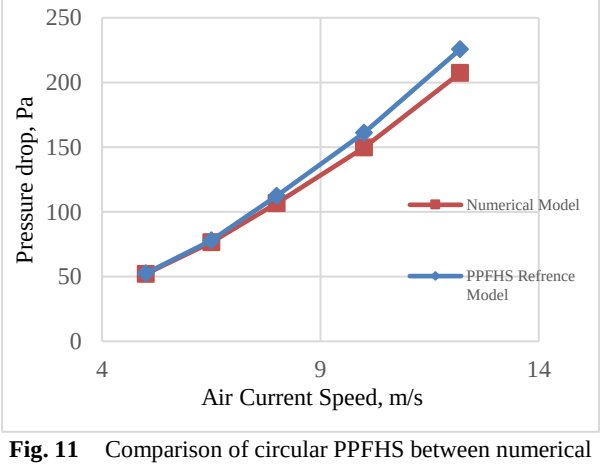

Fig. 11 Comparison of circular PPFHS between numerical and reference model.

5 RESULTS AND DISCUSSION

In this experiment, 7 models of heatsinks were compared under different velocity inputs and different heat fluxes. The peak temperatures of these different models are shown in "Figs. 12, 13, and 14" for each heat flux respectively. These figures show that the heat sink with angled square pins has the lowest peak temperature when compared to the rest of the models. The circular pin and square pin heatsink with 0 degrees' deflection angle has nearly the same peak temperature with the highest difference of fewer than 2 degrees Kelvin. The truncated cone pin heat sink is the next coldest heat sink, Because of its geometry and having less cross-area with air compared to the circular and square pin heatsink. This is the same for the cone pin heatsink.

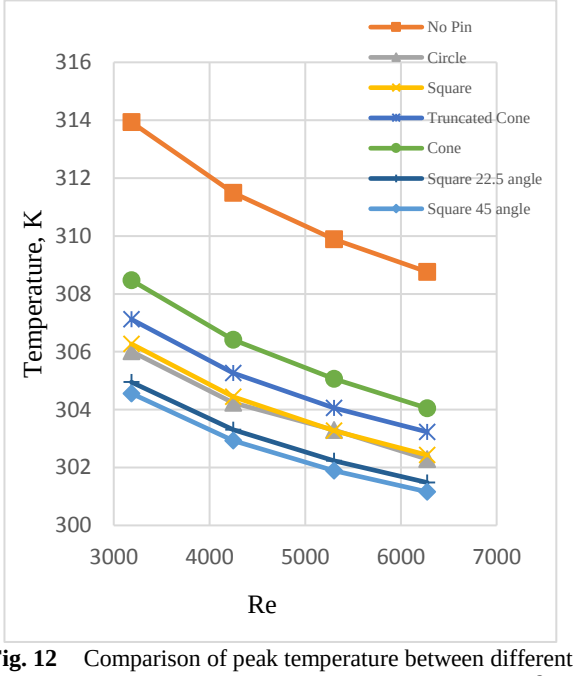

Fig. 12 Comparison of peak temperature between different models of heatsink with thermal heat flux of 0.5 W/cm^2.

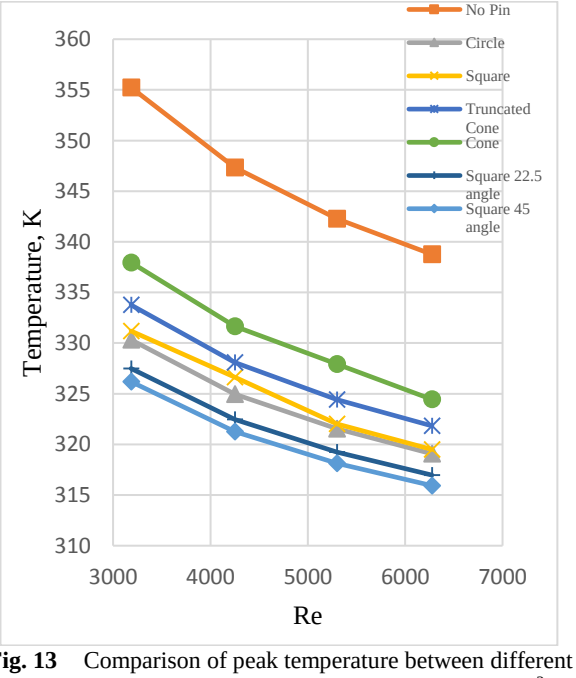

Fig. 13 Comparison of peak temperature between different models of heatsink with thermal heat flux of 1.5 W/cm^2.

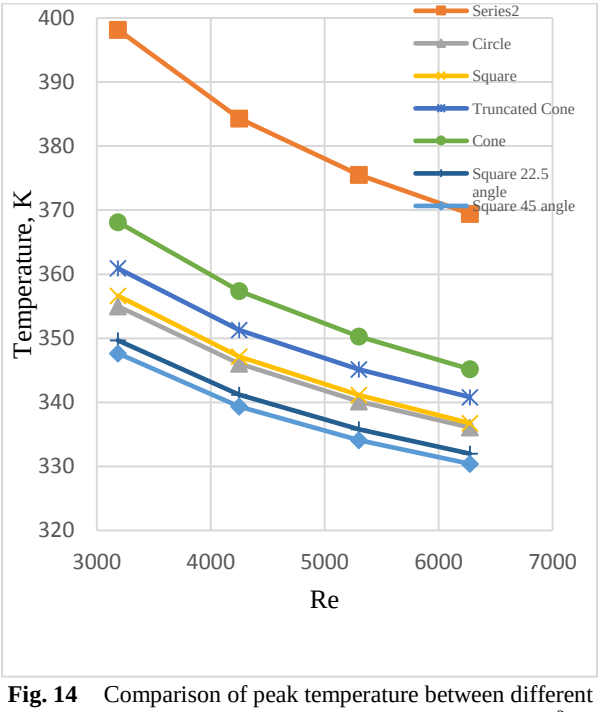

Fig. 14 Comparison of peak temperature between different models of heatsink with thermal heat flux of 2.5 W/cm^2.

The plate-fin heat sink has the highest max temperature out of all of these models, having its highest temperature reaction near 400 Kelvin in one of the experiments. This result shows that even having a simple 3 pin per layer decreases the peak temperature by over 30 degrees in higher heat fluxes. Figures 15, 16 and 17 show the pressure drop between the inlet and outlet of the numerical model. The figures show that the square pin heatsinks have the most pressure drop when compared to the other heatsink models due to their shape and geometry.

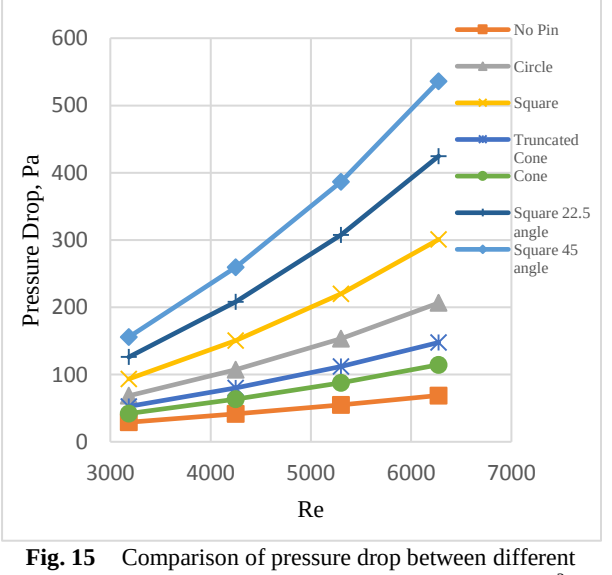

Fig. 15 Comparison of pressure drop between different models of heatsink with thermal heat flux of 0.5 W/cm^2.

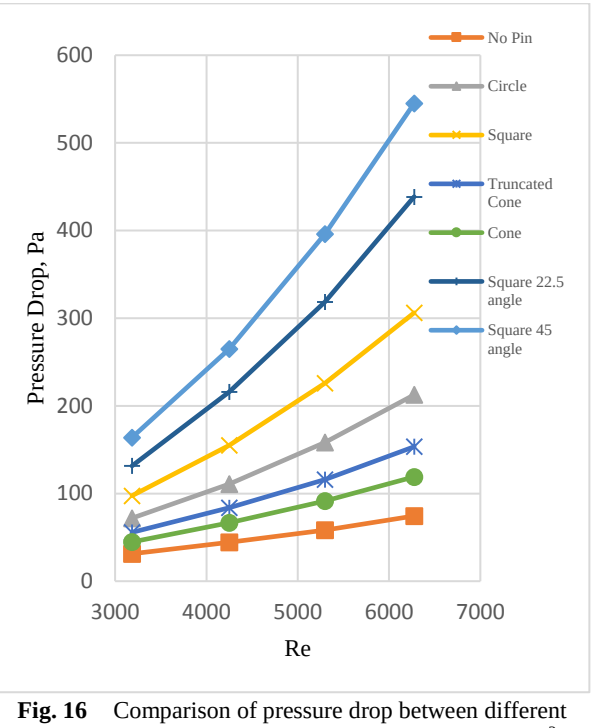

Fig. 16 Comparison of pressure drop between different models of heatsink with thermal heat flux of 1.5 W/cm^2.

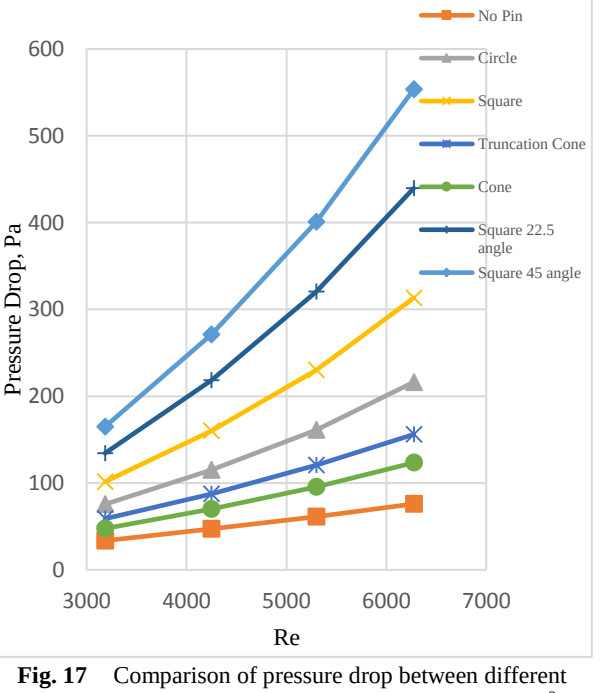

Fig. 17 Comparison of pressure drop between different models of heatsink with thermal heat flux of 2.5 W/cm^2.

It also shows that by tilting the pin in the square model heatsink by 22.5 and 45 degrees, the pressure drops increase by at least 34 percent and 66 percent, respectively. With increasing the coolant airspeed and therefore with the increase of the Reynolds number, the pressure drop difference between the square model with 0-degree angle deflection compared to the circular

model changes between 30% up to 45% with the increase of inlet speed. It can be concluded that despite having nearly the same peak temperature, the amount of energy required for cooling the square pin fin heat sin is about 30 to 45 percent more than the circular pin fin heat sink. The other models are also shown here have less pressure drop due to their shape and geometry not obscuring the airflow between the fins compared to the circular and square shape models of pin fin heatsink. The truncated cone despite having a higher peak temperature consumes up to 27 percent less energy compared to the circular pin model. The cone-shaped pin fin heat sink has the least pressure drop when compared to the other pin-based model heat skinks even though it has a higher peak temperature. The PFHT heatsink has the least pleasure drop due to having no obstruction for the airflow, therefore, uses the least energy comparatively but when comparing the peak temperature, it has the highest of all of the heatsink models.

Figures 18, 19 and 20 show the Nusselt number of each of the models for different Reynolds number with different heat fluxes. Comparing the Nusselt number of these models shows that the Nusselt number of the truncated cone pin fin heat sink is only about 5 percent less than the circular pin fin heat skink while the Nusselt number of the cone-shaped pin heat sink is 10 to 11 percent less than the circular model.

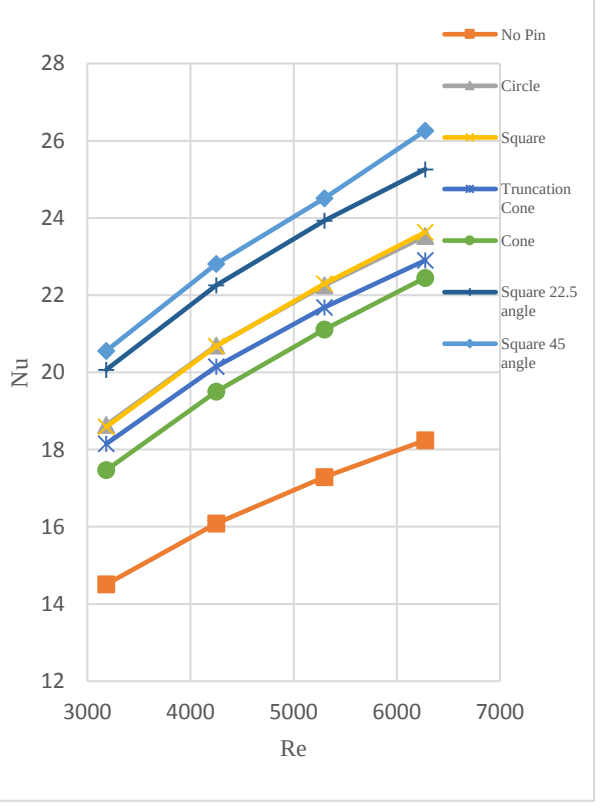

Fig. 18 Comparison of Nusselt number between different models of heatsink with thermal heat flux of 0.5 W/cm^2.

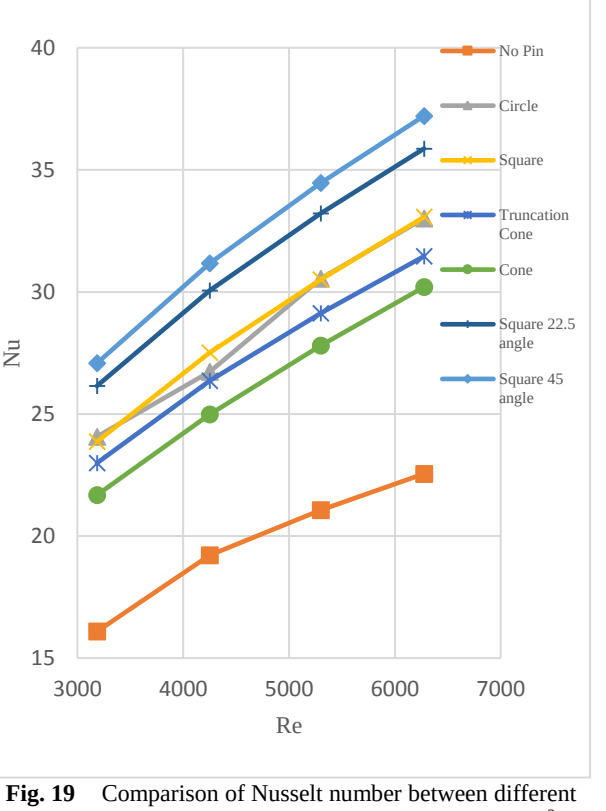

Fig. 19 Comparison of Nusselt number between different models of heatsink with thermal heat flux of 1.5 W/cm^2.

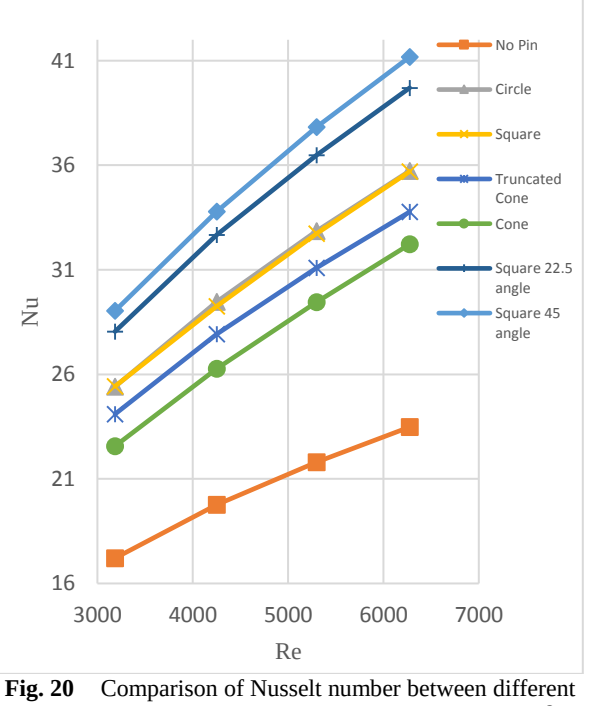

Fig. 20 Comparison of Nusselt number between different models of heatsink with thermal heat flux of 2.5 W/cm^2.

This shows that despite having less Nusselt number, the energy required to cool the heatsinks is significantly less for both of the cone-shaped models. by looking at the

pressure figures, it can also be interpreted that the square shape and the circular shape pin fin heat sink work better in slower air currents. The highest Nusselt number belongs to the square pinned hit sin with a 45-degree deflection angle. This is due to the change of the angle in the square pin and how air contacts more surface area compared to the square pin with no deflection angle which would increase thermal performance. When compared to the circular and the square pin model with no deflection angle, by changing the deflection angle by 22.5 and 45 degrees, the Nusselt number would increase by 7.6 and 11 percent for lower fluxes. In higher fluxes, the difference is increased to 10.3 and 14.2 percent, respectively. Truncated cone pin heat sink when compared to the circle pin heat sink has 2.6 percent up to 5.1 percent less Nusselt number.

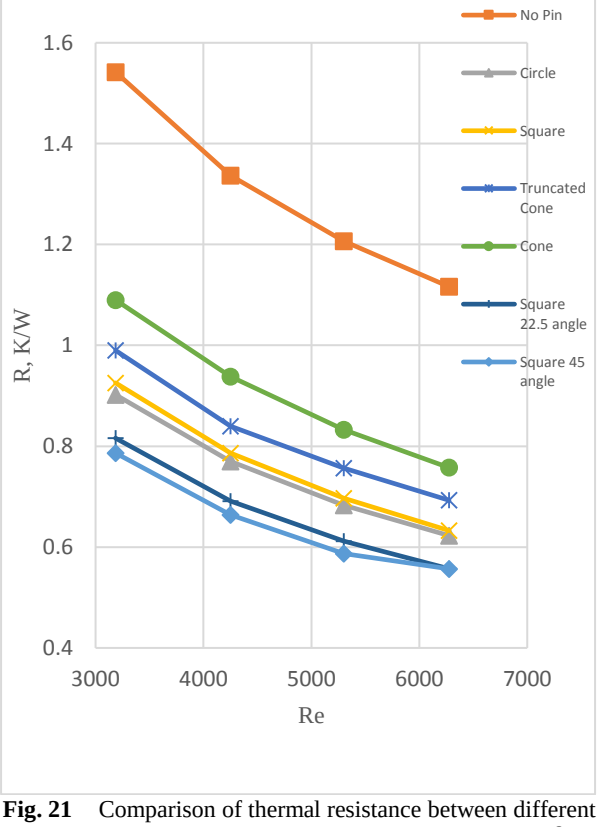

Fig. 21 Comparison of thermal resistance between different models of heatsink with thermal heat flux of 0.5 W/cm^2.

Figures 21, 22 and 23 show the thermal resistance of the models for different Reynolds number and different heat fluxes. The same explanation for the Nusselt number can also be attributed to the thermal resistance of each model. The square pin heat sink model comes on top with having the least thermal heat resistance out of all the heatsink models while the truncated cone and cone pin heatsink models have higher heat resistance due to having higher temperature compared to the models mentioned above.

The thermal performance of the square model heat sink with 22.5- and 45-degrees deflection angle is increased by 9.6 and 12 percent when compared to the circular pin model heat sink.

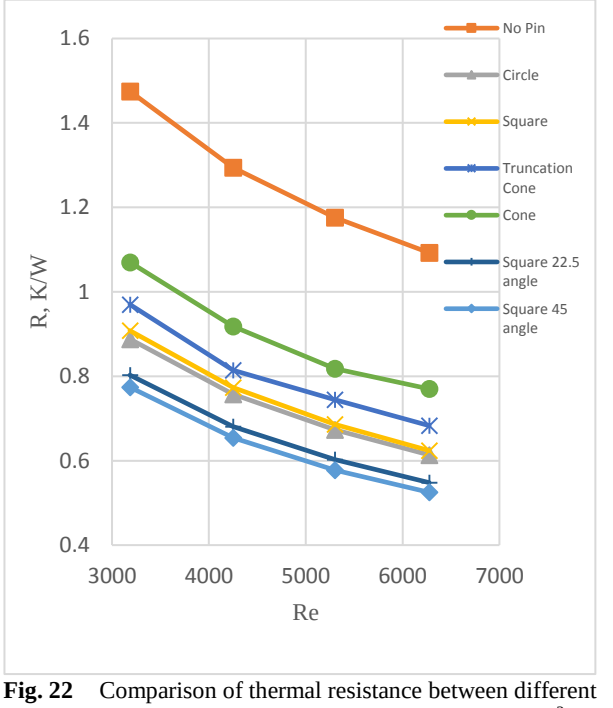

Fig. 22 Comparison of thermal resistance between different models of heatsink with thermal heat flux of 1.5 W/cm^2.

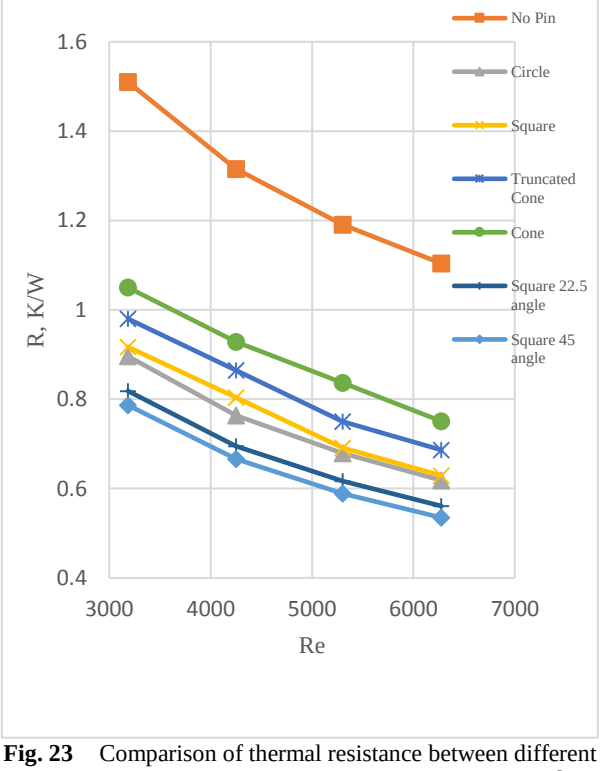

Fig. 23 Comparison of thermal resistance between different models of heatsink with thermal heat flux of 2.5 W/cm^2.

Figures 24, 25, and 26 show the energy consumption for each of these heatsink models. The square-shaped pin heatsink model uses the most energy and the PFHS uses the least amount of energy.

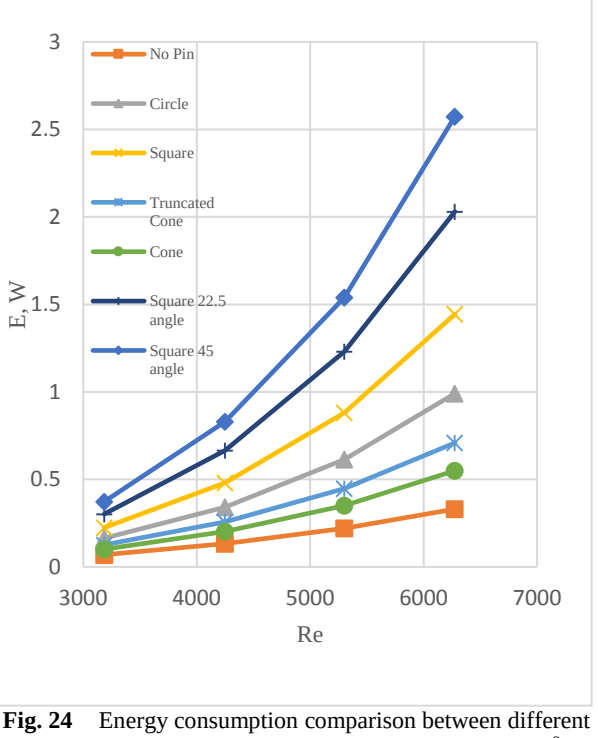

Fig. 24 Energy consumption comparison between different models of heatsink with thermal heat flux of 0.5 W/cm^2.

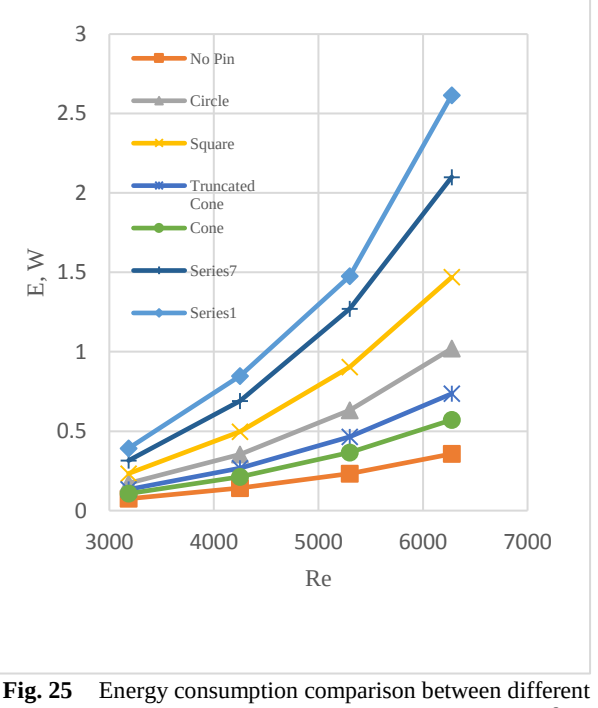

Fig. 25 Energy consumption comparison between different models of heatsink with thermal heat flux of 1.5 W/cm^2.

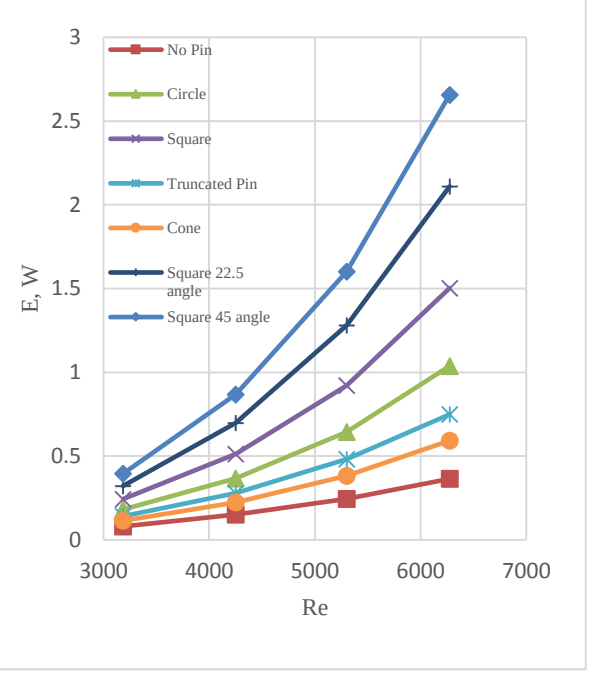

Fig. 26 Energy consumption comparison between different models of heatsink with thermal heat flux of 2.5 W/cm^2.

The geometry and the shape of the pin between the fin in the heatsink have a profound effect on pressure drop that even changing the angle of attack will increase the pressure drop considerably. This correlates to the amount of energy used for cooling these models of heat sinks. Figures 27 to 32 show the thermal contours of the different models of heat sink under the same velocity and heat flux of 8 m/s and 1.5 watts per centimeter square. The air passing through between the fins gets heated up by the fins and the pins. It also shows how are the transfers between the fin and pins and the air by convection. When comparing the circle-shaped pin, the size of the area decreases for the truncated cone and the cone pin model heatsink thereby increasing maximum temperature but reducing pressure drop compared to the regular circle-shaped pin heat sink model. it also shows that by turning the pin in square model heatsinks, it can reduce maximum temperature while increasing pressure drop.

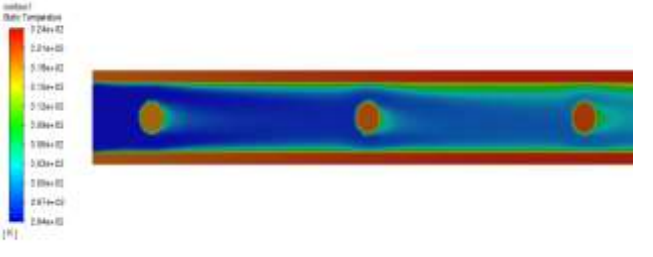

Fig. 27 Temperature contour of Circle Pin Heatsink model with the velocity of 8 m/s with thermal heat flux of 1.5 W/cm.

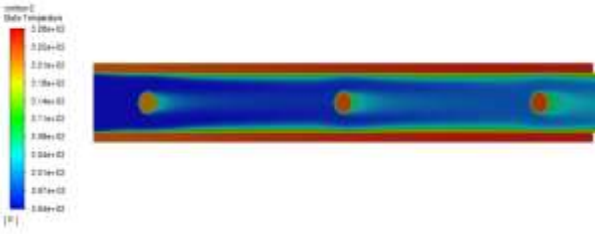

Fig. 28 Temperature contour of truncated cone pin heatsink model with the velocity of 8 m/s with thermal heat flux of 1.5 W/cm^2.

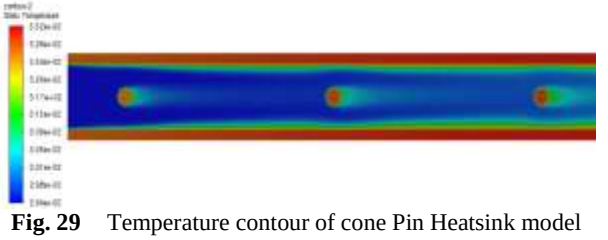

Fig. 29 Temperature contour of cone Pin Heatsink model with the velocity of 8 m/s with thermal heat flux of 1.5 W/cm^2.

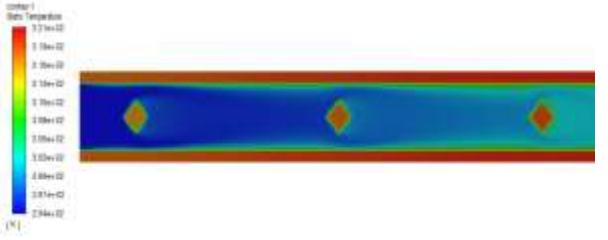

Fig. 30 Temperature contour of 45-degree angle square Pin Heatsink model with the velocity of 8 m/s with thermal heat flux of 1.5 W/cm^2.

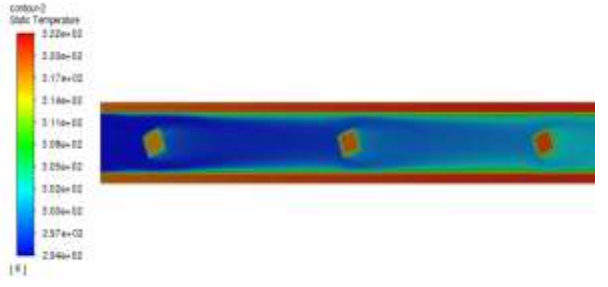

Fig. 31 Temperature contour of 22.5-degree angle square Pin model with the velocity of 8 m/s with thermal heat flux of 1.5 W/cm^2.

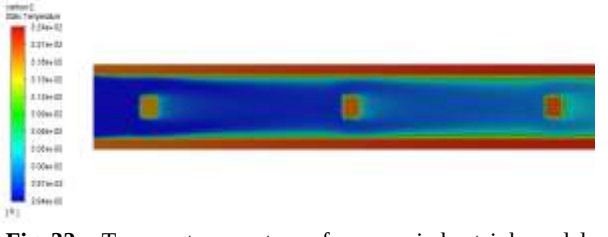

Fig. 32 Temperature contour of square pin heatsink model with the velocity of 8 m/s with thermal heat flux of 1.5 W/cm^2.

Figures 33 to 38 show the velocity of the heat sin models with the velocity of 8m/s. It shows how the air interacts with the pin between the fin in these heatsinks models. Also shows us how the air current moves around the pins. The circle model air current counter is similar to that of a cylinder with the difference that the diameter changes with height change. The square models show how the air staggers when approaching the square pin. This staggering increases by changing the angle of the square pin.

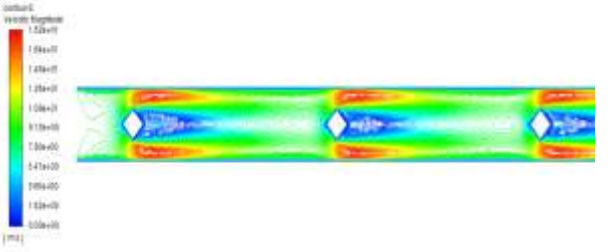

Fig. 33 Velocity contour of 45-degree angle square Pin Heatsink model with the velocity of 8 m/s with thermal heat flux of 1.5 W/cm^2.

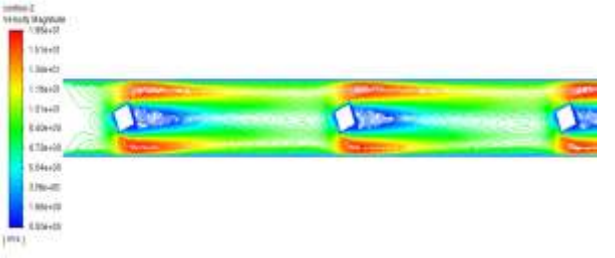

Fig. 34 Velocity contour of 22.5-degree angle square Pin model with the velocity of 8 m/s with thermal heat flux of 1.5 W/cm^2.

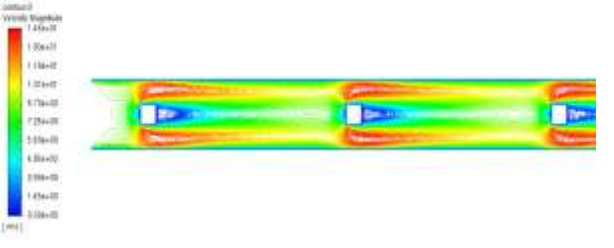

Fig. 35 Velocity contour of square pin heatsink model with the velocity of 8 m/s with thermal heat flux of 1.5 W/cm^2.

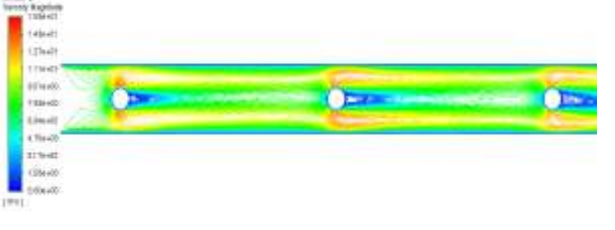

Fig. 36 Velocity contour of truncated cone pin heatsink model with the velocity of 8 m/s with thermal heat flux of 1.5 W/cm^2.

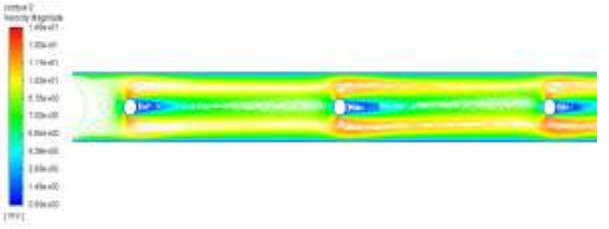

Fig. 37 Velocity contour of cone Pin Heatsink model with the velocity of 8 m/s with thermal heat flux of 1.5 W/cm^2**.**

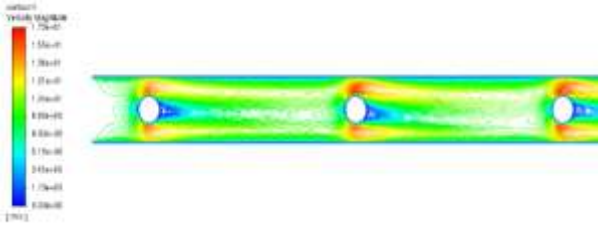

Fig. 38 Velocity contour of Circle Pin Heatsink model with the velocity of 8 m/s with thermal heat flux of 1.5 W/cm^2.

6 CONCLUSIONS

In this Numerical experiment, several models of heatsinks with different pin models (except for the PFHS) were compared in different factors such as peak temperature, heat resistance, thermal performance, and energy consumption. The results are as follows:

1- With the increase of Reynolds, number increases flow resistance and therefore it will increase the pressure drop in each model of the heatsink. The square pin has the most pressure drop out of all of these models due to its geometry therefore it consumes the most energy when compared to the other models.

2- By changing the angle of attack, the pressure drop for the square pin heatsink increased due to more air hitting the pins. This increase for 22.5 and 45 angles of deflection is measured to be at least more than 34 and 66 percent compared to the square pin heatsink model with zero angles of deflection.

3- The cone-shaped pin fin heat sink model has less Nusselt number compared to the rest of the models but consumes the least amount of energy for cooling. Therefore, it is far more economical to use these models at higher velocity compared to the other models of heatsinks.

4- The PFHS has the least pressure drop due to having no pin in front of the air current making it ideal for certain heat sink designs. It has the highest thermal resistance and the lowest Nusselt number compared to the rest of the models. It also shows that adding a simple 3 pins for each layer of the heatsink thermal performance by at least 28 percent.

5- The truncated cone and cone model show us that changing the model's geometry can help us reduce pressure drop with the sacrifice of little thermal performance.

6- Changing the angle of deflection for the square by 22.5 and 45 degrees increases the thermal performance of the square pin heat sink by at least 9.6 and 12 percent respectively compared to the regular square pin heat sink model.

7 APPENDIX OR NOMENCLATURE

Nomenclature	Greek symbols
Latin Symbols	P Dimensionless pressure
A Areas [m^2]	σ Constant In the turbulent model
C Constant in turbulent model	δ Fin spacing [mm]
H Height [m]	Δ Differential
L Distance from base In x-direction [m]	μ Viscosity [$N.s/m^2$]
N Fin number [-]	ρ Density [$kg.m^{-3}$]
p Pressure [Pa]	θ Dimensionless temperature
E Pumping power [W]	Subscripts
Q Heating power [W]	i, j Repeated-subscript indices
R Resistance [$K.W^{-1}$]	in Inlet
Re Reynolds number [-]	t Turbulent Flow
T Temperature [K]	out Outlet
x, y, z Cartesian coordinates	th Thermal
X, Y, Z Dimensionless Cartesian Coordinates	p Flow passage
U, V, W Dimensionless velocity	s Solid
D_H Hydraulic diameter	w Wall
Nu Nusselt Number	f Fluid

REFERENCES

[1] Hosseini, S. M., Safaei, M. R., Goodarzi, M., Alrashed, A. A. A. A., and Nguyen, T. K., New Temperature, Interfacial Shell Dependent Dimensionless Model for Thermal Conductivity of Nanofluids, International Journal of Heat and Mass Transfer, Vol. 114, 2017, pp. 207-210, https://doi.org/10.1016/j.ijheatmasstransfer.2017.06.061

[2] Talebi, M., Tabibian, M., Magnetic Field Effect on Ferro-Nanofluid Heat Transfer in a Shell and Tube Heat Exchanger with Seven Twisted Oval Tubes, ADMT Journal, Vol. 15, No. 2, 2022, pp. 39-48, 10.30495/admt.2022.1937049.1300.

[3] Kurşun, B., Sivrioğlu, M., Heat Transfer Enhancement Using U-Shaped Flow Routing Plates in Cooling Printed Circuit Boards, Journal of the Brazilian Society of Mechanical Sciences and Engineering, Vol. 40, No. 1, 2018, pp. 1-14.

[4] Ghasemi, S. E., Ranjbar, A. A., and Hosseini, M. J., Experimental Evaluation of Cooling Performance of Circular Heat Sinks for Heat Dissipation from Electronic Chips Using Nanofluid, Mechanics Research Communications, Vol. 84, 2017, pp. 85-89,https://doi.org/10.1016/j.mechrescom.2017.06.009.

[5] Sadeghi, H., Izadpanah, E., Babaie Rabiee, M., and Hekmat, M. H., Effect of Cylinder Geometry on The Heat Transfer Enhancement of Power-Law Fluid Flow Inside a Channel, Journal of the Brazilian Society of Mechanical Sciences and Engineering, Vol. 39, No. 5, 2017, pp. 1695-1707, 10.1007/s40430-016-0695-3.

[6] Ghani, I. A., Kamaruzaman, N., and Sidik, N. A. C., Heat Transfer Augmentation in A Microchannel Heat Sink with Sinusoidal Cavities And Rectangular Ribs, International Journal of Heat and Mass Transfer, Vol. 108, 2017, pp. 1969-1981, https://doi.org/10.1016/j.ijheatmasstransfer.2017.01.046.

[7] Mousavi, H., Rabienataj Darzi, A. A., Farhadi, M., and Omidi, M., A Novel Heat Sink Design with Interrupted, Staggered and Capped Fins, International Journal of Thermal Sciences, Vol. 127, 2018, pp. 312-320, https://doi.org/10.1016/j.ijthermalsci.2018.02.003.

[8] Jajja, S. A., Ali, W., Ali, H. M., and Ali, A. M., Water Cooled Minichannel Heat Sinks for Microprocessor Cooling: Effect of Fin Spacing, Applied Thermal Engineering, Vol. 64, No. 1, 2014, pp. 76-82, https://doi.org/10.1016/j.applthermaleng.2013.12.007.

[9] Patel, N., Mehta, H. B., Experimental Investigations on A Variable Channel width Double Layered Minichannel Heat Sink, International Journal of Heat and Mass Transfer, Vol. 165, 2021, pp. 120633, https://doi.org/10.1016/j.ijheatmasstransfer.2020.120633.

[10] Abbasian Arani, A. A., Akbari, O., Safaei, M. R., Marzban, A., Alrashed, A., Ahmadi, G., and Nguyen, T., Heat Transfer Improvement of Water/Single-Wall Carbon Nanotubes (SWCNT) Nanofluid in A Novel Design of a Truncated Double-Layered Microchannel Heat Sink, International Journal of Heat and Mass Transfer, Vol. 113, 2017, pp. 780-795, 10.1016/j.ijheatmasstransfer.2017.05.089.

[11] Engerer, J. D., Doty, J. H., and Fisher, T. S., Transient Thermal Analysis of Flash-Boiling Cooling in the Presence of High-Heat-Flux Loads, International Journal of Heat and Mass Transfer, Vol. 123, 2018, pp. 678-692, https://doi.org/10.1016/j.ijheatmasstransfer.2018.02.109.

[12] Al-damook, A., Alkasmoul, F., Heat Transfer and Airflow Characteristics Enhancement of Compact Plate-Pin Fins Heat Sinks-A Review, Propulsion and Power Research, Vol. 7, No. 2, 2018, pp. 138-146, https://doi.org/10.1016/j.jppr.2018.05.003.

[13] Yang, Y. T., Peng, H. S., Investigation of Planted Pin Fins for Heat Transfer Enhancement in Plate Fin Heat Sink, Microelectronics Reliability, Vol. 49, No. 2, 2009, pp. 163-169, https://doi.org/10.1016/j.microrel.2008.11.011.

[14] Li, H. Y., Chao, S. M., Measurement of Performance of Plate-Fin Heat Sinks with Cross Flow Cooling, International Journal of Heat and Mass Transfer, Vol. 52, No. 13, 2009, pp. 2949-2955, https://doi.org/10.1016/j.ijheatmasstransfer.2009.02.025.

[15] Alam, M. W., Bhattacharyya, S., Souayeh, B., Dey, K., Hammami, F., Rahimi-Gorji, M., and Biswas, R., CPU Heat Sink Cooling by Triangular Shape Micro-Pin-Fin: Numerical Study, International Communications in Heat and Mass Transfer, Vol. 112, 2020, pp. 104455, https://doi.org/10.1016/j.icheatmasstransfer.2019.104455.

[16] Haghighi, S. S., Goshayeshi, H. R., and Safaei, M. R., Natural Convection Heat Transfer Enhancement in New Designs of Plate-Fin Based Heat Sinks, International Journal of Heat and Mass Transfer, Vol. 125, 2018, pp. 640-647, https://doi.org/10.1016/j.ijheatmasstransfer.2018.04.122.

[17] Ahmed, H. E., Salman, B. H., Kherbeet, A. S., and Ahmed, M. I., Optimization of Thermal Design of Heat Sinks: A Review, International Journal of Heat and Mass Transfer, Vol. 118, 2018, pp. 129-153, https://doi.org/10.1016/j.ijheatmasstransfer.2017.10.099.

[18] Kim, S. J., Kim, D. K., and Oh, H. H., Comparison of Fluid Flow and Thermal Characteristics of Plate-Fin and Pin-Fin Heat Sinks Subject to a Parallel Flow, Heat Transfer Engineering, Vol. 29, No. 2, 2008, pp. 169-177, 10.1080/01457630701686669.

[19] Ambreen, T., Kim, M.-H., Flow and Heat Transfer Characteristics Over a Square Cylinder with Corner Modifications, International Journal of Heat and Mass Transfer, Vol. 117, 2018, pp. 50-57, https://doi.org/10.1016/j.ijheatmasstransfer.2017.09.132.

[20] Scholten, J. W., Murray, D. B., Unsteady Heat Transfer and Velocity of a Cylinder in Cross Flow—I. Low Freestream Turbulence, International Journal of Heat and Mass Transfer, Vol. 41, No. 10, 1998, pp. 1139-1148, https://doi.org/10.1016/S0017-9310(97)00250-0.

[21] Bhattacharyya, S., Das, S., Sarkar, A., Guin, A., and Mullick, A., Numerical Simulation of Flow and Heat Transfer Around Hexagonal Cylinder, International Journal of Heat and Technology, Vol. 35, No. 2, 2017, pp. 360-363.

[22] Benim, A. C., Pasqualotto, E., and Suh, S. H., Modelling Turbulent Flow Past a Circular Cylinder by RANS, URANS, LES and DES, Progress in Computational Fluid Dynamics, An International Journal, Vol. 8, No. 5, 2008, pp. 299-307.

[23] Nilpueng, K., Mesgarpour, M., Asirvatham, L. G., Dalkılıç, A. S., Ahn, H. S., Mahian, O., and Wongwises,

S., Effect of Pin Fin Configuration on Thermal Performance of Plate Pin Fin Heat Sinks, Case Studies in Thermal Engineering, Vol. 27, 2021, pp. 101269.

[24] Nilpueng, K., Wongwises, S., Thermal Performance Investigation of a Plate Fin Heat Sink Equipped with Twisted Tape and Perforated Twisted Tape, Journal of Thermal Science and Technology, Vol. 16, No. 2, 2021, pp. JTST0024-JTST0024, 10.1299/jtst.2021jtst0024.

[25] Sertkaya, A. A., Ozdemir, M., and Canli, E., Effects of Pin Fin Height, Spacing and Orientation to Natural Convection Heat Transfer for Inline Pin Fin and Plate Heat Sinks by Experimental Investigation, International Journal of Heat and Mass Transfer, Vol. 177, 2021, pp. 121527, https://doi.org/10.1016/j.ijheatmasstransfer.2021.121527.

[26] El-Said, E. M. S., Abdelaziz, G. B., Sharshir, S. W., Elsheikh, A. H., and Elsaid, A. M., Experimental Investigation of The Twist Angle Effects on Thermo-Hydraulic Performance of a Square and Hexagonal Pin Fin Array in Forced Convection, International Communications in Heat and Mass Transfer, Vol. 126, 2021, pp. 105374, https://doi.org/10.1016/j.icheatmasstransfer.2021.105374.

[27] Singh, N. R., Onkar, S., and Ramkumar, J., Thermo-Hydraulic Performance of Square Micro Pin Fins under Forced Convection, Journal homepage: http://iieta. org/journals/ijht, Vol. 39, No. 1, 2021, pp. 170-178.

[28] Mate, D. M., Tale, V. T., Effects of Pin Fin Arrangement Its Heat Transfer Characteristics on Performance of Heat Sink, Materials Today: Proceedings, Vol. 43, 2021, pp. 2377-2382.

[29] Davoudi, A., Daneshmand, S., Monfared, V., and Mohammadzadeh, K., Numerical Simulation on Heat Transfer of Nanofluid in Conical Spiral Heat Exchanger, Progress in Computational Fluid Dynamics, an International Journal, Vol. 21, No. 1, 2021, pp. 52-63.

[30] Yuan, W., Zhao, J., Tso, C. P., Wu, T., Liu, W., and Ming, T., Numerical Simulation of the Thermal Hydraulic Performance of a Plate Pin Fin Heat Sink, Applied Thermal Engineering, Vol. 48, 2012, pp. 81-88, 10.1016/j.applthermaleng.2012.04.029.

[31] Li, H. Y., Chen, K. Y., and Chiang, M. H., Thermal-Fluid Characteristics of Plate-Fin Heat Sinks Cooled by Impingement Jet, Energy Conversion and Management, Vol. 50, No. 11, 2009, pp. 2738-2746, https://doi.org/10.1016/j.enconman.2009.06.030.

[32] Sparrow, E. M., Ramsey, J. W., and Altemani, C. A. C., Experiments on In-Line Pin Fin Arrays and Performance Comparisons with Staggered Arrays, 1980.

[33] Yu, X., Feng, J., Feng, Q., and Wang, Q., Development of a Plate-Pin Fin Heat Sink and Its Performance Comparisons with A Plate Fin Heat Sink, Applied Thermal Engineering, Vol. 25, No. 2, 2005, pp. 173-182, https://doi.org/10.1016/j.applthermaleng.2004.06.016.

Int. J. Advanced Design and Manufacturing Technology, 2022, Vol. 15, No. 4, pp. 61-70

DOI: 10.30486/admt.2023.1960408.1355 ISSN: 2252-0406 https://admt.isfahan.iau.ir

Experimental Analysis of Effective Parameters on the Bowing Defect of Symmetrical U-Section in Roll Forming Production

Amin Poursafar, Saeid Saberi *, Rasoul Tarkesh Esfahani, Meisam Vahabi, Javad Jafari Fesharaki

Department of Mechanical Engineering, Najafabad Branch, Islamic Azad University, Najafabad, Iran.
E-mail: amin.poursafar@smc.iaun.ac.ir, saeid_saberi@yahoo.com, ra_tarkesh@pmc.iaun.ac.ir, m.vahabi@pmc.iaun.ac.ir, jafari@pmc.iaun.ac.ir
*Corresponding author

Received: 6 June 2022, Revised: 29 September 2022, Accepted: 23 October 2022

Abstract: The roll forming process plays a critical role in producing various sections used in industries. Also, the quality of these products is strongly affected by the thickness of the strip, the distance between stands, the section web, the flower pattern, and the plastic anisotropy. Therefore, the influences of practical factors on the bowing defect of the symmetrical U-section are experimentally and mathematically characterized in the present research. The investigated material is DC03 (1.0347) steel. Different prediction models such as linear and non-linear model based on the general full-factorial design of experiment are used to predict the effect of following factors on the bowing defect. Accuracy of the analytical model was verified by comparing the output results with the practical data. Results show that the strip thickness of investigated material, the flower pattern, and the section web have the most significant effect on the bowing defect. Also, the anisotropic properties of the investigated material and the inter distance have the minor impact on the bowing defect, but the effect of material with considering the anisotropic properties on increasing the accuracy of process simulation results is very impressive and increases the accuracy of simulation results from 84% to 91%. Finally, the predicted bowing defect using the modified two-factor model was in 91% agreement with the experimental results.

Keywords: Bowing Defect, Design Of Experiments, Full Factorial, Roll Forming, Symmetrical, U- Section

Biographical notes: Amin Poursafar received his MSc in Mechanical Engineering from Urmia university, in 2006 and he is now a PhD student in Mechanical Engineering at IAU, Najafabad branch. His research interest is metal forming and machining**. Saeid Saberi** received his PhD and MSc in Mechanical Engineering from Graz University of Technology, in 2004 and 2009. His research interests include machine visioning, forming processes, and modern production. **Rasoul Tarkesh Esfahani** received his PhD and MSc from Kashan University in 2004 and 2009, respectively. His research interests include solving the challenges of the aviation industry. **Meisam Vahabi** received his PhD and MSc in Mechanical Engineering from Amirkabir University of Technology, in 2004 and 2010, respectively. His research interests include smart material, gear box design, optimizing, tool design, and MEMS. **Javad Jafari Fesharaki** received his PhD, MSc and BSc in Mechanical Engineering from Kashan University, in 2004, 2008 and 2010, respectively. His research interests include functionally graded material, and piezoelectric patch.

Research paper

1 INTRODUCTION

The roll forming process consists of several forming stands with the various forming rolls where the strip with different materials, such as steel, and non-steel, approaches the final geometry at several stands. The stand of the roll forming process consists of a combination of various rollers that create a flower pattern of the profile, and these stands consist of a set of upper and lower rollers for this purpose. Side rollers are used to prevent strip misalignment to improve the forming conditions. One of the most significant advantages of this process is that the thickness does not change during the process. All these features allow to product the various sections with a uniform cross-section longitudinally with the best quality. The most essential features of this type of forming process that has made the overall process uniform is that the power used in all stands is the same.

In this process, the velocity gradient in each stand, which is along with increasing the diameter of the rollers, prevents the sheet from wrinkling. This issue is critical in the case of low-thickness strips, because in the case of thicker strips, wrinkling and bowing defect occur less frequently [1]. Generally, the strip is continuously formed at ambient temperature into a desired cross-section (open or close section) through the forming rolls [2]. Figure 1 shows the schematic of process and the bowing defect; According to "Fig. 1", the bowing defect is accrued in the perpendicular direction to the formed section axes.

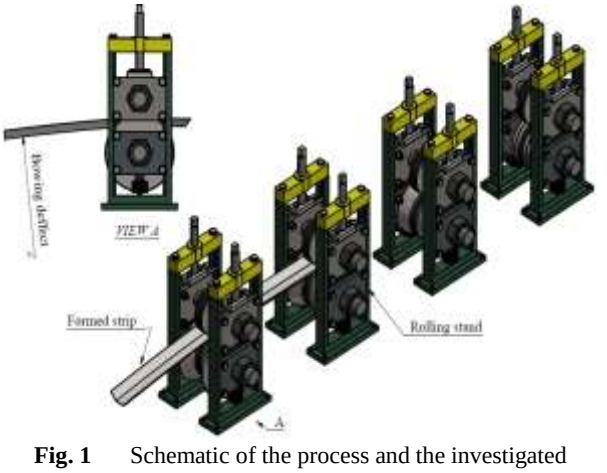

Fig. 1 Schematic of the process and the investigated bowing defect.

It was shown that the bowing defect could be reduced as much as possible by changing the relative height of the rollers of each stand concerning each other, as well as using extra rolls called straighter at the end of the production line [3]. Bhattacharyya et al. showed that the distance between the stands in a roll forming could be significant on the bowing defect. Also, the results of their research show the impact of the thickness, the flower pattern, and the wall length on the bowing defect [4]. Bhattacharyya et al. studied on the effects of the flower pattern on the strains which accrues along with longitudinal direction, and their results showed that the effect of the start and the final forming stands are greater than other stands [5]. Duncan and Zhou investigated the parameters affecting the symmetric part of the U-channel and the hat-shaped section in the multi-stand process. The results of their research revealed the transverse, the longitudinal, and the shear strains as significant factors [6]. By using five sets of rolling stand and choosing a symmetrical section, Sheu found the significant impact of the flower pattern, the velocity of rolls, the friction, and the rolls radius on the bowing defect. The results showed that the velocity and the flower pattern have the greatest effect [7]. Tehrani et al. used ABAQUS software and used the localized buckling at the edge of formed strip as a constraining factor in the roll forming of the symmetrical section of the U-channel. Investigation showed that the amount of bending in the first forming stand should be optimized to prevent the localized edge buckling [8]. Shirani et al. investigated the effects of different on-line factors on the bowing defect of the pre-punched symmetrical U-shaped section. In this study, the stand level height, the bend angle of increment (flower pattern), and the distance between forming stands are considered as input factors, and the circularity of punched-holes after forming took as the result. Finally, the thickness of the strip is presented as the most effective factor on the holes circularity [9]. Shirani et al. also investigated the bowing defect of the U-section product. They investigated different factors like the thickness, the side length, and the flower pattern on the bowing defect and conducted a series of practical tests and verified the results with the ABAQUS software results. The results showed that the thickness and the flower pattern have the greatest effect on the bowing defect of the pre-punched strip [10]. Shirani et al. continued to investigate the effective factors on the torque of the forming stand. Their results showed that increasing the bending angle in each stand increased the required torque, and the torque also moves up with increases in the thickness [11]. Lindgren studied on alloy steel, especially high-strength for producing the symmetrical channel. The longitudinal strain of the formed strip edge decreased with the increase in the inter distance [12]. Salmani et al. predicted the bowing defect using regression models and artificial neural networks. The results of this research show that the regression prediction model and the artificial neural network model are suitable for predicting the process defects [13]. The simulation was performed based on METAFOR software code by Bui for symmetrical U-shaped sections. The results show that the distance of stands, the forming velocity, the friction between the rollers, the

mechanical properties of the strip, and the strip are effective on the longitudinal strains [14]. Lindgren et al. presented a full factorial-based model that the flower pattern was considered as an input factor. The results of this research show that the section web and the flower pattern significantly affect the length of deformation needed for forming at each stand. Also, the strain of the strip has shown a significant increase with increasing the strip thickness [15]. Zeng et al. investigated the U-channel section using 3D finite element analysis by ABAQUS software. In this research, a statistical relationship for roller design is presented. In this research, by using four-factor models between the flower pattern and the spring back, the number of forming stands was reduced [16]. Punin et al. investigated the reduction of the bowing defect by considering the forming stand. The distance between forming stands, the flower pattern, and the thickness have the greatest effect on the bowing defect [17]. Cha et al. investigated the effect of strains along the forming direction on the final geometry of the product. In this research, high-strength steel was selected, and by creating additional pressure on the sheet along the thickness, the effects of the bowing defect were significantly reduced [18]. Wiebenga et al. studied the bowing defect and the spring-back on a V-shaped channel, and by optimizing the inter distance, product defects were reduced [19]. Safdarian et al. investigated the impact of different factors on the bowing defect and the strains on the roll forming process. The results indicated that increase in the flower pattern and the thickness of the strip increase the strain in the forming direction [20]. Shirani et al. studied on the over-bending defects. The results showed that this defect could be decreased by decreasing the flower pattern [21]. Heydari et al. worked on accumulative roll bonding (ARB) to produce especial composites. The results indicated that mechanical properties of samples improved with increasing the temperature of ARB cycles. But in ambient temperature, ARB cycles, the sample toughness and the sample elongation decreased [22]. Heydari et al. also worked on the asymmetric roll bonding process. They used ABAQUS software to model the deformation of samples. The results showed that increasing the strain at the bimetal interface leads to improvement of the bonding quality [23]. Sattar et al. worked on a special notched U-section in the cold forming production. The results indicated that with increasing the diameter of punched holes, the buckling of the section wall increases [24].

The impact of the anisotropic properties on the bowing defect was not investigated. The costs of designing and manufacturing forming rollers for manufacturers of roll forming products show that providing accurate simulation models with the ability to estimate the final shape of the product is very important. Therefore, in this research, a finite element model considering the impact of material properties especially definition of anisotropic properties on the bowing defect of the product was investigated with 91% accuracy using a linear and non-linear numerical model along with simulation in ABAQUS software.

2 MATERIAL AND METHODS

The target product which is selected was a special basic U-section with a 45° bend angle on side walls. The schematic characteristics of the selected section are presented in “Fig. 2”.

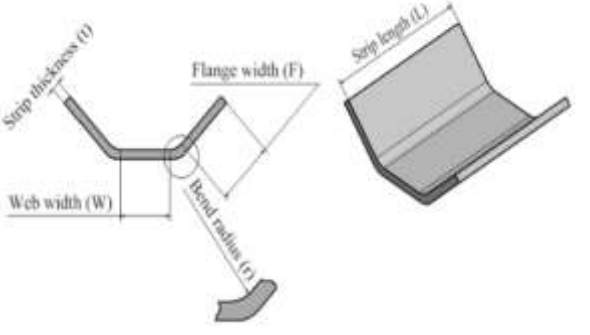

Fig. 2 Characteristics of the investigated U-channel section.

The DC03 (1.0347) steel is used for this study. This type of steel is common and widely used in the structural and construction industry. The engineering stress-strain curve of investigated steel was obtained using the procedure according to ASTM E8 standard. The result of test for DC03 steel in two different directions is presented in “Fig. 3”.

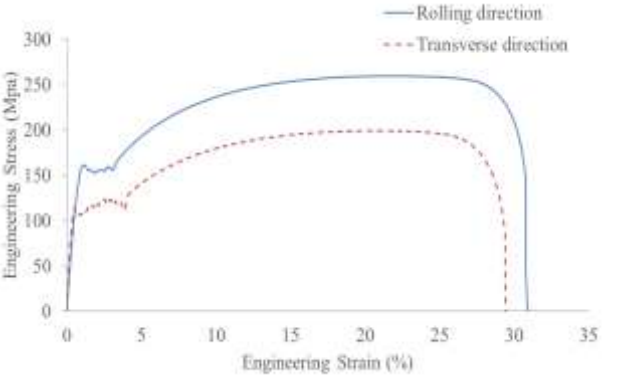

Fig. 3 The engineering stress-strain curve for 1.0347 steel

To analyses, the anisotropy, half of the samples were re-annealed to be made isotropic properties. The mechanical properties of the strips are presented in “Table 1”.

Table 1 Mechanical and mass density of the investigated material

Elastic modulus (Mpa)	207000
Poisson ratio	0.3
Elastic strain limitation	0.002
Density (Kg/m³)	7800
Elongation (%)	45
Yield (Mpa)	
Thk. =2 (mm)	213
Thk. =2.5 (mm)	210

"Table 2" shows the investigated affected values studied in this research. These values are considered with the capabilities of the roll forming apparatus used to perform practical tests.

Table 2 levels of input factors for the investigated design of experiment

Factor	Values	
Flower pattern (angle increment)	□15	□22.5
Section web(w)	40 mm	20 mm
Thickness (t)	2.5 mm	2 mm
Distance between stands(d)	500 mm	300 mm
Structure condition (H)	Re-Annealed	Anisotropic

The complete data of experiments and simulations are presented in "Table 3".

Table 3 The complete data of experiments and simulations

Test No.	Structure condition	Thickness mm	Width of section, mm	Angle increment, degree	Distance between stands, mm	Simulation bowing defect, mm	Experimental bowing defect, mm
1	Iso	2	20	22.5	500	5.62	9.37
2	Iso	2.5	40	22.5	500	7.23	10.04
3	Aniso	2.5	20	15	500	25.63	12.26
4	Aniso	2	20	15	300	7.40	7.50
5	Aniso	2	20	15	500	1.97	5.24
6	Iso	2.5	20	15	500	23.61	32.59
7	Aniso	2	20	22.5	300	8.87	20.12
8	Iso	2.5	40	15	300	24.84	22.60
9	Iso	2.5	20	15	300	4.09	7.39
10	Aniso	2	40	22.5	500	2.10	5.56
11	Iso	2	40	15	300	12.42	15.67
12	Iso	2	40	15	500	10.74	15.23
13	Aniso	2.5	40	22.5	300	12.88	13.42
14	Aniso	2.5	40	15	300	28.86	42.08
15	Aniso	2.5	20	15	300	5.53	22.30
16	Iso	2.5	40	15	500	33.14	42.65
17	Iso	2	20	15	300	10.66	19.76
18	Iso	2.5	20	22.5	500	13.82	16.80
19	Iso	2	40	22.5	300	1.89	6.89
20	Aniso	2	40	22.5	300	1.89	6.58
21	Aniso	2	20	22.5	500	4.39	8.35
22	Iso	2	20	22.5	300	10.90	16.32
23	Aniso	2.5	20	22.5	500	14.72	16.68
24	Iso	2.5	40	22.5	300	9.18	7.65
25	Iso	2	40	22.5	500	2.13	2.65
26	Iso	2	20	15	500	3.56	6.11
27	Aniso	2	40	15	300	11.34	16.55
28	Aniso	2.5	40	15	500	35.86	23.56
29	Iso	2.5	20	22.5	300	13.25	19.20
30	Aniso	2	40	15	500	11.46	12.03
31	Aniso	2.5	20	22.5	300	14.62	16.65
32	Aniso	2.5	40	22.5	500	7.29	12.68

Aniso=Anisotropic
Iso=Isotropic(Re-Annealed)

The investigated roll forming machine includes a 45-kilo-watt motor supplier with the ability to transmit power to seven forming stands. The device is equipped with a precise speed adjustment unit, precise sets of gearboxes, and set of guide rolls were also used to prevent the movement of the pre-formed strip in the side direction. Figure 4 shows the roll forming apparatus which are used for practical tests.

Fig. 4 Roll forming apparatus of the investigated machine.

The forming speed process was determined to be 22 mm/sec according to the precise control conditions of practical tests. Forming rolls are combined into two pieces. The flat disc (B) was used to perform different section webs, and the angled rolls (A) were used to perform bending angles. Figure 5 shows the assembly of the disc and the bending rolls.

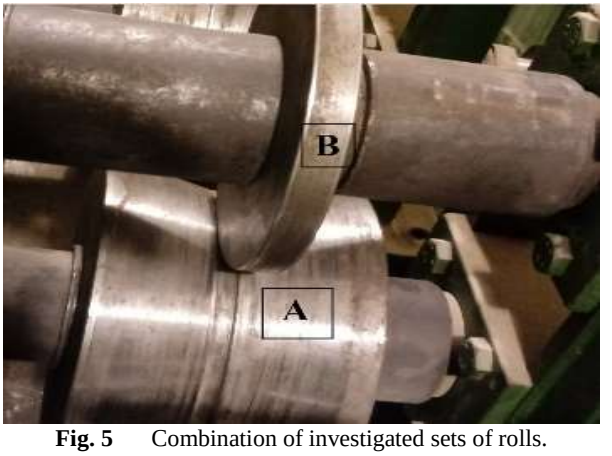

Fig. 5 Combination of investigated sets of rolls.

National Instruments Vision Software with 12-megapixel camera have been used to measure the defect of samples; In this measurement method, the difference between the end points position of the sample and the mid-position of it was measured as bowing defect according to "Fig. 6".

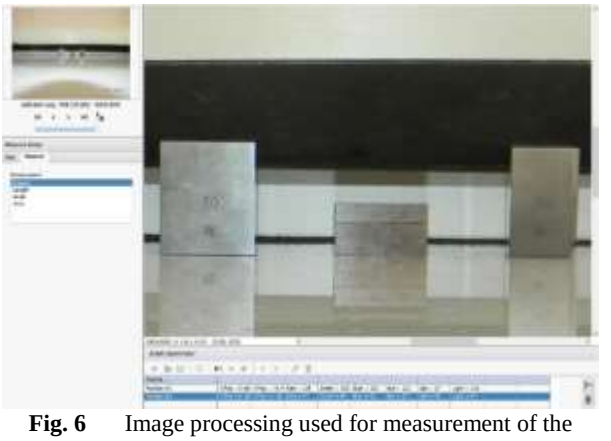

Fig. 6 Image processing used for measurement of the bowing defect.

The gauge block was used to convert the Acquisition data to dimension. To reduce the measurement error in this method, the measurements were performed in three stages for the rolled samples, and the average of the obtained measurements was considered the bowing defect.

3 PROCESS SIMULATION

The finite element simulation modelling of the roll forming was performed in ABAQUS software; the investigated model is shown in "Fig. 7".

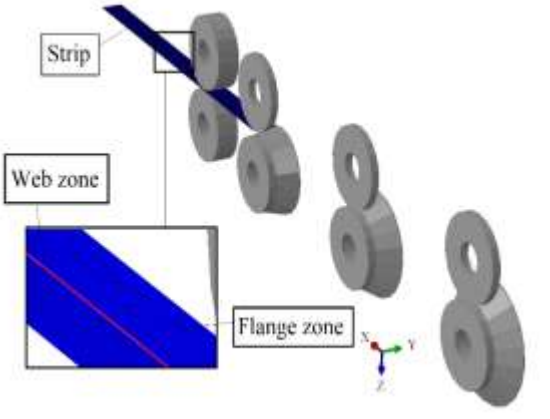

Fig. 7 Finite element model and the mesh zone detail.

The model includes the sheet strip and forming rolls with the same dimension as the rolls used in the practical tests. In the examined model, the forming rolls were defined as an analytical rigid part, and the sheet strip was designed as a shell part. To measure the longitudinal strain, a path was created on the edge and, the bottom of the samples, which is called the flange path and the web path. The distribution of the strain along the rolling direction is presented in "Fig. 8".

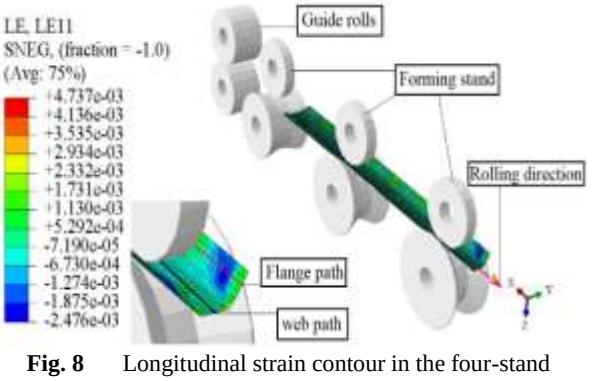

Fig. 8 Longitudinal strain contour in the four-stand forming simulation.

To obtain the optimized distribution of meshes, two different zones were defined for meshing, which is

presented in "Fig. 7". Considering that the sheet strip is defined as a shell type, S4R element used for shell type parts with five points for integration in the direction of the thickness were selected [8]. To define the friction condition between the forming rolls and the sheet strip, a penalty coefficient of 0.2 was considered. The gap size in all forming stands was considered according to the thickness of the sheet strip. To model the strip for both non-homogeneous and homogeneous states, anisotropy properties were assessed using the Hill 48 equation and calculated R-values coefficient. Since the raw material is affected by the rolling production conditions, and according to "Fig. 3", the mechanical properties of it were different in rolling and transverse directions. Hill introduced a yield criterion, which is given in "Eq. (1)" [25].

$$2f = F(\sigma_{22} - \sigma_{33})^2 + G(\sigma_{33} - \sigma_{11})^2 + H(\sigma_{11} - \sigma_{22})^2 + 2L{\sigma_{23}}^2 + 2M{\sigma_{31}}^2 + 2N{\sigma_{12}}^2 \quad (1)$$

In "Eq. (1)", f is the Hill yield function, and the material constants are defined with F, G, H, L, M, and N. Six yield strain ratios r_{11}, r_{22}, r_{33}, r_{12}, r_{13}, and r_{23} are calculated according to "Eq. (6), Eq. (7), Eq. (8), and Eq. (9)". The plane strain condition eliminated the L and M constants from "Eq. (1)" [25]. To determine the coefficients, the standard test of the samples was performed according to ASTM E8. According to this standard, the measurements of the strain ratio in three rolling, transverse, and thickness directions were performed using special strain gauges; the coefficients were calculated according to "Eq. (2) to Eq. (9)". The obtained plastic strains ratio (r_{xy}) or Lankford coefficients from the specified test are shown in "Table 4". In "Table 4", the number 1 is rolling direction and 2 is transverse direction and 3 is thickness direction.

$$F = \frac{1}{2}\left(\frac{1}{{r_{22}}^2} + \frac{1}{{r_{33}}^2} - \frac{1}{{r_{11}}^2}\right) \quad (2)$$

$$G = \frac{1}{2}\left(\frac{1}{{r_{33}}^2} + \frac{1}{{r_{11}}^2} - \frac{1}{{r_{22}}^2}\right) \quad (3)$$

$$H = \frac{1}{2}\left(\frac{1}{{r_{11}}^2} + \frac{1}{{r_{22}}^2} - \frac{1}{{r_{33}}^2}\right) \quad (4)$$

$$N = \frac{3}{2r_{12}^2} \quad (5)$$

$$r_{11} = r_{13} = r_{23} = 1 \quad (6)$$

$$r_{22} = \sqrt{\frac{r_{90}(r_0+1)}{r_0(r_{90}+1)}} \quad (7)$$

$$r_{33} = \sqrt{\frac{r_{90}(r_0+1)}{(r_{90}+r_0)}} \quad (8)$$

$$r_{12} = \sqrt{\frac{3r_{90}(r_0+1)}{(2r_{45}+1)(r_{90}+r_0)}} \quad (9)$$

Table 3 Calculated R-values of the investigated material

Test No.	r_{22}	r_{33}	r_{12}
1	1.026	1.293	5.112
2	1.018	1.25	5.23
3	1.015	1.307	5.025
r_{11}, r_{13}, r_{23}	1		

4 RESULTS

Investigation of different input factors on the bowing defects was done using design expert software. The analytical model was obtained from the full-factorial design of experiment. Examination and analysis of the simulation results and experiments illustrated the robustness of the analysis and results. "Table 5" shows the complete data of variance analysis of the investigated model.

Table 4 Variance analysis of complete data for modified two-factor model

Factor	Sum of squares	DOF	Mean square	F-value	P-value
Model	2359.2	11	214.5	13.8	< 0.0001
A-Structure condition	1.86	1	1.86	0.12	0.7327
B-Thickness	873.66	1	873.7	56.3	< 0.0001
C-Section web	62.16	1	62.16	4.01	0.059
D-Flower pattern	452.31	1	452.3	29.2	< 0.0001
E-Distance between stands	18.98	1	18.98	1.22	0.2818
AB	19.08	1	19.08	1.23	0.2805
BC	58.94	1	58.94	3.8	0.0654
BD	100.78	1	100.8	6.5	0.0191
BE	159.47	1	159.5	10.3	0.0044
CD	510.48	1	510.5	32.9	< 0.0001
DE	101.49	1	101.5	6.54	0.0188
Residual	310.21	20	15.51	-	-
Cor total	2669.4	31	-	-	-

Based on this analysis, if the F-value of variance analysis is large and the root-mean-square is close enough to 1, the model's accuracy can be assured. Considering the F-value and R-square of linear, two-factor, and three-factor fitted models are presented in "Fig. 9", according to F-value of 13.83 and R-square of 0.91, the modified two-factor model is accurate enough for prediction of bowing defect. If P<0.05 for the factors examined in this model, it indicates the effect of that factor on the bowing defect [24]. Figure 9 shows the comparison between F-value and R-square in different states, including linear, two-factor, and three-factor models. Figure 10 illustrates the actual vs. predicted values of the analytical bowing defect model. The density of the data around the central line, and the obtained R-square, proves the correctness of the modified two-factor model.

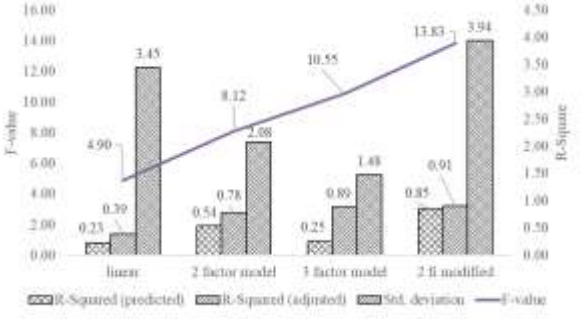

Fig. 9 R-square and F-value for investigated models.

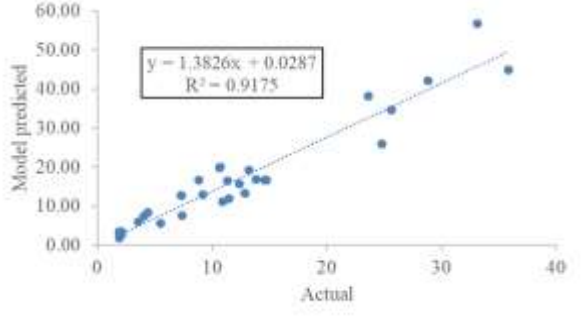

Fig. 10 Comparing actual and model predictions of the bowing defect.

According to the results of the model, it can be seen that the bowing defect is increased with increases in the thickness. According to "Eq. (10)", increasing the thickness reduces the length of the deformation when the strips enter the forming stand, and according to "Eq. (11)", it increases the longitudinal strain [26].

$$L = \sqrt{\frac{8a^3\theta}{3t}} \tag{10}$$

$$\varepsilon = \sqrt{1 + 2\left(\frac{a}{L}\right)^2 (1 - cos\,\theta)} - 1 \tag{11}$$

All the parameters used in "Eq. (10) and Eq. (11)" are shown in "Fig. 11". Considering the fix value for the angle at each stand (θ) and the wall length of section (a), the length for the roll forming process at each stand (L) is decreased with increasing the thickness.

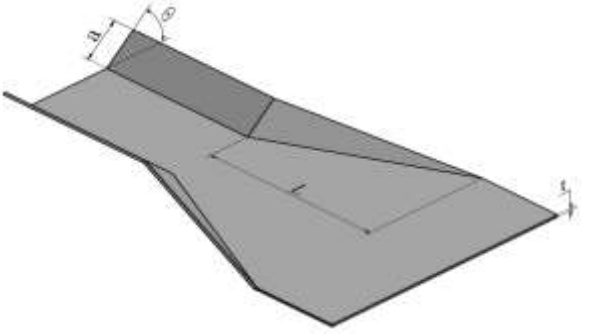

Fig. 11 Significant parameters of forming process.

The effect of the thickness on the bowing defect both in the experimental and the simulation is presented in "Fig. 12". As it is shown in "Fig. 12" with increasing the thickness the bowing defect is increased.

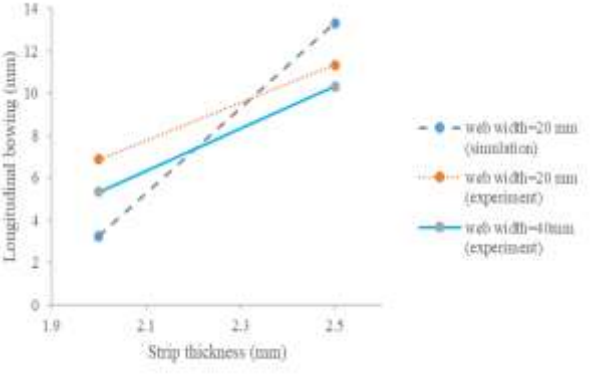

Fig. 12 Effect of the thickness on the bowing defect in experiment and simulation.

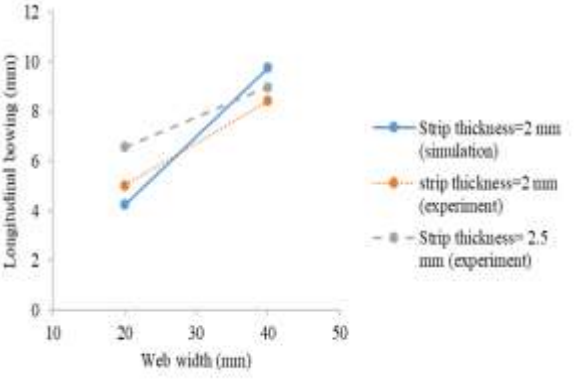

Fig. 13 Effect of section web on the bowing defect in experiment and simulation.

The effect of the section web on the bowing defect is presented in "Fig. 13". Accordingly, expanding the section web increases the bowing defect. Increasing the section web reduces the bending resistance during bending, and then increases the bowing defect of the product. In addition, with considering to "Eq. (10)", expanding the wall length of section (a) increases the strip length that enter the stands [27]. The effect of the stand longitudinal distance on the bowing defect is shown in "Fig. 14". As it is shown, with increasing the stand longitudinal distance, the bowing defect of the sample is decreased. Also, according to "Fig. 15", with decreasing the flower pattern, the bowing defect can be decreased. It can be resulted that reducing the flower pattern minimizes the strains difference between the section wall and the section web, so the bowing defect is reduced [26].

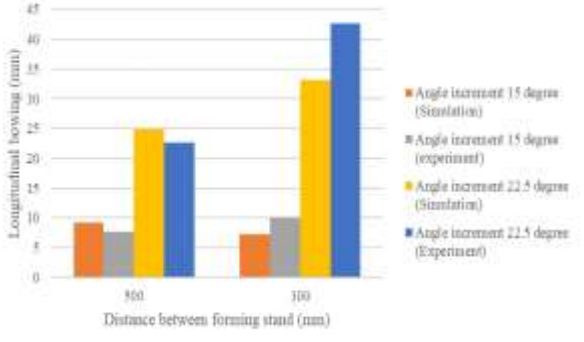

Fig. 14 Effect of the stand longitudinal distance on the bowing defect in experiment and simulation.

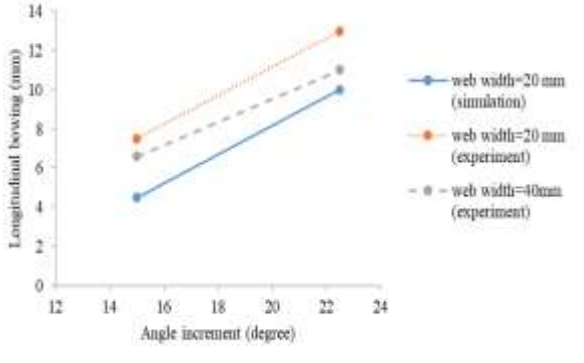

Fig. 15 Effect of the angle incrementation on the bowing defect in experiment and simulation.

As shown in "Fig. 14 and Fig. 15", the bowing defect was decreased with reducing the flower pattern increment. Also, with reduction of the section web dimension, the bowing defect decreases more. According to "Fig. 16", both the results of experiments and the results of simulations show the insignificant impact of the structure condition on the bowing defect, but anisotropic or isotropic properties have a significant impact on the consequences of finite elements results, and the accuracy of the model has increased from 84% to 91%.

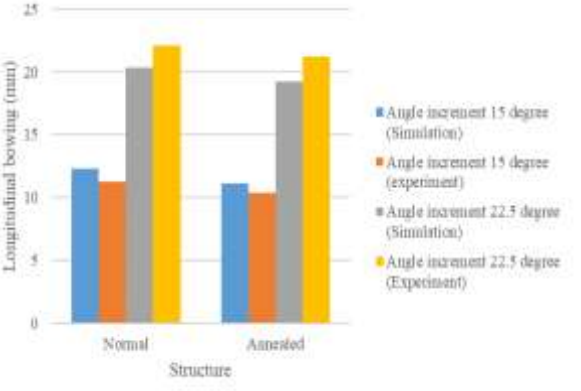

Fig. 16 Effect of structure on the bowing defect.

This result proves that the coefficient of anisotropic properties should be considered in definition of strip material properties for the simulation model. The comparison of the simulation results vs. practical tests is presented in "Fig. 17".

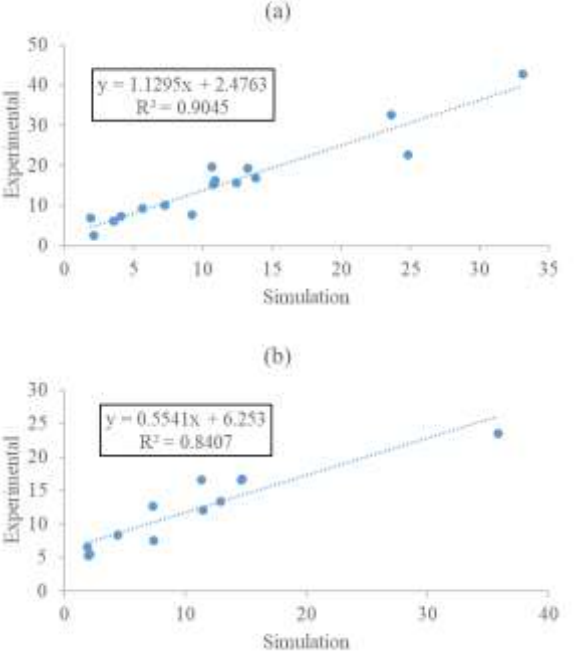

Fig. 17 Simulation vs. experimental values of bowing defect: (a): with anisotropy consideration, and (b): Without anisotropy consideration.

The analytical models, based on both experimental results and the simulation data, were presented in "Fig. 9". Also, the modified two-level of influential factors are analyzed. By checking the R-square value obtained from the analytical model (91%), the accuracy of the model could be confirmed. P-value, which was mentioned

before, shows the impact of the investigated factor on the bowing defect. The low value of this coefficient expresses the intensity of the parameter on the bowing defect. Equation (12) shows the analytical model where A is the structure condition, B is the thickness, C is the width of the section, D is the flower pattern, and E is the distance between stands.

$$Bowing = 11.93 + 0.24A + 5.23B + 1.39C - 3.76D + 0.77E + 0.77AB + 1.36BC + 1.77BD + 2.23BE - 3.99CD - 1.78DE \quad (12)$$

The accuracy of the modified two-factor analytical model values is presented in "Table 6". The coefficient of variation is calculated from "Eq. (13)" [27]. In "Eq. (13)", S_{dev} is standard deviation and M is the mean values, which are calculated from the selected model according to "Table 6".

$$Coefficient\ of\ variation(\%) = \frac{S_{dev}}{M} \times 100 \quad (13)$$

Table 5 Accuracy of the selected analytical model on the bowing defect

Model	R^2 adjusted	Standard deviation	Mean	C.V. %
Modified Two factors	0.91	3.94	11.93	33

Figure 18 shows the Pareto chart of the investigated factors on the bowing defect. The strip thickness has the most remarkable effect and anisotropy properties has the most minor impact on the bowing defect. Also, the flower pattern effect on the bowing defect is significant.

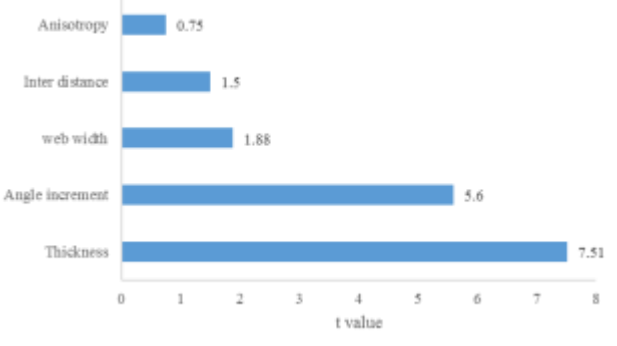

Fig. 18 The impact severity of the investigated parameters on the bowing defect.

5 CONCLUSION

The results of the current research show the effects of the parameters listed in "Table 2" on the bowing defect as follows:

- The thickness of the strip is the most influential factor in the bowing defect of symmetrical U-shaped channels. The bowing defect is directly related to sheet thickness. In other words, with the constant value of the flower pattern and the section web, increasing the thickness reduces the required strip length at each stand of the forming process, followed by an increase in bowing defect.
- The flower pattern influences the bowing defect as a second influential factor. Reducing the angle increment change in each stand reduces the bowing defect. It should be noted that the reduction of angle increment in each stand means an increase in the number of forming stands, which can lead to an increase in the cost of making rollers to create more stands, which makes choosing the optimal value for the flower pattern very essential. The optimal value is considered 15-degree incrementation.
- The section web is another significant parameter in the bowing defect of symmetrical U-shaped channels. By reducing the cross-section web, the difference in generated strain between the section wall and the web area is reduced, and reduces the bowing defect. The distance between stands does not have significant impact on the bowing defect of symmetrical U-shaped channels.
- Plastic anisotropy has a significant impact on the results of finite element simulation, and the accuracy of the simulation has increased from 84% to 91%.
- The analytical models, based on both experimental results and the simulation data, showed that the modified two-level model has the reasonable R-square value (91%) and the accuracy of the model could be confirmed.

REFERENCES

[1]Halmos, G. T., Roll Forming Handbook, 2005. DOI: 10.1201/9781420030693.

[2]Shirani Bidabadi, B., Moslemi Naeini, H., Azizi Tafti, R., and Barghikar, H., Experimental Study of Bowing Defects in Pre-Notched Channel Section Products in The Cold Roll Forming Processint, J. Adv. Manuf. Technol., Vol. 87, No. 1–4, 2016, pp. 997–1011, DOI: 10.1007/s00170-016-8547-y.

[3]Ona, H., Experiments into the Cold Roll Forming of Straight Asymmetrical Channels, J. Mech. Work. Technol., Vol. 8, No. 83, 1983, pp. 273–291.

[4]Bhattacharyya, D., Smith, P. D., Thadakamalla, S. K., and Collins, I. F., The Prediction of Roll Load in Cold Roll-Forming, J. Mech. Work. Technol., Vol. 14, No. 3, 1987, pp. 363–379, DOI: 10.1016/0378-3804(87)90019-2.

[5]Bhattacharyya, D., Smith, P. D., The Development of Longitudinal Strain in Cold Roll Forming and Its Influence

on Product Straightness, leAdv. Technol. Plast., Vol. 1, 1984, pp. 422–427.

[6]Panton, S., Duncan, J., and Zhu, S., Longitudinal and Shear Strain Development in Cold Roll Forming, J. Mater. Process. Technol., Vol. 60, 1996, pp. 219–224, DOI: 10.1016/0924-0136(96)02333-3.

[7]Sheu, J. J., Simulation and Optimization of The Cold Roll-Forming Process AIP Conf. Proc., Vol. 1, 2004, pp. 452–457, DOI: 10.1063/1.1766566.

[8]Tehrani, M. S., Hartley, P., Naeini, H. M., and Khademizadeh, H., Localised Edge Buckling in Cold Roll-Forming of Symmetric Channel Section Thin-Walled Struct., Vol. 44, No. 2, 2006, pp. 184–196, DOI: 10.1016/j.tws.2006.01.008.

[9]Shirani Bidabadi, B., Moslemi Naeini, H., Azizi Tafti, R., and Mazdak, S., Experimental Investigation of The Ovality of Holes on Pre-Notched Channel Products in The Cold Roll Forming Process, J. Mater. Process. Technol., Vol. 225, 2015, pp. 213–220, DOI: 10.1016/j.jmatprotec.2015.06.008.

[10] Shirani Bidabadi, B., Moslemi Naeini, H., Salmani Tehrani, M., and Barghikar, H., Experimental and Numerical Study of Bowing Defects in Cold Roll-Formed, U-Channel Sections, J. Constr. Steel Res., Vol. 118, 2016, pp. 243–253, DOI: 10.1016/j.jcsr.2015.11.007.

[11] Shirani Bidabadi, B., Moslemi Naeini, H., Azizi Tafti, R., and Tajik, Y., Optimization of Required Torque and Energy Consumption in The Roll Forming Process, Int. J. Interact. Des. Manuf., Vol. 13, No. 3, 2019, pp. 1029–1048, DOI: 10.1007/s12008-019-00564-9.

[12] Lindgren, M., Cold Roll Forming of a U-Channel Made of High Strength Steel, J. Mater. Process. Technol., Vol. 186, No. 1–3, 2007, pp. 77–81, DOI: 10.1016/j.jmatprotec.2006.12.017.

[13] Poursina, M., Salmani Tehrani, M., and Poursina, D., Application of BPANN and Regression for Prediction of Bowing Defect in Roll-Forming of Symmetric Channel Section, Int. J. Mater. Form., Vol. 1, No. 1, 2008, pp. 17–20, DOI: 10.1007/s12289-008-0057-5.

[14] Bui, Q. V., Ponthot, J. P., Numerical Simulation of Cold Roll-Forming Processes, J. Mater. Process. Technol., Vol. 202, No. 1–3, 2008, pp. 275–282, DOI: 10.1016/j.jmatprotec.2007.08.073.

[15] Lindgren, M., An Improved Model for The Longitudinal Peak Strain in The Flange of a Roll Formed U-Channel Developed by FE-Analyses Steel Res. Int., Vol. 78, No. 1, 2007, pp. 82–87, DOI: 10.1002/srin.200705863.

[16] Wei Zhang, H., Zhong Liu, L., Hu, P., and Hua Liu, X., Numerical Simulation and Experimental Investigation of Springback in U-Channel Forming of Tailor Rolled Blank, J. Iron Steel Res. Int., Vol. 19, No. 9, 2012, pp. 8–12, DOI: 10.1016/S1006-706X(13)60002-3.

[17] Punin, V. I., Kokhan, L. S., and Morozov, Y. A., Reduction of the Length of Strip Rolled on Roll-Forming Machines Metallurgist, Vol. 56, No. 11–12, 2013, pp. 938–940, DOI: 10.1007/s11015-013-9678-0.

[18] Gi Cha, W., Kim, N., Study on Twisting and Bowing of Roll Formed Products Made of High Strength Steel, Int. J. Precis. Eng. Manuf., Vol. 14, No. 9, 2013, pp. 1527–1533, DOI: 10.1007/s12541-013-0206-8.

[19] Wiebenga, J. H., Weiss, M., Rolfe, B., and Van Den Boogaard, A. H., Product Defect Compensation by Robust Optimization of a Cold Roll Forming Process, J. Mater. Process. Technol., Vol. 213, No. 6, 2013, pp. 978–986, DOI: 10.1016/j.jmatprotec.2013.01.006.

[20] Safdarian, R., Moslemi Naeini, H.,The Effects of Forming Parameters on The Cold Roll Forming of Channel Section Thin-Walled Struct., Vol. 92, 2015, pp. 130–136, DOI: 10.1016/j.tws.2015.03.002.

[21] Shirani Bidabadi, B., Moslemi Naeini, H., Safdarian, R., and Barghikar, H., Investigation of Over-Bending Defect in The Cold Roll Forming of U-Channel Section Using Experimental and Numerical Methods, Proc. Inst. Mech. Eng. Part B J. Eng. Manuf., Vol. 236, No. 10, 2022, pp. 1380–1392, DOI: 10.1177/09544054221076628.

[22] Heydari Vini, M., Farhadipour, P., Fabrication of AA1060/Al2O3 Composites by Warm Accumulative Roll Bonding Process and Investigation of its Mechanical Properties and Microstructural Evolution ADMT J., Vol. 10, No. 4, 2017, pp. 91–98, [Online] Available: https://admt.majlesi.iau.ir/article_537192.html.

[23] Heydari, V. M., Saeed, D., Bonding Evolution of Bimetallic Al/Cu Laminates Fabricated by Asymmetric Roll Bonding, Adv. Mater. Res., Vol. 8, No. 1, 2019, pp. 1–10, DOI: 10.12989/AMR.2019.8.1.001.

[24] Sattar, S., Mazdak, S., and Sharifi, E., Numerical Analysis of Circular Pre-notched U-Channel Section Distortions in Cold Roll-Forming ProcessADMT J., Vol. 10, No. 2, 2017, pp. 121–131, [Online] Available: https://admt.majlesi.iau.ir/article_535020.html.

[25] Hill, R., Orowan, E., A Theory of the Yielding and Plastic Flow of Anisotropic Metals, Proc. R. Soc. London. Ser. A. Math. Phys. Sci., Vol. 193, No. 1033, 1948, pp. 281–297, DOI: 10.1098/rspa.1948.0045.

[26] Han, Z. W., Liu, C., Lu, W. P., and Ren, L. Q., Simulation of a Multi-Stand Roll-Forming Process for Thick Channel Section, J. Mater. Process. Technol., Vol. 127, No. 3, 2002, pp. 382–387, DOI: 10.1016/S0924-0136(02)00411-9.

[27] Mander, S. J., Panton, S. M., Dykes, R. J., and Bhattacharyya, D., Chapter 12 Roll Forming of Sheet Materials, in Composite Sheet Forming, Vol. 11, D. B. T. C. M. S. Bhattacharyya, Ed. Elsevier, 1997, pp. 473–515, DOI: https://doi.org/10.1016/S0927-0108(97)80014-8.

Int. J. Advanced Design and Manufacturing Technology, 2022, Vol. 15, No. 4, pp. 71-83

DOI: 10.30486/admt.2023.1960198.1354 *ISSN: 2252-0406* *https://admt.isfahan.iau.ir*

Experimental Investigation and Modeling of Bubble Departure Frequency for Nucleate Pool Boiling Heat Transfer of Pure Liquids on Flat Heater

Samane Hamzekhani, Farhad Shahraki*, Davood Mohebbi-kalhori
Department of Chemical Engineering,
University of Sistan and Baluchestan, P.O. Box 98164-161, Zahedan, Iran
E-mail: s.hamzehkhani@pgs.usb.ac.ir, fshahraki@eng.usb.ac.ir, davoodmk@eng.usb.ac.ir
*Corresponding author

Mohammad Reza Fardinpour
Department of Chemical Engineering,
Mahshahr Branch, Islamic Azad University, Mahshahr, Iran
E-mail: Fardinpour.mohamad@gmail.com

Received: 2 June 2022, Revised: 31 August 2022, Accepted: 17 September 2022

Abstract: In the present study, the response surface methodology is used to predict the bubble departure frequency of pure liquids using experimental data. Water, ethanol and methanol pure liquids were used as the testing fluid. The effects of vapor and liquid density difference, vapor and liquid viscosity, surface tension, thermal conductivity, heat flux on the vapor bubbles departure frequency on the heat transfer of boiling pool of pure liquids were investigated by response surface methodology. The results showed that the output of the Response surface methodology had a good overlap with the data of bubbles departure frequency of pure liquids. Also, the results for the bubble departure frequency show a good overlap between the models presented by the researchers and the experimental data and have good accuracy. In this research, a new model for the prediction of vapor bubble departure frequency, based on the Buckingham theory, in nucleate boiling is proposed, which predicts the experimental data with a satisfactory accuracy (9%).

Keywords: Bubbles Departure Frequency, Pool Boiling, Pure Liquid, Response Surface Methodology

Biographical notes: Samane Hamzekhani is currently a PhD candidate at Sisatan and Bluchestan University of Zahedan, Iran. He received his MSc in Chemical Engineering from Mahshar branch, IAU in 2014. **Farhad Shahraki** is currently a Professor at the Department of Chemical Engineering, Sistan and Baluchestan University. His current research interest includes simulation and Optimization. He received his PhD in Chemical Engineering from England University of Manchester in 2001. **Davood Mohebbi-kalhori** is currently an Assistant Professor at the Department of Chemical Engineering, Sistan snd Bluchestan University. He received his PhD in Chemical Engineering from Canada University of Sherbooke in 2008. **Mohammad Reza Fardinpour** received his MSc in Chemical Engineering from Mahshar Branch, IAU, Mahshar, Iran in 2013.

Research paper

1 INTRODUCTION

Evaporation at the solid-liquid phase interface is called boiling. The use of boiling phenomenon has been a topic that has been considered by researchers in this field for many years to increase the heat transfer coefficient and several studies have been conducted by researchers [1-10]. This process is one of the most widely used processes used in the industries such as oil, petrochemical, internal combustion engines and refrigerators due to its high heat transfer coefficient.

Bubble dynamics play a key role in the development of any analytical model for predicting heat transfer coefficient of pool boiling. Bubble dynamic parameters such as bubble departure frequency, bubble departure diameter and nucleation site density as well as the behavior of bubbles in the growth cycle and their departure from the surface are the basic mechanisms in modeling the boiling heat transfer process. One of the key and influential parameters on bubble dynamics is the frequency of bubble departure from the surface. The relations between f and D_b for an isolated bubble region in nucleate boiling are reported by Peebles and Garber [11], Cole [12] and others.

They [11] proposed the relation as:

$$f * D_b = 1.8 * \left(\frac{t_G}{t_G + t_W} \right) * \left(\frac{\delta g \Delta \rho}{\rho_L^2} \right)^{0.25} \quad (1)$$

Assuming the hydrodynamic region and the balance between drag and buoyancy forces, Cole [12] has proposed the following Equation.

$$f = \sqrt[2]{\frac{4g(\rho_L - \rho_v)}{(3D_b \rho_L)}} \quad (2)$$

McFadden et al. [13] proposed the following Equation through dimensional analysis and available data.

$$f D_b^{0.5} = 17.5 \frac{cm^{0.5}}{s} \quad (3)$$

Zuber [14] has presented the following Equation by examining the available relationships and experimental data and according to the observations of Jacob et al.

$$D_b f = \frac{1.18}{2} \left[\frac{\delta g (\rho_{L-} \rho_v)}{\rho_L^2} \right]^{\frac{1}{4}} \quad (4)$$

Many correlations have been developed for the prediction of the bubble departure frequency for the nucleate pool boiling condition for different applications; the most important ones are summarized in "Table 1".

In this study, experiments related to the vapor bubble departure frequency on the flat surface for pool boiling of water, ethanol and methanol have been performed. Predicting bubble frequency from the proposed valid models requires calculation of parameters such as bubble diameter, bubble growth time and waiting time, which have their own complexities and limitations. The novelty of this paper is the use of response surface methodology to predict the bubble departure frequency based on heat flux and physical properties and the results of experiments performed in this study and data from the proposed models.

Table 1 Correlations suggested for the prediction of bubble departure frequency

Reference	Correlation
Peebles and Garber [11]	$f * D_b = 1.8 * \left(\frac{t_G}{t_G + t_W} \right) * \left(\frac{\delta g \Delta \rho}{\rho_L^2} \right)^{0.25}$
Cole [12]	$f = \sqrt[2]{\frac{4g(\rho_L - \rho_v)}{(3D_b \rho_L)}}$
McFadden [13]	$f D_b^{0.5} = 17.5 \frac{cm^{0.5}}{s}$
Zuber [14]	$D_b f = \frac{1.18}{2} \left[\frac{\delta g (\rho_{L-} \rho_v)}{\rho_L^2} \right]^{\frac{1}{4}}$
Ivey [15]	(a) $\frac{f * D_b^{0.5}}{g^{0.5}} = 0.9$ (b) $\frac{f * D_b^{0.75}}{g^{0.5}} = 0.44(cm^{0.25})$
Stephen [16]	$f * D_b = \frac{1}{\pi} \left[\frac{g}{2} (D_b + \frac{4\delta}{\rho_L g D_b}) \right]^{0.5}$
Jacob and Fritz [17] Hamzekhani [18]	$f * D_b = 0.078$ $\frac{(f)_{solution}}{(f)_{water}} = 0.004(q)^{0.4527 - 0.4453x}$ $x \neq 0$

2 LABORATORY MACHINE AND TEST METHOD

2 .1. Heating Surface

Boiling tests were performed on flat surfaces made of stainless steel with a diameter of 20 mm and a length of 150 mm with a roughness of 0.09 μm by surface roughness tester model TR100/110.

2.2. Laboratory Machine

Figure 1 demonstrates the experimental setup of pool boiling used in this study with all the specifications. The main components of the device include: experiment container, main heater, auxiliary heater, power supply,

and condenser and measuring equipment (temperature, pressure, ampere (current) and voltage).

Fig. 1 Scheme of pool boiling laboratory machine.

The test container is made of stainless steel 304, a cubic shape with inner dimensions of 20 cm * 15 cm * 20 cm. To observe the boiling process, a window with dimensions of 6 * 6/5 cm is embedded in the body of the container. All connections of the test container and windows have been leaked. The main stainless-steel heater is cylindrical and has 6 holes with a diameter of 1 mm to measure surface temperature. Type k thermocouples (with accuracy ±0.1k) were used to measure the surface temperature. To apply heat power to the heat transfer surface, a heater cartridge with 1cm diameter and 10cm length with power of 650 w is placed in the centre of the main heater. Cylindrical PTFE insulation with internal diameter of 20 mm and external diameter of 70 mm was utilized to prevent wasting heat. Two Viton O-Rings with diameter of 20 and 65 mm with a temperature of 300 ° C were used to leak the space between the test and the insulation container as well as the heater and insulation surface. To measure the liquid bulk temperature, two PT100 thermocouples are installed at two different locations and also to ensure the boiling fluid temperature, a thermocouple is installed on the upper part of the container (vapour phase). A condenser consisting of a spiral tube made of copper was used to condense the vapours. A barometer and a safety valve are installed to control the pressure in the body of the container. To adjust the voltage and reach the considered power at each stage of the experiment, a power supply of 300 watts made in Emersun was used. For imaging, a camera with a quality of 1200 frames per second with a shutter speed of 60 frames per second via a high magnification power is employed to calculate the bubble dynamic.

2.3. Experimental Method

Before each experiment, the test container is washed, dried, and leaked. Experiments were performed using deionized water under saturated conditions at 98 kPa. Experiments were repeated in two steps to make sure that precise outcomes have been obtained. After loading the tank with the experiment fluid, the auxiliary heater inside the chamber is switched on to bring the set to the saturation mode and after reaching the corresponding temperature, the main heater enters the circuit. Also, if needed to maintain fluid saturation, the auxiliary heater remains in the circuit especially at low fluxes (the input voltage to the auxiliary heater can be controlled). In this study, the criterion for maintaining saturation conditions is to compare the bulk temperature with the fluid saturation temperature at the experiment pressure. After reaching the saturated fluid condition, first the voltage of the power supply of heater is set to the highest voltage considered and after obtaining stable conditions, the relevant data is recorded. In this study, after reaching the stainless-steel cylinder temperature changes of 0.1 ° C and stability of these conditions for 3 minutes, the relevant data were recorded. To reach the next points of experiment, the heater voltage is reduced by step of 10 volts. This reduction has continued until the end of the bubble removal process. All the above steps for ethanol and methanol have been repeated after performing the tests for pure water, and all data were recorded and analysed.

3 CALCULATIONS AND ACCURACY

3.1. Calculation

Heat transfer coefficient of pool boiling can be calculated based on Newton's cooling Equation (Equation (11)).

$$h = \frac{q}{T_w - T_b} \tag{11}$$

In Equation (11), Tw is the surface temperature, Tb is the mass temperature and q is the heat flux applied to the liquid from the heater surface that from Equation (12) (assumption of linearity of distribution of temperature) and Equation (13) (Joule's the first law) can be calculated.

$$q = -k \left.\frac{dT}{dz}\right|_{surface} = -k \frac{Ti - T1}{\Delta Taxial} \tag{12}$$

$$q = \frac{V.I}{\pi.R^2} \tag{13}$$

In Equations (12) and (13), Z is the axial direction, I is the current intensity, V is the voltage and R is the radius of the heat transfer surface. According to the insulation around the heater by PTFE, it is assumed that the supposition of governing one-dimensional conductivity heat transfer mechanism in central direction is acceptable for this research. The analogy between the heat flux calculated from Equation (12) and (13) based on "Fig. 2" confirms this hypothesis and the absence of heat loss in radial direction.

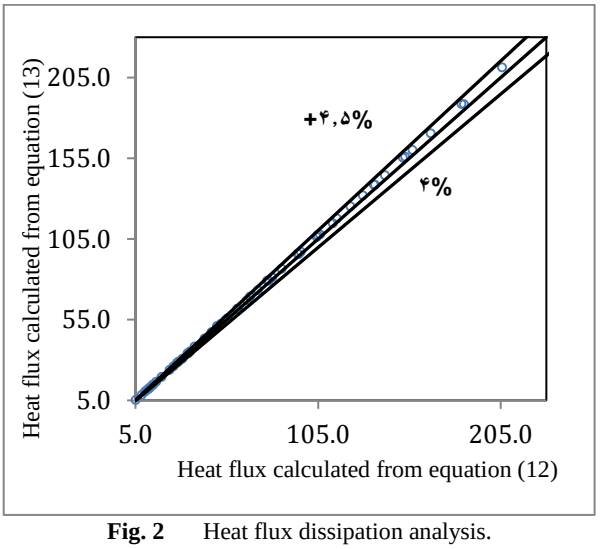

Fig. 2 Heat flux dissipation analysis.

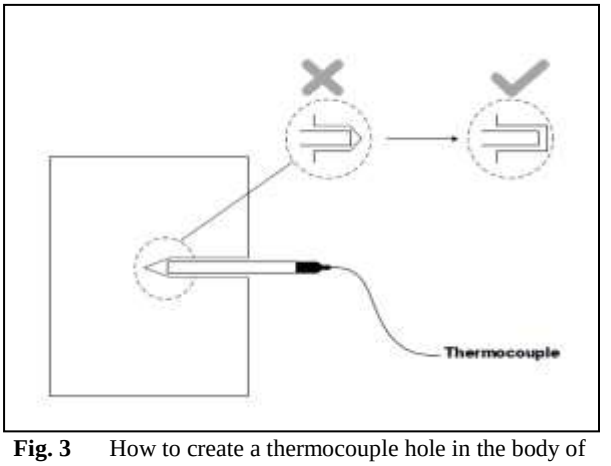

Fig. 3 How to create a thermocouple hole in the body of the main heater.

As it is shown in "Fig. 2", this difference is less than 4.5%. Two k-type thermocouples were installed at r = +0.5, r = -0.5 to measure the temperature distribution and ensure radial heat transfer. The results showed that the temperature at these two points is the same at each heat flux. Therefore, radial heat transfer can be neglected [19]. However, in this study, the heat loss rate has been considered for heat flux calculations. Also, based on the temperatures measured by the thermocouples, different graphs were obtained at each heat flux with high accuracy (R = 0.99) ("Fig. 3"). The diagrams confirm linearity of distributing temperature in central direction (z). Therefore, for calculating T_w, Equation (15) can be used [20].

$$T = \alpha + \beta Z \tag{14}$$

Since at $z = 0, T = T_W$

Thus, we have:

$$T_W = \alpha \tag{15}$$

3.2. Accuracy

In this research, the following cases are considered in the design of the device and the experiment method to prevent error in the measurement of the parameters.

1- Using silicon paste with high thermal conductivity in the hole related to the thermocouples as well as between the main heater and the cartridge heater supplying heat power to remove the air layer and contact resistance

2-The flat end of the holes related the thermocouples in the main heater body using a lathe to remove the spatial layer ("Fig. 4").

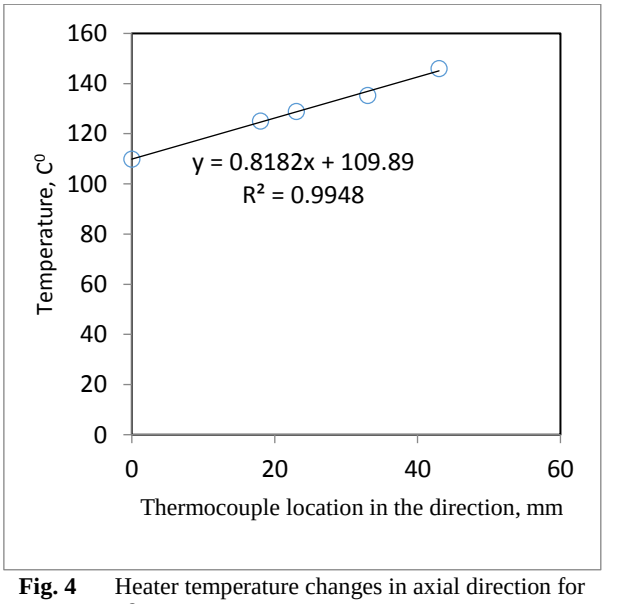

Fig. 4 Heater temperature changes in axial direction for 211 kW/m^2 heat flux and extraction of linear temperature relationship to determine surface temperature (for 211 KW/m^2 thermal fluid T_w = a = 109.89 in Equation 14).

3- Before each test step to remove air bubbles, the fluid heating process is performed at a point close to the saturation temperature.

4- The area around the test vessel is also completely insulated by fiberglass so that the temperature of the boiling fluid does not drop rapidly from saturation.

5- PTFE Teflon thermal insulation has been used to prevent heat loss of the original heater.
6- In this survey, Equation (16) is used to calculate the error of the calculated parameters.

$$v_p = \sqrt{\sum_{i=t}^{n}\left(\frac{\partial p}{\partial a_i}Ua_i\right)^2} \quad (16)$$

Where, P is the parameter considered, a is the measured parameter and U is the error related to the measured parameter. In this study, the maximum error measured for heat flux and heat transfer coefficient is 3.5% and 4.2%, respectively. "Table 2" shows the error values of the equipment used.

Table2 Error of calculated parameters and used equipment.

Parameter	Instrument	Uncertainty
Dimension	Coliseum	0.127%
Temperature	K-Tp	0.1K
Ampere	Keithley digital multi-meter	1%
Voltage	Keithley digital multi-meter	0.1V
Bulk temperature	Pt100	0.1K
Heat transfer surface area		0. 2538%
Heat flux		1.43-1.01%
Heat transfer coefficient		2.34-1.49%

4 RESULTS AND DISCUSSIONS

4.1. Validation of the Experimental Setup

In order to evaluate the accuracy of the laboratory device, the pure water data with the valid models provided by the researchers were evaluated. The results along with the heat transfer coefficient calculated from Gorenflo's [21], Alavi Fazel's [22], Stephan-Abdolsalam' s [16] and Rohsenow' s [23] have been shown in "Fig. 5".
Figure 5 shows a good overlap between the experimental data and the predicted values of the Equations with a mean absolute error of about 11% for Gorenflo's correlation 13% for Alavi Fazel's correlation, 2% for Stephan-abdelsalam's correlation and 9% for Rohsenow's correlation.

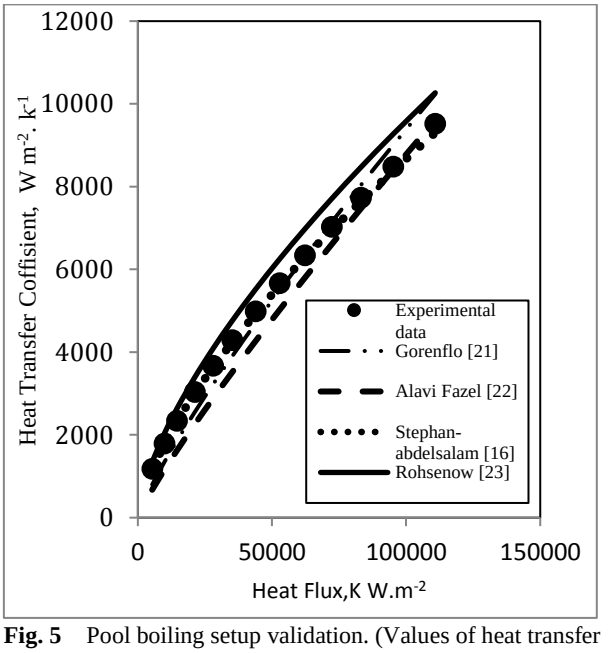

Fig. 5 Pool boiling setup validation. (Values of heat transfer coefficient with changes in heat flux).

5 BUBBLE DYNAMIC

After performing experiments and recording data and images related to the behavior of vapor bubbles in different heat fluxes for water, ethanol and methanol, the image data were analyzed by Edius software. At each heat flux, three 3-minute films have been recorded in stable conditions. The vapor bubble departure frequency is calculated for 10 to 30 nucleation sited and the average values obtained have been recorded as the bubble departure frequency for the test fluid at the corresponding heat flux. Figure 6 shows the bubble frequency changes for water, ethanol, and methanol with heat flux. As shown in "Fig. 6", the frequency of vapor bubbles has increased with increasing heat flux. Reducing the waiting time of bubbles and increasing the growth rate of vapor bubbles and reducing the growth time of bubbles by increasing the heat flux are the causes of this phenomenon (Equation (17)).

$$f = \frac{1}{t_w + t_G} \quad (17)$$

Where, t_w and t_G are waiting time and growth time, respectively.

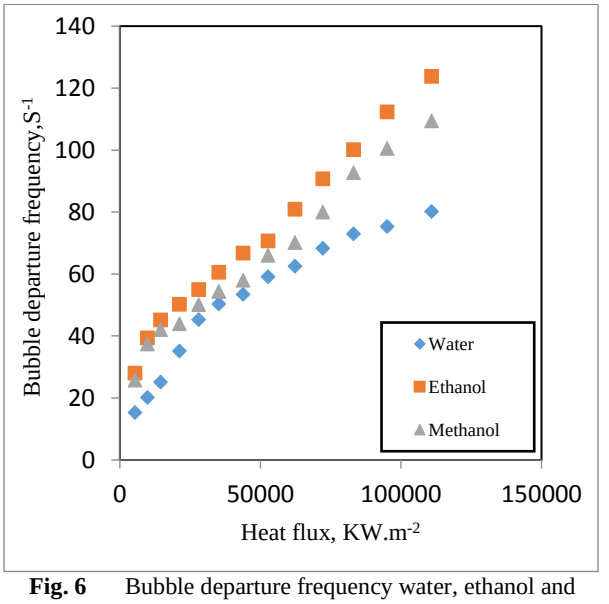

Fig. 6 Bubble departure frequency water, ethanol and methanol at various heat fluxes.

In studies conducted by [12-16], [18], the proposed relationships for bubble frequency include the diameter of the vapor bubbles. In most of the proposed Equations, the bubble frequency calculation Equation has been proposed as the product of the bubble diameter multiplied by the bubble frequency with a certain power. These results show a close and inverse correlation between these two parameters. In this research, the Zuber Equation has been used to calculate the bubble diameter Zuber [14]. Figure 7 shows the bubble diameter changes with increasing heat flux for water, ethanol and methanol.

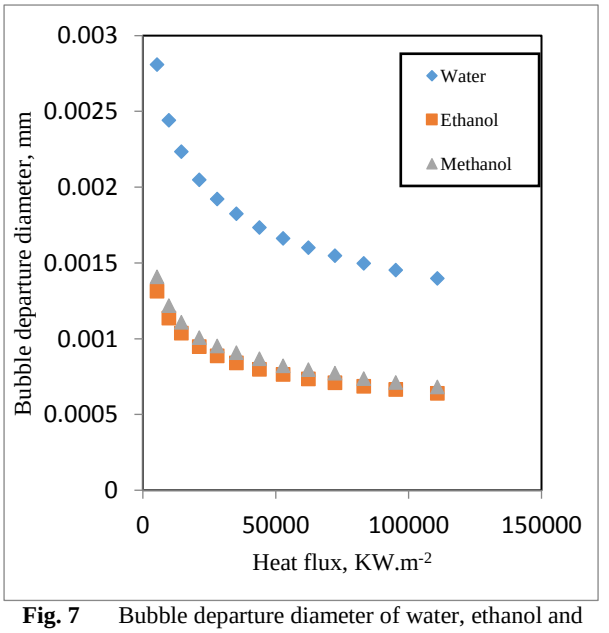

Fig. 7 Bubble departure diameter of water, ethanol and methanol at various heat fluxes.

According to Figure 7, the diameter of the vapor bubbles decreases for all three fluids tested with increasing heat flux. Also, water has the highest and ethanol the lowest bubble diameters. In confirmation of this result and the inverse relationship between diameter and frequency of vapor bubbles as shown in "Fig. 6", water has the highest and ethanol the lowest values of the bubble frequency. Figure 8 clearly shows this relationship.

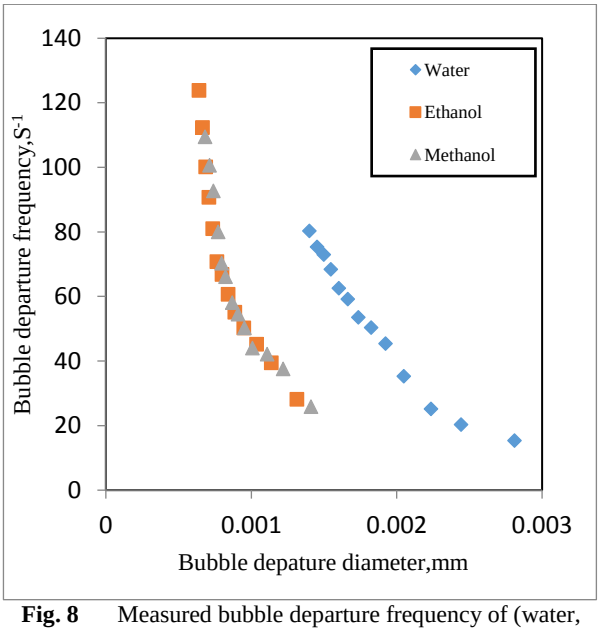

Fig. 8 Measured bubble departure frequency of (water, ethanol and methanol) compared with Bubble departure diameter model Zuber [14].

Figure 9 shows the changes in heat transfer coefficient with heat flux for water, ethanol and methanol.

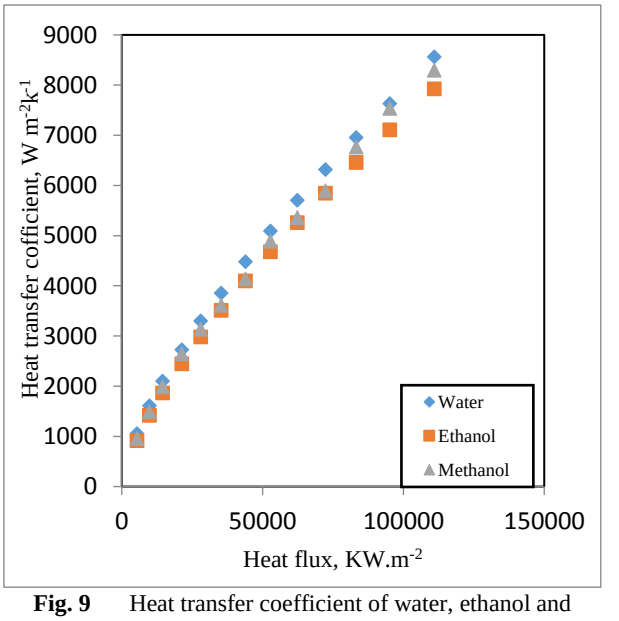

Fig. 9 Heat transfer coefficient of water, ethanol and methanol at various heat fluxes.

The results show that the highest heat transfer coefficient is associated with water and the lowest has been obtained for ethanol. From the perspective of vapor bubble dynamics and based on "Figs. (6-9)", ethanol with the highest bubble frequency and lowest bubble diameter values has had the lowest heat transfer coefficient and, water with the highest bubble diameter values and the lowest bubble frequency values has the highest heat transfer coefficient. Based on this, it can be concluded that the effect of bubble diameter over the bubble frequency on the heat transfer coefficient is dominant. Figures (10-12) shows a comparison between the laboratory data and the proposed relationships for the bubble frequency. In this study, the Zuber Equation has been used to calculate the bubble diameter.

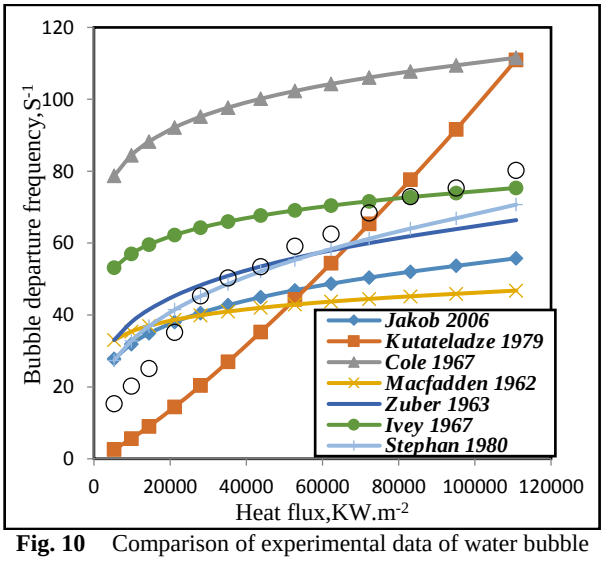

Fig. 10 Comparison of experimental data of water bubble departure frequency with experimental relationships.

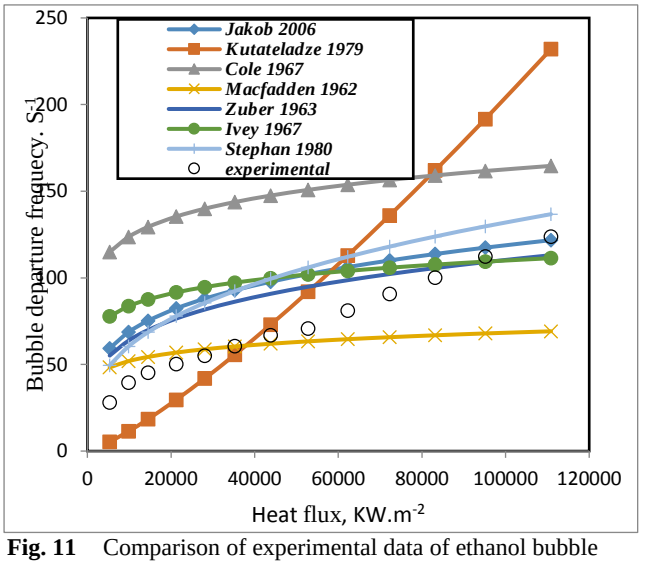

Fig. 11 Comparison of experimental data of ethanol bubble departure frequency with experimental relationships.

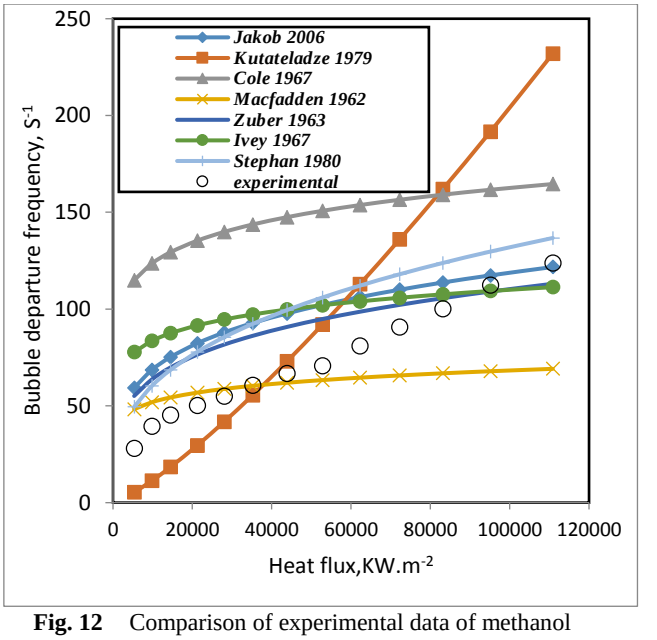

Fig. 12 Comparison of experimental data of methanol bubble departure frequency with experimental relationships.

"Table 3" shows the mean error between the experimental data and the presented relationships.

Table 3 The mean error between the experimental data and the presented relationships

Average percentage error	Jakob 2006 [18]	Kutateladze 1979 [24]	Cole 1967 [12]	Zuber 1963 [14]	Ivey 1967 [15]	Stephan 1980 [16]
Water	28.8	70.8	50.1	19.5	27.2	15.2
Ethanol	28.2	88.4	52.2	24.4	31.5	28.9
Methanol	30.1	77.4	55.4	26.1	34.3	30.7

As shown in Table 3, there is a good overlap between the experimental data and the relationships presented. Peebles, Mikic and Rohsenow, models have not been studied due to the need for growth time, waiting time and lack of access to this data of Peebles and Garber [11], Mikic and Rohsenow [23].

6 EXPERIMENTAL DESIGNS

5.1. Response Surface Methodology

In Response Surface Methodology (RSM), a model with the form of "Eq. (18)" is fitted to experimental data and, by optimization methods, the best coefficients for the model are calculated.

$$Y = \beta_0 + \sum_{i=1}^{k} \beta_i x_i + \sum\sum_{i<j} \beta_{ij} x_i x_j + \sum_{i=1}^{k} \beta_{ij} x_i^2 + \varepsilon \quad (18)$$

Where, K is the number of factors, x_i are linear terms (input variables), x_i^2 are quadratic terms, and $x_i x_j$ are interaction terms, Y is the corresponding response (experimental data).

β_0, β_i, β_{ij} and β_{ii} are the coefficients of the model. The adequacy of the model and significance of the coefficients should be analyzed by statistical methods. An analysis of variance (ANOVA), F-value, P-value of the model, R^2-adjusted and R^2 statistic was performed to evaluate significant differences between factors and to validate the model and check the adequacy of the developed model [25-26]. Central composite design (CCD) is one of the most popular RSM techniques. In the present study, the experiments were designed by the CCD technique. This technique was used to investigate the effect five parameters of pool boiling system for bubble departure frequency as the response. Vapor-liquid density difference, vapor-liquid viscosity, surface tension, thermal conductivity, heat flux were chosen as the parameters and bubble departure frequency was chosen as the response.

7 RESULT AND DISCUSSIONS

In this study, three pool boiling systems for modeling and optimization of bubble departure frequency were considered. The effects of five main parameters on the bubble departure frequency were performed based on the Central Composite Design (CCD). Low and high values of the pool boiling systems designed variables, which are used for experimental design, can be seen in "Table 4". Data obtained from simulations were investigated for the response of three systems, using the models named linear, two-factor interaction (2FI), quadratic and cubic.

Table 4 Low and high values of the pool boiling systems designed variables

Material	Factor	Unit	Coded factor level	
Water			-1	1
	q	W/m^2	110862	5335.32
	k	W/m.s	0.6710	0.6697
	pl-pv	Kg/m^3	958.85	954.83
	μl-μv	Pa.s	12.765	11.0419
	□	N/m	0.0580	0.0566
Methanol				
	q	W/m^2	5335.3	110862
	k	W/m.s	0.1861	0.18769
	pl-pv	Kg/m^3	737.21	743.864
	μl-μv	Pa.s	33.362	37.8457
	□	N/m	0.0176	0.01845
Ethanol				
	q	W/m^2	5335.3	110862
	k	W/m.s	0.1548	0.1569
	pl-pv	Kg/m^3	723.30	730.062
	μl-μv	Pa.s	33.362	37.8457
	□	N/m	0.0164	0.01703

"Table 5" shows the results for each of the process conditions suggested by the RSM design for pool boiling system. Furthermore, considering the values of standard deviation, higher R^2, adjusted R^2 and predicted R^2 of the two-factor interaction (2FI), model was found for bubble departure frequency. The model summary statistics and the results of ANOVA analysis for selecting the model of bubble departure frequency for three systems are shown in "Table 6". "Table 7" gives an insight into the linear, interaction and quadratic effects of the factors for the responses investigated. According to the experimental results for water, methanol and ethanol pool boiling system which are reported in "Table 4", and Equation 18, the response surface models with actual variables have been written responses as:

Table 5 RSM results for three pool boiling system

Material	Run	q	k	pl-pv	μl-μv	□	f
Water		W/m^2	W/m.s	Kg/m^3	Pa.s	N/m	1/S
	1	5335.32	0.66978832	958.8	12.7	0.05808	15.324
	2	9837.59	0.66997	958.2	12.5	0.05789	20.2332
	3	14508.9	0.67011	957.8	12.3	0.0577	25.158
	4	21229.7	0.67025	957.4	12.1	0.0575	35.21
	5	28035.9	0.67037	957.0	11.9	0.05746	45.3256
	6	35229.7	0.670488	956.6	11.8	0.05734	50.3698
	7	43836.5	0.67058	956.3	11.6	0.05723	53.485
	8	52795.5	0.67067	956.0	11.5	0.05713	59.125
	9	62249.7	0.67074	955.8	11.4	0.05705	62.564
	10	72259.09	0.67083	955.5	11.3	0.0569	68.398
	11	83139.5	0.67090	955.3	11.2	0.0568	72.956
	12	95135.3	0.67097	955.0	11.1	0.05678	75.3
	13	110861.9	0.671047	954.8	11.0	0.05669	80.265

Methanol							
	1	5335.32	0.18769	743.8	22.9	0.01845	25.825
	2	9837.59	0.18747	742.9	21.6	0.01814	37.5055
	3	14508.9	0.18732	742.2	20.7	0.01809	42.1125
	4	21229.7	0.18717	741.6	19.9	0.01803	44.004
	5	28035.9	0.18698	740.8	18.8	0.01795	50.2
	6	35229.7	0.18681	740.0	17.9	0.01789	54.455
	7	43836.5	0.18664	739.3	17.0	0.01782	58.0635
	8	52795.5	0.18660	739.1	16.7	0.01780	66.095
	9	62249.7	0.18643	738.4	15.9	0.01774	70.2455
	10	72259.09	0.18629	737.8	15.2	0.01769	80.0213
	11	83139.5	0.18629	737.8	15.2	0.01769	92.7
	12	95135.3	0.18622	737.5	14.8	0.01766	100.6
	13	110861.9	0.1861	737.2	14.5	0.017	109.43
Ethanol							
	1	5335.3	0.67104	730.0	37.8	0.01703	28.115
	2	9837.5	0.15697	729.6	37.5	0.01699	39.4275
	3	14508.9	0.15685	729.1	37.1	0.01694	45.1675
	4	21229.7	0.15668	728.2	36.6	0.01687	50.275
	5	28035.9	0.15642	728.1	36.5	0.01686	55.06
	6	35229.7	0.15639	727.0	35.7	0.01676	60.6025
	7	43836.5	0.15603	726.1	35.1	0.01667	66.81
	8	52795.5	0.15575	725.3	34.6	0.01660	70.725
	9	62249.7	0.15549	725.0	34.4	0.01657	80.9978
	10	72259.0	0.1554	724.7	34.3	0.01655	90.74
	11	83139.5	0.15532	724.1	33.9	0.01649	100.147
	12	95135.3	0.15513	723.7	33.6	0.01645	112.325
	13	110861.9	0.15498	723.3	33.3	0.01641	123.81

Table 6 Model summary statistics and analysis of variance (ANOVA) of the RSM model corresponding to the response: performance

Material		Sum of Squares	df	Mean Square	F Value	p-value Prob > F
Water						
	Model	5596.32	5	1119.26	580.30	< 0.0001
	Linear	R^2=0.9976	R^2adj=0.9959	R^2 pre=0.9921		Suggested
Methanol						
	Model	7850.49	5	1570.10	338.35	< 0.0001
	Linear	R^2=0.995	R^2adj =0.992	R^2 pre=0.9913		Suggested
Ethanol						
	Model	10130.92	5	2026.18	814.76	< 0.0001
	Linear	R^2=0.9971	R^2adj =0.995	R^2 pre=0.991		Suggested

Table 7 ANOVA results for the terms of the second-order polynomial Equations for ethanol, methanol, water

Material		Sum of Squares	df	Mean Square	F Value	p-value Prob > F
Water						
	A-q	1.29	1	1.29	0.6709	0.4397
	B-	13.05	1	13.05	6.77	0.0354
	C-k	12.92	1	12.92	6.70	0.036
	D-pl-pv	13.05	1	13.05	6.76	0.0354
	E-μl-μv	13	1	13	6.74	0.0356
Methanol						
	A-q	92.36	1	92.36	19.90	0.0029
	B-	7.33	1	7.33	1.58	0.2490
	C-k	0.4712	1	0.4712	0.1015	0.7593
	D-pl-pv	0.4795	1	0.4795	0.1033	0.7573
	E-μl-μv	0.4023	1	0.4023	0.0867	0.7770

Ethanol						
	A-q	54.02	1	54.02	21.72	0.0023
	B-□	15.49	1	15.49	6.23	0.0412
	C-k	15.53	1	15.53	6.24	0.0411
	D-pl-pv	15.15	1	15.15	6.09	0.0429
	E-μl-μv	15.64	1	15.64	6.29	0.0405

Equation (19) obtained for water shows that surface tension, thermal conductivity, liquid-vapor viscosity difference and heat flux in a linear manner with a negative constant slope have the highest effect on bubble departure frequency, and liquid-vapor density difference affects the bubble departure frequency linearly with positive slope.

$$f = -3.71336E + 08 - 0.00057 * q - 1.39351E + 09 * \sigma - 2.48563E + 08 * k + 6.533069E + 05 * \rho_l - \rho_v - 5.82733E + 05 * \mu_l - \mu_v \quad (19)$$

The Equation obtained for methanol shows that the liquid-vapor density difference and heat flux in a linear manner and with a negative constant slope have the maximum effect on bubble departure frequency, where the effect of density is greater than the heat flux. The remaining three parameters linearly and with a negative coefficient affect the bubble departure frequency, which respectively, the thermal conductivity, surface tension and the liquid-vapor viscosity difference have the greatest decrease on the bubble frequency.

$$f = +1.04321E + 05 + 0.000824 * q - 38801.86 * \sigma - 4.81617E + 06 * K + 1074.95762 * \rho_l - \rho_v - 32.47335 * \mu_l - \mu_v \quad (20)$$

The Equation obtained for ethanol shows that surface tension and heat flux affect linearly and with the highest positive slope, and thermal conductivity, the liquid-vapor viscosity difference and the liquid-vapor density difference have the greatest negative effect on the bubble departure frequency in linear form, respectively. Also, no interaction effect, quadratic effect and cubic effect between parameters on response f were detected.

$$f = +3.47767E + 08 + 0.000933 * q + 1.29096E + 10 * \sigma - 2.87797E + 09 * k - 1.4939E + 05 * \rho_l - \rho_v - 1.80158E + 05 * \mu_l - \mu_v \quad (21)$$

The values of the responses determined using the regression Equations were compared with the obtained experimental data, and the results are presented in "Fig. 13". As can be seen, the model shows the good prediction of the experimental data. Therefore, based on the statistical tests and data comparison the models can be considered adequate for water, ethanol, methanol pool boiling system simulations and optimization.

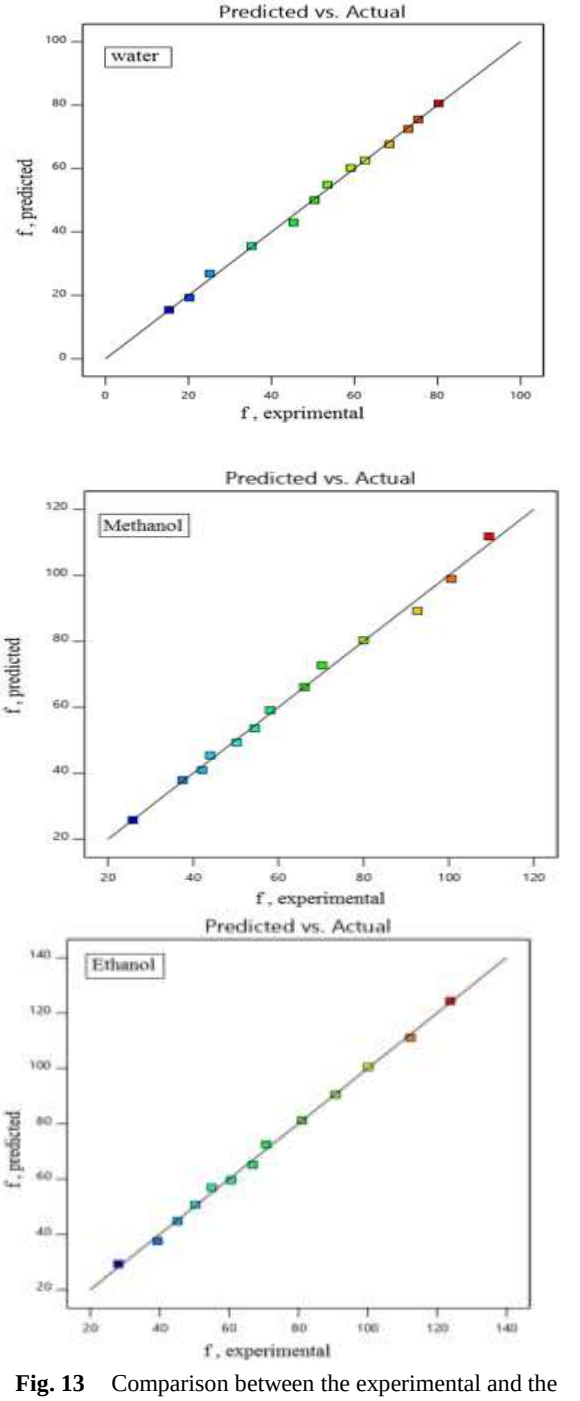

Fig. 13 Comparison between the experimental and the predicted water, methanol and ethanol pool boiling process performance index (f) determined by the RSM model.

As it can be seen in "Tables 5 and 6", P-value is smaller than 0.0001, the F-values are so high, and the coefficient of multiple determinations (R^2) and the adjusted statistic coefficient (R^2_{adj}) are in agreement for the response. According to this tables, it can be deduced that the linear model was significant and adequate to represent the actual relationship between the response (f) and five variables (vapor-liquid density difference, vapor-liquid viscosity, surface tension, thermal conductivity, heat flux) for three pool boiling systems.

8 NEW MODEL

In this study, based on dimensional analysis, a quasi-experimental model has been proposed to calculate the bubbles departure frequency. Parameters such as bubbles departure frequency, vapor-liquid density difference, vapor density, heat flux, surface tension, liquid viscosity, vapor viscosity, liquid thermal conductivity, vapor thermal conductivity, ratio of fluid contact angle to water contact angle can be effective as 10 effective parameters with four MLTΘ dimensions. According to $\boldsymbol{\pi}$ Buckingham's theory, dimensionless groups are obtained as follows:

$$\pi_1 = \frac{\rho_v}{\Delta\rho} \tag{22}$$

$$\pi_2 = \frac{q}{\delta f} \tag{23}$$

$$\pi_3 = \frac{\mu_L}{\mu_v} \tag{24}$$

$$\pi_4 = \frac{k_v}{k_l} \tag{25}$$

$$\pi 5 = \frac{\theta_{fluid}}{\theta_{water}} \tag{26}$$

Based on dimensionless groups (22) to (26), relationship (27) is established.

$$\frac{q}{\delta f} = f\left((\frac{\rho_v}{\Delta\rho}),(\frac{\mu_L}{\mu_v}),(\frac{k_v}{k_l}),(\frac{\theta_{fluid}}{\theta_{water}})\right) \tag{27}$$

According to relationship (27), there is:

$$f = C_0(\frac{\rho_v}{\Delta\rho})^{C_1}(\frac{\mu_L}{\mu_v})^{C_2}(\frac{k_v}{k_l})^{C_3}(\frac{\theta_{fluid}}{\theta_{water}})^{C_4}(\frac{q}{\delta})^{C_5} \tag{28}$$

In this research, using the MATLAB program and the data of the bubble frequency, the coefficients C_0 to C_5 have been calculated and the proposed model has been presented as Equation (29).

$$f = 0.4(\frac{\rho_v}{\Delta\rho})^{0.0625}(\frac{\mu_L}{\mu_v})^{0.035}(\frac{k_v}{k_l})^{0.1}(\frac{\theta_{fluid}}{\theta_{water}})^{1.0625}(\frac{q}{\delta})^{0.5} \tag{29}$$

Figure 14 shows a comparison between the experimental data and the proposed model. The error rate calculated based on Equation (27) is less than 9% (water 4%, ethanol 7%, methanol 1%).

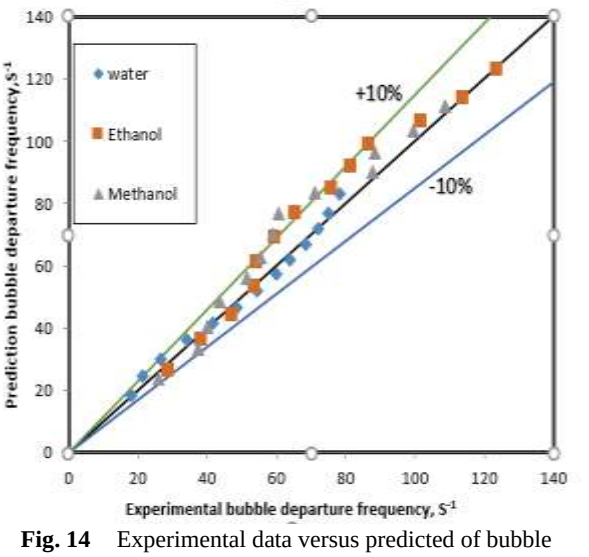

Fig. 14 Experimental data versus predicted of bubble departure frequency by the new model.

9 CONCLUSIONS

In this study, the bubble departure frequency on a flat surface for boiling pool water, ethanol and methanol using a response surface methodology has been discussed and the following results have been obtained.

1- Based on the data obtained for heat transfer coefficient, the experimental data showed the best overlap with the models proposed by Stephan-abdelsalam (error 2%) and Rohsenow (error 9%).
2- The results show an increase in the bubble frequency with an increase in heat flux. Reducing the growth time and waiting time of the bubble by increasing the heat flux is the cause of this phenomenon. Water and ethanol have the lowest and highest bubble frequencies, respectively.
3- The Bubble diameter decreases with increasing the heat flux. Water and ethanol have the highest and lowest bubble diameters, respectively.

4- According to the results, with decreasing bubble diameter, the bubbles departure frequency increased. Other proposed models have confirmed such a result.
5- The results for the bubble departure frequency show a good overlap between the experimental models and the laboratory data.
6- The data obtained for the bubble departure frequency show a good overlap between the experimental results and the predicted results of the RSM.
7- In this research, a quasi-experimental model has been presented based on the data of the bubble departure frequency and using dimensional analysis and MATLAB program for the bubbles departure frequency of pure liquids (water, ethanol and methanol). The error of the model with experimental results has been less than 9%.

10 APPENDIX OR NOMENCLATURE

D	*Diameter (m)*
f	*Bubble departure frequency (s^{-1})*
g	*Gravity ($m\ s^{-2}$)*
h	*Heat transfer coefficient ($W\ m^{-2}\ K^{-1}$)*
I	*Electrical current (A)*
K	*Thermal conductivity ($W\ m^{-1}K^{-1}$)*
q	*Heat flux ($W\ m^{-2}$)*
t	*Time (s)*
T	*Temperature (K)*
V	*Velocity ($m\ s^{-1}$) or Voltage (V)*
p	*Density ($kg\ m^{-3}$)*
□	*Surface tension ($N\ m^{-1}$)*
Δ	*Difference*
μ	*Dynamic viscosity (Pa s)*

Subscripts

b	*Bubble*
l	*Liquid*
v	*Vapor*
G	*Growth*
W	*Waiting*

ACKNOWLEDGMENTS

Writers of this article are inclined to acknowledge University of Sistan and Baluchestan for their financial and mental assistance

REFERENCES

[1] Vasei Moghadam, A., Goshayeshi, H. R., Experimental Investigation of Pool Boiling of Single Wall Carbon Nanotubes (SWCNTs) with Different Grooved Surfaces, Int J Advanced Design and Manufacturing Technology, Vol. 12, 2019, pp. 77-84.

[2] Gajghate, S. S., Barathula, S., Das, S., Saha, B. B., and Bhaumik, S., Experimental Investigation and Optimization of Pool Boiling Heat Transfer Enhancement Over Graphene-Coated Copper Surface, J. Therm. Anal. Calorim, Vol. 140, 2020, pp. 1393–1411.

[3] Hamzekhani, S., Maniavi Falahieh, M., Kamalizadeh, M. R., and Salmaninejad, M., Bubble Dynamics for Nucleate Pool Boiling of Water, Ethanol and Methanol Pure Liquids under the Atmospheric Pressure, Journal of Applied Fluid Mechanics, Vol. 8, 2015, pp. 893-898.

[4] Khooshehchin, M., Mohammadidoust, A., and Ghotbinasab, S., An Optimization Study on Heat Transfer of Pool Boiling Exposed Ultrasonic Waves and Particles Addition, International Communications in Heat and Mass Transfer, Vol. 114, 2020, pp. 104558.

[5] Sarafraz, M. M., Experimental Investigation on Pool Boiling Heat Transfer to Formic Acid, Propanol And 2-Butanol Pure Liquids the Atmospheric Pressure, Journal of Applied Fluid Mechanics, Vol. 6, 2013, pp. 73-79.

[6] Sitter, J. S., Snyder, T. J., Chung, T. N., and Marslon, P. L., Terrestrial and Microgravity Pool Boiling Heat Transfer from A Wire in An Acoustic Field, Int. J. Heat Transfer, Vol. 41, 1998, pp. 2143-2155.

[7] Hamzekani, S., Maniav Falahieh, M., and Akhbari, A., Bubble Departure Diameter in Nucleate Pool Boiling at Saturation: Pure Liquids and Binary Mixtures, Int. J. Refrigeration, Vol. 46, 2014, pp. 50-58

[8] Gupta, S. K, Misra, R. D., Experimental Study of Pool Boiling Heat Transfer on Copper Surfaces with Cu-Al2O3 Nanocomposite Coatings, International Communications in Heat and Mass Transfer, Vol. 97, 2018, pp. 47-55.

[9] Choi, G., Shim, D. I., Lee, D., Kim. B. S., and Cho, H. H., Enhanced Nucleate Boiling Using a Reduced Graphene Oxide-Coated Micropillar, International Communications in Heat and Mass Transfer, Vol. 109, 2019, pp.104331.

[10] Alavi Fazel, S. A., A Genetic Algorithm-Based Optimization Model for Pool Boiling Heat Transfer on Horizontal Rod Heaters at Isolated Bubble Regime, Heat Mass Transfer, Vol. 53, 2017, pp. 2731-2744

[11] Peebles, F. N., Garber, H. J., Studies on Motion of Gas Bubbles in Liquids, Chem. Eng. Prog, Vol. 49, 1953, pp. 88–97.

[12] Cole. R., Bubble Frequencies and Departure Volumes at Sub Atmospheric Pressures, AICHE J, Vol. 13, 1967, pp. 779-783

[13] McFadden, P. W., Grassman, P., The Relation Between Bubble Frequency and Diameter During Nucleation Pool Boiling, International Journal Heat Mass Transfer, Vol. 5, 1962, pp.169-173

[14] Zuber, N., Nucleate Boiling the Region of Isolated Bubbles Similarity with Natural Convection, Int. J. Heat Mass Transfer, Vol. 6, 1963, pp. 53–65.

[15] Ivey, H., Relationships Between Bubble Frequency Departure Diameter and Rise Velocity in Nucleate Boiling, International Journal Heat and Mass Transfer, Vol. 10,1967, pp 1023-1040.

[16] Stephan, K., Abdelsalam, K., Heat Transfer Correlation for Natural Convection Boiling, International Journal of Heat and Mass Transfer, Vol. 23, 1980, pp. 73-87.

[17] Chen, Y., Groll, M., Mertz, R., and Kulenovic, R., Bubble Dynamics of Boiling of Propane and Iso-Butane on Smooth and Enhanced Tubes, Experimental Thermal and Fluid Science, Vol. 28, 2004, pp. 171–178.

[18] Kim, J., Kim, M. H., On the Departure Behaviors of Bubble at Nucleate Pool Boiling, International Journal of Multiphase Flow, Vol. 32, 2006, pp. 1269–1286.

[19] Hamzekhani, S., Maniavi Falahieh, M., Kamalizadeh, M. R., and Salmaninejad, M., Bubble Dynamics for Nucleate Pool Boiling of Water, Ethanol and Methanol Pure Liquids under the Atmospheric Pressure, Journal of Applied Fluid Mechanics, Vol. 8, 2015, pp. 893-898.

[20] Sarafraz, M. M., Hormozi, F., Experimental Investigation on The Pool Boiling Heat Transfer to Aqueous Multi-Walled Carbon Nanotube Nanofluids on The Micro-Finned Surfaces, International Journal of Thermal Sciences, Vol. 100, 2016, pp. 255-266.

[21] Gorenflo, D., Pool Boiling. In: VDI Heat Atlas (chapter Ha), 1993.

[22] Alavi fazel, S. A., Roumana, S., Bubble Dynamics for Nucleate Pool Boiling of Electrolyte Solutions, J. Heat Transfer, Vol. 132, 2010, pp. 1-7.

[23] Mikic, B. B., Rohsenow, W. M., Bubble Growth Rates in Non-Uniform Temperature Field, progress in Heat and Mass Transfer, Vol. 2, 1969, pp. 283-293.

[24] Kutatelaze, S. S., Gognim, I. I., Growth Rate and Detachment Dimeter of a Vapor Bubble in Free Convection Boiling of a Saturated Liquid, High Temp, Vol. 17, 1979, pp. 667-671.

[25] Hamzekhani, S., Sardashti Birjandi, M. R., and Shahraki, F., Modeling and Optimization of the Bubble Detachment Diameter for a Pool Boiling System, Chem. Eng, Technol, Vol. 45, 2022, pp. 1–13.

[26] Muthuvelayudham, R., Viruthagir, T., Application of Central Composite Design Based Response Surface Methodology Inparameter Optimization And On Cellulase Production Using agricultural Waste, International Journal of Agricultural and Biosystems Engineering, Vol. 4, 2010, pp. 12-19.

Int. J. Advanced Design and Manufacturing Technology, 2022, Vol. 15, No. 4, pp. 85-94

DOI: 10.30486/admt.2023.1963242.1367 ISSN: 2252-0406 https://admt.isfahan.iau.ir

Evaluation of Sperling's Index in Passenger and Freight Trains Under Different Speeds and Track Irregularities

Sajjad Sattari
Department of Mechanical Engineering,
Najafabad Branch, Islamic Azad University, Najafabad, Iran
E-mail: sajjad.sattari@gmail.com

Mohammad Saadat*, Sayed Hasan Mirtalaie, Mehdi Salehi, Ali Soleimani
Department of Mechanical Engineering,
Najafabad Branch, Islamic Azad University, Najafabad, Iran
E-mail: saadat@pmc.iaun.ac.ir, mirtalaie@pmc.iaun.ac.ir,
mehdi.salehi@pmc.iaun.ac.ir, soleimani@pmc.iaun.ac.ir
*Corresponding author

Received: 13 July 2022, Revised: 24 September 2022, Accepted: 25 September 2022

Abstract: The two factors of track irregularity and train speed affect the dynamic behavior of rail vehicles and can lead to an increase in dynamic forces, a decrease in ride comfort, and derailment in some cases. In this paper, the effect of train speed increase and different conditions of track irregularity on ride comfort and ride quality are investigated. For this purpose, first, two freight and passenger train models have been modeled in UM software, and then the effect of train speed increase and track irregularities (different US federal classes) have been studied with Sperling's index. A freight train with the model of 18-100 and 3-piece bogie and a TGV high-speed train with 10 wagons were simulated. The results showed that in Sperling's index, with the increase in the train speed and irregularity amplitude, the value of ride comfort and ride quality generally increased. For example, in the passenger train and irregularity classes 5 and 4, with the increase in train speed from 10 to 100 m/s, the Sperling's index values changed from 0.66 to 1.99 and from 0.78 to 2.25, and increased 200% and 188%, respectively. In other words, at a speed of 10 m/s, passengers' comfort is just noticeable, while at a speed of 100 m/s and class 4, the situation is more pronounced but not unpleasant and the system should be monitored.

Keywords: Numerical Simulation, Railway Vehicles, Ride Comfort, Ride Quality, Sperling's Index, Track Irregularities

Biographical notes: Sajad Sattari is a PhD candidate of Mechanical Engineering at Islamic Azad University of Najafabad (IAUN), Iran. His current research focuses on railway engineering and solid mechanics. He received his MSc in Mechanical Engineering from IAUN in 2016. **Mohamad Saadat** is Assistant Professor of mechanical engineering at IAUN. His current research interest includes control, mechatronics, and hybrid electric vehicles. He received his PhD in Mechanical Engineering from IUT in 2016. **Sayed Hasan Mirtalaie** is Assistant Professor of mechanical engineering at IAUN. His current research interest includes dynamic and vibration. He received his PhD in Mechanical Engineering from UK in 2017. **Mehdi Salehi** is Assistant Professor of Mechanical Engineering at IAUN. He received his PhD in Mechanical Engineering from IUT in 2011. **Ali Soleimani** is Assistant Professor of mechanical engineering at IAUN. He received his PhD in Mechanical Engineering from TMU in 2016.

Research paper

1 INTRODUCTION

All industries, including the railway industry, need accurate modeling and simulations. The dynamic performance of railway vehicles, which generally includes two parts of comfort and safety, is evaluated with indicators of ride quality, wagon stability, etc. Ride comfort is one of the most important indicators of a railway vehicle, which has a relatively complex concept, and its general definition is the ability to suspend a railway vehicle to maintain movement within the range of human comfort or within the range necessary to ensure no damage. Ride comfort during movement is affected by various factors including vibration, temperature, sound, seat characteristics, etc. But in the dynamic criteria of checking ride comfort, only part of the comfort that is affected by the vibrations of the vehicle movement is considered. Passenger trains usually consist of a carbody and two (and/or three) bogies. In a railway system, the most effective factors in ride comfort are the suspension system between the carbody and the bogie (secondary suspension system) and the suspension system between the bogie and the wheelsets (primary suspension system), and the effect of structure flexibility of the carbody and bogies is much less than the effect of suspension systems. Also, due to being metal, the wheels are almost rigid (compared to the suspension system) [1-6]. On the other hand, with the rapid development of the rail transport industry, determining the working range at high speed and away from hunting instability is one of the important issues. Hunting in a critical state, along with wheel wear and fatigue, can lead to derailment and accidents. Knowing the dynamic behavior of the rail vehicle is not only necessary for the designer, but it can also represent the performance of the rail vehicle and applied forces to the rail. The consequences of hunting can be mentioned as the lack of comfort sense for passengers, increasing the cost of repairs, and large lateral forces that cause damage to the train, track, and derailment. Therefore, in the current research, one of the consequences of the hunting phenomenon, which means passenger discomfort, was evaluated [5].

After modelling a train in universal mechanism (UM), Nasr et al. [1] investigated the dynamic behavior of the model and the Sperling's index in the speed range of 10 to 25 m/s by applying the track irregularity. Their results showed that increasing the speed increases the Sperling's index and decreases passengers' comfort. Halladin et al. [4] compared the comfort methods of a tramway system on different tracks with a field (experimental) test. Younesian et al. [7] optimized and checked the life of the wagon suspension system, considering the ride comfort as the limiting factor. Gangadharan et al. [8] also conducted research on analytical and laboratory evaluation of ride comfort. Goga et al. [9] optimized the vehicle suspension system using 4-DOF model, they ignored the vibrations around the longitudinal axis of the carbody. Sun et al. [10] investigated the effect of the suspension system of the carbody on the ride comfort of high-speed trains. Suarez et al. [11-12] analyzed the mutual influence of track quality, wheel-rail contact characteristics, and elastic characteristics of the train suspension system on safety, ride comfort, and rail fatigue. Baghmisheh et al. [13] optimized the car suspension system with the genetic algorithm, they used 2-DOF model to analyze car vibrations and by ignoring the effect of longitudinal and transverse accelerations, they reduced the average value of vertical accelerations (without calculating the ride comfort index). Ebadi et al. [2] analyzed wagon vibrations and the effect of track irregularities on ride comfort (MATLAB/Simulink). Various methods have been developed to evaluate passenger comfort, usually methods based on ISO-2631, and Sperling, known as Sperling's method or Wz comfort index method, are often used. The Wz comfort index method was presented by Sperling in Germany in the middle of the 20th century, and this method is still the most well-known evaluation method for passenger comfort and quality of railway vehicles. The UIC and the CEN, along with ISO, have published standards for the evaluation of the ride comfort of railway vehicles based on ISO-2631, UIC brochure 513R, standards EN-12299 and ISO-10056 through the ERRI [14-19].

In this paper, UM software has been used to simulate the 3D dynamics of rail vehicles. First, two freight and passenger train models were modeled, and then the Sperling's index was examined as one of the parameters for the evaluation of railway vehicles. To evaluate ride comfort, different researchers have used two experimental and simulation methods, each of which has advantages and limitations. In similar studies, researchers generally investigated the effect of one parameter, such as train speed, track irregularity, and/or other effective parameters. For example, in reference [1], an irregularity class has been investigated at several different speeds to evaluate the ride comfort (with UM), and/or in reference [2], the effect of irregularity in two irregularity classes 3 and 6 of the US has been checked (with MATLAB/Simulink). In this research, a wide range of speed changes as well as a wide range of track irregularities with different amplitudes have been investigated to evaluate the ride comfort for both freight and passenger train models.

2 EVALUATION OF RIDE COMFORT

One of the methods of evaluating the ride quality and comfort of railway vehicles is the ride index Wz method, which was introduced by Sperling. Ride comfort should

be evaluated according to the effect of mechanical vibrations of the vehicle on passengers. Constants and different speeds can be evaluated to show ride quality and ride comfort in different track irregularities. Appropriate validity, accurate numbers, and easy interpretation are the advantages of Sperling's index. The Sperling's index is a function of the vehicle's vibration level and provides information about the dynamic behavior of the system, which enables the diagnosis and creation of solutions to improve the dynamic performance in terms of ride quality and ride comfort. This method is often used in all standard railway tracks (ballasted and slab tracks). The ranges of ride quality and ride comfort are presented in "Tables 1 and 2" [3-4].

Table 1 Scale for the ride quality

Ride quality	Vibration sensitivity
1.0	Very good
2.0	Good
3.0	Satisfactory
4.0	Acceptable for running
4.5	Not acceptable for running
5.0	Dangerous

Table 2 Scale for the ride index

Ride index	Vibration sensitivity
1.0	Just noticeable
2.0	Clearly noticeable
2.5	More pronounced but not unpleasant
3.0	Strong, irregular, but still tolerable
3.25	Very irregular
3.5	Extremely irregular, unpleasant, annoying, prolonged exposure intolerable
4.0	Extremely unpleasant; prolonged exposure harmful

Ride index Wz is weighted on the frequency range based on the following Equations (1) and (2):

$$W_z = \sqrt[10]{a^3 . B^3} \quad (1)$$

$$W_z = \sqrt[6.67]{a^2 . B^2} \quad (2)$$

The ride quality weighting factor B is calculated according to Equation (3):

$$B(f) = 1.14. \sqrt{\frac{[(1 - 0.056f^2)^2 + (0.645f)^2 . (3.55f^2)]}{[(1 - 0.252f^2)^2 + (1.547f - 0.00444f^3)^2] . (1 + 3.5}} \quad (3)$$

The ride comfort weighting factor B is calculated according to Equation (4):

$$B(f) = k. \sqrt{\frac{1.911f^2 + (0.25f^2)^2}{(1 - 0.277f^2)^2 + (1.563f - 0.0368f^3)^2}} \quad (4)$$

Where, k = 0.588 for vertical vibrations (B_s), and k = 0.737 for lateral vibrations (B_w). Values of weighting curves are plotted in the 0.5 to 30 Hz frequency range in 1/3 octave bands ("Fig. 1"), for further signal processing of peak acceleration values a peak [4], [20-22].

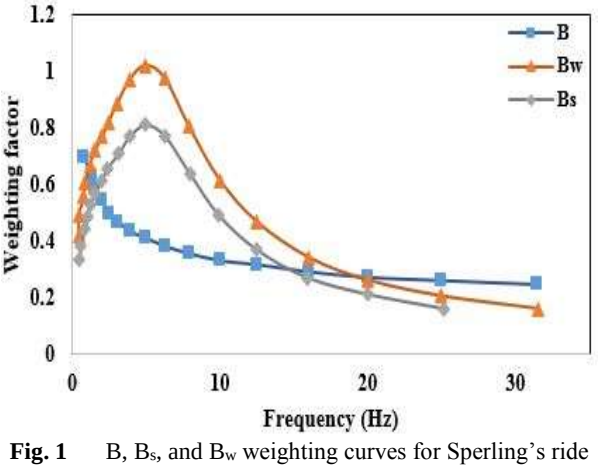

Fig. 1 B, B_s, and B_w weighting curves for Sperling's ride index.

3 SIMULATIONS

The study of train dynamic behavior is one of the most important studies in the railway industry. Considering that one of the goals of this industry is the safe transportation of passengers, dynamic simulator tools of the train are used to evaluate the safety of rolling stock. One of the tools used to simulate train dynamics is the use of Multi-Body Dynamics (MBDs) software. Among the dynamic software available in the industry, Universal Mechanism (UM), ADAMS, SIMPACK, ABAQUS, etc. can be mentioned [23-25]. Figure 2 showed a view of passenger and freight trains modelled in UM in detail. Also, the parameters and values of both trains are presented in "Tables 3 and 4". The main components of trains include the carbody, primary and secondary suspension systems, and wheelsets. The passenger train has a primary suspension system including vertical springs and dampers, which are located in "Fig. 2". In order to simulate the train's secondary suspension system, an air spring has been used between the bogie frame and the carbody (Nishimura model). In some studies, this train model has been used for simulations [1], [17-19].

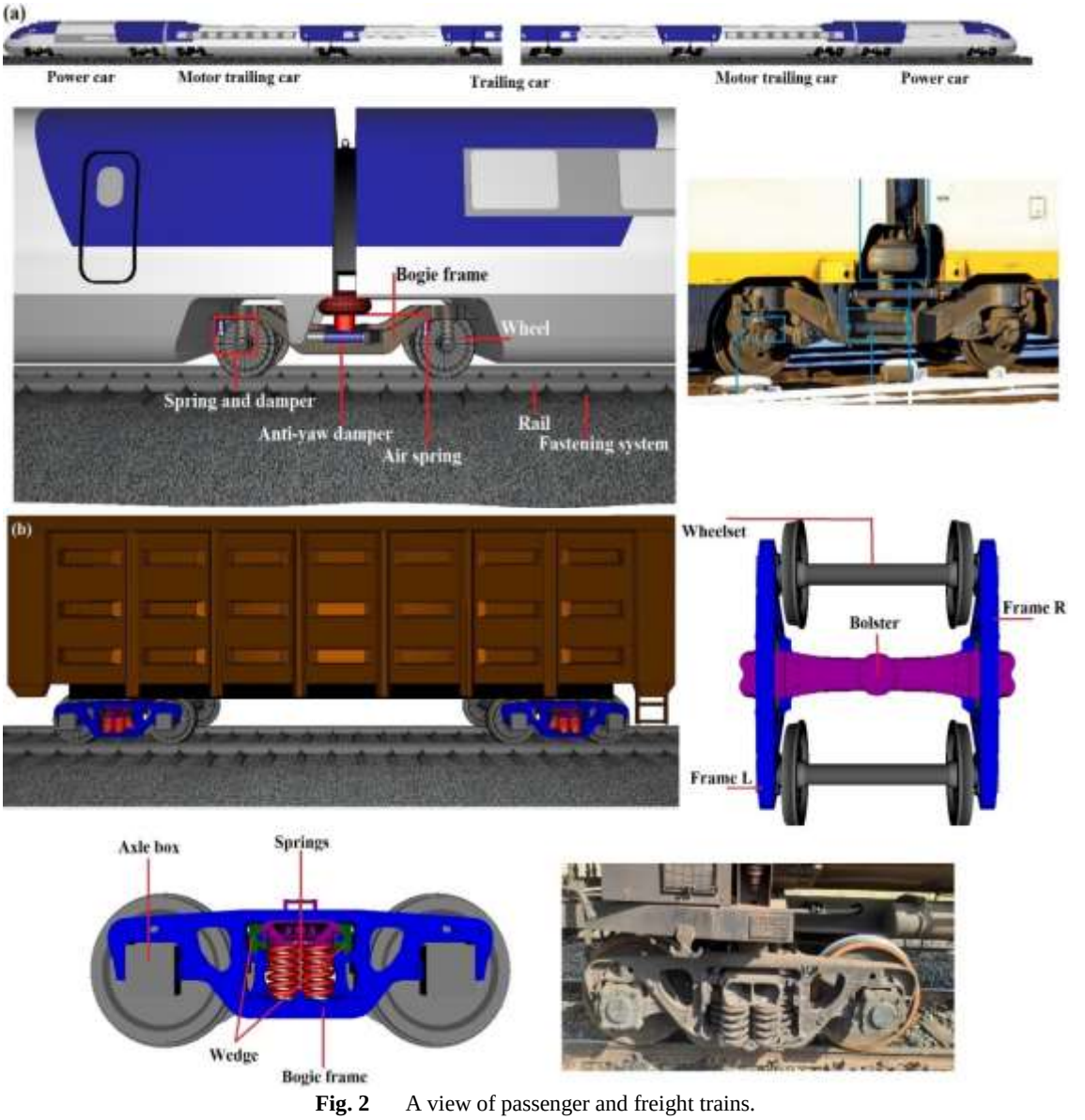

Fig. 2 A view of passenger and freight trains.

Table 1 Train-track parameters in passenger train

Parameters	Value and unit	Parameters		Value and unit
Carbody mass	33250 (kg)	Track	vertical and lateral stiffness	44×10^6, 18×10^6 (N/m)
Bogie frame mass	22963 (kg)		vertical and lateral damping	4×10^5, 1×10^5 (Ns/m)
Wheelset mass	2150 (kg)	Primary suspension	longitudinal, lateral, and vertical stiffness	4.08×10^7, 4.56×10^6, 1.40×10^6 (N/m)
Wheel radius	0.460 (m)	Secondary suspension	longitudinal, lateral, and vertical stiffness	3.50×10^5, 3.50×10^5, 1.71×10^6 (N/m)

Table 4 Train parameters in freight train

Parameters	Value and unit	Parameters	Value and unit
Mass of carbody	90000 (kg)	Lateral spring stiffness (one/double spring)	6.43×10^5 (N/m)
Mass of bolster	596.2 (kg)	Vertical spring stiffness (one/double spring)	6.32×10^5 (N/m)
Mass of wedge	21.6 (kg)	Contact stiffness (axle box)	1×10^8 (N/m)
Mass of side frame (+springs)	526.3 (kg)	Contact damping (axle box)	3×10^4 (Ns/m)
Wheel radius	0.475 (m)	Coefficient of friction in axle box contact	0.3
Coefficient of friction (wedge)	0.3		

In order to simulate a freight train, the three-piece bogie type 18-100 is used in the countries of America, Russia, China, Canada, India, Australia, Brazil, etc. Generally, three-piece bogies simulations are based on models of a wedge frictional system. The inertia properties of wedges are ignored and the linear model of tangential contact forces is used. The bogie has rigid contacts between side frame and axleboxes, carbody and bolster in the center plate and side bearings including clearances, between frictional wedges and bolster or side frame. The rail is considered a massless force element, the stiffness and damping of the rail are considered, but the inertial properties are not considered. Hertzian solution and FASTSIM algorithm by Kalker as well as modified non-elliptic multipoint contact model are used. Some researchers used this train model for dynamic simulations [26-30]. After completing the simulation of the train's dynamic characteristics in the UM input section, the UM simulation section has been used to simulate the dynamic behaviour of the system. In order to solve the wheel and rail contact equations, Kalker nonlinear theory has been used, which calculates the geometric parameters of the wheel and rail using the FASTSIM solver algorithm. Power Spectral Density (PSD) function is the most important and commonly used statistical function to express the track irregularity taken as a stationary random process. Based on a large number of field measured data, the Federal Railroad Administration of America (FRA) obtained the irregularity power spectral density function of rail track, which was fitted to a function expressed by cutoff frequency and roughness constant. The track irregularity in the US can be divided into six levels [31-34]. The parameters of this function are presented in "Table 5". In the next part of the paper, the irregularity diagrams and the amplitude of them are presented.

Table 5 Parameters of American track irregularity PSD function

Parameter	Parameter values for different line levels					
	1 (worst)	2	3	4	5	6 (best)
A_v (cm^2 rad/m)	1.2107	1.0181	0.6816	0.5376	0.2095	0.0339
A_a (cm^2 rad/m)	3.3634	1.2107	0.4128	0.3027	0.0762	0.0339
(rad/m)Ω_s^2	0.6046	0.9308	0.8520	1.1312	0.8209	0.4380
(rad/m)Ω_c^2	0.8245	0.8245	0.8245	0.8245	0.8245	0.8245

4 RESULT AND DISCUSSION

The irregularity of rail surface is one of the most influential parameters in the efficiency of the rolling stock systems and especially passenger type. In "Fig. 3", the track irregularities in different classes can be seen for simulation. Classes 4, 5, and 6 have been added in common for both trains, class 1 for freight trains, and irregularity of Tehran metro for passenger trains. The irregularity amplitude for classes 1, 4, 5, 6, and Tehran's metro is about 35, 15, 10, 5, and 3 mm, respectively. One of the advantages of numerical simulation compared to field test is that in order to evaluate the ride comfort and ride quality of a railway system, it is possible to change various values of a railway system, including train speed, track conditions, defects, etc., and evaluate the results. Figure 4 shows the acceleration-time diagram of carbody and bogie frame vibration (vertical accelerations). These charts are an important indicator for evaluating ride comfort with Sperling's index. Similar to "Fig. 4", after applying the desired parameters as input, the acceleration of the carbody is taken as the output of the system, and then, depending on the desired goal, the data is used to calculate the ride comfort. In "Figs 5, 6, and 7" the simultaneous effect of train speed and different conditions of random track irregularities with various severities is presented. At different speeds and different irregularities of the track, the vertical Sperling's index has been reported the irregularities significantly excite the strong vibration between the vehicle and the track. This not only reduces the ride quality of the train but also causes the failure of parts of the wheel and railway system and reduces the quality of the track. In "Figs. 5, 6, and 7", Sperling's method is presented as an important indicator to evaluate passenger comfort. In the passenger train and the Sperling's index, with the increase of train speed and irregularity amplitude, the value of ride comfort has generally increased. For example, in the irregularity of classes 6 and 5, with the increase in speed from 10 to 100 m/s, the Sperling's index values changed from 0.61 to 1.86 and from 0.66 to 1.99 and increased about 200%. In a constant irregularity amplitude, for example, class 4, with the increase in speed from 10 to 100 m/s, Sperling's index has increased by about 188% and changed from clearly noticeable to more pronounced but not unpleasant. According to Sperling's index, in all the studied speeds and irregularities, carbody acceleration amplitude is in a suitable range and passenger comfort is in a good condition. As for motions and vibrations, Sperling's index is often considered an acceptable value for ride comfort on trains [6]. The studies of Dumitriu et al. [3], Haladin et al. [4], and Sadeghi et al. [20-21] also have similar results to the current paper. In general, ride comfort has increased by increasing train speed.

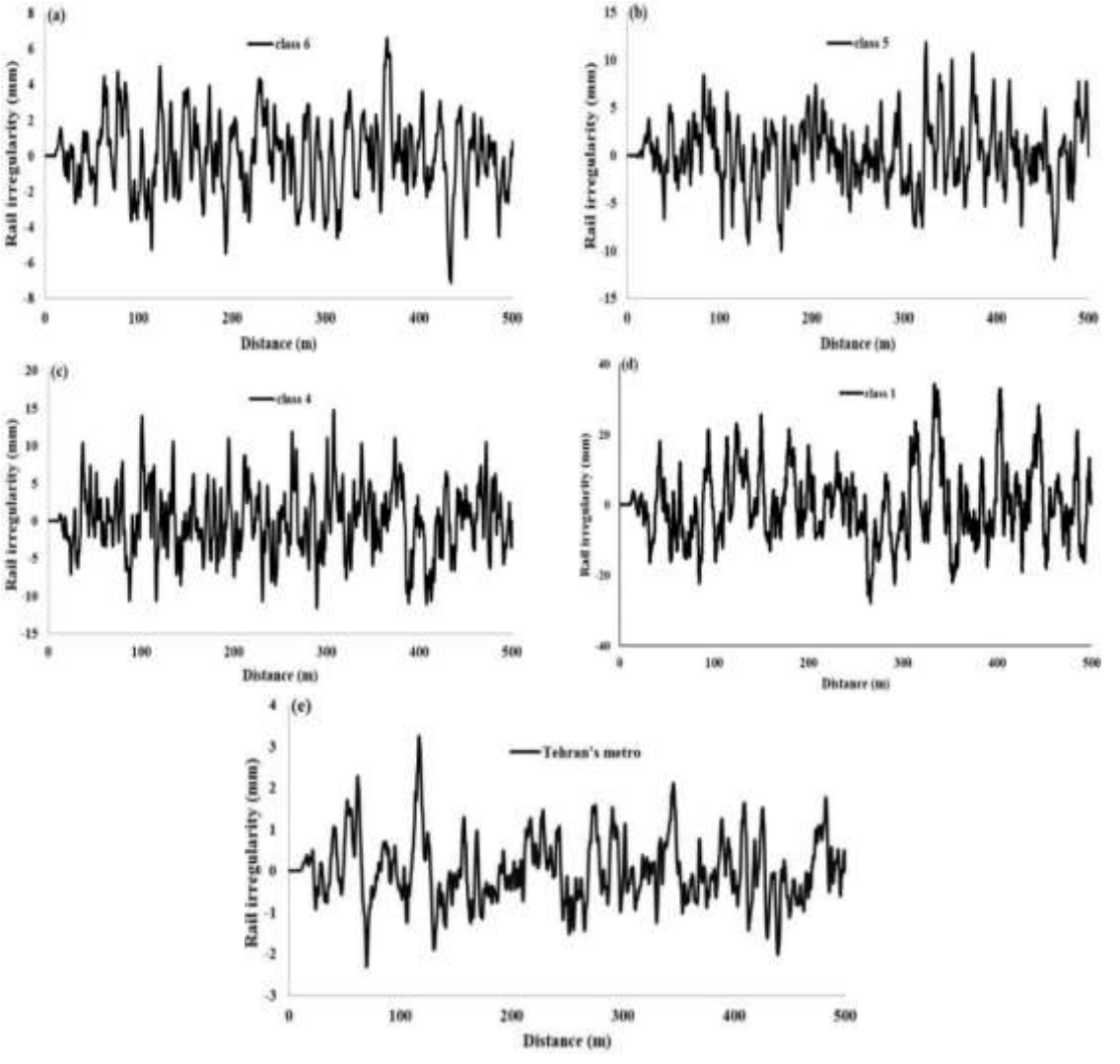

Fig. 3 Track irregularities of different classes.

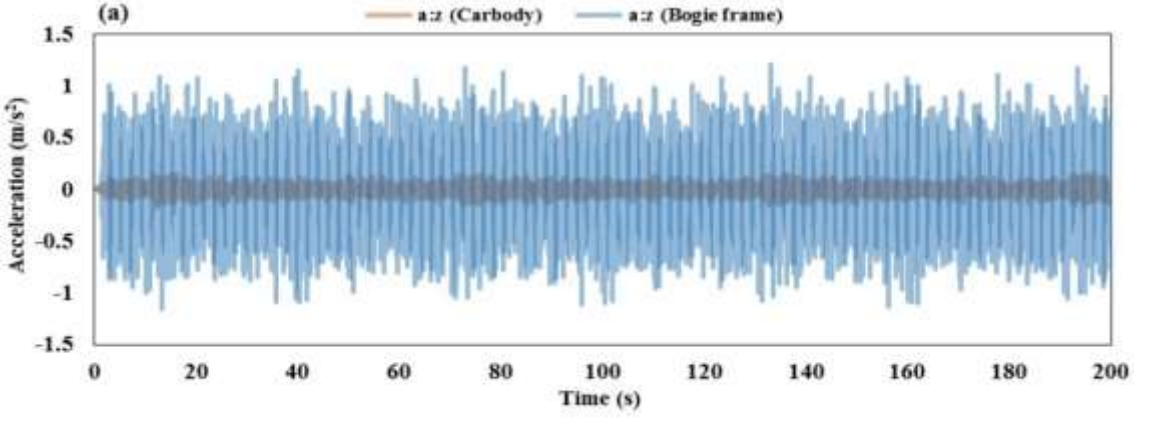

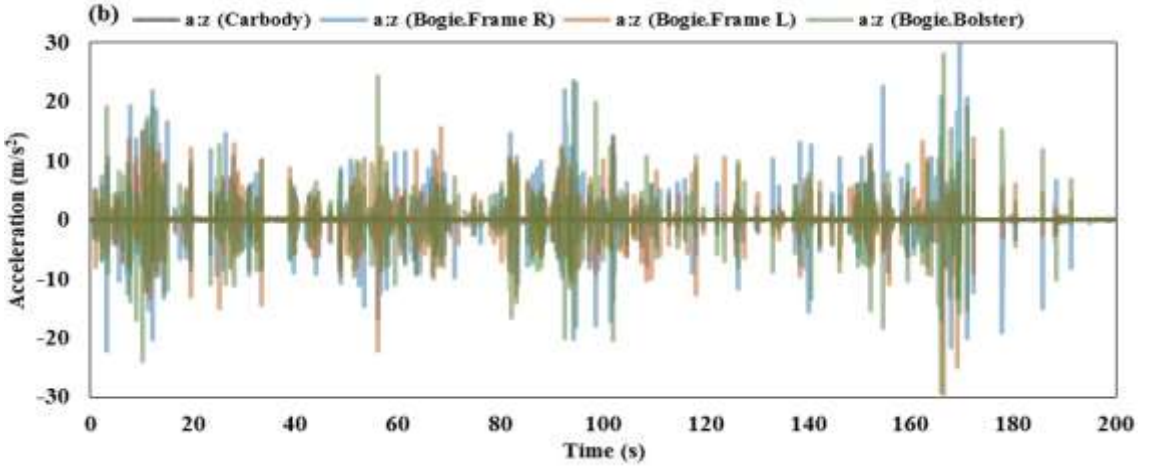

Fig. 4 Acceleration-time diagram: (a): passenger train, and (b): freight train.

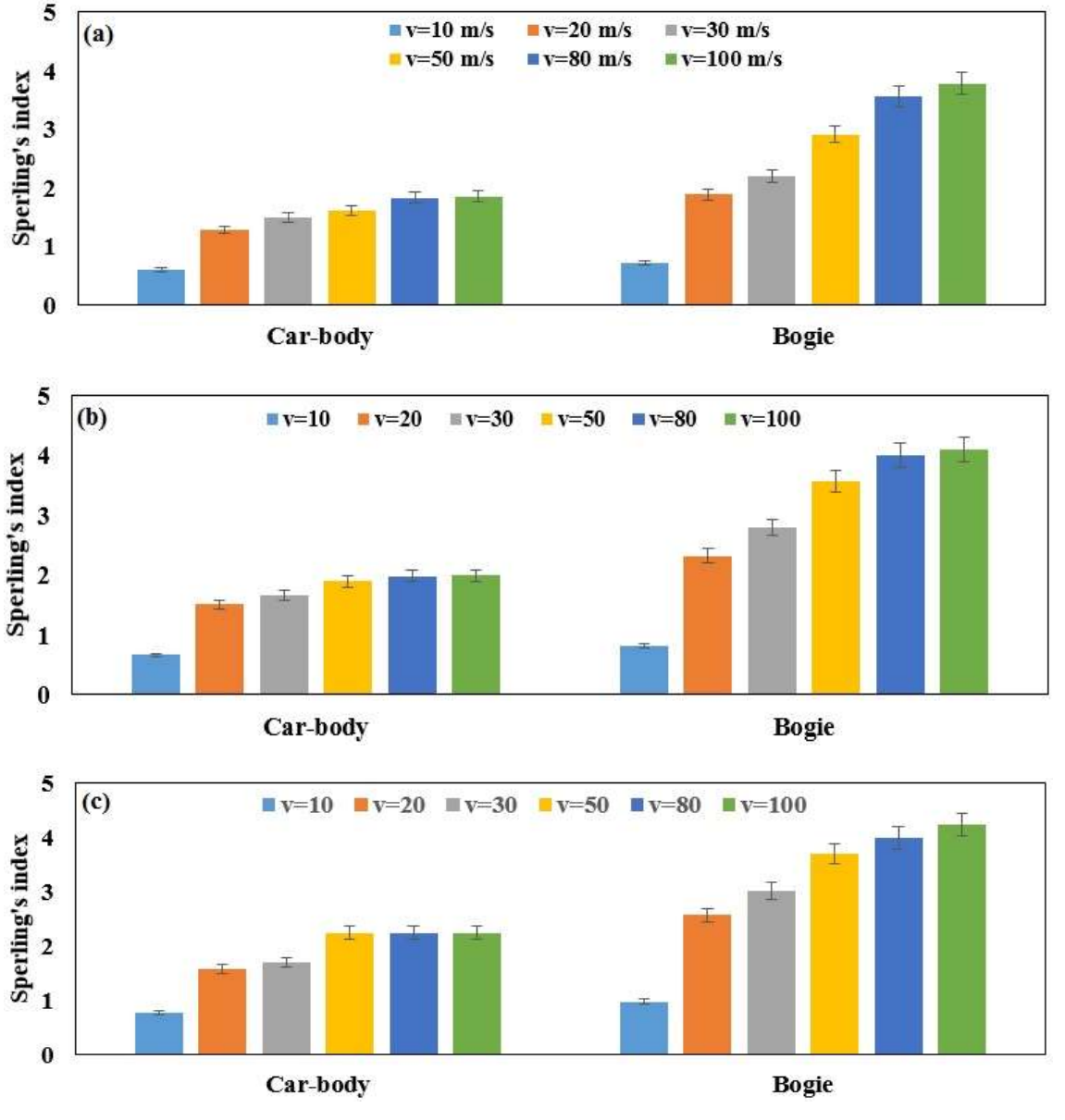

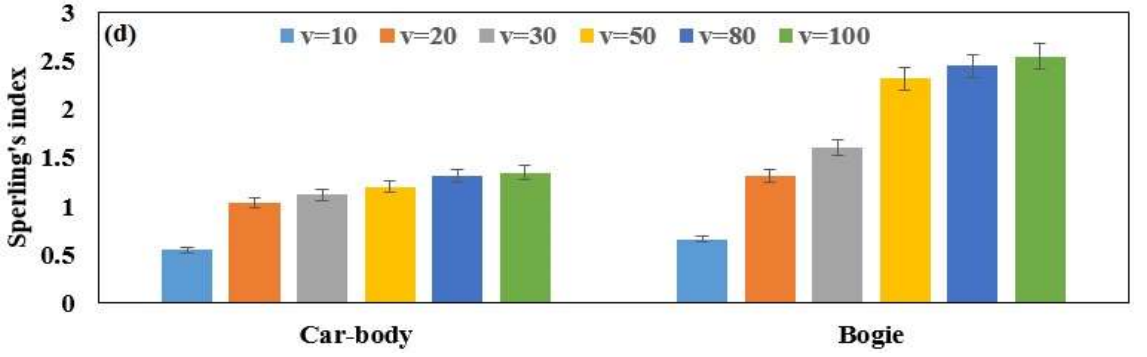

Fig. 5 Sperling's index in passenger train: (a): class 6, (b): class 5, (c): class 4, (d): Tehran's metro.

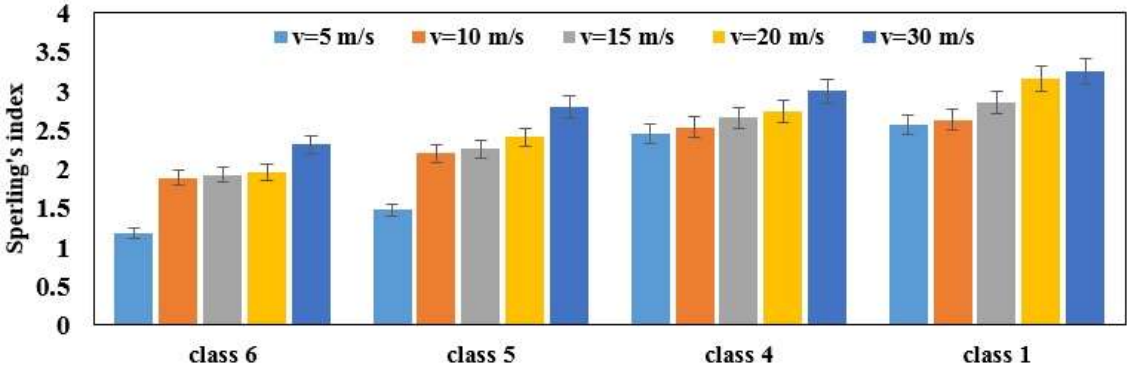

Fig. 6 Sperling's index in freight train.

In the freight train and the Sperling's index, with the increase in the train speed and irregularity amplitude, the value of ride comfort has increased. For example, in the irregularity of classes 6 and 5, with an increase in speed from 5 to 30 m/s, the Sperling's index values changed from 1.18 to 2.32 and from 1.48 to 2.80 and increased about 96% and 89%, respectively. Sperling's index shows that the ride comfort is suitable in classes 6 and 5, and in high irregularity amplitudes (classes 4 and 1) and at high speeds, it is sometimes an inappropriate situation. For example, in class 1 and at speed 5 m/s, the state of ride comfort is almost suitable (strong, irregular, but still tolerable mode), while at speed 30 m/s, the ride comfort is not suitable and changes to extremely irregular mode. In freight trains, it is better to compare the ride quality index, in which case the situation is good (less than 4). Of course, the lower the train speed and irregularity amplitude, the better the ride quality index will be, and the vehicle and track will have fewer defects and dangers. The simulation results showed that in different classes, with an increase in speed higher than 35 m/s, the freight train has an accident and derailment.

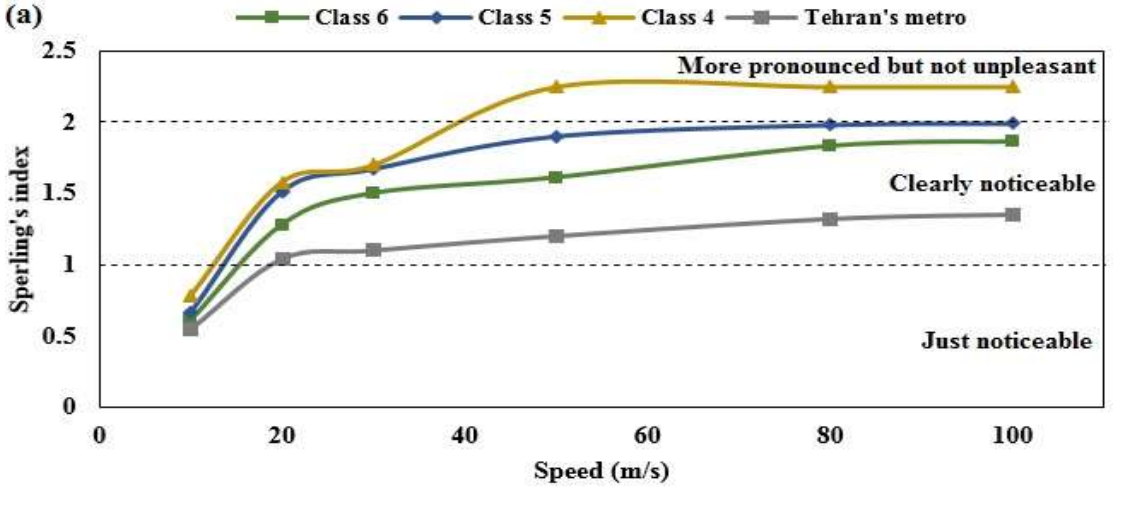

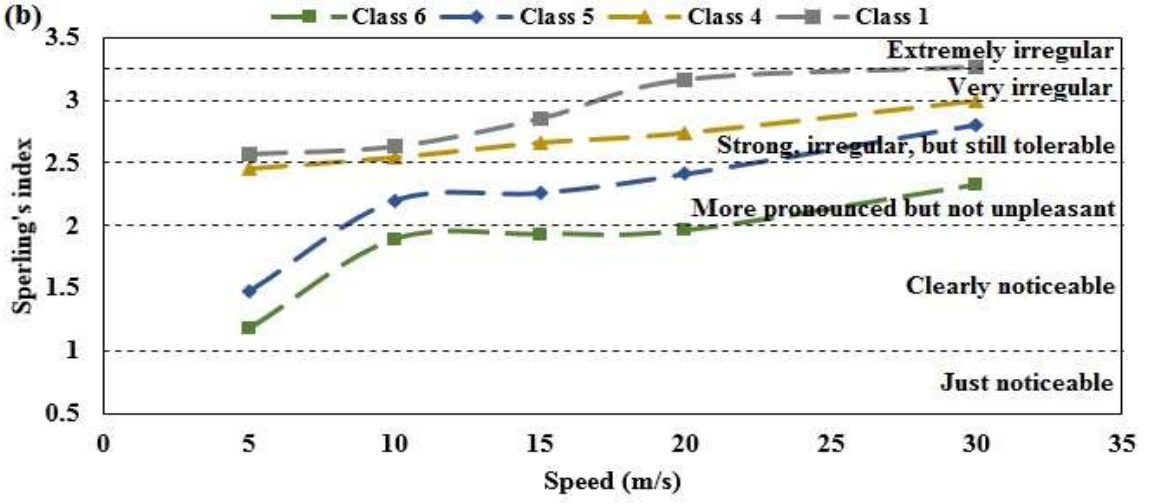

Fig. 7 Comparison of Sperling's index at different conditions: (a): passenger and (b): freight trains.

5 CONCLUSIONS

In this paper, the dynamic behavior of a passenger train and a freight train while passing over an irregular track was investigated. For this purpose, UM multibody dynamic software was used for modeling and simulation. The irregularity of the rail surface was simulated for several different track classes using random data (Using the irregularity spectrum of US tracks). An important dynamic index, namely the ride comfort, was analyzed. During a parametric study, the effect of track irregularity and train speed was investigated. The results showed that the ride comfort is strongly affected by the train speed and track irregularity. The irregularities significantly excite the strong vibration between the vehicle and the track. This not only reduces the quality of the train but also causes the failure of parts of the wheel and rail system and reduces the quality of the track.

REFERENCES

[1] Nasr, A., Taheri, M. M. N., and Shahravi, M., Tehran Subway Rolling Stock Dynamic Analysis, Transportation research, Vol. 17, No. 1, 2020, pp. 61-70.

[2] Ebadi Rajoli, J., Molatefi, H. A., Analysis of Wagon Vibration and Investigation of Track Irregularities Effect on the Ride Comfort, Quarterly Journal of Transportation Engineering, Vol. 7, No. 2, 2015, pp. 251-261.

[3] Dumitriu, M., Stănică, D. I., Study on the Evaluation Methods of the Vertical Ride Comfort of Railway Vehicle—Mean Comfort Method and Sperling's Method, Applied Sciences, Vol. 11, No. 9, 2021, pp. 3953.

[4] Haladin, I., Lakušić, S., and Bogut, M., Overview and Analysis of Methods for Assessing Ride Comfort on Tram Tracks, Građevinar, Vol. 71, 2019, pp. 901-921.

[5] Ghazavi, M, Azari Nejad, M, and Rahmanian, S., Dynamic Analysis of the Derailment of High-Speed Railway Vehicle on A Curved Path with Longitudinal Displacement, Modares Mechanical Engineering, Vol. 15, No. 5, 2015, pp. 309-318.

[6] Jiang, Y., Chen, B. K., and Thompson, C., A Comparison Study of Ride Comfort Indices Between Sperling's Method and EN 12299, International Journal of Rail Transportation, Vol. 7, No. 4, 2019, pp. 279-296.

[7] Younesian, D., Nankali, A., Spectral Optimization of High-Speed Train Suspension Systems, International Journal of Vehicle Structures & Systems, Vol. 1, 2009.

[8] Gangadharan, K. V., Sujatha, C., and Ramamurti, V., Experimental and Analytical Ride Comfort Evaluation of a Railway Coach, Mechanical Engg. Deptt., National Institute of Technology Karnataka, Surathkal, 2004.

[9] Goga, V., Kľúčik, M., Optimization of Vehicle Suspension Parameters with use of Evolutionary Computation, Procedia Engineering, Vol. 48, 2012, pp. 174-179.

[10] Sun, X., Research of Simulation on the Effect of Suspension Damping on Vehicle Ride, Energy Procedia, Vol. 17, 2012, pp. 145-151.

[11] Suarez, B., Influence of the Track Quality and of the Properties of the Wheel–Rail Rolling Contact on Vehicle Dynamics, Vehicle System Dynamics, Vol. 51, No. 2, 2013, pp. 301-320.

[12] Suarez, B., Assessment of the Influence of the Elastic Properties of Rail Vehicle Suspensions on Safety, Ride

Quality and Track Fatigue, Vehicle System Dynamics, Vol. 51, 2012.

[13] Vakil Baghmisheh, M. T., Application of Genetic Algorithms in Optimal Design of a Passive Suspension System a Vehicle Subjected to Random Excitations of Actual Road, Modares Mechanical Engineering, Vol. 10, No. 4, 2010, pp. 1-12.

[14] Vongierke, H. E. The ISO Standard: Guide for the Evaluation of Human Exposure to Whole-Body Vibration, in NASA. Langley Res. Center The 1975 Ride Quality Symp., 1975.

[15] Standardization, I. O. f., Mechanical Vibration and Shock: Evaluation of Human Exposure to Whole-body Vibration, International Organization for Standardization, 1985.

[16] Khalid, H., Turan, O., and Bos, J. E., Guide to Measurement and Evaluation of Human Exposure to Whole-Body Mechanical Vibration and Repeated Shock Guide to Measurement and Evaluation of Human Exposure to Whole-Body Mechanical Vibration and Repeated Shock 30, 1987, Journal of Marine Science and Technology, Vol. 16, No. 2, 2011, pp. 214-225.

[17] Railways, I. U. O., UIC Code 513, R: Guidelines for Evaluating Passenger Comfort in Relation to Vibration in Railway Vehicles, International Union of Railways, 1995.

[18] CEN, E., Railway Applications–Ride Comfort for Passengers–Measurement and Evaluation, Railway Applications-Ride Comfort for Passengers-Measurement and Evaluation, 2009, pp. 12299.

[19] Standardization, I. O. f., Mechanical Vibration: Measurement and Analysis of Whole-Body Vibration to Which Passengers and Crew Are Exposed in Railway Vehicles, International Organization for Standardization Geneva, 2001.

[20] Sadeghi, J., Rabiee, S., and Khajehdezfuly, A., Effect of Rail Irregularities on Ride Comfort of Train Moving Over Ballast-Less Tracks, International Journal of Structural Stability and Dynamics, Vol. 19, No. 6, 2019, pp. 1950060.

[21] Sadeghi, J., Rabiee, S., and Khajehdezfuly, A., Development of Train Ride Comfort Prediction Model for Railway Slab Track System, Latin American Journal of Solids and Structures, Vol. 17, No. 7, 2020, pp. 1-22.

[22] Kumar, V., Rastogi, V., and Pathak, P. M., Simulation for Whole-Body Vibration to Assess Ride Comfort of a Low–Medium Speed Railway Vehicle, Simulation, Vol. 93, No. 3, 2017, pp. 225-236.

[23] Zakeri, J., Impact of Heavy Urban Rail Vehicles Running Over Light Rail Turnouts, Proceedings of the Institution of Mechanical Engineers, Part F: Journal of Rail and Rapid Transit, Vol. 235, No. 3, 2021, pp. 300-312.

[24] Aziznia, M., Owhadi, A., and Shadfar, M., Analysis of wheel and rail Hertzian and Non-Hertzian Contact Theories Using UM Software Considering the Effect of Rail Inclination on Wheel Wear, International Journal of Railway Research, Vol. 8, No. 2, 2021, pp. 21-32.

[25] Kalker, J. J., Three-Dimensional Elastic Bodies in Rolling Contact, Springer Science & Business Media, Vol. 2, 2013.

[26] Pogorelov, D., Simulation of Freight Car Dynamics: Mathematical Models, Safety, Wear. 2009.

[27] Kovalev, R., Freight Car Models and Their Computer-Aided Dynamic Analysis, Multibody System Dynamics, Vol. 22, 2009, pp. 399-423.

[28] Zakharov, S., Computer-Aided Simulation of The Influence of Track and Vehicle Parameters on Wheel/Rail Intraction Characteristics, 2009.

[29] Bernal, E., Spiryagin, M., and Cole, C., Onboard Condition Monitoring Sensors, Systems and Techniques for Freight Railway Vehicles: A Review. IEEE Sensors Journal, Vol. 19, No. 1, 2019, pp. 4-24.

[30] Yazykov, V., Numerical Simulation of Railway Vehicle Derailments, 2010.

[31] Kargarnovin, M. H., Ride Comfort of High-Speed Trains Travelling Over Railway Bridges, Vehicle System Dynamics, Vol. 43, No. 3, 2005, pp. 173-197.

[32] Kargarnovin, M. H., Nonlinear Vibration and Comfort Analysis of High-Speed Trains Moving Over Railway Bridges, Vol. 2, 2004.

[33] Yang, H., Z. Chen, and Zhang, H., Vibration of Train-Rail-Bridge Interaction Considering Rail Irregularity with Arbitrary Wavelength, International Journal of Engineering, Vol. 28, No. 4, 2015, pp. 516-522.

[34] Au, F., Wang, J., and Cheung, Y., Impact Study of Cable-Stayed Railway Bridges with Random Rail Irregularities, Engineering Structures, Vol. 24, No. 5, 2002, pp. 529-541.

Int. J. Advanced Design and Manufacturing Technology, 2022, Vol. 15, No. 4, pp. 95-104

DOI: 10.30486/ADMT.2023.1962704.1364 ISSN: 2252-0406 https://admt.isfahan.iau.ir

Function Generation Synthesis of the Four-bar Linkage Based on Four and Five Precision Points using Newton-HCM

Seyed Mojtaba Varedi-Koulaei*
Department of Mechanical and Mechatronics Engineering,
Shahrood University of Technology, Iran
E-mail: varedi@shahroodut.ac.ir
*Corresponding author

Received: 6 July 2022, Revised: 25 September 2022, Accepted: 4 October 2022

Abstract: The length values selection for a determined type of linkage to achieve the necessary task, dimensional synthesis, is classified into three classes based on the mechanism's task: function generation, path generation, and motion generation. The case considered in this study, Function generation synthesis, aims to create a relation between the angular motions of the input and output links of the mechanism. For this problem, a semi-analytical method called the Newton-HCM is used for numerical solutions, which combines Newton's method with the semi-analytical Homotopy Continuation Method (HCM). Function generation synthesis of a planar four-bar linkage for four and five precision points is the main challenge of the current study, which is highly nonlinear and complicated to solve. Numerical examples of the function generation problem for a four-bar linkage with four and five precision points are presented and authenticate the excellent performance of the proposed algorithm.

Keywords: Function Generation Synthesis, HCM, Newton's Method, Planar Four-Bar Linkage, Precision Points

Biographical notes: Seyed Mojtaba Varedi-Koulaei is an assistant professor at the Shahrood University of Technology, Department of Mechanical and Mechatronics Engineering. He acquired his undergraduate and graduate degrees from Mazandaran University in 2006 and 2008, respectively. He received his PhD in Mechanical Engineering from the Babol Noshirvani University of Technology in 2015, with a dissertation entitled: "Optimal design of the parallel mechanisms considering joints clearance" under the supervision of Prof. H. M. Daniali. His research interest includes Robotics, Dynamics, Mechanism Design, and Machine learning. Moreover, he makes an effort to work on advanced subjects, such as the design of compliant mechanisms, medical instruments, rehabilitation devices, etc.

Research paper

1 INTRODUCTION

Various analytical and numerical methods are used to solve different engineering problems [1-2]. The solution's convergence and accuracy depend on the problem's type, its degree of non-linearity, and the utilized solution method. Dimensional synthesis of the planar four-bar linkage based on the function generation purpose is the main challenge of the current study. Determining the length values for a determined linkage type to achieve the necessary task is called dimensional synthesis. Dimensional synthesis can be classified into three classes based on the mechanism's task: function generation, path generation, and motion generation [3]. The purpose of the function generator mechanism is to create a relation between the angular motions of the input and output links. The path generation mechanism moves a particular point of the mechanism along prescribed points. Motion generation is similar to path generation, except that the position and orientation of the rigid body are considered together.

Chebyshev [4] and Freudenstein [5] presented beginning studies on this problem. Chebyshev solved this problem in 1854 for a straight-line path problem with a determined interval for the input link [4], also known as Chebyshev's fundamental theorem. Moreover, Freudenstein presented a simple position Equation for the four-bar linkage in 1954 [5]. This simplification results in its broad application for finding solutions to several problems, including mechanism analysis and synthesis. Modern approaches in mechanism synthesis problems result from recent improvements in calculations, using powerful calculators, genetic and evolutionary algorithms, and artificial neural networks. Rao [6-7] has optimized a 4bar linkage using Freudenstein's Equation for three precision points by minimizing the least-squares of error. Sun [8] has used the quadratic interpolation method to decrease the error of the designed four-bar linkage. Chen [9] has performed a study compared to Rao's [7] by optimizing the function generation four-bar linkage using Mudguardt's method and improving the error value. Guj et al. [10] proposed an optimization algorithm using the penalty function method to reduce the inertial force in the four-bar mechanism to optimize the high-speed mechanisms. For spatial 4-link mechanisms, Soylemez and Freudenstein [11] have optimized the transmission force for the skew crank-and-rocker linkage and the skew slider-crank mechanism. Gosselin and Angeles [12] proposed an algorithm for minimizing the transmission defect in planar and spherical function generator mechanisms. Angeles et al. [13-14] optimized the coupler curve in the path generator and the motion generator four-bar linkage using the unconstrained nonlinear least square optimization. Shariati and Norouzi [15] used the SQP method to find the optimal mechanism for five precision point syntheses of the four-bar linkages. Moreover, some researchers consider joints clearance in their design process [16-18]. Daniali et al. [16] proposed a new algorithm for simultaneous kinematic and dynamic optimization. Their method reduced the path generation error arising from joints clearance. The possibility, powerfully and simplicity of the evolutionary and genetic algorithms used for solving a wide range of problems, especially mechanism synthesis, are described in publications [18-22]. For instance, Sardashti et al. [18] synthesized the free defect four-bar linkage with clearance joints using the particle swarm optimization method. They considered branch and circuit defects in their design process and designed the mechanism without these defects. Moreover, Penunuri et al. [19] used the differential evaluation method for synthesizing the mechanisms with single and hybrid tasks. Shpli [20] used the GA method for synthesizing the path generator four-bar linkage with maximum mechanical advantage. Bustos et al. [21] used an algorithm with a combination of the finite element method and the genetic algorithm. Cabrera et al. [22] utilized the genetic algorithm for optimal synthesis of the mechanisms, too. Recently, advancements in numerical calculations and the mathematical theory of polynomials led to new solutions called continuation (or homotopy) methods. Wampler [23-25] used this method for kinematic analysis of the mechanisms. He extracted all solutions of a system of algebraic polynomial Equations using numerical continuation. After that, some researchers have used this approach in the mechanism design field [26-29]. Varedi et al. [26] used the homotopy continuation method (HCM) for solving the forward kinematics problem of the 3UPU parallel robot. Tari et al. [27] utilized HCM to exclude the unwanted solutions arising in kinematics problems. Moreover, he used this approach for kinetostatic synthesis of a compliant four-bar mechanism [28]. Furthermore, the HCM method is utilized for the kinematic analysis of the parallel robots, too [29-30].

The current study presents a combination of Newton's method and the HCM algorithm for the numerical solution of the nonlinear Equations arising in function generation synthesis of a planar four-bar linkage based on the four and five precision points. Based on the highly nonlinear nature of these problems, the numerical methods used before have some drawbacks, described before. It is the first time the Newton-HCM algorithm has been utilized for function generation synthesis problems.

2 HOMOTOPY CONTINUATION METHOD (HCM)

Proper initial guesses and convergence possibility are two troublesome points in most numerical methods,

including the Newton–Raphson. The Newton-HCM can eliminate these deficiencies [24]; consequently, several researchers have been used this method in the past decades [23-26]. In the Newton-HCM method, firstly, some new functions are written using auxiliary homotopy functions, and then the Newton-Raphson method is used for solving this system of nonlinear Equations.

If a system of nonlinear Equations is considered as:

$$F(X)=0 \quad \text{i.e} \begin{cases} a(x,y,\dots,z)=0, \\ b(x,y,\dots,z)=0, \\ \cdot \\ \cdot \\ \cdot \\ \cdot \end{cases} \tag{1}$$

One can solve these Equations using the iterative algorithm of Newton's method as:

$$\begin{bmatrix} \frac{\partial a(x_n,y_n,\dots)}{\partial x} & \frac{\partial a(x_n,y_n,\dots)}{\partial y} & . & . & . \\ \frac{\partial b(x_n,y_n,\dots)}{\partial x} & \frac{\partial b(x_n,y_n,\dots)}{\partial y} & . & . & . \\ . & . & . & & \\ . & . & & . & \\ . & . & & & . \end{bmatrix} \begin{bmatrix} x_{n+1}-x_n \\ y_{n+1}-y_n \\ . \\ . \\ . \end{bmatrix} = \begin{bmatrix} -a(x_n,y_n,\dots) \\ -b(x_n,y_n,\dots) \\ . \\ . \\ . \end{bmatrix} \tag{2}$$

HCM approach converts this system of nonlinear Equations to new ones by eliminating some terms and adding auxiliary homotopy functions, which leads to solving these Equations more efficiently. Indeed, Newton's method is used for solving the new system of Equations, which is easier, and its solutions are accessible. The converted system of Equations, called homotopy continuation functions, is as follows [23-25]:

$$H(X,t) \equiv t\,F(X) + (1-t)A(X) = 0 \tag{3}$$

Where, $A(X)$ are new simple Equations for initializing the solution process or auxiliary homotopy functions that must be solved easily. Moreover, t is an iteration setting parameter that changes from 0 to 1 and defines two boundary conditions [23-25]:

$$H(X,0)=A(X), \quad H(X,1)=F(X) \tag{4}$$

The above Equation shows that HCM solves $A(X)=0$ at the first iteration (when $t=0$), and solves $F(X)=0$ at the final iteration (when $t=1$). All of these solutions in each iteration are using Newton's method:

$$\begin{bmatrix} \frac{\partial H_1(x_n,y_n,\dots)}{\partial x} & \frac{\partial H_1(x_n,y_n,\dots)}{\partial y} & . & . & . \\ \frac{\partial H_2(x_n,y_n,\dots)}{\partial x} & \frac{\partial H_2(x_n,y_n,\dots)}{\partial y} & . & . & . \\ . & . & . & & \\ . & . & & . & \\ . & . & & & . \end{bmatrix} \begin{bmatrix} x_{n+1}-x_n \\ y_{n+1}-y_n \\ . \\ . \\ . \end{bmatrix} = \begin{bmatrix} -H_1(x_n,y_n,\dots) \\ -H_2(x_n,y_n,\dots) \\ . \\ . \\ . \end{bmatrix} \tag{5}$$

Indeed, the HCM iterative algorithm transforms the converted system's solution into the numerical results of the basic system of Equations. The HCM's purpose is to solve the $H(X,t)=0$ instead of $F(X)=0$ by changing the parameter t from 0 to 1. This algorithm leads to avoiding divergence in the numerical solution of the system of nonlinear Equations.

3 PLANAR FOUR-BAR MECHANISM

The simplest closed-loop mechanism is the four-bar linkage, which has four rigid links and four revolute joints. A typical planar four-bar linkage is shown in Fig.1. In this figure, the lengths of the links A_0B_0, A_0A, AB and B_0B are denoted by the angles l_1, l_2, l_3 and l_4, respectively. A_0B_0 is fixed while the two links A_0A and B_0B can only rotate about their respective fixed axes A_0 and B_0. Moreover, their position angles are indicated respectively by ψ and φ. The link connected to the actuator or driving motor is called the input link (A_0A) and B_0B is known as the output link. In "Fig. 1", if the vector x is along the ground, the vectors of A_0A, A_0B_0 and B_0B are:

$$\overrightarrow{A_0A} = \begin{bmatrix} l_2\cos\psi \\ l_2\sin\psi \end{bmatrix}, \quad \overrightarrow{A_0B_0} = \begin{bmatrix} l_1 \\ 0 \end{bmatrix}, \quad \overrightarrow{B_0B} = \begin{bmatrix} l_4\cos\varphi \\ l_4\sin\varphi \end{bmatrix} \tag{6}$$

Therefore, the vector of the coupler link can be obtained as:

$$\begin{aligned}\overrightarrow{AB} &= \overrightarrow{A_0B_0} + \overrightarrow{B_0B} - \overrightarrow{A_0A} \\ &= \begin{bmatrix} l_1 + l_4\cos\varphi - l_2\cos\psi \\ l_4\sin\varphi - l_2\sin\psi \end{bmatrix}\end{aligned} \tag{7}$$

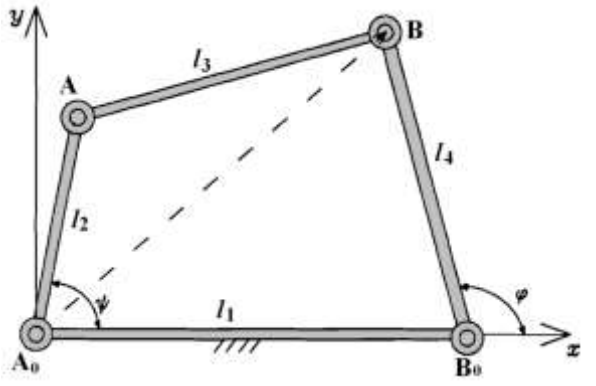

Fig. 1 Planar four-bar mechanism.

The length of the coupler link is designated as l_3. Thus, one can write:

$$\begin{aligned}l_3^2 = (l_1 + l_4\cos\varphi - l_2\cos\psi)^2 \\ + (l_4\sin\varphi - l_2\sin\psi)^2\end{aligned} \tag{8}$$

Simplifying "Eq. (8)", Freudenstein obtained a simple scalar Equation [5]:

$$k_1 + k_2\cos\varphi - k_3\cos\psi = \cos(\psi - \varphi) \tag{9}$$

Where:

$$\begin{aligned}k_1 &= \frac{l_1^2 + l_2^2 + l_4^2 - l_3^2}{2l_2l_4} \\ k_2 &= \frac{l_1}{l_2} \\ k_3 &= \frac{l_1}{l_4}\end{aligned} \tag{10}$$

Equation (9) is known as the Freudenstein Equation and is readily applicable to the kinematics analysis of planar four-bar linkage. However, in a planar four-bar mechanism, the functional relationship $\varphi = \varphi(\psi)$ between output and input angles depends on three independent parameters (k_1, k_2, k_3).
If the lengths of the links (l_1, l_2, l_3 and l_4) are known, one can obtain parameters (k_1, k_2, k_3) from "Eq. (11)", and therefore, the output angle φ can be determined in any input angle ψ. This is done utilizing tan-half-angle identities:

$$\begin{aligned}T &= \tan\left(\frac{\varphi}{2}\right) \\ \sin\varphi &= \frac{2T}{1+T^2} \\ \cos\varphi &= \frac{1-T^2}{1+T^2}\end{aligned} \tag{11}$$

Substituting of the preceding Equation into "Eq. (9)", a quadratic Equation in T is achieved:

$$A(\psi)T^2 + B(\psi)T + C(\psi) = 0 \tag{12}$$

Where:

$$\begin{aligned}A(\psi) &= (k_1 - k_2) + (1 - k_3)\cos\psi \\ B(\psi) &= -2\sin\psi \\ C(\psi) &= (k_1 + k_2) - (1 + k_3)\cos\psi\end{aligned} \tag{13}$$

Considering "Eq. (12)", the solution can be found by utilizing the well-known method for the roots of the quadratic Equation.
On the other hand, if the parameters (k_1, k_2, k_3) are known and supposing $l_1 = 1$, one can find the length of the link as:

$$\begin{aligned}l_2 &= \frac{1}{k_2} \\ l_4 &= \frac{1}{k_3} \\ l_3 &= \sqrt{1 + l_2^2 + l_4^2 - \frac{2k_1}{k_2k_3}}\end{aligned} \tag{14}$$

4 FUNCTION GENERATION SYNTHESIS

Function generation synthesis is the problem of obtaining link's lengths, l_1, l_2, l_3 and l_4, for a determined set of input and output angles values, ψ_i and φ_i. For function generation synthesis based on three precision points, "Eq. (9)" can be utilized directly. Given three pairs of the input and output angles (ψ_i, φ_i), i=1,2,3, one can use these angle pairs in "Eq. (9)" to get three linear Equations in k_1, k_2, and k_3:

$$\begin{aligned}k_1 + k_2\cos\varphi_i - k_3\cos\psi_i \\ = \cos(\psi_i - \varphi_i) \quad , i = 1..3\end{aligned} \tag{15}$$

"Eq. (16)" shows this system of linear Equations in matrix form.

$$\begin{bmatrix} 1 & \cos\varphi_1 & -\cos\psi_1 \\ 1 & \cos\varphi_2 & -\cos\psi_2 \\ 1 & \cos\varphi_3 & -\cos\psi_3 \end{bmatrix} \begin{Bmatrix} k_1 \\ k_2 \\ k_3 \end{Bmatrix} = \begin{bmatrix} \cos(\psi_1 - \varphi_1) \\ \cos(\psi_2 - \varphi_2) \\ \cos(\psi_3 - \varphi_3) \end{bmatrix} \tag{16}$$

Once k_1, k_2, and k_3 are resulting from the solution of the linear system of Equations ("Eq. (16)"), the link's lengths can be obtained easily using "Eq. (14)".
It has shown that the function generation synthesis problem for three precision points is easy and straightforward because the system of Equations is linear. However, if precision points are more than three, the system of Equations becomes nonlinear, and therefore, one must use other analytical or numerical solutions for them. For designs with a higher number of precision points, two new variables (ψ_0 and φ_0) indicating the rotation angles from undefined and arbitrary starting points are proposed by Freudenstein.

4.1. Four-Precision Points (4PP)

There are four angle pairs in the 4PP problem, and utilizing "Eq. (9)" for these pairs leads to four Equations. Thus, in this case, ψ_0 is considered as the fourth unknown parameter. Indeed, the input angle ψ, is considered as the sum of two angles, the reference angle ψ_0, and the variable angle $\Delta\psi_i$:

$$\psi_i = \psi_0 + \Delta\psi_i, \quad i = 1..4 \tag{17}$$

Substituting "Eq. (17)" in "Eq. (9)" for four angle pairs are as follows:

$$\begin{aligned} k_1 + k_2\cos\varphi_i - k_3\cos(\psi_i + \psi_0) \\ = \cos(\psi_i + \psi_0 - \varphi_i) \quad , i \\ = 1..4 \end{aligned} \tag{18}$$

Therefore, The Equations in "Eq. (18)" are a set of four nonlinear Equations with four unknowns: k_1, k_2, k_3 and ψ_0. This system of nonlinear Equations can be solved using the Newton-HCM.
Based on "Eq. (18)", the homotopy continuation functions can be written as follows:

$$\begin{aligned} &(k_1 + k_2\cos\varphi_1 - k_3\cos(\psi_1 + \psi_0) \\ &\quad - \cos(\psi_1 + \psi_0 - \varphi_1)) \times t \\ &\quad + (1-t) \times G_1 = 0 \\ &(k_1 + k_2\cos\varphi_2 - k_3\cos(\psi_2 + \psi_0) \\ &\quad - \cos(\psi_2 + \psi_0 - \varphi_2)) \times t \\ &\quad + (1-t) \times G_2 = 0 \\ &(k_1 + k_2\cos\varphi_3 - k_3\cos(\psi_3 + \psi_0) \\ &\quad - \cos(\psi_3 + \psi_0 - \varphi_3)) \times t \\ &\quad + (1-t) \times G_3 = 0 \\ &(k_1 + k_2\cos\varphi_4 - k_3\cos(\psi_4 + \psi_0) \\ &\quad - \cos(\psi_4 + \psi_0 - \varphi_4)) \times t \\ &\quad + (1-t) \times G_4 = 0 \end{aligned} \tag{19}$$

The solution of these Equations can be obtained by changing the auxiliary homotopy functions (G_i) and solved by the Newton-Raphson method.

4.2. Five-Precision Points (5PP)

For the 5PP problem, one can add the other reference angle φ_0 to the Equations ($\varphi_i = \varphi_0 + \Delta\varphi_i$). Therefore, "Eq. (18)" changes to:

$$\begin{aligned} k_1 + k_2\cos(\varphi_i + \varphi_0) - k_3\cos(\psi_i + \psi_0) \\ = \cos(\psi_i + \psi_0 - (\varphi_i \\ + \varphi_0)) \quad , i = 1..5 \end{aligned} \tag{20}$$

Following the previous section, we have five unknowns: k_1, k_2, k_3, ψ_0 and φ_0. As a result, "Eq. (20)" is a set of five nonlinear Equations with five unknowns. Therefore, homotopy continuation functions are as follows:

$$\begin{aligned} &(k_1 + k_2\cos\varphi_1 - k_3\cos(\psi_1 + \psi_0) \\ &\quad - \cos(\psi_1 + \psi_0 - \varphi_1)) \times t \\ &\quad + (1-t) \times G_1 = 0 \\ &(k_1 + k_2\cos\varphi_2 - k_3\cos(\psi_2 + \psi_0) \\ &\quad - \cos(\psi_2 + \psi_0 - \varphi_2)) \times t \\ &\quad + (1-t) \times G_2 = 0 \\ &(k_1 + k_2\cos\varphi_3 - k_3\cos(\psi_3 + \psi_0) \\ &\quad - \cos(\psi_3 + \psi_0 - \varphi_3)) \times t \\ &\quad + (1-t) \times G_3 = 0 \\ &(k_1 + k_2\cos\varphi_4 - k_3\cos(\psi_4 + \psi_0) \\ &\quad - \cos(\psi_4 + \psi_0 - \varphi_4)) \times t \\ &\quad + (1-t) \times G_4 = 0 \\ &(k_1 + k_2\cos\varphi_5 - k_3\cos(\psi_5 + \psi_0) \\ &\quad - \cos(\psi_5 + \psi_0 - \varphi_5)) \times t \\ &\quad + (1-t) \times G_5 = 0 \end{aligned} \tag{21}$$

It is worth noting that the solution of the above nonlinear Equations ("Eqs. (19) and (21)") has many answers; however, we choose one of the answers, which satisfies some constraints, including Grashof criteria, free defects, etc.

5 NUMERICAL EXAMPLES

Consider a planar four-bar linkage to produce the precision points of "Table 1". (For the 4PP problem: i=1...4 and for the 5PP problem: i=1...5). Fixed variations for the homotopy parameter t and the initial guesses for the unknown parameters are considered as $\Delta t = 0.0001$ and $[k_{1,0}, k_{2,0}, k_{3,0}, \psi_{0,0}, \varphi_{0,0}] = [1,1,1,1,1]$, respectively. The auxiliary homotopy functions along with the results of the solution of the two problems are given in "Table 2".

Table 1 Desired values for the input and output angles

	$i=1$	$i=2$	$i=3$	$i=4$	$i=5$
ψ_i (deg)	100	123	141	158	188
φ_i (deg)	38.5	61	77	90.5	108

Using "Eq. (14)", one can obtain lengths of the link as "Table 3". Moreover, we show the reference angles ψ_0 and φ_0 (in degree) in this table. These values must be added to the values of "Table 1". The reason is, here, the designed mechanisms show these new values in their input and output angles. These new values are shown in "Table 4".

Table 2 The auxiliary homotopy functions and their results

Problem	auxiliary homotopy functions (G_i)					Results				
	G_1	G_2	G_3	G_4	G_5	k_1	k_2	k_3	ψ_0	φ_0
4PP	k_1	$-k_2$	$-k_3$ -1	$\cos\psi_0$	---	1.0797	-0.5083	-0.4497	5.3558	---
5PP	$-k_1$	$-k_2$	$-k_3$	$-\sin\psi_0$	$-\cos\psi_0$	1.1697	0.9165	0.8222	2.4188	3.3032

Table 3 Link's lengths of the designed mechanisms

Problem	l_1	l_2	l_3	l_4	ψ_0 (deg)	φ_0(deg)
4PP	1	-1.9673	0.6072	-2.2236	306.86°	---
5PP	1	1.0911	0.7518	1.2162	138.58°	189.26°

Table 4 New values for input and output angles of the two problems

Problem	Angles	$i=1$	$i=2$	$i=3$	$i=4$	$i=5$
4PP	ψ_i (deg)	46.86	69.86	87.86	104.86	---
	φ_i (deg)	38.50	61.00	77.00	90.50	---
5PP	ψ_i (deg)	238.58	261.58	279.58	296.58	326.58
	φ_i (deg)	227.76	250.26	266.26	279.76	297.26

Figure 2a shows the mechanism designed for the first problem in four positions. Moreover, one can plot the diagram of θ_4 (or φ) with respect to θ_2 (or ψ) for this mechanism ("Fig. 2b"). These figures show that the designed mechanism precisely covers the values of "Table 4". Furthermore, for a better comparison, "Fig. 3" shows these precision points separately.

Similarly, these figures can be plotted for the second problem. Figure 4 shows the mechanism designed for the five-precision point problem. One can find the best matching between "Fig. 4a and Fig. 4b". Moreover, detailed angles for these five precision points are shown in "Fig. 5".

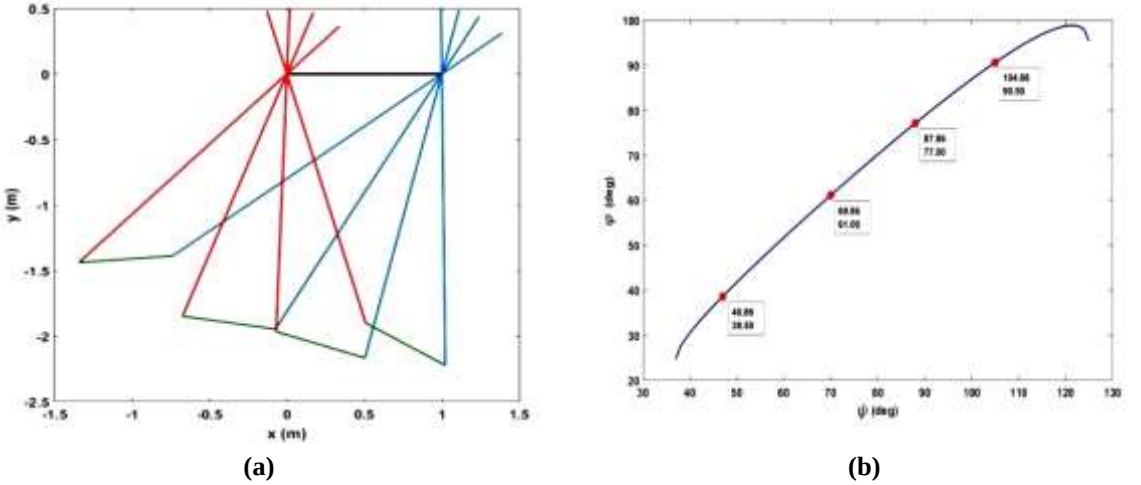

(a) **(b)**

Fig. 2 The designed mechanism for the 4PP problem.

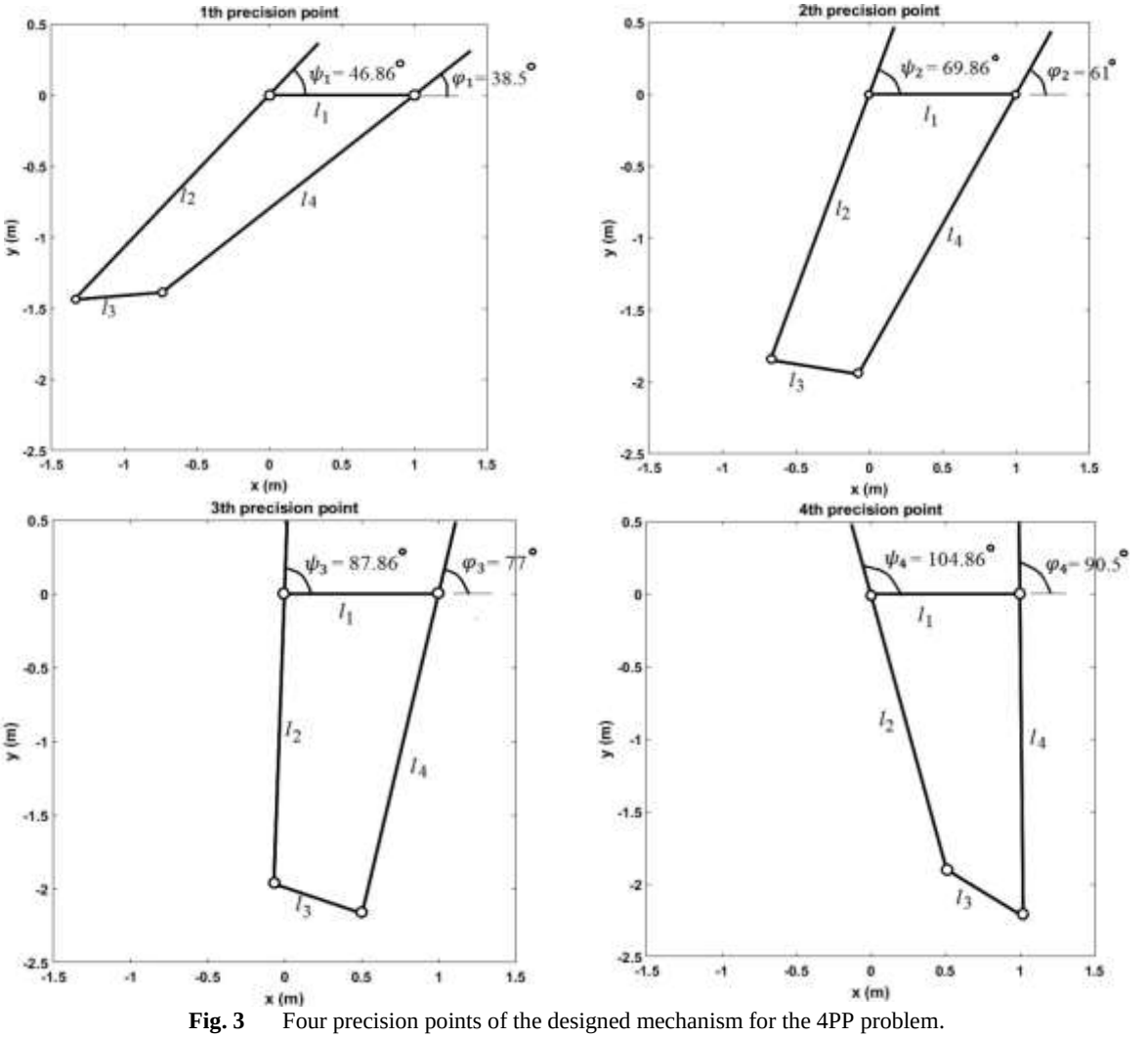

Fig. 3 Four precision points of the designed mechanism for the 4PP problem.

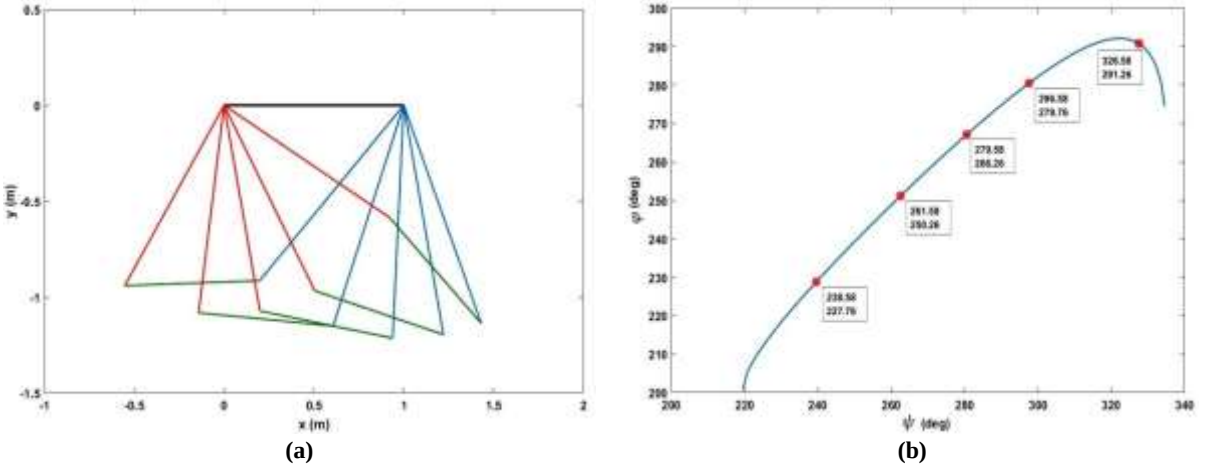

(a) **(b)**

Fig. 4 The designed mechanism for the 5PP problem

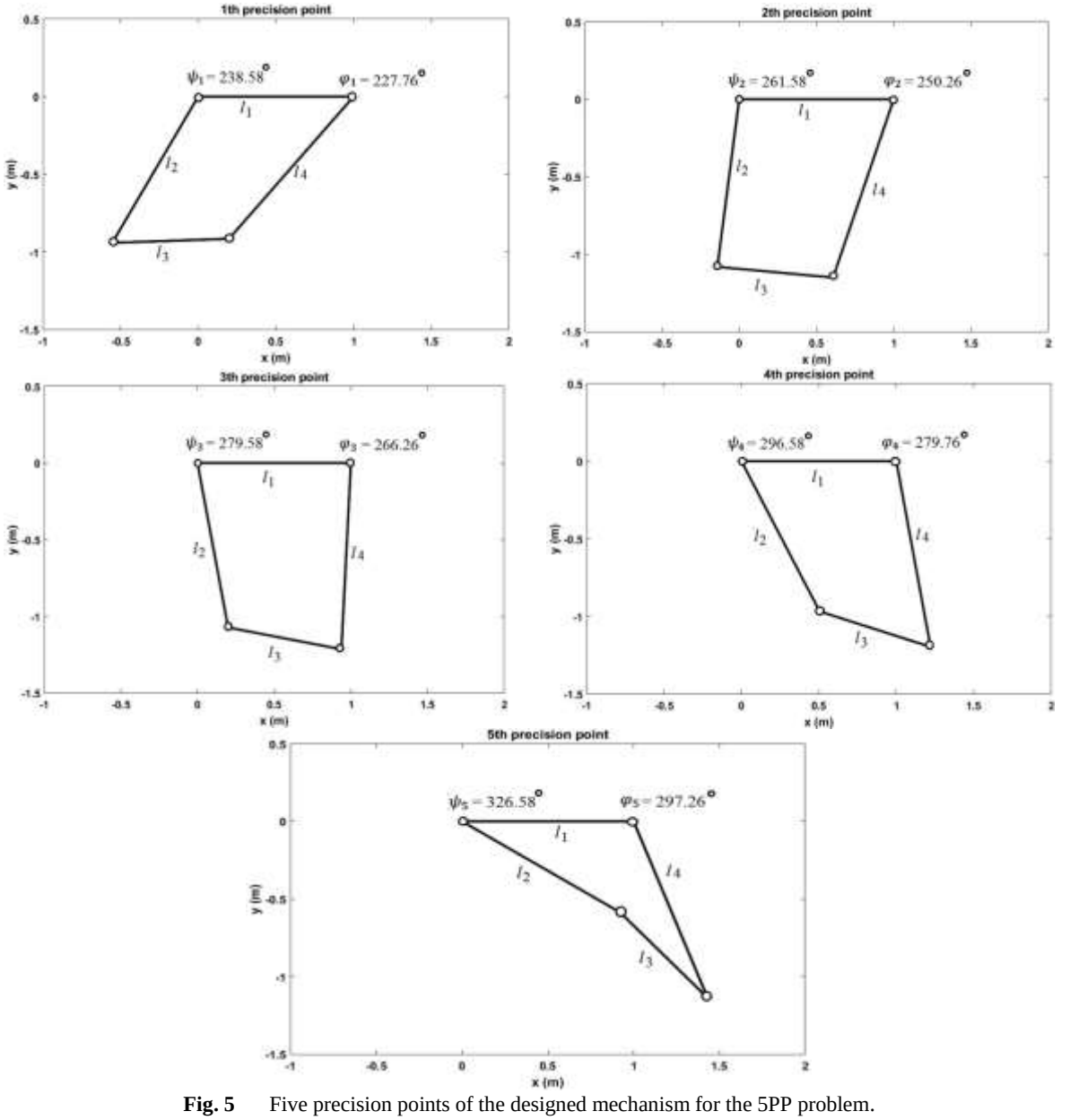

Fig. 5 Five precision points of the designed mechanism for the 5PP problem.

If the number of precision points is more than five, then the problem does not have any precise solution; this is because the number of the Equation is more than the unknowns (the maximum number of unknowns for this problem is five). Therefore, one must search for solutions with the minimum error by using the optimization algorithms.

6 CONCLUSIONS

This research uses a powerful approach to solve the nonlinear Equations arising in the function generation synthesis of the planar four-bar mechanism. The problem has been considered in two cases: with four and five precision points. The solution procedure is based on the Newton-HCM, combining numerical and semi-analytical methods.

The Equations reveal that the synthesis problem leads to a system of nonlinear Equations by four Equations and four unknown parameters for the 4PP problem and a system of nonlinear Equations by five Equations and five unknown parameters for the 5PP problem. Both cases have been solved and using the Numerical examples show that the considered algorithm is capable and highly accurate for the mechanism synthesis problem, and the designed mechanisms precisely cover the desired values.

REFERENCES

[1] Kachapi, S. H., Ganji, D. D., Davodi, A. G., and Varedi, S. M., Periodic Solution for Strongly Nonlinear Vibration Systems by He's Variational Iteration Method, Mathematical Methods in the Applied Sciences, Vol. 32, No. 18, 2009, pp. 2339-2349, DOI: 10.1002/mma.1135.

[2] Kosari, A., Jahanshahi, H., and Razavi, A. A., Design of Optimal PID, Fuzzy and New Fuzzy-PID Controller for CANSAT Carrier System Thrust Vector, ADMT Journal, Vol. 8, No. 2, 2015, pp. 1-9.

[3] Varedi-Koulaei, S. M., Rezagholizadeh, H., Synthesis of the Four-Bar Linkage as Path Generation by Choosing the Shape of The Connecting Rod, Proceedings of the Institution of Mechanical Engineers, Part C: Journal of Mechanical Engineering Science, Vol. 234, No. 13, 2020, pp. 2643-2652, DOI: 10.1177/0954406220908616.

[4] Chebyshev, P. L., Theorie Des Mecanismes Connaissent Comme Parallelogrames, Memoires Presenes à l'Academie Imperial Des Sciences De St.- Petersbourg Par Divers Savants, 1854, pp. 539-568.

[5] Freudenstein, F., An Analytical Approach to The Design of Four-Link Mechanisms, Trans. ASME, Vol. 76, 1954, pp. 483–492, DOI: 10.1115/1.4014881.

[6] Rao, A. C., Kinematic Design of Four-Bar Function Generators with Optimum Sensitivity, Mech Mach Theory, Vol. 10, 1975, pp. 531–535, DOI: 10.1016/0094-114X(75)90008-7.

[7] Rao, A. C., Optimum Design of Four-Bar Function Generators with Minimum Variance Criterion, J Optim Theory Appl, Vol. 29, No. 1, 1979, pp. 147–153, DOI: 10.1007/BF00932641.

[8] Sun, W., Optimum Design Method for Four-Bar Function Generators, J. Optim Theory Appl, Vol. 38, No. 2, 1982, pp. 287–293, DOI: 10.1007/BF00934089.

[9] Chen, F. Y., Chan, V. L., Dimensional Synthesis of Mechanisms for Function Generator Using Marguardt's compromise, J. Eng Ind, Vol. 96, 1974, pp. 131–137, DOI: 10.1115/1.3438287.

[10] Guj, G., Dong, Z. Y., and Giacinto, M. D., Dimensional Synthesis of Four Bar Linkage for Function Generation with Velocity and Acceleration Constraints. Meccanica, Vol. 16, No. 4, 1981, pp. 210–219, DOI: 10.1007/BF02128323.

[11] Söylemez, E., Freudenstein, F., Transmission Optimization of Spatial 4-Link Mechanisms, Mech Mach Theory, Vol. 17, No. 4, 1982, pp. 263–283, DOI: 10.1016/0094-114X(82)90050-7.

[12] Gosselin, C., Angeles, J., Optimization of Planar and Spherical Function Generators as Minimum-Defect Linkages, Mech Mach Theory, Vol. 24, No. 4, 1989, pp. 293–307, DOI: 10.1016/0094-114X(89)90049-9.

[13] Angeles, J., Alivizatos, A., and Akhras, R., An Unconstrained Nonlinear Least-Square Method of Optimization of RRRR Planar Path Generators, Mech Mach Theory, Vol. 23, No. 5, 1988, pp. 343–353, DOI: 10.1016/0094-114X(88)90048-1.

[14] Akhras, R., Angeles, J., Unconstrained Nonlinear Least-Square Optimization of Planar Linkages for Rigid-Body Guidance, Mech Mach Theory, Vol. 25, No. 1, 1990, pp. 97–118, DOI: 10.1016/0094-114X(90)90110-6.

[15] Shariati, M., Norouzi, M., Optimal Synthesis of Function Generator of Four-Bar Linkages Based on Distribution of Precision Points, Meccanica, Vol. 46, 2011, pp. 1007–1021, DOI: 10.1007/s11012-010-9357-1.

[16] Daniali, H. M., Varedi, S. M., Dardel, M., and Fathi, A., A Novel Algorithm for Kinematic and Dynamic Optimal Synthesis of Planar Four-bar Mechanisms with Joint Clearance, Journal of Mechanical Science and Technology, Vol. 29, No. 5, 2015, pp. 2059-2065, DOI: 10.1007/s12206-015-0426-1.

[17] Farajtabar, M., Daniali, H. M., and Varedi, S. M., Pick and Place Trajectory Planning of Planar 3-Rrr Parallel Manipulator in The Presence of Joint Clearance, Robotica, Vol. 35, No. 2, 2017, pp. 241-253. DOI: 10.1017/S0263574714002768.

[18] Sardashti, A., Daniali, H. M., and Varedi, S. M., Optimal Free-Defect Synthesis of Four-Bar Linkage with Joint Clearance Using PSO Algorithm, Meccanica, Vol. 48, No. 7, 2013, pp. 1681-1693, DOI: 10.1007/s11012-013-9699-6.

[19] Penunuri, F., Peon Escalante, R., Villanueva, C. and Pech Oy, D., Synthesis of Mechanism for Single- and Hybrid-Tasks Using Differential Evolution. Mech Mach Theory, Vol. 46, No. 10, 2011, pp. 1335-1349, DOI: 10.1016/j.mechmachtheory.2011.05.013.

[20] Shpli, O. A., Genetic Algorithms in Synthesis of Path Generator Four-Bar Mechanism with Maximum Mechanical Advantage. ASM 2007, The 16th IASTED International Conference on Applied Simulation and Modelling; 2007 Aug 29-31, Palma de Mallorca, Spain, California: ACTA Press, pp. 154-161.

[21] Fernández-Bustos, I., Aguirrebeitia, J., Avilés, R., and Angulo, C., Kinematical Synthesis of 1-Dof Mechanisms Using Finite Elements and Genetic Algorithm, Finite Elements in Analysis and Design, Vol. 41, No. 15, 2005, pp. 1441-1463, DOI: 10.1016/j.finel.2005.04.001.

[22] Cabrera, J. A., Simon, A., and Prado, M., Optimal Synthesis of Mechanisms with Genetic Algorithms, Mech Mach Theory, 37, 2002, pp. 1165–1177, DOI: 10.1016/S0094-114X(02)00051-4.

[23] Wampler, C. W., Solving the Kinematics of Planar Mechanisms, ASME Journal of Mechanical Design, Vol. 121, 1999, pp. 387-391, DOI: 10.1115/1.2829473.

[24] Wampler, C.W., Solving the Kinematics of Planar Mechanisms by Dixon Determinant and a Complex-Plane Formulation, ASME J. Mechanical Design, Vol. 123, 2001, pp. 3382–387, DOI: 10.1115/1.1372192.

[25] Wampler, C. W., Sommese, A. J., Numerical Algebraic Geometry and Algebraic Kinematics, Acta Numerica, 2011, pp. 469–567, DOI: 10.1017/S0962492911000067.

[26] Varedi, S. M., Daniali, H. M., and Ganji, D. D., Kinematics of an Offset 3-Upu Translational Parallel Manipulator by The Homotopy Continuation Method, Nonlinear Analysis: Real World Applications, Vol. 10, 2009, pp. 1767–1774, DOI: 10.1016/j.nonrwa.2008.02.014.

[27] Tari, H., Su, H. J., and Li, T. Y., A Constrained Homotopy Technique for Excluding Unwanted Solutions from Polynomial Equations Arising in Kinematics Problems, Mech Mach Theory, Vol. 45, No. 6, 2010, pp. 898–910, DOI: 10.1016/j.mechmachtheory.2010.01.002.

[28] Tari, H. Su, H. J., A Complex Solution Framework for The Kinetostatic Synthesis of a Compliant Four-Bar Mechanism, Mech Mach Theory, Vol. 46, No. 8, 2011, pp. 1137–1152, DOI: 10.1016/j.mechmachtheory.2011.03.003.

[29] Shafiee-Ashtiani, M., Yousefi-Koma, A., Keshavarz, H., and Varedi-Koulaei, S. M., Real Time Direct Kinematics Solution of 3-RPS Parallel Robot Using a Semi-Analytical Homotopy Method, Modares Mechanical Engineering, Vol. 17, No. 6, 2017, pp. 303-310 (in Persian).

[30] Varedi-Koulaei, S. M., Rahimi, M., Direct Kinematics Solution of 3-RCC Parallel Robot using a Semi-Analytical Homotopy Method, ADMT Journal, Vol. 12, No. 1, 2019, pp. 1-12.

Int. J. Advanced Design and Manufacturing Technology, 2022, Vol. 15, No. 4, pp. 105-112

DOI: 10.30486/admt.2022.1962069.1363 *ISSN: 2252-0406* *https://admt.isfahan.iau.ir*

Fuzzy Tracking Control of the 3PRR Parallel Rehabilitation Robot

Moosarreza Shamsyeh Zahedi, Zahra Fathipour*
Department of Mathematics,
Payame Noor University, Tehran, Iran
E-mail: m.s.zahedi@pnu.ac.ir, Zahra.fathipour@yahoo.com
*Corresponding author

Majid Anjidani
Department of Computer Engineering and Information Technology,
Payame Noor University, Tehran, Iran
E-mail: M_anjidani@pnu.ac.ir

Received: 2 July 2022, Revised: 6 October 2022, Accepted: 12 October 2022

Abstract: In this study, a couple of 3PRR parallel robot is used for the rehabilitation process of a patient to eliminate a walking disability and leads to his treatment. The 3PRR robot has three degrees of freedom, provided by three prismatic actuators. Also using a couple of them, can quickly rehabilitate and provide the rehabilitation movements of a patient in the walking process. In this study, the extraction of kinematic and dynamic Equations of the robot was investigated, and a fuzzy-logic-based controller is performed. This controller has the ability to repel unwanted disturbances to follow the desired path. All modelling was simulated by MATLAB software. The simulation results show that using the mathematical model and controller, it is easy to go any desired path in the workspace; and this controller will be able to repel environmental disturbances like the sudden movement of patients.

Keywords: Fuzzy Tracking Control, Modeling, 3PRR Parallel Robot, Rehabilitation, Walking Operation

Biographical notes: Moosarreza Shamsyeh Zahedi received his PhD from the University of Pune-India in 2007 in the field of Applied Mathematics. He is now an assistant professor at PNU. More than 15 papers and 2 published books are the results of his research so far. His research interests include image processing and fractal application in biology. **Zahra Fathipour** is a PhD candidate at PNU in the field of Applied Mathematics. She received her MSc in Applied Mathematics from Kerman University in 2010. Her research interests include modelling dynamic systems, optimization, and control. **Majid Anjidani** received his PhD from IUST in 2017 in the field of Computer Engineering. His research interests include robotics, machine vision, machine learning, and virtual reality.

Research paper

1 INTRODUCTION

By definition, a stroke is the loss of brain function due to a disorder or blockage of a blood vessel. As a result, the damaged part of the brain cannot function normally, leading to the inability to move one or more limbs [1]. According to statistics, about eight hundred thousand people in the United States have a stroke each year, and only three hundred thousand people can survive after a stroke. This number reaches two million people in China every year. Even in Canada, 50,000 people have a stroke each year. After treatment, vital signs become stable; but brain damage is not reversible. Among the patients who survive, most patients develop mobility impairment for a long time [2]. According to the theory of brain flexibility, if patients are trained in rehabilitation for some time, part of the movement ability can be restored [3]. However, the recovery process is time-consuming; and it needs experienced therapists. As a result, the need to use a rehabilitation robot is well seen [4]. Since 1980, various types of robotic therapy devices have been studied in different countries [5]. For this reason, research on a rehabilitation robot was performed to correct the gait operations of a person with mobility impairments. The studied mechanism is shown in "Fig. 1". In this mechanism, two parallel robots with three degrees of freedom create the required gait pattern by moving the legs, while the body weight is supported by a restraint system. This design is based on previous studies [6-9] on the parameters of the footpath in human gait; it consists of three main movements: moving (vertical and horizontal), raising the leg, and lowering the leg, which must be considered and fully simulated.

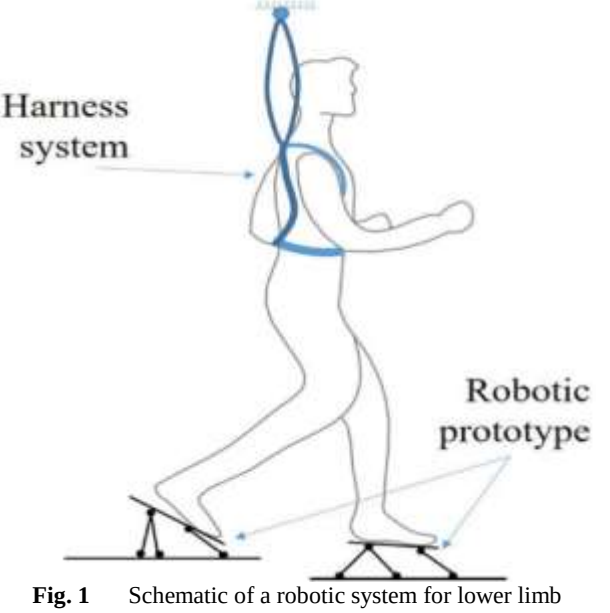

Fig. 1 Schematic of a robotic system for lower limb rehabilitation [9].

In this rehabilitation mechanism, each leg needs a parallel robot consisting of three linear actuators positioned in the same directions. The parallel robot is shown in "Fig. 2".

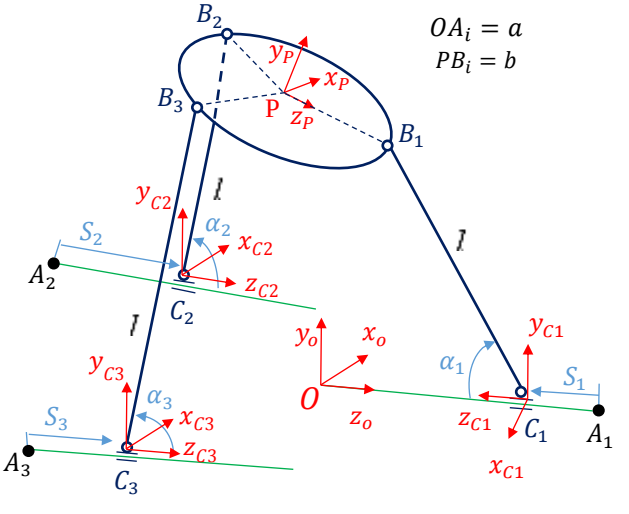

Fig. 2 Schematic of the 3PRR robot.

Each robot end-effector is supported by three links with passive and active prismatic joints. The movements of linear actuators create the required paths in the end-effector; which follows a pre-calculated gait pattern. The

training path can be achieved by combining three types of movements: 1- Transfer along the actuator axis while maintaining the direction and height of the footplate. This movement is achieved by moving all three actuators equally and in one direction. 2- It is possible to make net changes in the height of the end-effector by moving the same amount, in two parallel actuators in one direction and a third in the opposite direction. 3- Orientation of the end-effector by moving each of the actuators while the other is fixed; or it moves at different velocities, it is supplied. The exact path of rehabilitation depends on the age, weight, and height of the patient based on the type of injury or problem and the considerations of the physiotherapist. Parallel robots have been noted for their velocity, robustness, accuracy, and high loading capabilities.

One of the robots that can be considered as a kind of Stewart robot [10] as the most famous parallel robot is a robot with three degrees of freedom and the name 3PRR, which is considered in this study. The 3PRR robot has more freedom to move on the horizontal plane than the Stewart robot due to the presence of prismatic joints. The end-effector of this robot is connected to the prismatic joints with three links and does not have the problem of multiple links of the Stewart robot (6 links). As mentioned, not much research has been done on modelling and controlling this robot. The only case in which the robot has been modelled has focused on its structural optimization [9]. In other studies, on the 3PRR robot, the robot studied moved in two dimensions, which is different from the current spatial robot [11-16]; and the path of sliders was not similar to the robot under study [17-18].

For this reason, attention was paid to the research background of robots similar to the 3PRR spatial robot. One of the robots that are very similar to the robot is called 3PRS. In 2005, Li and Xu [19] proposed the exact solution of the inverse kinematics, and numerical solution forward kinematics, of the 3PRS robot. Then, its dynamic Equations were studied. In 2010, Tsai and Yuan performed an inverse dynamics analysis of the 3PRS robot by analysing the reaction forces acting on the joints and simulating it in a circular path [20]; in 2011, they solved its forward dynamics in the mentioned method and controlled it [21].

Then in 2014, they solved forward dynamics by taking into account the friction force [22]. In one of the latest studies, Tourajizadeh and Gholami modelled and optimally controlled the 3PRS robot [23]. They used the Lagrange method to model the robot. Their work will be the basis for modelling the present study [23-24]. The results of experimental and theoretical research indicate the fact that to control the motion of systems that have complex or nonlinear dynamics, the use of fuzzy controllers is a powerful tool [25]. In addition, the use of this type of controller can increase the robustness of the system to changes in environmental disturbances [26]. The proposed fuzzy controller tracks the desired path by overcoming the disturbances and tries to place the actuators in that path. In this regard, the fuzzy control of a parallel robot was performed [27]. The results of the movement of this robot indicate very good control of the robot and its acceptable velocity of movement.

In this paper, the kinematic and dynamic modeling of the 3PRR robot has been extracted by the Lagrange method, which according to the literature has not been similar and no research has been done in this field. Furthermore, the robust control of the 3PRR robot is modeled and implemented using the fuzzy fuzzy-logic inference, which is the most important innovation of this paper. The imbalance of the patient while using the rehabilitation robot, which causes the robot to experience external disturbances due to sudden movements, is the importance of implementing such a controller; and the necessity of such a controller seems vital.

For this purpose, a fuzzy controller was designed based on Mamdani inference. Using the obtained model and the controller designed for this parallel rehabilitation robot, the required path for rehabilitation of the patient's ankle in the presence of external force (patient weight) was well-traveled. In this paper, forward and inverse kinematics of the robots were extracted. Then, using the Lagrangian method, the dynamic Equations of the robot were obtained and after removing the Lagrangian coefficients, it was modelled in the form of state space. Then, the fuzzy controller was designed based on Mamdani's inference. Finally, all Equations obtained in MATLAB software were simulated and controlled.

2 KINEMATIC MODELING

Due to the similarity between 3PRR and 3PRS robots, the method used in [23] was used to model the 3PRR rehabilitation robot. As shown in "Fig. 2", point O is the origin of the reference coordinates and point A_i is the beginning of the prismatic rail.

$$o = \begin{bmatrix} 0 \\ 0 \\ 0 \end{bmatrix}, A_1 = \begin{bmatrix} 0 \\ 0 \\ a \end{bmatrix}, A_2 = \begin{bmatrix} b\frac{\sqrt{3}}{2} \\ 0 \\ -a \end{bmatrix}, A_3 = \begin{bmatrix} -b\frac{\sqrt{3}}{2} \\ 0 \\ -a \end{bmatrix}. \quad (1)$$

Where, a is the length of the prismatic joint rail. Denavit-Hartenberg method was used to select the coordinate systems and the link DH parameters extracted according to the [28] ("Table 1").

Table 1 DH parameters of the Links

Link	e	β	d	Θ
OC1	0	180	$a - s_1$	180
OC2	b	0	$-a + s_2$	0
OC3	-b	0	$-a + s_3$	0

Where, e (distance between the previous z-axis and the new z-axis along the new x-axis), β (angle between the previous z-axis and the new z-axis around the new x-axis), d (vertical distance between the origin of the previous coordinate and the new ones along the axis of the previous z), and Θ (the angle between the axes of the previous x and the new x around the axis of the previous z). The homogeneous transfer matrix according to the parameters of "Table 1" is as follows:

$$\begin{cases} H_{c_1}^{o} = R_{z,\theta_1} T_{z,d_1} T_{x,e_1} R_{x,\beta_1} \\ H_{c_2}^{o} = R_{z,\theta_2} T_{z,d_2} T_{x,e_2} R_{x,\beta_2} \\ H_{c_3}^{o} = R_{z,\theta_3} T_{z,d_3} T_{x,e_3} R_{x,\beta_3} \end{cases} \quad (2)$$

Where, $R_{z,\theta}$ is the rotation about the z-axis as much as θ and $T_{z,d}$ is the translations along the z-axis and is equal to d. The position of the B_i relative to the C_i local coordinate is:

$$B_i^{c_i} = \begin{bmatrix} 0 \\ l\ sin\alpha_i \\ l\ cos\alpha_i \end{bmatrix} \quad (3)$$

Where, l is the length of the links and α_i is the angle of the i[th] link connected to the C_i joint with its carrier rail. The position of point B_i in the reference coordinate connected to point O is as follows:

$$\begin{bmatrix} B_i^o \\ 1 \end{bmatrix}_{(s_i,\alpha_i)} = H_{c_i}^{o} \begin{bmatrix} B_i^{c_i} \\ 1 \end{bmatrix}, \quad i = 1,2,3 \quad (4)$$

The rotation angles of the moving plane around the coordinate axes of the reference coordinate connected to the O point were considered as yaw, pitch, and roll, the final rotation matrix will be as follows:

$$R_{\varphi,\theta,\psi} = \begin{bmatrix} c\varphi c\theta & -s\varphi c\psi + c\varphi s\theta s\psi & s\varphi s\psi + c\varphi s\theta c\psi \\ s\varphi c\theta & c\varphi c\psi + s\varphi s\theta s\psi & -c\varphi s\psi + s\varphi s\theta c\psi \\ -s\theta & c\theta s\psi & c\theta c\psi \end{bmatrix} \quad (5)$$

Given the positions of the point $p = [x\ y\ z]^T$ we have:

$$[B_1^o \quad B_2^o \quad B_3^o]_{(x,y,z,\psi,\theta,\varphi)} = p[1 \quad 1 \quad 1] + R_{\varphi,\theta,\psi} \begin{bmatrix} 0 & \frac{b\sqrt{3}}{2} & \frac{-b\sqrt{3}}{2} \\ 0 & 0 & 0 \\ b & \frac{-b}{2} & \frac{-b}{2} \end{bmatrix} \quad (6)$$

Finally, the kinematic constraints of the robot, for use in system dynamics modeling, were obtained from the equality of the Equations (5) and (7) as follows:

$$\begin{bmatrix} f_1 \\ \vdots \\ f_9 \end{bmatrix} = \begin{bmatrix} B_1^o \\ B_2^o \\ B_3^o \end{bmatrix}_{(x,y,z,\psi,\theta,\varphi)} - \begin{bmatrix} B_1^o \\ B_2^o \\ B_3^o \end{bmatrix}_{(s_i,\alpha_i)} = 0 \quad (7)$$

3 DYNAMIC MODELING

The end-effector of the robot is circular, and the whole mass can be assumed at the center of the mass. To the modelling of the dynamics of the system, [x, y, z, ψ, θ, ϕ, α_1, α_2, α_3, S_1, S_2, S_3]^T were used as twelve generalized coordinates. The kinetic energy of the robot is equal to [29]:

$$\begin{cases} T_p = \frac{1}{2}\left(\omega_p^T I_p \omega_P + M V_p^T V_P\right) \\ T_l = \frac{1}{2}\sum_{i=1}^{3}\left(\omega_i^T I_{li} \omega_i + m V_i^T V_i\right) \end{cases}, T = T_p + T_l \quad (8)$$

T_p and M are the mass and energy of the end-effector. T_l and m are the mass and energy of the links. I_p is the moment of inertia of the end-effector and I_{li} is the moment of inertia of the i[th] link, and both rea relative to the reference coordinates. The moment of inertia of each link was written on the coordinate $(xyz)_{li}$ ((shown in "Fig. 3"); And to transfer it to the reference coordinate, the rotation matrix of these two coordinates was used relative to each other.

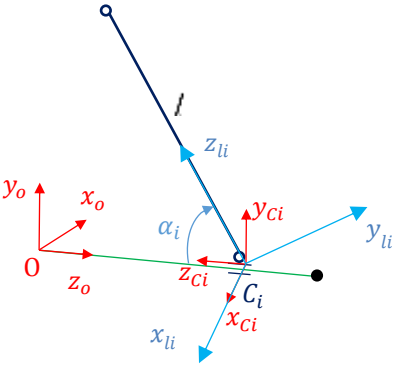

Fig. 3 Reference and local coordinates for calculating the moment of inertia of the links.

Also, the moment of inertia of the end-effector relative to the coordinate $(xyz)_p$ was written and taken to the reference coordinate. To calculate I_{li} and I_p can be written:

$$\begin{cases} I_p = \frac{1}{2} M b^2 R_{\varphi,\theta,\psi} \begin{bmatrix} 0.5 & 0 & 0 \\ 0 & 1 & 0 \\ 0 & 0 & 0.5 \end{bmatrix} R_{\varphi,\theta,\psi}^T, \\ I_{li} = \frac{1}{3} m l^2 R_{li}^o \begin{bmatrix} 1 & 0 & 0 \\ 0 & 1 & 0 \\ 0 & 0 & 0 \end{bmatrix} R_{li}^{oT}. \end{cases} \quad (9)$$

All velocities were written in the reference coordinate system:

$$\begin{cases} \omega_P = \begin{bmatrix} \dot{\psi} \\ \dot{\theta} \\ \dot{\phi} \end{bmatrix}, \quad v_P = \begin{bmatrix} \dot{x} \\ \dot{y} \\ \dot{z} \end{bmatrix}, \\ \omega_i = R_{Ci}^o \begin{bmatrix} -\dot{\alpha}_i \\ 0 \\ 0 \end{bmatrix}, \quad v_i = \frac{d}{dt} G_i . \\ G_i = H_{Ci}^o [0 \quad 0.5lsin(\alpha_i) \quad 0.5lcos(\alpha_i) \quad 1]^T \end{cases} \quad (10)$$

The potential energy of the robot is equal to:

$$U = Mgy + mg\frac{l}{2}\sum_{i=1}^{3} \sin(\alpha_i) \quad (11)$$

g is the acceleration of the earth's gravity. Lagrange's Equations of motion are equal to:

$$\begin{cases} \frac{d}{dt}\left(\frac{\partial L}{\partial \dot{q}_i}\right) - \frac{\partial L}{\partial q_i} + \sum_{k=1}^{9} \lambda_k \frac{\partial f_k}{\partial q_i} = Q_i \\ L = T - U \\ q = [x; y; z; \psi; \theta; \varphi; \alpha_1; \alpha_2; \alpha_3; s_1; s_2; s_3] \\ Q = [0; 0; 0; 0; 0; 0; 0; 0; 0; F_1; F_2; F_3] \end{cases} \quad (12)$$

Where, Q represents generalized forces. In this study, the friction force was negligible. f_k is the robot constraints obtained from Equation (7).

$$\begin{cases} \frac{d}{dt}\left(\frac{\partial L}{\partial \dot{q}_i}\right) = \frac{\partial}{\partial \dot{q}_j}\left(\frac{\partial L}{\partial \dot{q}_i}\right)\ddot{q}_j + \frac{\partial}{\partial q_j}\left(\frac{\partial L}{\partial \dot{q}_i}\right)\dot{q}_j, \\ \frac{\partial}{\partial \dot{q}_j}\left(\frac{\partial L}{\partial \dot{q}_i}\right) = m_{ji}, \quad \frac{\partial}{\partial q_j}\left(\frac{\partial L}{\partial \dot{q}_i}\right) = c_{ji}, \\ \frac{\partial L}{\partial q_i} = g_i, \quad \frac{\partial f_k}{\partial q_i} = a_{ki}. \end{cases} \quad (13)$$

Finally, the Equation of motion will be equal to:

$$M\ddot{q} + C\dot{q} - G + A^T\lambda = Q \quad (14)$$

Where, M is the inertia matrix, C is the Coriolis matrix, G is the gravity vector, A is the weight matrix of Lagrangian coefficients, and Q is the generalized force vector. To eliminate the Lagrangian coefficients from the Equation of motion, the null-space of the matrix A was obtained from the following definition [30]:

$$\begin{cases} AS = 0, \\ \vec{v} = [\dot{s}_1; \dot{s}_2; \dot{s}_3], \\ \dot{\vec{q}} = S\vec{v}, \\ \ddot{\vec{q}} = \dot{S}\vec{v} + S\dot{\vec{v}}. \end{cases} \quad (15)$$

Where, S is the null-space matrix. Multiplying S^T from the left in Equation (14) and placing the derivatives q of Equation 15 will give:

$$S^T M S\dot{\vec{v}} + S^T M\dot{S}\vec{v} + S^T CS\vec{v} - S^T G = S^T Q \quad (16)$$

Where, $S^T Q = \vec{F} = [F_1; F_2; F_3]$. To calculate the derivative of the null-space matrix, we can write:

$$\begin{cases} AS = 0 \rightarrow \dot{A}S + A\dot{S} = 0 \rightarrow \dot{S} = -A^{-1}\dot{A}S \\ A^{-1} = A^T(AA^T)^{-1} \end{cases} \quad (17)$$

By selecting $\vec{X}_{6\times1} = [S_1, S_2, S_3, v^T]^{\mathrm{T}}$ as the state space variables, the system state space form is equal to:

$$\begin{cases} \dot{\vec{X}} = \begin{bmatrix} \vec{v} \\ \dot{\vec{v}} \end{bmatrix} = \begin{bmatrix} \vec{v} \\ h \end{bmatrix} + \begin{bmatrix} [0]_{3\times3} \\ (S^T MS)^{-1} \end{bmatrix} \vec{F}, \\ h = (S^T MS)^{-1} S^T \left(G - CS\vec{v} - M\dot{S}\vec{v}\right). \end{cases} \quad (18)$$

4 CONTROLLER DESIGN

Fuzzy controllers have acceptable efficiency and performance in controlling the movement of robots as well as performing special maneuvers. One way to design a fuzzy controller is to break down complex system behaviors into multiple movements within the robot. After designing a suitable control algorithm for each section, their corresponding actions can be combined. In this paper, the fuzzy controller is designed in such a way that it can track the desired path well by determining the appropriate control force and has good resistance to initial disturbances. This controller is designed according to the if-then rules in the following form:

If s_i is A and $\dot{s}_i$ is B, then u_i is C (19)

The "and" and "or" operators are defined as follows:

$$\begin{aligned} \mu_{A\cup B} &= max(\mu_A(u), \mu_B(u)) \\ \mu_{A\cap B} &= min(\mu_A(u), \mu_B(u)) \\ \mu_{A\cup B} &= max(\mu_A(u), \mu_B(u)) \\ \mu_{A\cap B} &= min(\mu_A(u), \mu_B(u)) \end{aligned} \quad (20)$$

In the proposed controller, Mamdani fuzzy inference system was used along with the defuzzification method of the centroid. In the first step, the fuzzy controller, after receiving the inputs, performs the fuzzification process, then combines the membership functions based on

Mamdani inference using the fuzzy operator. In the next step, the values of the membership functions combine and the outputs are defuzzification. The input of the fuzzy system was selected as an error and its derivative of the desired value at a given time. The membership functions of these inputs were considered Gaussian functions. Position and velocity errors of the robot were selected as five functions [-2 -1 0 +1 +2], where the range of the changes between [-1 1]. This selection is a general case and a coefficient is assigned to the system error to change the velocity and position error range. For the output of the fuzzy system, which is the same control force required for the robot to move in the path, according to the Mamdani method, the membership functions of these outputs were considered Gaussian functions. Finally, a representation of the fuzzy system inputs and outputs is shown in "Fig. 4".

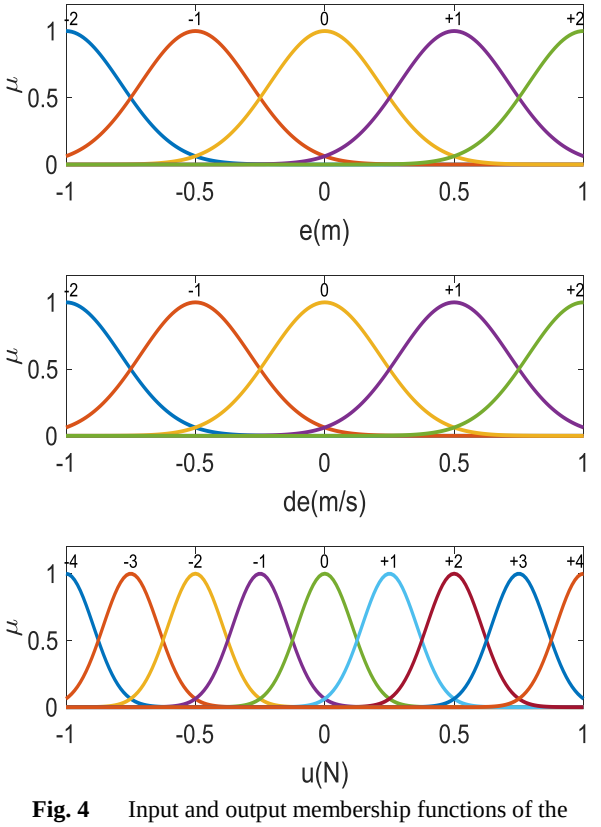

Fig. 4 Input and output membership functions of the Mamdani fuzzy system.

A set of fuzzy rules was chosen to extract the appropriate control force in "Table 2".

5 SIMULATION RESULTS

In this research, after the kinematic and dynamic modelling of the 3PRR rehabilitation robot, a designed controller was applied to the dynamic model. For this purpose, Equation (18) was used as the system. The values in Table 3 were used for simulation.

Table 2 Fuzzy Rules

Number	Fuzzy rules					
1	If "e" is	-2	and "de" is	-2	then "u" is	+4
2		-2		-1		+3
3		-2		0		+2
4		-2		+1		+1
5		-2		+2		0
6		-1		-2		+3
7		-1		-1		+2
8		-1		0		+1
9		-1		+1		0
10		-1		+2		-1
11		0		-2		+2
12		0		-1		+1
13		0		0		0
14		0		+1		-1
15		0		+2		-2
16		+1		-2		+1
17		+1		-1		0
18		+1		0		-1
19		+1		+1		-2
20		+1		+2		-3
21		+2		-2		0
22		+2		-1		-1
23		+2		0		-2
24		+2		+1		-3
25		+2		+2		-4

Table 3 Value of robot parameters

Parameter	symbol	Unit	value
Jacks' course	a	(m)	0.8
Radius of the moving platform	b	(m)	0.2
Length of the links	l	(m)	0.5
Mass of the moving platform	M	(kg)	1
Mass of the links	m	(kg)	0.1
Gravitational acceleration	g	(m/s2)	9.8

Due to the nature of the robot rehabilitation, the angle of the end-effector (φ) around the x-axis was considered as a sine wave with an amplitude of 20 degrees (0.35 rad). During this movement, the other angles of the end-effector should remain zero. Also, the motion of the end-effector in the directions x and z should be constant and zero. Such a move is desirable and will meet all rehabilitation needs. According to the expressed movement needs, and considering the inverse kinematic simulation, the movement path of the robot sliders is considered as follows, and was used to simulate the performance of the fuzzy controller in the tracking operation.

$$\begin{cases} s_1 = -0.05 - 0.42sin(t) \\ s_2 = 0.6 - 0.42sin(t) \\ s_3 = -0.3 + 0.42sin(t) \end{cases} \quad (21)$$

To bring the control scenario as close as possible to the real state, an external force of 20 N was applied to the end-effector in the opposite direction of the y-axis. This force can be equated to the condition in which an 80 N-weight patient enters the robot during a rehabilitation operation (half of the patient's weight will be borne by the harness system). The control force was determined using a fuzzy system designed and applying the existing rules in "Table 2" to the position and velocity error of the intended path and is applied to the robot prismatic actuators. The position and velocity of these actuators are shown in "Fig. 5".

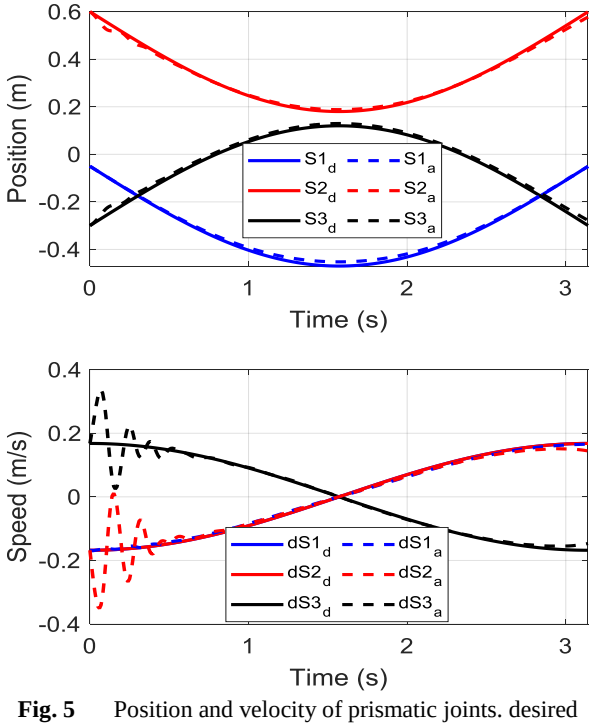

Fig. 5 Position and velocity of prismatic joints. desired path (d), the path taken by the controller (a).

As shown in the figure above, the fuzzy controller has been able to track the path required for rehabilitation and has followed it well. The application of an external force initially causes a small error in the position of the prismatic actuators, but fuzzy control has corrected this error by applying appropriate oscillations to the velocity of the sliders. The control forces applied to each prismatic actuator are shown in "Fig. 6".

As it turns out, the control force is applied uniformly and smoothly, and is well able to handle external loads (patient weight). The smoothness of the applied control force indicates the capability of the implemented controller. In addition, the minimum-maximum control force is obtained smoothly and the direction of force is gently sloping. This is very important in the use of control instruments and prevents possible breakdowns in the drive motors.

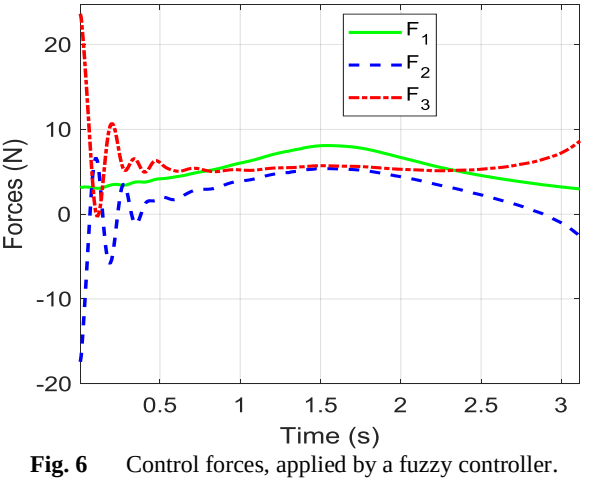

Fig. 6 Control forces, applied by a fuzzy controller.

6 CONCLUSIONS

In this study, kinematic and dynamic analysis of the 3PRR rehabilitation robot was performed and robot Equations of motions were obtained by the Lagrange method. Finally, robot control in tracking operations was performed without using system dynamic Equations and only using fuzzy logic. For this purpose, a fuzzy controller was designed based on Mamdani's inference. Using the obtained model and the controller designed for this parallel rehabilitation robot, the required path for rehabilitation of the patient's ankle in the presence of external force (patient weight) was well-traveled. During this operation, the tracking error is less than 3% and the applied control force has good smoothness and a gentle slope.

REFERENCES

[1] Wolfe, C. D., The Impact of Stroke, British Medical Bulletin, Vol. 56, No. 2, 2000, pp. 275-286.

[2] Tyson, S. F., Hanley, M., Chillala, J., Selley, A., and Tallis, R. C., Balance Disability After Stroke, Physical Therapy, Vol. 86, No. 1, 2006, pp. 30-38.

[3] French, B., Thomas, L. H., Leathley, M. J., Sutton, C. J., McAdam, J., Forster, A., and Watkins, C. L., Does Repetitive Task Training Improve Functional Activity After Stroke? A Cochrane Systematic Review and Meta-Analysis, Journal of Rehabilitation Medicine, Vol. 42, No. 1, 2010, pp. 9-15.

[4] Wang, M., Design and Analysis of an Adjustable Wrist Rehabilitation Robot, 2014: (PhD Thesis).

[5] Siciliano, B., Khatib, O., Force Control, Luigi Villani, Joris De Schutter, Springer handbook of robotics. Springer-Verlag Berlin Heidelberg, 2008.

[6] Mariani, B., Hoskovec, C., Rochat, S., Büla, C., Penders, and J., Aminian, K., 3D Gait Assessment in Young and Elderly Subjects Using Foot-Worn Inertial Sensors, Journal of Biomechanics, Vol. 43, No. 15, 2010, pp. 2999-3006.

[7] Dadashi, F., Mariani, B., Rochat, S., Büla, C. J., Santos-Eggimann, B., and Aminian, K., Gait and Foot Clearance Parameters Obtained Using Shoe-Worn Inertial Sensors in a Large-Population Sample of Older Adults, Sensors, Vol. 14, No. 1, 2014, pp. 443-457.

[8] Zhang, C., Lan, B., Matsuura, D., Mougenot, C., Sugahara, Y., and Takeda, Y., Kinematic Design of a Footplate Drive Mechanism Using a 3-DOF Parallel Mechanism for Walking Rehabilitation Coordinate, Journal of Advanced Mechanical Design, Systems, and Manufacturing, Vol. 12, No. 1, 2018, pp. JAMDSM0017-JAMDSM0017.

[9] Valdez, S. I., Gutierrez-Carmona, I., Keshtkar, S., and Hernandez, E. E., Kinematic and Dynamic Design and Optimization of a Parallel Rehabilitation Robot, Intelligent Service Robotics, Vol. 13, No. 3, 2020, pp. 365-378.

[10] Stewart, D., A Platform with Six Degrees of Freedom, Proceedings of the Institution of Mechanical Engineers, Vol. 180, No. 1, 1965, pp. 371-386.

[11] Caro, S., Chablat, D., Ur-Rehman, R., Wenger, P., Multiobjective Design Optimization of 3–Prr Planar Parallel Manipulators, in Global Product Development : Springer, 2011, pp. 373-383.

[12] Javid, G., Akbarzadeh, M. R., Akbarzadeh, A., Nabavi, S. N., Trajectory Tracking of 3-PRR Parallel Manipulator with PI Adaptive Fuzzy Terminal Prismatic Mode Controller, 1st International E-Conference on Computer and Knowledge Engineering (ICCKE), 2011, pp. 156-161: IEEE.

[13] Si, G., Chu, M., Zhang, Z., Li, H., and Zhang, X., Integrating Dynamics into Design and Motion Optimization of a 3-PRR Planar Parallel Manipulator with Discrete Time Transfer Matrix Method, Mathematical Problems in Engineering, Vol. 1, No.1, 2020, pp. 126-131.

[14] Staicu, S., Inverse Dynamics of the 3-PRR Planar Parallel Robot, Robotics and Autonomous Systems, Vol. 57, No. 5, 2009, pp. 556-563.

[15] Zhang, X., Mills, J. K., Cleghorn, W. L., Effect of Axial Forces on Lateral Stiffness of a Flexible 3-PRR Parallel Manipulator Moving with High-Velocity, in 2008 International Conference on Information and Automation, 2008, pp. 1458-1463: IEEE.

[16] Zhao, B., Zhang, X., Zhan, Z., Wu, Q., and Zhang, H., Multi-scale Graph-guided Convolutional Network with Node Attention for Intelligent Health State Diagnosis of a 3-PRR Planar Parallel Manipulator, IEEE Transactions on Industrial Electronics, Vol. 1, No. 1, 2021, pp. 556-563.

[17] Kumar, P., Sudheer, A., Workspace Optimization of 3PRR Parallel manipulator for drilling operation using Genetic Algorithm, in Proceedings of the Advances in Robotics, 2017, pp. 1-5.

[18] Selvakumar, A. A., Karthik, K., Kumar, A., Sivaramakrishnan, R., and Kalaichelvan, K., Kinematic and Singularity Analysis of 3 PRR Parallel Manipulator, in Advanced Materials Research, Vol. 403, 2012, pp. 5015-5021.

[19] Li, Y., Xu, Q., Kinematics and Inverse Dynamics Analysis for a General 3-PRS Spatial Parallel Mechanism, Robotica, Vol. 23, No. 02, 2005, pp. 219-229.

[20] Tsai, M. S., Yuan, W. H., Inverse Dynamics Analysis for a 3-PRS Parallel Mechanism Based on a Special Decomposition of The Reaction Forces, Mechanism and Machine Theory, Vol. 45, No. 11, 2010, pp. 1491-1508.

[21] Tsai, M. S., Yuan, W. H., Dynamic Modeling and Decentralized Control of a 3 PRS Parallel Mechanism Based on Constrained Robotic Analysis, Journal of Intelligent & Robotic Systems, Vol. 63, No. 3-4, 2011, pp. 525-545.

[22] Yuan, W. H., Tsai, M. S., A Novel Approach for Forward Dynamic Analysis of 3-PRS Parallel Manipulator with Consideration of Friction Effect, Robotics and Computer-Integrated Manufacturing, Vol. 30, No. 3, 2014, pp. 315-325.

[23] Tourajizadeh, H., Gholami, O., Optimal Control and Path Planning of a 3PRS Robot Using Indirect Variation Algorithm, Robotica, Vol. 38, No. 5, 2020, pp. 903-924.

[24] Tourajizadeh, H., Gholami, O., A New Optimal Method for Calculating the Null Space of a Robot using NOC Algorithm; Application on Parallel 3PRS Robot, ADMT Journal, Vol. 13, No. 1, 2020, pp. 1-15.

[25] Azarafza, R., Mohammadhoseni, S., and Farrokhi, M., Free Chattering Fuzzy Sliding Mode Controllers to Robotic Tracking Problem, ADMT Journal, Vol. 5, No. 2, 2012.

[26] Ghafouri, M., Daneshmand, S., Design and Evaluation of an Optimal Fuzzy Pid Controller for an Active Vehicle Suspension System, Transactions of Famena, Vol. 41, No. 2, 2017, pp. 29-44.

[27] Vermeiren, L., Dequidt, A., Afroun, M., Guerra, and T. M., Motion Control of Planar Parallel Robot Using the Fuzzy Descriptor System Approach, ISA Transactions, Vol. 51, No. 5, 2012, pp. 596-608.

[28] Spong, M. W., Hutchinson, S., Vidyasagar, M., Robot Modeling and Control, Jon Wiley & Sons, Inc., ISBN-100-471-649, 2005.

[29] Jazar, R. N., Advanced Dynamics: Rigid Body, Multibody, and Aerospace Applications, John Wiley & Sons, 2011.

[30] Liang C., M. Lance, G., A Differentiable Null Space Method for Constrained Dynamic Analysis, Journal of Mechanisms, Transmissions, and Automation in Design, Vol. 109, No. 3, 1987, pp. 405-411.

Int. J. Advanced Design and Manufacturing Technology, 2022, Vol. 15, No. 4, pp. 113-123

DOI: 10.30486/admt.2023.1962376.1362 *ISSN: 2252-0406* *https://admt.isfahan.iau.ir*

Modeling of Turbulent Flow Around a Square Obstacle using a Generated Mesh by Image Processing Method

Bahador Abolpour *

Department of Chemical Engineering,
Sirjan University of Technology, Sirjan, Iran
E-mail: bahadorabolpor1364@sirjantech.ac.ir
*Corresponding author

Rahim Shamsoddini

Department of Mechanical Engineering,
Sirjan University of Technology, Sirjan, Iran
E-mail: bahadorabolpor1364@gmail.ac.ir

Received: 2 July 2022, Revised: 2 October 2022, Accepted: 4 October 2022

Abstract: The mesh generation process as a time-consuming and computational effort in the numerical methods always has been paid attention to by researchers to provide more accurate and fast methods. In this study, an accurate, fast, and user-friendly method of mesh generation has been developed by combining the image processing method with Computational Fluid Dynamics (CFD). For this purpose, a turbulent flow around a single square as a bluff body is simulated by homemade code using MATLAB software as a test case to illustrate the mentioned method. The conservative Equations have been discretized using the finite volume method based on the Power-la scheme. Utilizing useful filters on the imported gray-scale digital image provides edge detection of the obstacle in the computational domain. After the edge detection step, an orthogonal, structured, and staggered mesh is generated.

Keywords: CFD, Image Processing, Modelling, Turbulent Flow

Biographical notes: Bahador Abolpour received his PhD in Chemical Engineering from the University of Shahid Bahonar, Kerman in 2013. He is currently an Associate Professor at the Department of Chemical Engineering, Sirjan University of Technology, Kerman Iran. His current research interest includes CFD simulation of turbulent flows, heat and mass transfer, optimization algorithms, and image processing method-based mesh generation. **Rahim Shamsoddini** is an Associate Professor at the Department of Mechanical Engineering, Sirjan University of Technology, Kerman, Iran. He received his PhD in Mechanical Engineering from Yazd University, Yazd, Iran in 2014. His current research focuses on fluid mechanics, SPH, and CFD-based modelling of fluid behaviors.

Research paper

1 INTRODUCTION

The numerical and experimental investigation of the physical phenomena in order to simulate fluid flows in nature and industry have always been researchers' and scientists' interests [1-5], [15], [17], [28], [30]. The experimental approach is a straightforward method of observing physical phenomena and the used sensor's accuracy is a crucial challenge in this method. With the comprehensive development of computing software, the numerical method become a more efficient and useful method for simulating and obtaining accurate results. Dividing the computational domain into finite cells (named meshes) or elements, is essential for numerical studies and always is a challenging step for researchers to produce suitable mesh configurations and reduce the time and cost of generation. Using the image processing method as a straightforward and efficient method for determining the computational field geometry and generating mesh by an imported digital image can reduce the time and cost of computation noticeably. Nowadays, with the widespread use of smartphones, digital cameras, and the Internet, utilizing digital images is more user-friendly.

Hale [16] developed an algorithm to minimize the potential energy by combining a digital image with a structure of ordered points, which are called atoms. This method computed atom coordinates and distances, and a suitable mesh grid was generated to obtain further computations, like flow simulation. Kocharoen et al. [21] investigated a method for generating a mesh structure of image representation. An elimination scheme was used to remove nonessential nodes. Cuadros-Vargas et al. [10] presented I-mesh's algorithm, which automatically produced mesh from digital images. This method could recognize different regions and boundaries. Barber et al. [6] developed a method for generating a mesh from a medical image based on volumetric registration. Fang and Boas [12] used a three-dimensional mesh generation software that contained several free mesh processing. It generated a quality tetrahedral or triangular mesh in three and two dimensions. Wang et al. [33] developed a new way of converting digital images into grids. Lassoued et al. [22] presented a valuable method to convert low-quality digital images into mesh grids for the fluid flow field. After generating mesh grids, the Navier-Stokes Equations were solved by a direct numerical scheme without any turbulent consumption. Bonabi and Hemati [36] provide a procedure (ruled, skinning, and global approximation) in order to model bone surface by extracting points from the segmentation of different regions of CT scan digital images. Their results showed that 99.74% of obtained points by their developed methods have a maximum difference of 0.25 to 0.75mm from the benchmark data and acceptable accuracy for medical usage. Vini and Daneshmand [37] investigated the asymmetric roll bonding process to obtain Al/Cu bimetallic laminates. The deformation of samples has been simulated using the finite element method. Additionally, scanning electron microscopy has been used for peeling tests of the surface.

The aim of the present study is to develop image processing-based mesh generation for computational fluid dynamics methods. The simultaneous simulations of turbulent flow and image processing in a single developed code have not been seen in previous works. For this purpose, a turbulent fluid flow around a single square obstacle is simulated. This work's innovation is related to developing a new mesh generation process and solving the turbulent flow field Equations by a developed homemade code simultaneously utilizing MATLAB software. Additionally, the presented method can be used for optimum shape design. A merge of simulation steps and matrix operations in the present code helps us to combine the computational operations and subsequently increase the calculation time and cost. The developed code automatically detects boundaries by processing the pixels of digital images. After generating the mesh, the Equations of continuity, momentum, and turbulence are solved numerically using the finite volume method. A progressed version of this code can be used in multi-task applications in different industry branches such as shape optimization of the bluff body to drag reduction and increase the lift force.

2 METHODOLOGIES

2.1. Principles

Fluid flow produces different aerodynamic forces when it passes over any object due to pressure gradient and fluid viscosity distribution. The flow field's square obstacle is case study research in CFD. Due to the sharp square corners, the passing fluid flow has been separated, and vortices are generated downstream. Also, by increasing the fluid's velocity (i.e., increasing Reynolds number), a turbulence flow appears. To simulate the numerical method's flow and solve the governing Equations, we need to divide the computational field into small cells.

2.2. Image Processing Procedure

Figure 1 illustrates a two-dimensional imported grayscale digital image of a square in JPEG format. Each pixel of this image has been examined by image processing. Two filters have been imposed in this method, contrast and brightness filters, which have been used to remove all imported image noises. Each color has a specific code for recognition in the image processing method. The arrangement of color codes differs from 0 to 255 for this grayscale image. A third

filter has been used to eliminate color tones and sort them into black and white categories. The color tone upper than 200 is referred to as white, and lower than 200 is referred to as black. This range of filtered colors has been converted to the corresponding numeric values 0 and 1, similar to those of black and white.

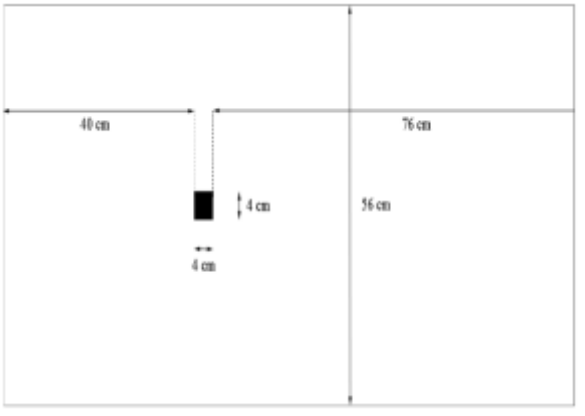

Fig. 1 Imported gray scale digital JPEG format image of domain and obstacle with related geometries.

The edge detection process detects each edge of the given square individually. Considering one of the obstacle nodes (with a 0 value for its *I, J* label, as a black pixel), it's left, right, upper, and bottom neighbour nodes indicate the type of this node of the body. If the pixel value of *I+1, J* node be equal to 1, the *I, J* node is a right-side edge of the body. Other side edges and corners of this body can be detected using a similar procedure. Seeing the side of the bluff body edges is a crucial step in order to calculate surface tension on each node of the body walls. The developed code solved the governing Equations based on the finite volume method by considering the appropriate turbulence model and performing the matrix form calculations after creating grid mesh. [34-35].

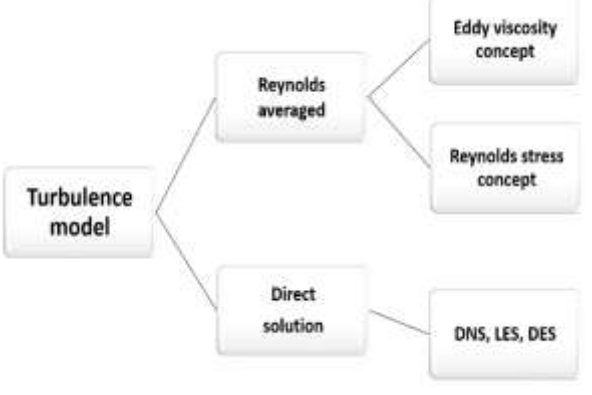

Fig. 2 The classification of turbulence models based on solution types.

2.3. Governing Equations

The classification of turbulence models based on solution types has been illustrated in "Fig. 2". One of the most common turbulent models for solving the turbulent flow field is the *k-ε* model, which exists in Reynolds averaged group. This model includes two different transport Equations (i.e. *k* as turbulent kinetic energy and *ε* as turbulent dissipation) to illustrate the flow's turbulent properties.

The steady-state governing Equations have been illustrated as follows according to Einstein's notation, which has been solved concurrently [2]:

$$\frac{\partial \overline{u}_i}{\partial x_i} = 0 \tag{1}$$

$$\rho \overline{u}_j \frac{\partial \overline{u}_i}{\partial x_j} = \frac{\partial}{\partial x_j}\left[-\overline{P}\delta_{ij} + \mu\left(\frac{\partial \overline{u}_i}{\partial x_j} + \frac{\partial \overline{u}_j}{\partial x_i}\right) - \rho \overline{u_i' u_j'}\right] + \rho g_i \tag{2}$$

$$\rho \frac{\partial (k\overline{u}_i)}{\partial x_i} = \frac{\partial}{\partial x_j}\left[\left(\mu + \frac{\mu_t}{\sigma_k}\right)\frac{\partial k}{\partial x_j}\right] - \rho \overline{u_i' u_j'} - \rho\varepsilon \tag{3}$$

$$\rho \frac{\partial (\varepsilon\overline{u}_i)}{\partial x_i} = \frac{\partial}{\partial x_j}\left[\left(\mu + \frac{\mu_t}{\sigma_\varepsilon}\right)\frac{\partial \varepsilon}{\partial x_j}\right] + C_{\varepsilon 1}\frac{\varepsilon}{k}\left(-\rho \overline{u_i' u_j'}\frac{\partial \overline{u}_j}{\partial x_i}\right) - C_{\varepsilon 2}\rho\frac{\varepsilon^2}{k} \tag{4}$$

In order to solve governing Equations, Boussinesq approximation has been used as following [2]:

$$\rho \overline{u_i' u_j'} = \mu_t\left(\frac{\partial \overline{u}_i}{\partial x_j} + \frac{\partial \overline{u}_j}{\partial x_i}\right) - \frac{3}{2}\rho k \delta_{ij} \tag{5}$$

2.4. The Chien's Model for Low Reynolds k-ε Model

Chien's low Reynolds *k-ε* model is a suitable turbulent model for solving this turbulent flow field [26]. This model has accurate and highly acceptable numerical properties. The dissipation rate has been split into two-part, isotropic and anisotropic parts. In the dissipation rate transport Equation, the *ε* term has been considered isotropic. For the anisotropy part, an expression for dissipation rate close to the wall boundary condition has been achieved, which has been added to the dissipation rate appearing in the *k* transport Equation [9], [29]. Low Reynolds *k-ε* model can be written in a general form like:

$$\frac{\partial}{\partial t}(\rho k)+\frac{\partial}{\partial x_j}[\rho k u_j-(\mu+\frac{\mu_t}{\sigma_k})\frac{\partial k}{\partial x_j}]=P_k-\rho\varepsilon-\rho D \tag{6}$$

$$\frac{\partial}{\partial t}(\rho\varepsilon)+\frac{\partial}{\partial x_j}[\rho\varepsilon u_j-(\mu+\frac{\mu_t}{\sigma_\varepsilon})\frac{\partial \varepsilon}{\partial x_j}]= (C_{\varepsilon 1}f_1P-C_{\varepsilon 2}f_2\rho\varepsilon)\frac{\varepsilon}{k}+\rho \mathrm{E} \tag{7}$$

The steady-state distributions of k and ε have been presented by Launder and Spalding based on the k-ε turbulent as follows:

$$\frac{\partial[u_i k]}{\partial x_i}=\frac{\partial}{\partial x_i}[v+\frac{v_t}{\sigma_k}\frac{\partial k}{\partial x_i}]+P_k-\varepsilon \tag{8}$$

$$\frac{\partial[u_i \varepsilon]}{\partial x_i}=\frac{\partial}{\partial x_i}[v+\frac{v_t}{\sigma_\varepsilon}\frac{\partial \varepsilon}{\partial x_i}]+C_{\varepsilon 1}P_k\frac{\varepsilon}{k}-C_{\varepsilon 2}\frac{\varepsilon^2}{k} \tag{9}$$

The production term P_k in both of these Equations has been calculated as $P_k=C_\mu\varepsilon S^2$, where $S=\frac{k}{\varepsilon}\sqrt{\frac{1}{2}\left[\frac{\partial u_i}{\partial x_j}+\frac{\partial u_j}{\partial x_i}\right]^2}$. Franke and Rodi [14] explained the standard k-ε turbulent model in through with false calculation for turbulent kinetic energy production in the stagnant region. Kato and Launder et al. [20], [23] introduced a modified form of the standard k-ε turbulent model by replacing the strain stress term (S) with a vorticity term ($\Omega=\frac{k}{\varepsilon}\sqrt{\frac{1}{2}\left[\frac{\partial u_i}{\partial x_j}-\frac{\partial u_j}{\partial x_i}\right]^2}$) in the production term of kinetic energy in the governing Equation ($P_k=C_\mu\varepsilon S\Omega$).

For the first time, the concept of eddy viscosity was introduced by Boussinesq in 1877. In this concept, the turbulence stresses are related to mean flow to represent the governing Equations [8]. Eddy viscosity was referred to the flow as a function, not to the fluid. For turbulence flow, this function started to amplify. The behaviour of eddy viscosity depends on the existence of eddies; for example, it has been investigated that in the convective mixed layer, the behaviour of eddy viscosity is weaker [23]. It has been considered that each component of velocity variables includes two terms of stable and fluctuated parts (i.e. $u=\bar{u}+u'$ and $v=\bar{v}+v'$). By substituting velocity component into momentum Equations, applying Reynolds averaging rules, and simplifying for a steady and incompressible flow gives:

$$\frac{\partial}{\partial x_i}(\rho u_i u_j)=-\frac{\partial \hat{P}}{\partial x_j}+\frac{\partial}{\partial x_i}\left[\mu_{eff}(\frac{\partial u_i}{\partial x_j}+\frac{\partial u_j}{\partial x_i})\right]+S_{u_i} \tag{10}$$

Where $\mu_{eff}=\mu+\mu_t$, $\hat{P}=P-\frac{1}{3}\mu_{eff}\nabla u+\frac{2}{3}\rho k$ and $S_{u_i}=\frac{\partial \mu_{eff}}{\partial x_j}\frac{\partial u_j}{\partial x_i}-\frac{\partial \mu_{eff}}{\partial x_i}\frac{\partial u_j}{\partial x_j}$. It is worth noting that calculating the momentum Equation in laminar flow, S_{u_i} which has been omitted in Equation (10), $\hat{P}$ will be equal to P and μ_{eff} equal to μ without considering the turbulent term in the Equation S_{u_i}.

The boundary conditions for the computational field have been demonstrated in "Fig. 3". At the inlet, constant variables have been concerned, and at the outlet, the gradient of variables along the x-axis has been neglected. The written code sets velocity components equal to zero behind the square. This code detects the inserted square downstream in the flow field as a bluff body. It sets all velocity components along with downstream-direction equal to zero at the first calculative iteration. This trick decreases the calculation time and increases the convergence chance of this numerical method. The inlet velocity has been chosen based on Lyn et al. study [24].

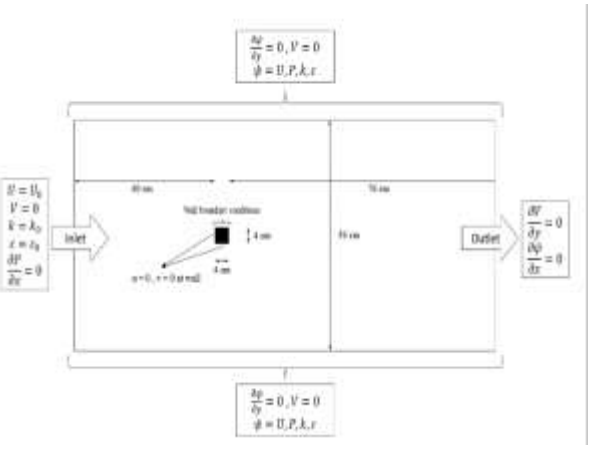

Fig. 3 Boundary condition of computation field at inlet, outlet and at the edge of bluff body.

The inlet turbulent kinetic energy ($k_0=\frac{3}{2}(T_u u_0)^2$) was calculated from the Equation of the isotropic turbulence, and Kolmogorov expression has been used for

dissipation term ($\varepsilon_0 = C_{\mu_0} \frac{k^{1.5}}{L_\varepsilon}$), which was extracted from the eddy-viscosity relation [33].

3 NUMERICAL SOLUTIONS

Generating mesh grids for the computation field in order to calculate the governing Equation in each cell is the main task in our work. The written code processes imported digital images, and after detecting edges, mesh grids based on the staggered grid have been generated. *P*, *k* and ε have been stored at nodal points (*I*, *J* labelled points) as a scalar quantity and vector variables (*u* and *v*) have been stored at cell faces, which *u*-velocity has been stored at *i, J* point and *v*-velocity have been stored at *I,j* point. The schematic of produced mesh grids from image processing by our code based on staggered grid mesh has been shown in "Fig. 4". In this Figure, filled circles illustrate edges of the body, and circled dots are nodal points of grid mesh in which scaler quantities (i.e. *P*, *k*, and ε) have been calculated. Extrapolation is necessary for calculating any variables at nodes near boundaries. The artificial symmetrical nodes, outside of the computational domain, have been shown in "Fig. 4".

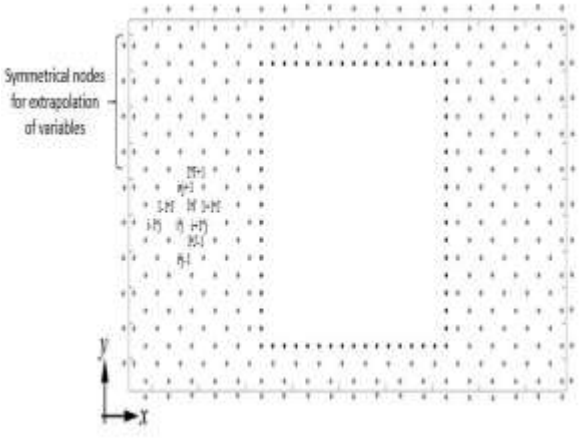

Fig. 4 Generated cell nodes based on stagger grid and illustration of produced symmetrical nodes for extrapolation of calculated variables at the boundary.

Computational fluid dynamics as a powerful computer-aided tool enables us to numerically solve governing Equations of fluid in a computational field's discrete space, called a cell, and simulate fluid properties. This simulation has been performed on the flow field, inside or around the modelled object. CFD provides virtual laboratory space and simulates all physical phenomena. With the considerable advancement of computer processing devices, very high-quality rendering can be seen. Our numerical method in CFD is based on the finite volume method, in which the integrals of the governing conservation Equations are discretized. The Finite Volume Method (FVM) is extensively used in fluid field calculations in addition to the finite difference and finite element methods. Numerous reasons, such as simple understanding and ease of use in structured and unstructured grids, have made this method very comprehensive. After converting the computational field into a set of small cells, each parameter's average value in the center of the cell has been considered, which is the main difference between the finite volume method and other methods. One of this method's essential features is that the main Equations of mass, momentum, and energy, after discretization, will be calculated in each cell, the conservation is satisfied automatically [19].

In this work, the governing Equation has been discretized based on the Power-law differencing scheme of Patankar. This scheme was developed based on the analytical solution of the convection-diffusion Equation. The Power-law scheme is useful to remove false diffusion error. This scheme is more accurate than the Hybrid scheme and has sufficient control over the Peclet number of cells. If cell *Pe* number be more than 10, the diffusion term will set to zero [31]. To overcome the checkerboard problem of pressure field and coupling of the pressure-velocity field, a staggered grid and SIMPLE (Semi-Implicit Method for Pressure Linked Equations) algorithm have been utilized. The decoupling between velocity and pressure field, named odd-even decoupling, is a discretization error in collocated grids and causes checkerboard patterns for pressure. One of the simplest ways to avoid this issue is utilizing the staggered grid. The staggered grid's main idea is to evaluate scalar variables (pressure, density, temperature, etc.) at nodal and velocity components evaluated on staggered grids centered on the cell faces. The mesh arrangement for two-dimensional flow has been shown in "Fig. 5".

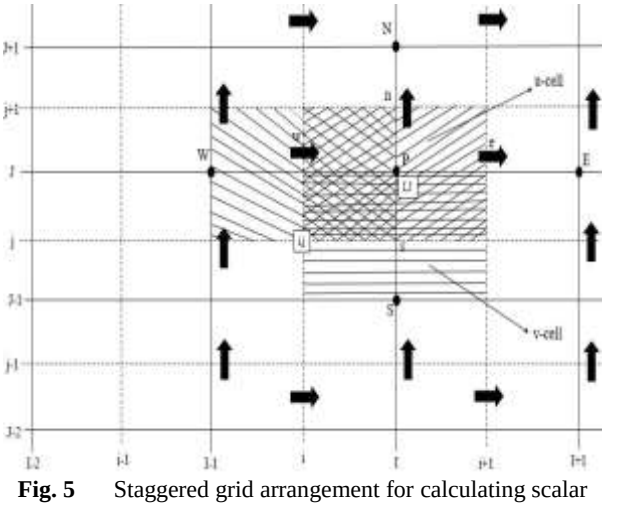

Fig. 5 Staggered grid arrangement for calculating scalar and vector variables.

The pressure as a scalar variable has been stored at the nodes, but velocities have been evaluated on the grid nodes' cell faces. Horizontal faces store *u* velocity, and verticals store *v* components of velocity, whereas in a collocated grid, all variables of the flow field have been stored at the cell center. The staggered grid's most common usage is compressible or incompressible flow in a structured grid. The staggered grid produces a numerical error on an unstructured mesh grid with skewness [31].

The numerical solution approach in CFD produces numerical errors that cause oscillations in solution, and consequently, written code has diverged. Some multiplied factors have been presented as a relaxation factor to converge solution and increase stability, which plays a crucial role in stable condition. The value upper than one is called the over-relaxation factor, and lower than 1 is the under-relaxation factor. All variables have been corrected in any cell of mesh for each iteration in SIMPLE family algorithms. The correction procedure for pressure has been obtained by adding guessed pressure field with correction as $P^{new} = P^{*} + P'$ which star represents guessed value and prime illustrates correction. The under-relaxation factor, which has been implemented in these relations, has been written $P^{new} = P^{*} + \alpha_p P'$. This Equation α_p is under relaxation factor for pressure, and its values vary from 0 to 1. If $\alpha_P = 1$ has been selected, guessed pressure filed corrected by correction value, and if $\alpha_P = 0$ will be selected no correction applied to the pressure field. Also, for other variables, under relaxation factor has been introduced as $\phi^{new} = \alpha_\phi \phi + (1-\alpha_\phi)\phi^{(n-1)}$, where ϕ has been replaced instead of velocity components (*u*, *v*), The turbulent kinetic energy (*k*), and dissipation term (ε). ϕ is corrected value of any variables in computation field and $\phi^{(n-1)}$ demonstrates the obtained value of ϕ in the previous iteration. The selected values for the under-relaxation factor have been shown in "Table 1". The default under relaxation parameters of Ansys-Fluent software [13] has been chosen for this simulation. Maximum 50000 iterations and minimum 10^{-6} accuracy have been considered for acceptable convergence of the calculated variables (*i.e. u*, *v*, *P*, *k*, and ε).

Table 1 Relaxation factor values for fluid flow parameters of domain.

u velocity	v velocity	Pressure	Turbulent kinetic energy	Dissipation term
α_u= 0.5	α_v= 0.5	$\alpha_p = 0.5$	$\alpha_k = 0.5$	$\alpha_\epsilon = 0.5$

4 RESULTS AND DISCUSSION

The predictions of the developed model have been verified using the experimental data of Lyn et al. [24], Durao et al. [11], and McKillop and Durst [25]. The calculated velocity components of *u* and *v* are the algebraic additions of the steady and perturbed velocity terms (i.e. $u = \bar{u} \pm u'$ and $v = \bar{v} + v'$). In the used experimental data, perturbed (u' and v') and steady velocity components ($\bar{u}$ and $\bar{v}$) have been calculated separately. But in our mathematical solution, the values of velocity (*u* and *v*) have been calculated directly. Therefore, the calculated velocity values should be in the ranges of $\bar{u} - u' < u < \bar{u} + u'$ and $\bar{v} - v' < v < \bar{v} + v'$. Figures 6 and 7 demonstrate the velocity component of *u* and *v*, respectively, along the *x*-axis and compared with experimental data [11], [24-25].

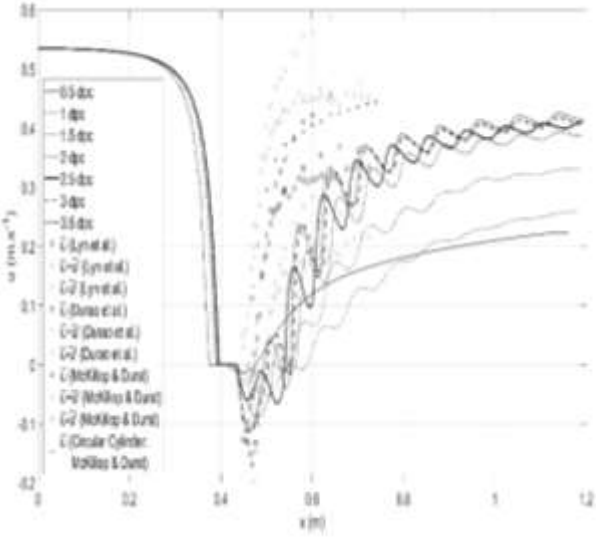

Fig. 6 *u*-velocity component along *x*-axis compared with experimental data and grid study results for different dpc values.

Figures 8 and 9 show *u* and *v* velocity profiles along the *y*-axis, similarly. Figures 6 to 9 also contain the grid study results based on dpc (dot per centimeter unit) which were chosen among 0.5 to 3.5 dpc. The obtained results for the 3 dpc resolution are similar to the results of the 3.5 dpc simulation. Attending to the 3 dpc simulations' lower calculation cost, this resolution is suitable for this simulation.

Figure 10 shows the calculated streamlines of this turbulent fluid flow around the square obstacle. The arrows illustrate the flow direction. The generated vortexes behind the bluff body have been observed in the coordinated field.

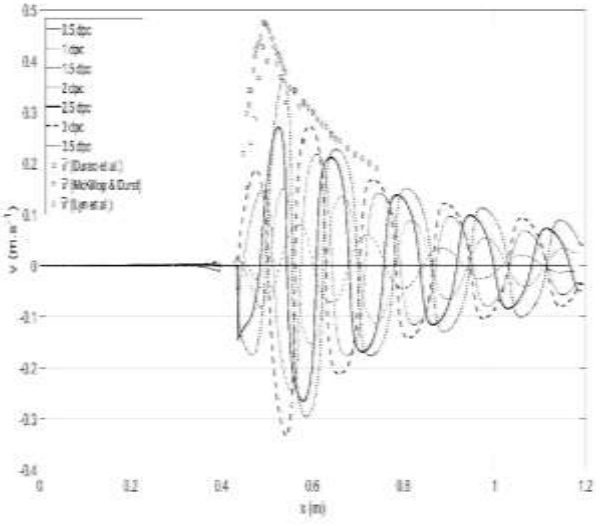

Fig. 7 *v*-velocity component along *x*-axis compared with experimental data and grid study results for different dpc values.

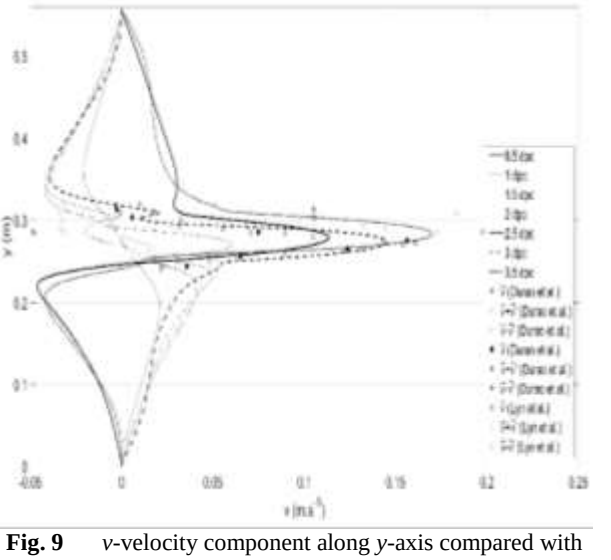

Fig. 9 *v*-velocity component along *y*-axis compared with experimental data and grid study results for different dpc values.

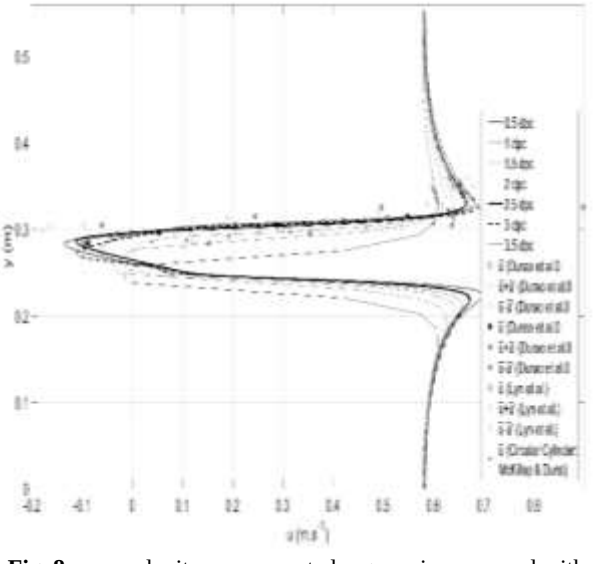

Fig. 8 *u*-velocity component along *y*-axis compared with experimental data and grid study results for different dpc values.

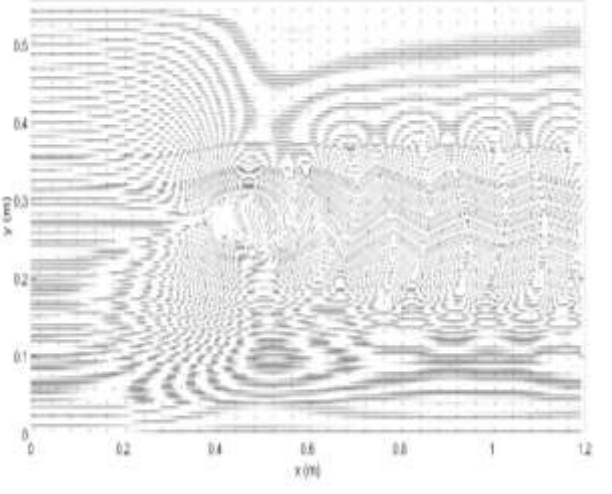

Fig. 10 Streamlines around obstacle as a bluff body.

Figure 11 demonstrates the contour of the pressure field and velocity vectors. The higher values of pressure contours in the square body's front show the stagnation point. The velocity got closer to zero value in this zone, and pressure reached maximum value. In the behind of the square, generated vortexes reduce pressure, and circulation zones have been developed. Arrows have presented the velocity vectors and their values in the flow field, especially in circulation zones.

The variation of kinetic energy and dissipation rate values have been illustrated in "Fig. 12". In "Fig. 12(a)", the contour of k has been shown. In the front of the square obstacle, the maximum value of k has been reached, but in circulation zones, this value has been decreased, sharply. The variation of kinetic energy value in circulation zones is significant too. In "Fig. 12(b)", the dissipation rate contour has been demonstrated. The lowest value of ε has been found in the front of the square obstacle, in the region, velocity values are closer to zero and in the downstream of the flow field. In circulation zones, the dissipation rate has been increased smoothly.

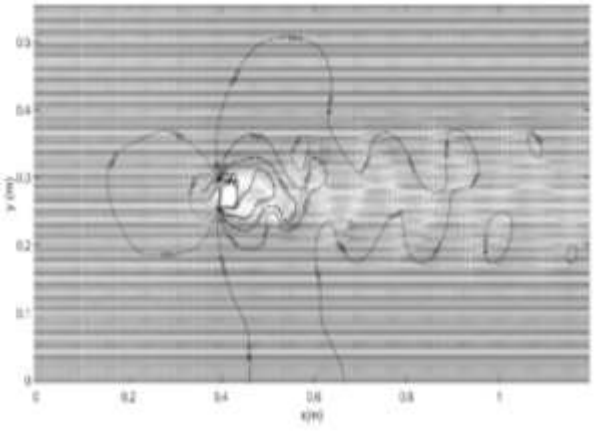

Fig. 11 Pressure contour and velocity vectors around square body.

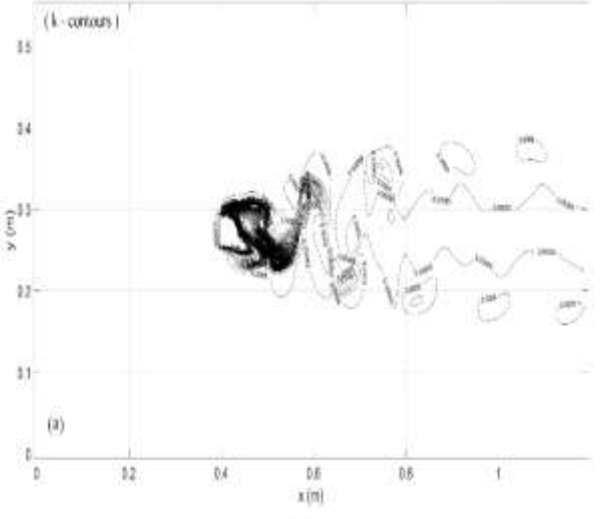

(a)

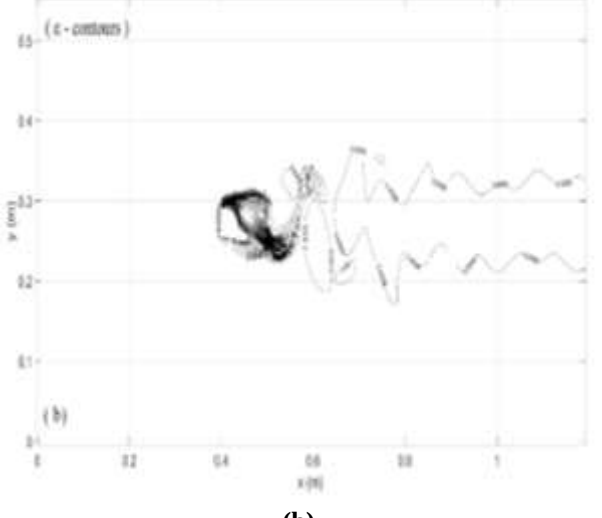

(b)

Fig. 12 (a): Kinetic energy contour plot around obstacle, and (b): dissipation rate contour plot.

Figure 13 shows the ratio of $\frac{\mu_{eff}}{\mu}$. Physically $\frac{\mu_{eff}}{\mu} = 1$ explains this fact that the turbulence does not affect viscosity, and the flow field's viscosity is equal to the viscosity of the fluid. The higher value of the turbulence effect on the viscosity of flow demonstrates the strength of the turbulence effect. The variation of viscosity in the flow field's circulation zones has been obtained from this Figure.

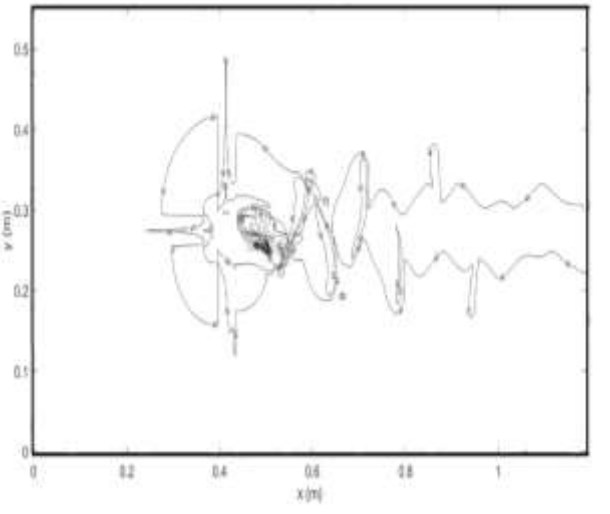

Fig. 13 The contour plot of effective viscosity and fluid viscosity rate.

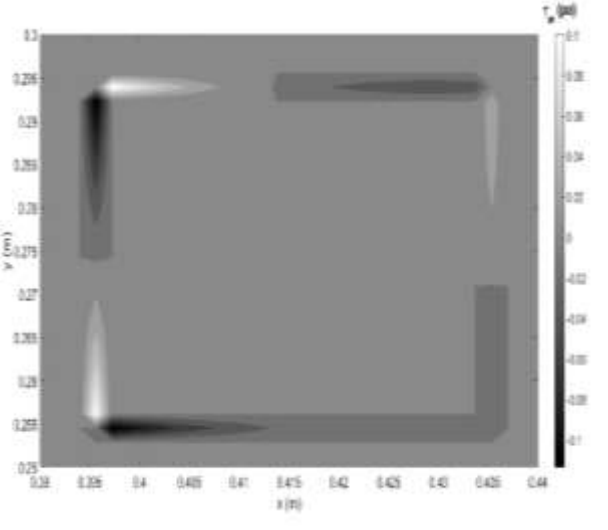

Fig. 14 Shear stress value near the wall of obstacle. Negative values refer to direction of velocity gradient on the wall.

The contour of wall shear stress (τ_w) on the square body's boundary edges has been shown in "Fig. 14", which is vital for calculating skin friction drag in

aerodynamics [18]. The variation of shear stress of the wall perpendicular to the boundary layer due to the velocity gradient along the *y*-axis has been calculated. The positive and negative values of τ_w are related to the direction of coordinates.

5 CONCLUSIONS

The main novelty of the present work was to provide simple, fast and accurate way to generate mesh generation procedure by combining computational fluid dynamics with image processing method for simulating the turbulent flow around any bluff bodies. Consequently, the developed homemade code utilized the image processing method to detect square obstacle edges as a bluff body in order to generate orthogonal, structured, and staggered mesh for the computational domain. The presented methos in this study, reduces the cost of calculation considerably due to the processing of imported images, generating meshes, and solving governing Equations were done automatically and simultaneously.

The modified Low-Reynolds Chien's model based on the k-ε turbulent model was used to simulate turbulent flow around a single square. The pressure and velocity field has been coupled by segregated mesh and power-law scheme. The governing Equations were discretized based on the finite volume approach. The brightness and contrast as an effective filter were considered to decrease the imported digital image noises. The results were verified with previous of the experimental works. The good agreement was seen. The shear stress over walls was calculated due to the viscosity effect and boundary layer effect. The velocity gradient perpendicular to each wall was estimated, for calculating skin friction drag. The shape optimization of bluff bodies is an ability of the current method that can be considered as future outlook.

6 NOMENCLATURES

$C_\mu, C_{\varepsilon 1}, C_{\varepsilon 2}$	Constants [9]: $C_\mu = 0.09, C_{\varepsilon 1} = 1.35, C_{\varepsilon 2} = 1.8$
dpc	Dot per centimeter
D, E	Additional source terms [9]: $D = 2\nu \frac{k}{y^2}$, $E = -2\nu \frac{\varepsilon}{y^2} exp - 0.5y^+$
f_μ, f_1, f_2	The damping functions [9]: $f_\mu = 1 - exp - 0.0115y^+$, $f_1 = 1,\ f_2 = 1 - 0.22exp - (\frac{Re_t}{6})^2$
g_i	Acceleration caused by an external physical force ($m.s^{-2}$)
k	The turbulent kinetic energy ($J.kg^{-1}$)
k_0	Initial kinetic energy term
k_{wall}	Kinetic energy near of the wall [9]: $k_{wall} = 0$
L_ε	The dissipation scale
P	Mean pressure (*Pa*)
$\overline{P}$	Average pressure (*Pa*)
P_k	The rate of production of turbulence kinetic energy [33]: $P_k = -\overline{u_i' u_j'} \frac{\partial u_i}{\partial x_j}$
Re_t	Reynolds number of turbulence flow [9]: $\mathrm{Re}_t = \frac{k^2}{\upsilon\varepsilon}$
S_{u_i}	Source term
T_u	Relative turbulence intensity [33]: $T_u = \frac{u_t}{u_0}$
u^*	Friction velocity [35]: $u^* = \sqrt{\frac{\tau_w}{\rho}}$
$\overline{u_j}, \overline{u_i}$	Components of the average velocity vector ($m.s^{-1}$)
u_j', u_i'	Components of the turbulent velocity vector ($m.s^{-1}$)
$\overline{u_i' u_j'}$	Reynolds stress components ($m^2.s^{-2}$) [2]
y^+	Normal distance in wall coordinates [9] $y^+ = \frac{u^* y}{\upsilon}$
δ_{ij}	Kronecker delta $\delta_{ij} = \begin{cases} 1 & i = j \\ 0 & i \neq j \end{cases}$
ε	Turbulent kinetic energy dissipation rate ($J.kg^{-1}$)
ε_0	Initial kinetic energy dissipation rate term
ε_{wall}	Kinetic energy dissipation rate [9]: $\varepsilon_{wall} = 0$
μ	The viscosity of fluid (*Pa.s*)

μ_t	Turbulent viscosity of the flow based on the k-ε model (*Pa.s*) [2]: $\mu_t = C_\mu f_\mu \rho \frac{k^2}{\varepsilon}$
μ_{eff}	The effective viscosity of fluid [7]: $\mu_{eff} = \mu_t + \mu$
υ	Kinematic viscosity of the fluid ($m^2.s$)
ρ	Density of the fluid ($kg.m^{-3}$)
$,\sigma_\varepsilon\ \sigma_k$	Turbulent Prandtl numbers [34]: $\sigma_k = 1, \sigma_\varepsilon = 1.3$
τ_w	Wall shear stress (*Pa*)

REFERENCES

[1] Abolpour, B., Investigating Effects of Molecular Structure on The Behavior of Saturated Liquid Hydrocarbons Using a Novel Semi-Empirical Equation of State, Fluid Phase Equilibria, Vol. 456, 2018, pp. 184-192.

[2] Abolpour, B., Afsahi, M. M., Goharrizi, A. S., and Azizkarimi, M., Study of the Motion and Deposition of Micro Particles in A Vertical Tube Containing Uniform Gas Flow, Heat and Mass Transfer, Vol. 53, No. 12, 2017, pp. 3517-3528.

[3] Abolpour, B., Afsahi, M. M., Yaghobi, M., Goharrizi, A. S., and Azizkarimi, M., Interaction of Heat Transfer and Gas Flow in A Vertical Hot Tube, Heat and Mass Transfer, Vol. 53, No. 7, 2017, pp. 2409-2417.

[4] Abolpour, B., and Shamsoddini, R., A Novel Scheme for Predicting the Behaviors of Liquid and Vapor Phases of Water Using the Ideal Gas Theory. International Journal of Thermodynamics, Vol. 21, No. 3, 2018.

[5] Afsahi, M. M., Abolpour, B., Kumar, R. V., and Sohrabi, M., Modeling of Noncatalytic Hydrogen Reduction of Molybdenum Disulfide in the Presence of Lime, by Complex Multistep Gas–Solid Reactions, Mineral Processing and Extractive Metallurgy Review, Vol. 34, No. 3, 2013, pp. 151-175.

[6] Barber, D. C., Oubel, E., Frangi, A. F., and Hose, D., Efficient Computational Fluid Dynamics Mesh Generation by Image Registration, Medical Image Analysis,Vol. 11, No. 6, 2007, pp. 648-662.

[7] Bosch, G., and Rodi, W., Simulation of Vortex Shedding Past a Square Cylinder Near a Wall, International Journal of Heat and Fluid Flow, Vol. 17, No. 3, 1996, pp. 267-275.

[8] Boussinesq, J., Thōrie Analytique de la Chaleur Mise en Harmonie Avec la Thermodynamique et Avec la Thōrie Mc□anique de la Lumi_re: Refroidissement et c□hauffement par Rayonnement, Conductibilit □des Tiges, Lames et Masses Cristallines, Courants de Convection, Thōrie Mc□anique de la Lumi_re, xxxii, 625, [1], 1903, Vol. 2, Gauthier-Villars.

[9] Chien, K. Y., Predictions of Channel and Boundary-Layer Flows with A Low-Reynolds-Number Turbulence Model, AIAA Journal, Vo. 20, No. 1, 1982, pp. 33-38.

[10] Cuadros-Vargas, A. J., Nonato, L. G., Minghim, R., and Etiene, T., Imesh: An Image Based Quality Mesh Generation Technique, XVIII Brazilian Symposium on Computer Graphics and Image Processing, 2005, (SIBGRAPI'05).

[11] Durao, D., Heitor, M., and Pereira, J., A Laser Anemometry Study of Separated Flow Around a Squared Obstacle, Laser Anemometry in Fluid Mechanics III, 1986, pp. 227-243.

[12] Fang, Q., Boas, D. A., Tetrahedral Mesh Generation from Volumetric Binary and Grayscale Images, IEEE International Symposium on Biomedical Imaging: From Nano to Macro, 2009.

[13] Fluent, A., ANSYS Fluent Theory Guide 15.0. ANSYS, Canonsburg, PA, 2013, 33.

[14] Franke, R., Rodi, W., Calculation of Vortex Shedding Past a Square Cylinder with Various Turbulence Models, In Turbulent Shear Flows Vol. 8, 1993, pp. 189-204.

[15] Goharrizi, A. S., Abolpour, B., Modeling an Industrial Sodium Bicarbonate Bubble Column Reactor, Applied Petrochemical Research, Vol. 4, No. 2, 2014, pp. 235-245.

[16] Hale, D., Atomic Images-A Method for Meshing Digital Images, IMR, 2001.

[17] Hosseini, S. M. J., Goharrizi, A. S., and Abolpour, B., Numerical Study of Aerosol Particle Deposition in Simple and Converging–Diverging Micro-Channels with A Slip Boundary Condition at The Wall, Particuology, Vol. 13, 2014, pp. 100-105.

[18] Houghton, E. L., Carpenter, P. W., Collicott, S. H., and Valentine, D. T. Chapter 1, Basic Concepts and Definitions, In E. L. Houghton, P. W. Carpenter, S. H. Collicott, & D. T. Valentine (Eds.), Aerodynamics for Engineering Students (Seventh Edition), Butterworth-Heinemann, 2017, pp. 1-86.

[19] Hirsch, C. Numerical Computation of Internal and External Flows, Computational Methods for Inviscid and Viscous Flows, Chichester, Vol. 2, 1990.

[20] Kato, M., The Modelling of Turbulent Flow Around Stationary and Vibrating Square Cylinders, Turbulent Shear Flow, 1993, pp. 16-18

[21] Kocharoen, P., Ahmed, K. M., Rajatheva, R., and Fernando, W., Adaptive Mesh Generation for Mesh-Based Image Coding Using Node Elimination Approach, IEEE International Conference on Communications, ICC, 2005.

[22] Lassoued, K., Sophy, T., Jouanguy, J., and Le-Moyne, L., Fluid Flow Simulation Over Complex Shape Objects Using Image Processing to Achieve Mesh Generation, International Journal of Simulation and Process Modelling, Vol. 12, No. 1, 2017, pp. 54-68.

[23] Launder, B. E., Sandham, N. D., Closure Strategies for Turbulent and Transitional Flows, Cambridge University Press, 2002.

[24] Lyn, D. A., Einav, S., Rodi, W., and Park, J. H. A Laser-Doppler Velocimetry Study of Ensemble-Averaged Characteristics of The Turbulent Near Wake of a Square Cylinder, Journal of Fluid Mechanics, Vol. 304, 1995, pp. 285-319.

[25] McKillop, A., Durst, F., A Laser Anemometry Study of Separated Flow Behind a Circular Cylinder, Laser Anemometry in Fluid Mechanics II, 1986.

[26] Patel, V. C., Rodi, W., and Scheuerer, G., Turbulence Models for Near-Wall and Low Reynolds Number Flows-A Review, AIAA Journal, Vol. 23, No. 9, 1985, pp. 1308-1319.

[27] Shamsoddini, R., Abolpour, B., A Geometric Model for A Vortex Tube Based on Numerical Analysis to Reduce the Effect of Nozzle Number, International Journal of Refrigeration, Vol. 94, 2018, pp. 49-58.

[28] Shamsoddini, R., Abolpour, B., Bingham Fluid Sloshing Phenomenon Modelling and Investigating in A Rectangular Tank Using SPH Method, Ships and Offshore Structures, 2020, pp. 1-10.

[29] Sondak, D. L. Wall functions For The K-[Epsilon] Turbulence Model in Generalized Non-Orthogonal Curvilinear Coordinates, 1992.

[30] Tahmasebi, M. K., Shamsoddini, R., and Abolpour, B., Experimental and Numerical Investigating the Effect of Baffle on the Shallow Water Sloshing in a Moving Tank using OpenFOAM Software. Modares Mechanical Engineering, Vol. 20, No. 2, 2020, pp. 353-359.

[31] Versteeg, H. K., Malalasekera, W., An Introduction to Computational Fluid Dynamics: The Finite Volume Method, Pearson Education, 2007.

[32] Wang, R., Gao, J., Gao, Z., Gao, X., and Jiang, H. Complex Network Theory-Based Condition Recognition of Electromechanical System in Process Industry, Science China Technological Sciences, Vol. 59, No. 4, 2016, pp. 604-617.

[33] Younis, B., Przulj, V., Computation of Turbulent Vortex Shedding, Computational Mechanics, Vol. 37, No. 5, 2006, pp. 408.

[34] Abolpour, B., Hekmatkhah, R., and Shamsoddini, R., Multi-Objective Optimum Design for Double Baffle Heat Exchangers, Thermal Science and Engineering Progress, Vol. 26, 2021, pp. 101132.

[35] Abolpour, B., Hekmatkhah, R., and Shamsoddini, R., Optimum Design for the Tesla Micromixer, Microfluidics and Nanofluidics, Vol. 26, No. 6, 2022, pp. 1-8.

[36] Asheghi Bonabi, I., Hemmati, S. J., Bone Surface Model Development Based on Point Clouds Extracted From CT Scan Images, ADMT Journal, Vol. 10, No. 2, 2017, pp. 61-70.

[37] Vini, M. H., Daneshmand, S., Bonding Evolution of Bimetallic Al/Cu Laminates Fabricated by Asymmetric Roll Bonding, Advances in Materials Research: AMR, Vol. 8, No. 1, 2019, pp. 1-10.

Int. J. Advanced Design and Manufacturing Technology, 2022, Vol. 15, No. 4, pp. 125-132

DOI: 10.30486/admt.2023.1961907.1358 ISSN: 2252-0406 https://admt.isfahan.iau.ir

Feed Stock Fabrication of AISI 4605 Steel for Fused Deposition Modeling and Sintering and Designing of Its Extruder Mechanism

Amir Hossein Rahimi*
Department of Mechanical Engineering,
K.N. Toosi University of Technology, Iran
E-mail: Ah.Rahimi@email.kntu.ac.ir
*Corresponding author

Jamal Zamani
Department of Mechanical Engineering,
K.N. Toosi University of Technology, Iran
E-mail: Zamani@kntu.ac.ir

Received: 26 June 2022, Revised: 19 September 2022, Accepted: 25 September 2022

Abstract: Fused Deposition Modeling and Sintering (FDMS) is one of the indirect and emerging processes of Additive Manufacturing (AM) for the production of metal parts, which is a combination of AM process and Metal Injection Molding (MIM). This study laboratory made a raw material (Feed Stock) composing of high percentage of metal powder (particle in nano-scale) and polymeric materials; and then, designed an extruder to simulate melting and extruding process by Computational Fluid Dynamic (CFD). The different variables such as the nozzle diameter (D) of 1, 2, 3 and 4 mm and compression zone length (L2) of 100, 200 and 300 mm were simulated to investigate their impacts on flow rate and required torque to rotate screw. The findings showed that components of feed stock for high physical and mechanical properties of FDMS should account for 55 wt.% of paraffin wax, 25 wt.% of polypropylene, 15 wt.% of carnauba wax and 5 wt.% of stearic acid with optimum percentage of metal powder of 90 wt.%. Also, the optimum value of extruder diameter and compression zone length were 2mm and 200 mm, respectively.

Keywords: Additive Manufacturing, AISI 460 Steel Alloy, Extruder Screw, Fused Deposition Modeling and Sintering

Biographical notes: Amir Hossein Rahimi received his MSc in Material Engineering from Malek Ashtar University of Technology (MAUT) in 2008 and currently is PhD student at Department of Mechanical Engineering in K.N. Toosi University of Technology. His current research interest includes Additive Manufacturing Technology. **Jamal Zamani** is full professor of Mechanical engineering at the University of KNTU. He received his PhD in Mechanical engineering from Tarbiyat Modares University in 2003. His current research focuses on AM and FDMS.

Research paper

1 INTRODUCTION

Additive Manufacturing is a term for a class of manufacturing techniques that use the process of layer-by-layer manufacturing using computer-aided design [1]. A wide range of raw materials, such as polymeric materials with low melting temperatures to metals and ceramics with high melting point with different forms of liquid, powder and wire are used in these processes [2]. Nowadays, research in the field of additive manufacturing is no longer focused on the production of polymer prototypes and the aim of developing these techniques is to produce functional metal parts with complex shapes, which cannot be easily produced by conventional methods that have applications in the field of aerospace, automobiles, fast tools and medicine [3]. The additive manufacturing process for the manufacturing of metal parts is divided into two categories: direct and indirect processes [4].

Direct processes include selective laser sintering, selective laser melting, laser metal deposition, electron beam melting and Binder Jetting [5-9]. The base material of most of these processes is based on powder and the energy required to melt the powder is supplied through laser beam or electron beam, which is both time-based and very costly. One of the new indirect processes in the manufacture of metal parts is Fused Deposition Melting and Sintering (FDMS).

This process is one of the most cost-effective additive manufacturing processes due to the low cost of equipment, easy operation and low cost of raw materials [10]. This process has four stages of compounding of raw material, printing the desired shape (green part), debinding and sintering [11-17]. The process of printing the part in this process is the same as fused Deposition Modelling Process (FDM), except that in the FDM process, flexible filaments with fixed diameter are always used, while, the FDMS feedstock contains high percentage of powder that increases the viscosity of the melt and makes it brittle [18-21].

Therefore, the design of the extruder in FDMS system is made custom for the selected feedstock. Rheology of raw material is the most important parameter for this reason [22]. Till date, few studies have been conducted on development of raw material of the FDMS process, but due to the great similarity between this material and the raw material in MIM process, same feedstock can be used with a little change in the percentage of its components [23].

One of the most widely used binding systems in MIM is based on polypropylene and paraffin wax-based. For example, a combination of polypropylene, paraffin wax, carnauba wax and stearic acid has been successfully applied as a binder system to produce porous micron parts made of austenitic stainless steel using steel powder [24]. In addition, various types of adhesive systems such as polypropylene base, wax base and ethylene vinyl acetate (EVA) base were used for metal injection molding of parts made of L316 stainless steel with nano meter dimensions [25].

In recant years, few researches have been conducted on the rheology of two-phase material (containing metal powder and polymeric system) used for FDMS process [26-30]. In this study, the 4605-steel feedstock has been optimized for the FDMS process and an optimized screw has been designed for extrusion of the selected feedstock. Moreover, previous works have not simulated an extrusion to melt this feed stock and compress them to satisfy the purpose of AM. Therefore, CFD approach was applied to investigate various variables such as diameter and compression zone length of extruder.

2 METHOD

In this research, first, the raw material feed is selected that contains binder constituents and optimum percentage of 4605 metal powder and in the next step, the screw of the extruder of the printer is designed on the bases of rheological properties.

2.1. Feedstock Preparation

The raw materials used in the FDMS process are a combination of metal powder and adhesive system, called feedstock. This material should be injectable in the first step so that it can be injected with the help of extruder and then it should have the highest allowable powder volume so that the final piece has the lowest porosity and the highest mechanical properties. There are many parameters including the size, shape and percentage of metal powder as well as polymer components and their percentage that influences the final properties of the product in this process.

In this research, AISI 4605 low alloy steel powder (Jiangxi Yuean Superfine Metal Co., Ltd., China) produced by gas atomizing method has been produced. "Table 1" shows the chemical composition, cumulation density, D-Value values as well as distribution slope parameter (Sw) of the powder used. The slope parameter of the distribution, which indicates the slope of the powder grain size distribution and indeed the slope of the normal logarithmic cumulative distribution curve, is measured by "Eq. (1)" [22]:

$$S_w = \frac{2/56}{log\left(\frac{d90}{d10}\right)} \quad (1)$$

Table 1 The specifications of AISI 4605 steel powder in this research

Apparent Density (g/cm^3)	Slope Parameter Distribution (Sw)	Particle Size Distribution (μm)			Chemical Composition (Wt%)				
		D_{10}	D_{50}	D_{90}	Fe	C	Ni	Mo	Si
2.6	4.53	1.97	3.92	7.23	Bal.	0.42	2.15	0.49	0.1

One of the important features of the powder used in the process is the widespread distribution of powder grains of different sizes, leading to high density in the final piece and the use of less adhesive system during the process. From the point of view of particle size distribution, the powder suitable for the injection process should have a distribution slope value greater than 2 and consequently the particle size distribution should be wide. Under these conditions, higher compression density is achievable and less adhesive system is required for raw material preparation. On the other hand, powders with high sw values (more than 7) with very narrow size distributions are not suitable for the injection process [31]. According to Equation (1), the distribution slope for the powder used in this study is 4.53. Therefore, the powder used has an acceptable distribution slope which makes it suitable for use in the injection process from the nozzle with the aim of increasing the compression density of the powder and consequently the density of the sintered piece. Also, to help with the sintering, the use of powder particles with sizes between 0.1 and 20 microns and spherical shape is suitable [32], in which spherical powder with an average of particles less than 10 microns has been used. Polypropylene has also been used as a backbone polymer. This polymer, which performs the task of maintaining the shape of the piece during the adhesion process and before sintering, has been used in many researches as a suitable material as backbone polymer [33]. In the following, paraffin wax and carnauba wax have been used as surface activators in order to create a bond between adhesive system and powder grains. These materials increase the stability of powder grains due to shear stress during the mixing process. Also, carnauba wax, due to its extensive decomposition temperature, helps to preserve the shape of the piece at the time of boiling spit to the backbone polymer [33]. Stearic acid has also been added to the adhesive system as a lubricant and terrier to improve flowability and lubrication [33-34]. This compound is similar to the study of S.Ahn [35] and Lin [36], which has 55 wt.% paraffin wax, 25 wt.% polypropylene, 15 wt.% carnaoba wax and 5 wt.% staric acid as the binder system. As mentioned above, one of the most important parameters in feedstock is the percentage of metal powder, the high percentage of which increases the properties of the final piece and at the same time increases the viscosity that makes the extruding work of the material difficult and therefore should be optimized. One of the methods for calculating the optimum amount of powder is to calculate the critical volume concentration of powder or CPVC, which is determined by calculating the maximum torque during the mixing of the binder and powder system [37]. In this study, the amount of torque in terms of time for mixing feedstock in different weight percentages of powder in the range of 87-95 wt.% was investigated and the critical volume concentration of the powder was calculated.

In order to prepare the adhesive system and perform the mixing of raw materials, HAAKE Rheomix PolyLab QC Lab Mix equipped with a pair of Z-shaped blades has been used. The mixing temperature is selected based on the maximum melting temperature of the adhesive system components (polypropylene), 190°C. According to similar researches [38]. mixing speed of 75 rpm and mixing time of 20 minutes were considered. After the mixing process, the mixture was cooled to room temperature and turned into granules.

2.2. Evaluation of Feed Properties of Raw Material Produced

In order to simulate the rheology of the material and design the nozzle of the printing machine, the feed parameters of the raw material are required. For this purpose, rheological properties of prepared feeds have been calculated using torque flow and rheological tests to determine the appropriate amount of adhesive system components.

3 DESIGNS OF FDMS NOZZLE

In order to study the relations governing the internal flow geometry of the FDMS nozzle (extruder) by considering the raw material feed rheology (melt flow index and feed material viscosity index) and the screw cylinders, computational fluid dynamics (CFD) using input parameters was given to the simulation software and finally, using the input parameters of the extruder nozzle (D) and the length of the compression zone (L2), the output flow rate of the raw material and the torque were calculated to determine the power of the screw actuation motor. The work is done.

The length of the compression zone (L2) is very important considering the compression ratio (ε). In a similar study, the length of this area is less than one third of screw [20]. Also, one of the most important parameters for designing the extruder of the FDMS device is determining the output diameter of the extruder nozzle (D), which has an important effect on the resolution of the printed sample. In the present study, the effects of

compaction zone lengths (L2) and different output diameters (D) on the feedstock melting process, screw pressure distribution, velocity distribution at output, torque required for screw rotation and average output flow were investigated.

In this research, a 25 mm diameter screw with a rotational speed of R =15 rpm and a cylinder with a fixed length of L =300mm were used in which a solid feedstock with ambient temperature (25 °C) enters the cylinder funnel. Feedstock extrusion temperature of 190 °C similar to previous researches [35-36] are fixed parameters in the simulation. The space between the screw and the cylinder is meshed by the snapy Hex-Mesh tool in Open-FOAM software, for which a three-dimensional unstructured mesh with 856,251 pieces is used.

To solve the phenomenon of melting and compaction of feedstock, the rho-Pimple-Foam solvent in Open-FOAM software is used to solve the flow in three-dimensional compressibility. The Equations of continuity, momentum and governing energy in the solvent are used according to Equations (2) to (7) [37]:

$$d\rho/dt+\nabla.(\rho V)=0 \quad (2)$$

$$D(\rho V)/Dt=\nabla.\sigma \quad (3)$$

$$\sigma=-pI+\tau=-pI+\mu[(\nabla.V)+(\nabla.V)^{T}]-2\mu/3\ (\nabla.V)I \quad (4)$$

$$D(\rho e)/Dt+\nabla.(\rho VV+pI)=\nabla.(k\nabla T)+\mu\Phi \quad (5)$$

$$e=1/2\ V^{2}+u \quad (6)$$

$$\Phi=\tau:\nabla V \quad (7)$$

Where, v, p, e, u and I represent the velocity, pressure, total energy, internal energy and matrix vectors, respectively. The parameters ρ, μ, and k also indicate density, viscosity, and heat transfer coefficient, respectively. In the momentum relation, the stress component (σ) consists of compressive, shear (τ) stresses and element volume changes. Also in the energy Equation, the effects of volume change and heat loss (Φ) due to viscosity are considered. Parameter (e) is also the sum of the kinetic and internal energy of the fluid. Shear stress on the extruder wall (τ), torque (T) and output flow (m □_o) are calculated using the following Equations:

$$\tau = \mu \frac{\partial U}{\partial n} \text{ on screw wall} \quad (8)$$

$$T = \iint r\,\tau\,dA\,dz \quad (9)$$

$$\dot{m}_o = \int \rho U dA \quad (10)$$

In Eq. (9), r, τ, dA represent the cross-sectional area of the element, the shear stress on the element and the distance of the element from the center of the rotating axis, respectively. The boundary conditions used in the simulation include the following:

- Boundary conditions at the aperture entrance:
  Material feed, or in other words, the inlet velocity is regulated by suction rotation and the inlet temperature of the material is assumed to be environmental 25℃.
- Boundary conditions at the orifice output:
  The output speed and temperature are adjusted according to the screw speed and the feedstock melt temperature.
- Cylinder inner wall boundary conditions:
  The velocity of the fluid inside the cylinder is a function of screw's rotational speed. For this purpose, a rotating axis is provided for it. Its rotation speed is 15rpm and its temperature is 190℃.

4 RESULTS

4.1. CPVC

Torque values versus the time for feed mixing for different weight percentages of powder (87-95 wt.%) are shown in "Fig. 1a". As can be seen in the figure, the average torque values increase linearly with increasing weight percentage of powder till 92 wt.%. This increase continues until the slope of the line changes abruptly due to the lack of binder, which is accompanied by an increase in friction between the excess amount of powder grains in the feed. Figure 1.b also shows the mean mixing torque values in different weight percentages of powder in the feed, which is plotted by passing a line through the average values for each weight percentage of powder in the feedstock.

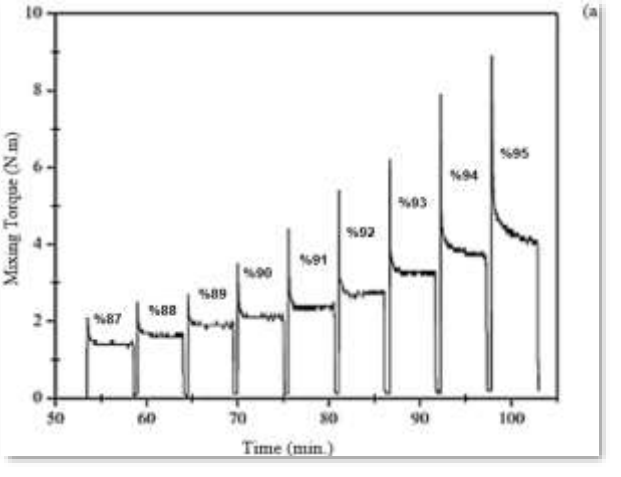

a

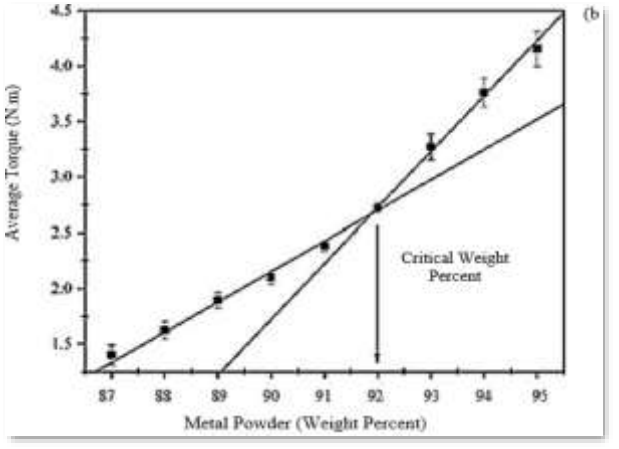

b

Fig. 1 The powder critical weight measurement: (a): mixing torque versus time at different powder weigh percentages, and (b): average torque at different powder weigh percent.

When the slope of the line begins to change, it means reaching the critical weight percentage of the powder. Finally, in order to increase the flowability and prevent instability of the rheological properties of the optimal powder content in the feedstock, it is usually considered to be 2 to 5% lower than the critical powder content in the feedstock [38], The weight content of the powder in the feed of the raw material is considered to be 90% by weight.

4.2. Viscosity

The results of rheological tests and how the viscosity logarithm changes according to the logarithm of the shear rate for the optimal adhesive system at 190 are shown in "Fig. 2".

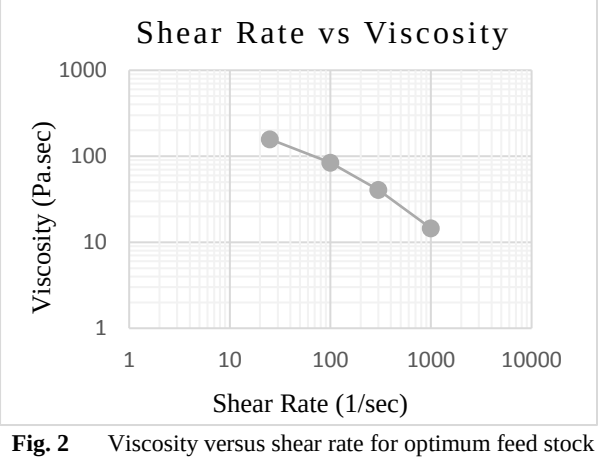

Fig. 2 Viscosity versus shear rate for optimum feed stock at different temperatures.

Sotomayor et al. [39] estimated the viscosity values for a successful injection molding (MIM) process to be less than 1000 Pa.s in the cut-off range between S-1100 to S-1 10,000. Therefore, from a rheological point of view, the results show that the feed can be injected in this interval.

4.3. Simulation Results

Figure 3a shows the effects of changes L2 and D on the torque required to extrude the raw material. As can be seen in the Figure, with increasing L2, first the torque decreases due to gradual melting and compaction of the melt, and then after L2 = 200 mm, it increases due to the enlargement of the compression zone and the melting zone. Increasing L2 leads to gradual compression of the raw material, which reduces the shear stress in the melt and increases the shear stress between the screw and the cylinder wall.

It can also be seen in "Fig. 3" that the torque decreases with increasing material flow and decreasing type I stress. The reason for the increase in torque at D = 1mm is that in a very small diameter of the nozzle, the stress of the first type is much higher than the second type. Figure 3b shows the effects of L2 and D on the output flow rate of the raw material.

As can be seen, with increasing L2, the output flow increases due to the gradual increase in pressure inside the extruder. An increase in D also indicates an increase in the flow rate. The reason for the sudden drop in flow velocity at D = 1 compared to other cylinder diameters is the presence of metal powder, which results in a high viscosity of the melt that must pass through a very small diameter of 1 mm.

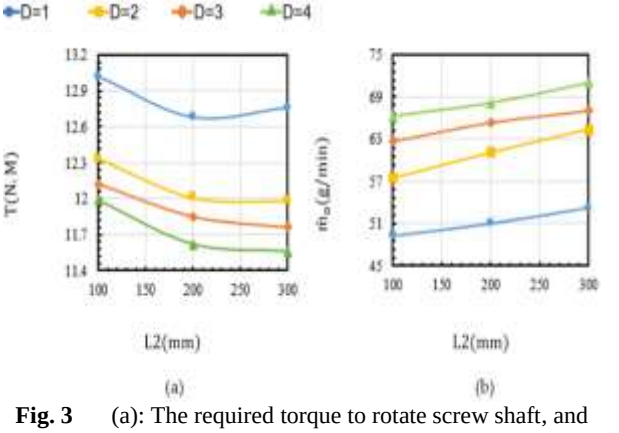

Fig. 3 (a): The required torque to rotate screw shaft, and (b): output flow rate ($\dot{m}_o$).

In "Fig. 4", the melting process is visible along the extruder for D = 2mm, in which blue represents the solid phase and red represents the liquid phase. In all cases it can be said that the feedstock melts at less than the first 0.25 L of screw. It is also observed that the increase in L2 has little effect on the melting zone.

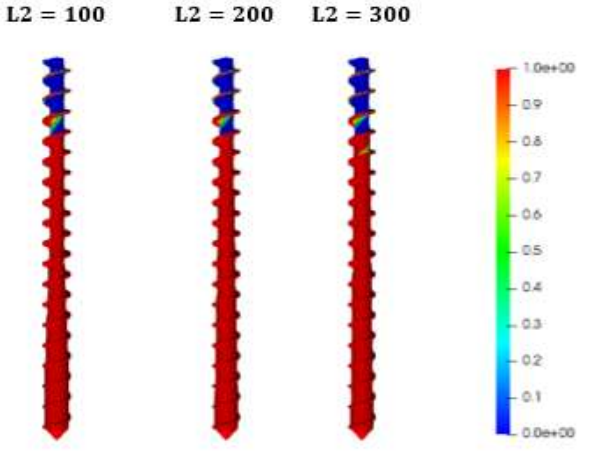

Fig. 4 Melting process along extruder for various L2 at D=2 mm.

Figure 5 shows the temperature distribution on the extruder at different diameters of the extruder cylinder. As can be seen, an increase in D increases the output flow, which in turn requires more heat to melt the raw material.

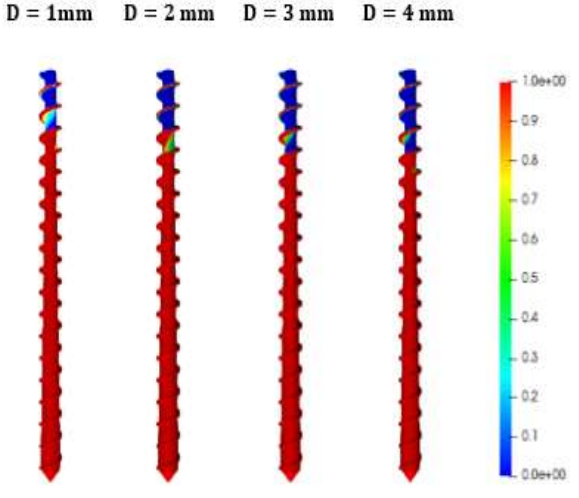

Fig. 5 Melting process along extruder for various D at L2=200 mm.

Figure 6 shows the pressure distribution on screw for different L2 values at D = 2mm and "Fig. 7" shows the pressure distribution on screw for different nozzle diameters at L2 = 200mm. All inlet pressure is atmospheric pressure, which increases to 0.75 L by moving along the screw axis and then decreases due to the discharge of melt out of the cylinder. It can also be seen that increasing L2 due to uniform compression of the melt reduces the maximum pressure and with increasing D the pressure inside the screw cylinder decreases and moves upwards of the extruder.

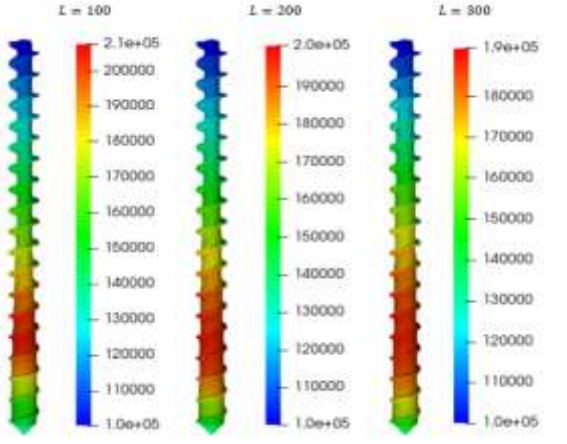

Fig. 6 Pressure distribution on screw shaft for various L2 at D=2 mm.

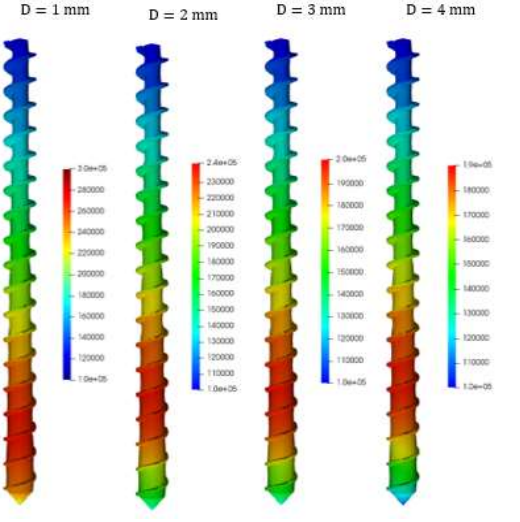

Fig. 7 Pressure distribution on screw shaft for various D at L2=200 mm.

The output velocity distribution for the extruder design and the flow rate distribution of the printed material in "Figs. 8 and 9" for different L2s at D = 2mm and different nozzle diameters at L2 = 200mm, are shown respectively. In all cases, the maximum velocity occurs in the center and near the nozzle walls. The results show that increasing L2 leads to increasing the maximum speed and increasing D leads to decreasing the maximum speed at the output.

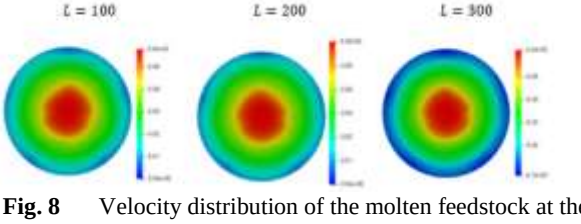

Fig. 8 Velocity distribution of the molten feedstock at the output for various L2 at D=2 mm.

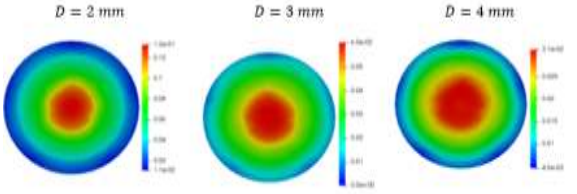

Fig. 9 Velocity distribution of the molten feedstock at the output for various D at L2=200 mm.

Figure 10a shows that by increasing L2, the maximum pressure inside the cylinder decreases. This causes the raw material to gradually thicken. On the other hand, increasing D makes it easier to extrude the molten raw materials in the extruder and reduces the maximum pressure. Figure 10b shows the maximum speed at the extruder output. As can be seen, the maximum velocity increases linearly with increasing L2. The output velocity can also be inversely related to D because the rotational speed of the screw axis is constant, so that increasing D reduces the velocity of the molten raw material. The reason for the decrease in extrusion speed with diameter D = 1 compared to diameter D = 2 can be related to the high viscosity of the feed melt and the high percentage of metal powder inside the raw material, which causes problems during the extrusion process at low diameters.

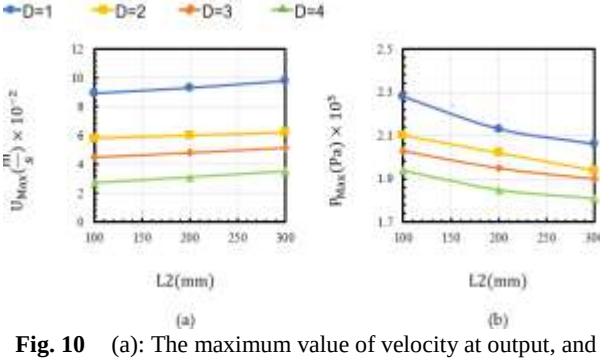

Fig. 10 (a): The maximum value of velocity at output, and (b): the maximum value of pressure inside extruder.

5 CONCLUSIONS

In this study, an binder system similar to that of S.Ahn and Kuang-hon Lin [35-36] containing 55 wt. % Paraffin wax, 25% polypropylene, 15% carnauba wax, and 5 wt. % Stearic acid was used according to the similarity of the powder used and the percentage of 4605 powder used was calculated using CPVC method equal to 90% by weight. Then, by extracting the rheological properties of the raw material, the extruder of the FDMS device has been designed. The effect of different compression lengths (L2) and extruder nozzle diameter (D) on melt temperature, pressure, outlet velocity and initial flow velocity were also investigated. In this study it was shown that the melt output from the nozzle D = 1mm was less than D = 2mm. This may be due to the higher melt stresses between the screw and the cylinder in the smaller nozzles. Also, it was shown that L2 = 200 mm leads to a softer melt with lower extrusion torque. Finally, it was found that the optimal design of the extruder with D = 2 and L2 = 200 mm with the required torque of 12N.M and the output melt flow of about 64 gr/min is a suitable design for the extruded feed 4605 made in this research.

REFERENCES

[1] ASTM Standard, F2792, Standard Terminology for Additive Manufacturing Technologies, ASTM International, West Conshohocken, Pennsylvania, 2012.

[2] West, A. P., Sambu, S. P., and Rosen, D. W., A Process Planning Method for Improving Build Performance in Stereolithography, Computer Aided Design, 2001, pp. 65–79.

[3] Li, N., Huang, S., Zhang, G., Qin, R., Liu, W., Xiong, H., Shi, G., and Blackburn, J., Progress in Additive Manufacturing on New Materials: A Review, J. Mater. Sci. Technol., Vol. 35, No. 2, 2019, pp. 242–269.

[4] Rahimi, A. H., Zamani, J., Development of a Feedstock for Additive Manufacturing of 4605 Steel Compact by FDMS Process, Transactions of the Indian Institute of Metals, 2022, pp. 1-7.

[5] Agarwala, M., Bourell, D., and Beaman, J., Direct Selective Laser Sintering of Metals, Rapid Prototyping, No. 1, 1995, pp. 26–36.

[6] Aghanajafi, C., Daneshmand, S., and Nadooshan, A. A., Influence of Layer Thickness on The Design of Rapid-Prototyped Models, Journal of aircraft, Vol. 46, No. 3, 2009, pp. 981-987.

[7] Korinko, P. S., Adams, T. M., Malene, S. H., Gill, D., and Smugeresky, J., Laser Engineered Net Shaping for Repair and Hydrogen Compatibility, Weld. J., Vol. 90, No. 9, 2011.

[8] Daneshmand, S., Ahmadi, A., and Aghanajafi, C., Design and Production of Wind Tunnel Testing Models with FDM Technology Using ABSi, International Journal of Manufacturing Research, Vol. 4, No. 2, 2009, pp. 120-136.

[9] Do, T., Seop Shin, Ch., Stetsko, D., VanConant, G., Vartanian, A., Pei, Sh., and Kwon, P., Improving Structural Integrity with Boron-Based Additives for 3D Printed 420 Stainless Steel, Procedia Manuf., Vol. 1, 2015, pp. 263–272.

[10] Rane, K., Strano, M., A Comprehensive Review of Extrusion-Based Additive Manufacturing Processes for Rapid Production of Metallic and Ceramic Parts, Adv. Manuf, Vol. 7, No. 2, 2019, pp. 155–173.

[11] Agarwala, M. K., Jamalabad, V. R., Langrana, N. A., Safari, A., Whalen Ph. J., and Danforth, S. C., Structural Quality of Parts Processed by Fused Deposition, Rapid Prototyp. J., Vol. 2, No. 4, 1996, pp. 4–19.

[12] Momeni, V., Hossein Alaei, M., Askari, A., Hossein Rahimi, A., and Nekouee, K., 2019. Effect of Carnauba Wax as A Part of Feedstock on The Mechanical Behavior

of a Part Made Of 4605 Low Alloy Steel Powder Using Metal Injection Molding, Material Wissen chaft und Werk Stoff Technik, Vol. 50, No. 4, 2019, pp. 432-441.

[13] Bin L., Yuxiang, W., Ziwei, L., and Tao, Zh., Creating Metal Parts by Fused Deposition Modeling and Sintering, Mater. Lett. 18, Vol. 263, 2020.

[14] Rahimnia, A., Hesarikia, H., Rahimi, A., Karami, S. and Kaviani, K., Evaluation and Comparison of Synthesised Hydroxyapatite in Bone Regeneration: as an in Vivo Study, Journal of Taibah University Medical Sciences, Vol. 16, No. 6, 2021, pp. 878-886.

[15] Tarafdar, A., Razmkhah, O., Ahmadi, H., Liaghat, G., Chitsaz Charandabi, S., and Rezaei Faraz, M., Effect of Layering Layout on The Energy Absorbance of Bamboo-Inspired Tubular Composites, Journal of Reinforced Plastics and Composites, 2022, pp. 07316844211063865.

[16] Agarwala, M. K., Van Weeren, R., Vaidyanathan, R., Carrasquillo, G., Jamalabad, V., Langrana, N., Safari, A., Garofalini, S. H., and Danforth, S. C., Structural Ceramics by Fused Deposition of Ceramics, Vol. 6, 1995. pp. 1–8.

[17] Agarwala, M. K., Van Weeren, R., Bandyopadhyay, A., Whalen, P. J., Safari and A., Danforth, S. C., Fused Deposition of Ceramics and Metals: An Overview, Proc. Solid Free. Fabr. Symp., 1996, pp. 385–392.

[18] Yang, X., Xie, H., He, Q., Zhou, Z., Xu, X., Zhang, L., and Xie, Z., Study of Thermal Degradation of Binders for Ceramic Injection Melding by TGA-FTIR, Ceram. Int, Vol. 45, No. 8, 2019, pp. 10707–10717.

[19] Momeni, V., Askari, A., Alaei, M.H., Rahimi, A.H., Nekouee, K., and Zangi, H., The Effect of Powder Loading and Binder System on The Mechanical, Rheological and Microstructural Properties Of 4605 Powder in MIM Process, Transactions of the Indian Institute of Metals, Vol. 72, No. 5, 2019, pp. 1245-1254.

[20] He, Q., Jiang, J., Yang, X., Zhang, L., Zhou, Zh., Zhong, Y., and Shen, Zh., Additive Manufacturing of Dense Zirconia Ceramics by Fused Deposition Modelling Via Screw Extrusion, Journal of the European Ceramic Society, Vol. 41, 2021, pp. 1033–1040.

[21] Boparai, K. S., Singh, R., and Singh, H., Development of Rapid Tooling Using Fused Deposition Modelling: A Review, Rapid Prototyping Journal, Vol. 22, No. 2, 2016, pp. 281–299.

[22] Huang, B., Liang, S., and Qu, X., The Rheology of Metal Injection Melding, J. Mater. Process. Technol., Vol. 137, No. 1, 2003, pp. 132–137.

[23] Gülsoy, H. Ö., German, R. M., Production of Micro-Porous Austenitic Stainless Steel by Powder Injection Molding, Scr. Mater., Vol. 58, No. 4, 2008, pp. 295–298.

[24] Supriadi, S., Baek, E. R., Choi, C. J., and Lee, B. T., Binder System for STS 316 Nano-Powder Feedstocks in Micro-Metal Injection Molding, J. Mater. Process. Technol., Vol. 187–188, 2007, pp. 270–273.

[25] Onbattuvelli, V. P., Enneti, R. K., Park, S. J., and Atre, S. V., The Effects of Nanoparticle Addition on SiC and AlN Powder-Polymer Mixtures: Packing and Flow Behavior, Int. J. Refract. Met. Hard Mater., Vol. 36, 2013, pp. 183–190.

[26] Bellini, A., Bertoldi, M., Liquefier Dynamics in Fused Deposition Modelling, Journal of Manufacturing Science and Engineering, Vol. 126, 2004, pp. 237-246.

[27] Sa'ude, N., Ibrahim, M., and Ibrahim, M. H. I., Melt Flow Behavior of Polymer Matrix Extrusion for Fused Deposition Modeling (FDM), Vol. 660, 2014, pp. 89–93, AMM.

[28] Cobos, C. M., Garzón, L., López Martinez, J., Fenollar, O., and Ferrandiz, S., Study of Thermal and Rheological Properties of PLA Loaded with Carbon and Halloysite Nanotubes for Additive Manufacturing, Rapid Prototyping Journal, Vol. 25 No. 4, 2019, pp. 738-743.

[29] Ramanath, H. S., Chua, C. K., and Leong, K. F., Melt Flow Behaviour of Poly-I Caprolactone in Fused Deposition Modelling, Journal of Material Science, Materials in Medicine, Vol. 19, No. 7, 2007, pp. 2541-2550.

[30] Nikzad, M., Masood, S. H., Sbarski, I., and Groth, A., Thermo-Mechanical Properties of a Metal-Filled Polymer Composite for Fused Deposition Modelling Applications, In: Proceedings of 5th Australasian Congress on Applied Mechanics, Brisbane, Australia: Australian Congress on Applied Mechanics, 2007.

[31] Sotomayor, M. E., Várez, A., and Levenfeld, B., Influence of Powder Particle Size Distribution on Rheological Properties of 316L Powder Injection Moulding Feedstocks, Powder Technol., Vol. 200, No. 1–2, 2010, pp. 30–36.

[32] Atre, S. V., Weaver, T. J., and German, R. M., Injection Molding of Metals and Ceramics, Metal Powder Industries Federation, 1998.

[33] Ho, Y. L., Lin, S. T., Debinding Variables Affecting the Residual Carbon Content of Injection-Molded Fe-2 Pct Ni steels, Metall. Mater. Trans. A, Vol. 26, No. 1, 1995, pp. 133–142.

[34] Matsuda, M., Miura, H., Mechanical Properties of Injection Molded Fe-6% Ni-0.4% C Steels with Varying Mo Contents of 0.5 to 2%, Met. Mater. Int., Vol. 9, No. 6, 2003, pp. 537–542.

[35] Ahn, S., Park, S. J., Lee, S., Atre, S. V., and German, R. M., Effect of Powders and Binders on Material Properties and Melding Parameters in Iron and Stainless-Steel Powder Injection Melding Process, Powder Technology, Vol. 193, 2009, pp. 162-169.

[36] Lin, K., Wear Behavior and Mechanical Performance of Metal Injection Molded Fe–2Ni Sintered Components, Mater. Des., Vol. 32, No. 3, 2011, pp. 1273–1282.

[37] Klainerman, S., Majda, A., CompressibL2e and IncompressibL2e fL2uids, Communications in Pure AppL2ied Mathematics, Vol. 35, 1982, pp.629-651.

[38] German, R. M., Bose, A., Injection Molding of Metals and Ceramics, Metal Powder Industries Federation, 1997.

[39] Sotomayor, M. E., Levenfeld, B., and Várez, A., Powder Injection Moulding of Premixed Ferritic and Austenitic Stainless-Steel Powders, Mater. Sci. Eng. A, Vol. 528, No. 9, 2011, pp. 3480–3488.

Preparation of Papers - Paper Title

Author 1*
Department of Xxxxxxx Engineering,
University of Xxxxxxxx, Country
E-mail: Jmechanic@iaumajlesi.ac.ir
*Corresponding author

Author 2
Department of Xxxxxxx Engineering,
University of Xxxxxxxx, Country
E-mail: Jmechanic@iaumajlesi.ac.ir

Received: 13 November 2011, Revised: 19 May 2012, Accepted: 23 July 2012

Abstract: These instructions give you guidelines for preparing papers for International Journal of Advanced Design and Manufacturing Technology. Use this document as a template if you are using Microsoft Word. Otherwise, use this document as an instruction set. This first paragraph is formatted in the abstract style. Abstracts are required only for regular, full-length papers. Be sure to define all symbols used in the abstract, and do not cite references in this section. Do not delete the blank line immediately above the abstract; it sets the footnote at the bottom of this column. Page margins are 2.26 cm top and 2.54 down; 1.69 cm gutter.

Keywords: About four key words or phrases in alphabetical order, separated by commas

Reference: to this paper should be made as follows: Author 1 and Author 2, ‘Paper Title’, Int J of Advanced Design and Manufacturing Technology, Vol. 2/No. 1, 2008, pp. 43–54, .

Biographical notes: T. H. Mohamadi received his PhD in Mechanical Engineering from University of IAU, Science and Research Branch, 2003. He is currently Assistant Professor at the Department of Mechanical Engineering, Majlesi University, Isfahan, Iran. His current research interest includes Rapid prototyping and Rapid Tooling. **B. M. Mansori** is Associate Professor of Mechanical engineering at the University of Majlesi, Iran. She received her PhD in Mechanical engineering from Isfahan University of Iran and a BSc in Manufacturing from the University of MIT, USA. Her current research focuses on fluid mechanics, thermodynamics and heat transfer.

NOTE AUTHORS

1 INTRODUCTION

This document is a template for Word (doc) versions. If you are reading a paper version of this document, so you can use it to prepare your manuscript. When you open template.doc, select "Page Layout" from the "View" menu in the menu bar (View | Page Layout), which allows you to see the footnotes. Then type over sections of template.doc or cut and paste from another document and then use mark up styles. The pull-down style menu is at the left of the Formatting Toolbar at the top of your Word window (for example, the style at this point in the document is "Text"). Highlight a section that you want to designate with a certain style, then select the appropriate name on the style menu. The style will adjust your fonts and line spacing. Do not change the font sizes or line spacing to squeeze more text into a limited number of pages. To insert images in Word, position the cursor at the insertion point and either use Insert | Picture | From File or copy the image to the Windows clipboard and then Edit | Paste Special | Picture (with "Float over text" unchecked). ADMT will do the final formatting of your paper.

2 PROCEDURE FOR PAPER SUBMISSION

All manuscripts are to be submitted online at MJME.ir. Select "Submit to ADMT," then click "Start New." Once you enter your e-mail address, you will receive an e-mail message containing your tracking number and password. This information will allow you to track your manuscript's status, update submission data, upload your manuscript and subsequent revisions, and communicate with the editors, through your Author Status Page, at anytime during the publication process. After entering all required submission data, you must use the "Upload Manuscript" feature of the Author Status Page to upload your submission. Remember that your document must be double spaced before you upload it. Please be sure the name of the file you upload for processing is short and simple (i.e., "msc12345.doc") with no spaces, tildes, symbols, or other unusual characters. Authors are encouraged to upload PDF and doc files. Failure to meet these requirements could result in a processing error that would require you to re-upload your manuscript. Once you have uploaded your manuscript, please inspect the file for accuracy. This step is required to complete your submission. If you experience difficulties with the upload and/or conversion of your manuscript, please submit your manuscript electronically for review as e-mail attachments. (jmechanic@iaumajlesi.ac.ir or journalmechanic@gmail.com)

3 EQUATIONS, NUMBERS, SYMBOLS, AND ABBREVIATIONS

Equations are centred and numbered consecutively, with equation numbers in parentheses flush right, as in Eq. (1). Insert a blank line on either side of the equation. First use the equation editor to create the equation. If you are using Microsoft Word, use either the Microsoft Equation Editor or the Math Type add-on (http://www.mathtype.com) for equations in your paper, use the function (Insert>Object>Create New>Microsoft Equation or Math Type Equation) to insert it into the document. Please note that "Float over text" should not be selected. To insert the equation into the document, do the following:

1. Select the "Equation" style from the pull-down formatting menu and hit "tab" once.
2. Insert the equation, hit "tab" again,
3. Enter the equation number in parentheses.

A sample equation is included here, formatted using the preceding instructions. To make your equation more compact, you can use the solid us (/) or appropriate exponents when the expression is five or fewer characters. Use parentheses to avoid ambiguities in denominators.

$$\int_0^{r_2} F(r,\varphi)\, dr\, d\varphi = [\sigma r_2 / (2\mu_0)] \cdot \int_0^{\infty} \exp(-\lambda\,|z_j - z_i\,|)\,\lambda^{-1}\, J_1(\lambda r_2)\, J_0(\lambda r_i)\, d\lambda\,. \tag{1}$$

Be sure that the symbols in your equation are defined before the equation appears, or immediately following. Italicize symbols (T might refer to temperature, but T is the unit tesla). Refer to "Eq. (1)," not "(1)" or "equation (1)" except at the beginning of a sentence: "Equation (1) is…" Equations can be labeled other than "Eq." should they represent inequalities, matrices, or boundary conditions. If what is represented is really more than one equation, the abbreviation "Eqs." can be used. Define abbreviations and acronyms the first time they are used in the main text. Very common abbreviations such as SI, ac, and dc do not have to be defined. Abbreviations that incorporate periods should not have spaces: write "P.R.," not "P. R." Delete periods between initials if the abbreviation has three or more initials; e.g., U.N. but ESA. Do not use abbreviations in the title unless they are unavoidable.

4 GENERAL GRAMMAR AND PREFERRED USAGE

Use only one space after periods or colons. Hyphenate complex modifiers: "zero-field-cooled magnetization." Avoid dangling participles, such as, "Using Eq. (1), the potential was calculated." [It is not clear who or what used

Eq. (1).] Write instead “The potential was calculated using Eq. (1),” or “Using Eq. (1), we calculated the potential.”Use a zero before decimal points: “0.25,” not “.25.” Use “cm2,” not “cc.” Indicate sample dimensions as “0.1 cm × 0.2 cm,” not “0.1 x 0.2 cm2.” The preferred abbreviation for “seconds” is “s,” not “sec.” Do not mix complete spellings and abbreviations of units: use “Wb/m2” or “webers per square meter,” not “webers/m2.” When expressing a range of values, write “7–9,” not “7~9.”A parenthetical statement at the end of a sentence is punctuated outside of the closing parenthesis (like this). (A parenthetical sentence is punctuated within parenthesis.) In American English, periods and commas are placed within quotation marks, like “this period.” Other punctuation is “outside”! Avoid contractions; for example, write “do not” instead of “don’t.” The serial comma is preferred: “A, B, and C” instead of “A, B and C.” If you wish, you may write in the first person singular or plural and use the active voice (“I observed that…” or “We observed that…” instead of “It was observed that…”). Remember to check spelling. If your native language is not English, please ask a native English-speaking colleague to proofread your paper. The word “data” is plural, not singular (i.e., “data are,” not “data is”). The subscript for the permeability of vacuum μ0 is zero, not a lowercase letter “o.” The term for residual magnetization is “remanence”; the adjective is “remanent”; do not write “remnance” or “remnant.” The word “micrometer” is preferred over “micron” when spelling out this unit of measure. A graph within a graph is an “inset,” not an “insert.” The word “alternatively” is preferred to the word “alternately” (unless you really mean something that alternates). Use the word “whereas” instead of “while” (unless you are referring to simultaneous events). Do not use the word “essentially” to mean “approximately” or “effectively.” Do not use the word “issue” as a euphemism for “problem.” When compositions are not specified, separate chemical symbols by en-dashes; for example, “NiMn” indicates the intermetallic compound Ni0.5Mn0.5 whereas “Ni–Mn” indicates an alloy of some composition NixMn1-x. Be aware of the different meanings of the homophones “affect” (usually a verb) and “effect” (usually a noun), “complement” and “compliment,” “discreet” and “discrete,” “principal” (e.g., “principal investigator”) and “principle” (e.g., “principle of measurement”). Do not confuse “imply” and “infer.”Prefixes such as “non,” “sub,” “micro,” “multi,” and “"ultra” are not independent words; they should be joined to the words they modify, usually without a hyphen. There is no period after the “et” in the abbreviation “et al.” The abbreviation “i.e.,” means “that is,” and the abbreviation “e.g.,” means “for example” (these abbreviations are not italicized).

5 UNITS

Use either SI (MKS) or CGS as primary units. (SI units are strongly encouraged.) English units may be used as secondary units (in parentheses). This applies to papers in data storage. For example, write “15 Gb/cm^2 (100 Gb/in^2).” An exception is when English units are used as identifiers in trade, such as “3½ in disk drive.” Avoid combining SI and CGS units, such as current in amperes and magnetic field in oersteds. This often leads to confusion because equations do not balance dimensionally. If you must use mixed units, clearly state the units for each quantity in an equation. The SI unit for magnetic field strength H is A/m. However, if you wish to use units of T, either refers to magnetic flux density B or magnetic field strength symbolized as μ0H. Use the center dot to separate compound units, e.g., “A·m^2.”

6 FIGURES, TABLES, AND OTHER IMAGES

Insert tables and figures within your document either scattered throughout the text or all together at the end of the file. Use the Table drop-down menu to create your tables; do not insert your figures in text boxes. Figures should have no background, borders, or outlines. In the electronic template, use the “Figure” style from the pull-down formatting menu to type caption text. You may also insert the caption by going to the Insert menu and choosing Caption. Make sure the label is “Fig.,” and type your caption text in the box provided. Captions are bold with a single tab (no hyphen or other character) between the figure number and figure description. See the Table 1 example for table style and column alignment. If you wish to centre tables that do not fill the width of the page, simply highlight and “grab” the entire table to move it into proper position.

Table 1 Transitions selected for thermometry

ν″	Frequency, cm^{-1}	FJ, cm^{-1}	Gν, cm^{-1}
0	44069.416	73.58	948.66
1	42229.348	73.41	2824.76
2	40562.179	71.37	4672.68
0	42516.527	1045.85	948.76

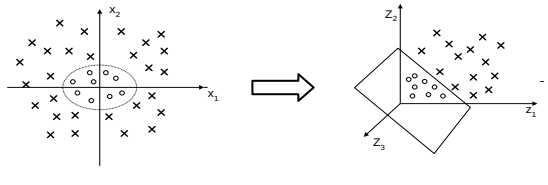

Fig. 1 Mapping nonlinear data to a higher dimensional feature space

Place figure captions below all figures. If your figure has multiple parts, include the labels "a)," "b)," etc., below and to the left of each part, above the figure caption. Please verify that the figures and tables you mention in the text actually exist. When citing a figure in the text, use the abbreviation "Fig." except at the beginning of a sentence. Do not abbreviate "Table." Number each different type of illustration (i.e., figures, tables, images) sequentially with relation to other illustrations of the same type. Figure axis labels are often a source of confusion. Use words rather than symbols wherever possible. As in the Fig. 1 example in this document, write the quantity "Magnetization" rather than just "M." Do not enclose units in parentheses, but rather separate them from the preceding text by commas. Do not label axes only with units. As in Fig. 1, for example, write "Magnetization, A/m" or "Magnetization, A · m−1," not just "A/m." Do not label axes with a ratio of quantities and units. For example, write "Temperature, K," not "Temperature/K." Multipliers can be especially confusing. Write "Magnetization, kA/m" or "Magnetization, 10^3A/m." Do not write "Magnetization (A/m) × 1000" because the reader would not then know whether the top axis label in Fig. 1 meant 16000 A/m or 0.016 A/m. Figure labels must be legible (approximately 8–12 point type).

7 CONCLUSION

Although a conclusion may review the main points of the paper, it must not replicate the abstract. A conclusion might elaborate on the importance of the work or suggest applications and extensions. Do not cite references in the conclusion as all points should have been made in the body of the paper. Note that the conclusion section is the last section of the paper to be numbered. The appendix (if present), acknowledgment, and references are listed without numbers.

8 APPENDIX OR NOMENCLATURE

Appendix or nomenclature, if needed, appears before the acknowledgements.

ACKNOWLEDGMENTS

The preferred spelling of the word "acknowledgment" in American English is without the "e" after the "g." Avoid expressions such as "One of us (S.B.A.) would like to thank…" Instead, write "F. A. Author thanks…" Sponsor and financial support acknowledgments are also to be listed in the "acknowledgments" section.

REFERENCES

Number citations consecutively in square brackets [1]. The sentence punctuation follows the brackets [2]. Multiple references [2], [3] are each numbered with separate brackets [1–3]. When citing a section in a book, please give the relevant page numbers [2]. In sentences, refer simply to the reference number, as in [3]. Do not use "Ref. [3]" or "reference [3]" except at the beginning of a sentence: "Reference [3] shows ...." Please note that the references at the end of this document are in the preferred referencing style. All references should be in 9-point font, with reference numbers inserted in superscript immediately before the corresponding reference. You are not required to indicate the type of reference; different types are shown here for illustrative purposes only.

Periodicals

[1] Vatistas, G. H., Lin, S., and Kwok, C. K., "Reverse Flow Radius in Vortex Chambers," AIAA Journal, Vol. 24, No. 11, 1986, pp. 1872- 1873.

[2] Dornheim, M. A., "Planetary Flight Surge Faces Budget Realities," Aviation Week and Space Technology, Vol. 145, No. 24, 9 Dec. 1996, pp. 44–46.

[3] Terster, W., "NASA Considers Switch to Delta 2," Space News, Vol. 8, No. 2, 13-19 Jan. 1997, pp., 1- 18.

All of the preceding information is required. The journal issue number ("No. 11" in Ref. 1) is preferred, but the month (Nov.) can be substituted if the issue number is not available. Use the complete date for daily and weekly publications. Transactions follow the same style as other journals; if punctuation is necessary, use a colon to separate the transactions title from the journal title.

Books

[4] Peyret, R., and Taylor, T. D., Computational Methods in Fluid Flow, 2nd ed., Springer-Verlag, New York, 1983, Chaps. 7, 14.

[5] Oates, G. C. (ed.), Aerothermodynamics of Gas Turbine and Rocket Propulsion, AIAA Education Series, AIAA, New York, 1984, pp. 19- 136.

[6] Volpe, R., "Techniques for Collision Prevention, Impact Stability, and Force Control by Space Manipulators," Teleoperation and Robotics in Space, edited by S. B. Skaar and C. F. Ruoff, Progress in Astronautics and Aeronautics, AIAA, Washington, DC, 1994, pp. 175–212.

Publisher, place, and date of publication are required for all books. No state or country is required for major cities: New York, London, Moscow, etc. A differentiation must always be made between Cambridge, MA, and Cambridge, England, UK. Note that series titles are in Roman type.

Proceedings

[7] Thompson, C. M., "Spacecraft Thermal Control, Design, and Operation," AIAA Guidance, Navigation, and Control Conference, CP849, Vol. 1, AIAA, Washington, DC, 1989, pp. 103–115

[8] Chi, Y., (ed.), Fluid Mechanics Proceedings, SP-255, NASA, 1993.

[9] Morris, J. D., "Convective Heat Transfer in Radially Rotating Ducts," Proceedings of the Annual Heat Transfer Conference, edited by B. Corbell, Vol. 1, Inst. of Mechanical Engineering, New York, 1992, pp. 227–234.

Reports, Theses, and Individual Papers

[10] Chapman, G. T., and Tobak, M., "Nonlinear Problems in Flight Dynamics," NASA TM-85940, 1984.

[11] Steger, J. L., Jr., Nietubicz, C. J., and Heavey, J. E., "A General Curvilinear Grid Generation Program for Projectile Configurations," U.S. Army Ballistic Research Lab., Rept. ARBRL-MR03142, Aberdeen Proving Ground, MD, Oct. 1981.

[12] Tseng, K., "Nonlinear Green's Function Method for Transonic Potential Flow," Ph.D. Dissertation, Aeronautics and Astronautics Dept., Boston Univ., Cambridge, MA, 1983.

Government agency reports do not require locations. For reports such as NASA TM-85940, neither insert nor delete dashes; leave them as provided. Place of publication should be given, although it is not mandatory, for military and company reports. Always include a city and state for universities. Papers need only the name of the sponsor; neither the sponsor's location nor the conference name and location are required. Do not confuse proceedings references with conference papers.

Electronic Publications

CD-ROM publications and regularly issued, dated electronic journals are permitted as references. Archived data sets also may be referenced as long as the material is openly accessible and the repository is committed to archiving the data indefinitely. References to electronic data available only from personal Web sites or commercial, academic, or government ones where there is no commitment to archiving the data are not permitted in the reference list.

[13] Richard, J. C., and Fralick, G. C., "Use of Drag Probe in Supersonic Flow," AIAA Meeting Papers on Disc [CD-ROM], Vol. 1, No. 2, AIAA, Reston, VA, 1996.

[14] Atkins, C. P., and Scantelbury, J. D., "The Activity Coefficient of Sodium Chloride in a Simulated Pore Solution Environment," Journal of Corrosion Science and Engineering [online journal], Vol. 1, No. 1, Paper 2, URL: http://www.cp/umist.ac.uk/JCSE/vol1/vol1.html [cited 13 April 1998].

[15] Vickers, A., "10-110 mm/hr Hypodermic Gravity Design A," Rainfall Simulation Database [online database], URL: http://www.geog.le.ac.uk/bgrg/lab.htm [cited 15 March 1998].

.

Always include the citation date for online references. Break Web site addresses after punctuation, and do not hyphenate at line breaks.

Computer Software

[16] TAPP, Thermochemical and Physical Properties, Software Package, Ver. 1.0, E. S. Microware, Hamilton, OH, 1992.

Include a version number and the company name and location of software packages.

Patents

Patents appear infrequently. Be sure to include the patent number and date.

[17] Scherrer, R., Overholster, D., and Watson, K., Lockheed Corp., Burbank, CA, U.S. Patent Application for a "Vehicle," Docket No. P-01-1532, filed 11 Feb. 1979.

Private Communications and Web Sites

References to private communications and personal Web site addresses are not permitted. Private communications can be defined as privately held unpublished letters or notes or conversations between an author and one or more individuals. Depending on the circumstances, private communications and Web site addresses may be incorporated into the main text of a manuscript or may appear in footnotes.

Unpublished Papers and Books

Unpublished works can be used as references as long as they are being considered for publication or can be located by the reader (such as papers that are part of an archival collection). If a journal paper or a book is being considered for publications choose the format that reflects the status of the work (depending upon whether it has been accepted for publication):

[18] Doe, J., "Title of Paper," Name of Journal (to be published).

[19] Doe, J., "Title of Chapter," Name of Book, edited by Publisher's name and location (to be published).

[20] Doe, J., "Title of Work," Name of Archive, Univ. (or organization) Name, City, State, Year (unpublished).

Unpublished works in an archive must include the name of the archive and the name and location of the university or other organization where the archive is held. Also include any cataloging information that may be provided. Always query for an update if a work is about to be published